OXIDATION AND METASOMATISM OF LITHOSPHERIC MANTLE BENEATH THE SOUTHERN SOUTH AMERICA

by

Jian Wang, B.Sc., M.Sc.

Thesis submitted to the

Faculty of Graduate & Postdoctoral Studies

in partial fulfillment of the requirements for the

Ph.D. degree in the Earth Sciences

Ottawa-Carleton Geoscience Centre

and

University of Ottawa

Ottawa, Canada

May, 2007

Your file Votre référence
ISBN: 978-0-494-49403-5
Our file Notre référence
ISBN: 978-0-494-49403-5

uOttawa

L'Université canadienne
Canada's university

FACULTÉ DES ÉTUDES SUPÉRIEURES ET POSTOCTORALES

uOttawa

L'Université canadienne
Canada's university

FACULTY OF GRADUATE AND POSDOCTORAL STUDIES

Jian Wang

AUTEUR DE LA THÈSE / AUTHOR OF THESIS

Ph.D. (Earth Sciences)

GRADE / DEGREE

Department of Earth Sciences

FACULTÉ, ÉCOLE, DÉPARTEMENT / FACULTY, SCHOOL, DEPARTMENT

Oxidation and Metasomatism of Lithospeheric Mantle Beneath the Southern South America

TITRE DE LA THÈSE / TITLE OF THESIS

Kéiko Hattori

DIRECTEUR (DIRECTRICE) DE LA THÈSE / THESIS SUPERVISOR

CO-DIRECTEUR (CO-DIRECTRICE) DE LA THÈSE / THESIS CO-SUPERVISOR

EXAMINATEURS (EXAMINATRICES) DE LA THÈSE / THESIS EXAMINERS

Keith Bell

Anthony Fowler

Dantel Canil

John Percival

Gary W. Slater

Le Doyen de la Faculté des études supérieures et postdoctorales / Dean of the Faculty of Graduate and Postdoctoral Studies

Summary

Cerro del Fraile and Pali Aike are the two Quaternary alkali basalt fields located ~250 and >400 km east to the western margin of the South American continent, respectively. The fields are the southernmost part of the Neogene Patagonian plateau basalt fields which were formed in response to the subduction of Chile ridge since middle Miocene.

This thesis has been presented as four papers (Chapters 1, 2, 3, and 4), each of the first three chapters written to address different themes of the research regarding oxidation state and metasomatism of lithospheric mantle beneath the southern South America. Chapter 1 reports the different metasomatic styles of sub-arc mantle peridotites from Cerro del Fraile alkali basalt field by fluids released from subducted slab, basaltic magma from underlying asthenospheric mantle, and the slab-melt. This chapter further discusses the changes of oxidation state because of the metasomatism. Chapter 2 is dealing with the origin and oxidation state of the subcontinental lithospheric mantle (SCLM) beneath Pali Aike alkali basalt field. This chapter also reports the characteristics and effects on oxidation state of metasomatism by an asthenospheric mantle-derived melt. Chapter 3 focuses on the origin of a particular rock, garnet orthopyroxenites from Pali Aike alkali basalt field, and discusses in detail the mobility of siderophile and chalcophile elements during metasomatism by the asthenospheric melt. Each chapter represents an independent paper submitted to refereed journal. Chapter 4 is a summary of my contributions. The method of presentation introduces some unavoidable redundancies, especially with respective to geological settings of study areas and the description of analytical methods.

Quaternary basalts in the Cerro del Fraile area contain two types of mantle xenoliths; coarse-grained (2-5 mm) C-type spinel harzburgites and lherzolites, and fine-grained (0.5-2 mm) intensely metasomatized F-type spinel lherzolites. C-type xenoliths show high Mg in olivine (Fo = 90-91) and a range in Cr# (0.17-0.34) in spinel. Two C-type samples contain solidified patches of melt that is now composed of minute grains of plagioclase + Cr-spinel + clinopyroxene + olivine. These patches of melts formed from pargasitic amphibole by decompression melting. High Ti contents and occurrence of relict Cr-spinel in these melts indicate that the amphibole formed from

spinel by interaction with the Ti-rich parental magma of the websterite veinlets. The fO_2 values of these two C-type xenoliths are low, ranging from ΔFMQ-0.2 to -0.4, consistent with their metasomatism by an asthenospheric mantle-derived melt. The rest of the C-type samples are free of patch "melt", but show cryptic metasomatism by slab-derived aqueous fluids, which produced high concentrations of fluid-mobile elements in clinopyroxenes, and higher fO_2 ranging from ΔFMQ +0.1 to +0.3.

F-type lherzolites are intensely metasomatized to form spinel with low Cr# (~ 0.13) and silicate minerals with low MgO; olivine (Fo = ~ 84), orthpyroxene [Mg# = Mg/(Mg + ΣFe) = ~ 0.86] and clinopyroxene (Mg# = ~ 0.88). Patches of "melt" are common in F-type samples and their compositions are also similar to pargasitic amphibole with low TiO_2 (< 0.56 wt%), Cr_2O_3 (< 0.55 wt%) and MgO (< 16.3 wt%). Low Mg# values of silicate minerals including the amphibole, together with the high ratios of Sr/Y and light rare earth elements (REE)/heavy REE in clinopyroxenes, suggest that the metasomatic agent was most likely a slab melt. F-type xenoliths show relatively low fO_2 (ΔFMQ-0.9 to -1.1) compared to C-type xenoliths and this is explained by the fusion of organic-rich sediments overlying the slab during the slab melt. The fusion of such wet sediments likely produced CH_4-rich fluids and reduced melts, that mixed with the slab melt. High U and Th in bulk rocks and clinopyroxene support the proposed interpretation.

Mantle xenoliths in the Quaternary Pali Aike alkaline basalts include lherzolites and harzburgites with and without garnet. The texture and mineralogy suggest that garnet peridotites formed from spinel peridotites due to cooling and/or pressure increase during or after stablization below the Paleozoic continental crust.

The values of fO_2 for the entire Pali Aike xenolith samples range from FMQ-0.33 to +0.75, which overall overlap those of abyssal peridotites, are lower than those for sub-arc mantle peridotites. The fO_2 data, together with the bulk rock major- and trace-element data, suggest that the subcontinental mantle lithosphere below Pali Aike formed through the accretion of oceanic lithosphere.

The metasomatism observed in the Pali Aike xenoliths reflect recent infiltration of

asthenosphere-derived melt through a slab window. The metasomatism resulted in the formation of Ti-phlogopite, Ti-amphibole, and ilmenite, and lowering of Mg and enrichment of Ti in bulk rocks and minerals. Extensive metasomatism also led to the replacement of olivine by orthopyroxene, forming orthopyroxenites. There are no discernible variations in fO_2 values between spinel- and garnet- facies peridotites and between metasomatized and non-metasomatized samples, suggesting the transformation process from spinel to garnet, and the infiltration of metasomatizing melt were not accompanied by changes of fO_2.

Pyroxenites are mainly garnet orthopyroxenites with minor olivine websterites. Orthopyroxenites contain minor, but common Ti-rich minerals and relict grains of olivine and clinopyroxene in secondary orthopyroxene and along the grain boundaries of orthopyroxene. The textural evidence suggests that secondary orthopyroxene in Pali Aike formed at the expense of olivine and clinopyroxene in garnet bearing harzburgites and lherzolites. The secondary orthopyroxene contains abundant fluid inclusions, relatively high TiO_2 (0.20 - 0.59 wt%), moderate Al_2O_3 (2.87 - 5.10 wt%) and Cr_2O_3 (0.09 - 0.48 wt%), and low Mg# (0.845 - 0.892) compared with orthopyroxene in garnet bearing peridotites in the area. The orthopyroxenite was likely formed from garnet bearing peridotites during extensive metasomatism by a Ti-rich melt. Injection of the melt also produced garnet orthopyroxenite veinlets with diffuse boundaries in peridotites. The mineralogy and mineral chemistry of veinlets are similar to those of discrete xenoliths, suggesting that orthopyroxenites form veins and veinlets in peridotites and that discrete orthopyroxenite xenoliths likely represent wide veins in peridotites. The concentrations of Cr, Ni and PGE in orthopyroxenites are high and similar to those of peridotites, suggesting that they are essentially immobile during the metasomatism and that the evolved metasomatizing melt did not introduce these elements to the orthopyroxenites. The melt brought alkalis, Ti, Si, Al, Cu, and S to the orthopyroxenites.

Secondary orthopyroxene in our samples contains higher Ti and Al and lower Mg than secondary orthopyroxene reported from sub-arc mantle peridotites from Avacha (Russia), Iraya (Philippines), and Colorado Plateau (USA) etc. High Ti and low Mg in our samples reflect that of

the metasomatizing melt, which was most likely an evolved alkali melt originated from the underlying asthenospheric mantle.

Acknowledgements

There are many people who provided guidance, support, and encouragement in different ways throughout the course of my PhD., all to whom I am truly thankful.

I would like to especially thank my supervisor Keiko Hattori, who proposed this project and provided constant encouragement and support throughout the thesis. Keiko's willingness and flexibility to always discuss aspects of the project, and her input and help with the thesis allowed for the smooth and timely completion of the project.

This project was funded by research grants from the National Science and Engineering Research Council (NSERC) to Keiko Hattori, which supported all aspects of the project including laboratory procedures. I would like to acknowledge Ontario Graduate Scholarships in Science and Technology (OGSST) as well as scholarships and travel grants from University of Ottawa.

I received technical support from many people including Ron Hartree (XRF), Monika Wilk-Alemany (ICP-MS and laboratory assistance), George Mrazek (thin sections), and Nimal Desilva (Cu and S analysis) at University of Ottawa, Peter Jones (EMP) and Lewis Ling (SEM) at Carleton University, and Lang Shi (EMP) at McGill University. Their assistance in sample analyses or sample preparation is greatly appreciated.

Chapter 1 of the thesis benefited from helpful comments by S. Arai and J. Hoefs. Chapter 2 benefited from helpful discussion with J-P. Li. Chapter 1 and 3 also benefited from helpful suggestions from J.W. Hedenquist before the final submission of these two manuscripts.

Many fellow graduate students and friends in the department of Earth Sciences provide enjoyable company as well as intellectual and scientific support.

Last but not least, I would like to thank my wife, X. Yu and my son Y-F Wang for putting up with nearly four years' separation. Their understanding, constant support, and love allowed me for concentrating on my project in the past four years.

Table of Contents

Chapter 2

Oxidation state of Paleozoic continental lithospheric mantle below southern South America

Chapter 3

Metasomatic origin of garnet orthopyroxenites and mobility of siderophile and chalcophile elements in the subcontinental lithospheric mantle underlying southern South America

Chapter 4

Conclusions

List of Figures

List of Tables

List of Appendices

Introduction

The subduction of Chile ridge since middle Miocene created a slab window between subducted Nazca plate and Antarctica plate. The development of slab window was accompanied by eruption of voluminous Neogene Patagonian plateau basalt field in the interior of the South American continent. Many mantle-derived xenoliths were brought to surface by these basaltic volcanic rocks. These mantle xenoliths provide information related to the origin of the mantle, metasomatism by slab melt/fluids and asthenospheric melt. Studies on these xenoliths also provide information of oxidation conditions of the underlying lithospheric mantle and changes of fO_2 during metasomatism by different agents. For this study, two areas were selected, Cerro del Fraile and Pali Aike. Cerro del Fraile area, ~ 250 km east to the Chile trench and ~ 25 km east to the Andean arc, is the southwestern part of the Patagonian plateau basalt field. Pali Aike area, over 400 km east to the trench and located in the interior of the continent, is the southernmost part of the Patagonian plateau basalt field.

Metasomatism is a process by which the bulk chemical composition of a rock is changed by the introduction of components to an external source or the removal of components to an external source. Mantle metasomatism is common in a variety of settings, and the metasomatizing agents could be slab-derived aqueous fluids, slab-melt, and asthenosphere-derived melt.

Studies of xenoliths from wedges overlying subduction zones suggest that the sub-arc mantle is commonly hydrated and enriched in fluid-soluble alkali and alkali-earth elements (e.g. Arai et al. 2004; Lee 2005). Subduction of young oceanic crust may result in partial melting of slabs themselves, producing adakitic arc magmas (e.g. Defant and Drummond 1990). Mantle wedges above such young hot slabs are metasomatized by slab melt (e.g. Rapp et al. 1999) and may have significantly different compositions compared to those overlying old slabs that dehydrate but do not melt. Most SCLM are variably depleted and their origin is commonly explained by the processes of underplating of mantle plumes (Herzberg 1999), or formation of highly refractory mantle in old wedge mantle (Parman et al. 2004). The mantle peridotites from Off-craton areas are relatively fertile in bulk rock composition compared to sub-arc mantle and typical SCLM and

these peridotites were considered to be derived from oceanic mantle that has been welded to Archean nucliei in plate collisions or interpreted as frozen asthenosphere accreted to the base of the lithosphere (Boyd 1989).

The sub-arc mantle in Cerro del Fraile and the SCLM beneath Pali Aike are relatively fertile, similar to off-craton and abyssal peridotites in both bulk rock and mineral compositions. Mantle xenoliths from both Cerro del Fraile and Pali Aike show evidence of extensive metasomatism by different agents. These metasomatizing events correspond to progressive subduction processes of Nazca plate and Chile ridge, formation of slab-window and upwelling of underlying asthenosphere. Subduction of old Nazca plate produced slab fluids which infiltrated the overlying peridotites. Subduction of the young Nazca plate prior to the subduction of the Chile Ridge likely produced slab melt below the study area, similar to the current production of adakitic magmas in the Austral volcanic zone (AVZ) by the subducted Antarctic plate (Stern and Kilian 1996). Finally, asthenosphere-derived melt through the slab window ascended and metasomatized overlying peridotites. Therefore, mantle xenoliths from the Cerro del Fraile and Pali Aike areas provide samples for the study of the interactions of slab fluid/melt with mantle peridotites, and asthenospheric melt with SCLM, respectively.

Oxidation state of the mantle plays an important role in many chemical and physical processes such as magma genesis, recycling of oceanic lithosphere, and metasomatism (Woodland and Koch 2003). For example, Sub-arc mantle maybe oxidized due to oxidized aqueous fluids released from subducted slab (e.g. Wood et al. 1990; Brandon and Draper 1996; Parkinson and Arculus 1999; Arai et al. 2003), and oxidized sub-arc mantle is conducive for the formation of high sulfur magmas (DeHoog et al. 2004) and giant Au and Cu deposits because metals can be effectively partitioned to partial melt under oxidized condition (Mungall 2002; Hattori and Keith 2001). However, it is not well understood why there is a significant variation in fO_2 in the lithospheric upper mantle, and how fO_2 changes during the processes of partial melting and metasomatic effects.

Chapter 1 and 2 present the mineralogy, mineral compositions and oxidation conditions of

representative samples of mantle xenoliths from Cerro del Fraile and Pali Aike, evaluates the origin of the underlying lithospheric mantle, document different styles of mantle metasomatism, and discusses the change in oxidation state during the metasomatism of the underlying mantle by various metasomatizing agents during the subduction of Nazca plate and Chile ridge.

Orthopyroxenites are common in Pali Aike area, but no studies were conducted to examine their origin because they are usually considered to be cumulates (e.g. Anhaeusser 2001; Maaløe 2005). Recently, secondary orthopyroxene formed after olivine by reacting with Si-rich fluids/melt released from down-going slab has been documented in several mantle wedges (e.g. Smith 2000; Arai et al. 2003, 2004). Silica -rich melt is also considered to be responsible for the high modal abundance of Orthopyroxene in lithospheric upper mantle underlying Archean cratons, such as Kaapvaal and Siberian cratons (Keleman et al. 1998).

Alkali-rich melt is not expected to cause Si enrichment in mantle peridotites because it has low activity of SiO_2. A recent study in western Japan suggests that alkali-rich melt is also capable to produce local enrichment of silica in mantle peridotites when the melt has been evolved to be Si rich (Arai et al. 2006). Chapter 3 reports the bulk rock compositions, mineralogy and mineral chemistry of garnet bearing orthopyroxenites in Quaternary alkali basalts in the Pali Aike area. The data and the textural evidence of rocks and minerals suggest that orthopyroxenites in Pali Aike area formed from garnet bearing peridotites during the injection of asthenospheric mantle-derived, Ti-rich melt.

Statement of original contributions

All figures, data (excluding trace elements of clinopyroxene and major elements of two Cerro del Fraile host basalts and one websterite) and interpretations used throughout this thesis result from my original work. The following represents the major findings of the research.

This research focuses on understanding of the metasomatism and oxidation state of lithospheric upper mantle beneath southern South America through an investigation of the petrology, mineralogy, and geochemistry of samples from the Cerro del Fraile and Pali Aike alkali

basalt fields. Fourty-one unaltered samples were examined for major and trace element geochemistry, PGE analysis, and petrographic studies.

This study has classified the Cerro del Fraile mantle xenoliths into coarse-grained C-type and fine-grained F-type peridotites based on their texture, grain sizes and the metasomatism. For the first time, I discussed the oxidation state of both C- and F-type xenoliths and its relations with metasomatic agents. This study proposes that F-type xenoliths were likely the mantle peridotites metasomatized by a slab-melt.

This research was the first to present a thorough data set of oxidation state of lithospheric mantle beneath southern South America. Based on these fO_2 data, combined with the evidence of mineral and bulk rock compositions of samples, this research supports that the SCLM beneath southern South America formed by accretion of oceanic lithosphere.

Metasomatic orthopyroxenites have been documented from several mantle wedges. This study found that the metasomatism by an asthenospheric melt caused Si-enrichment to form orthopyroxenites although alkali melt commonly has low Si activity. This is also the first systematic documentation of the combined behaviour of Cr, Ni, PGE, S and Cu in SCLM during the metasomatism by asthenospheric mantle-derived melt.

Contributions of collaborators

Dr. C. R. Stern of the University of Colorado at Boulder, USA provided samples from the Pali Aike area. Dr. R. Kilian of the Universität Trier, Germany provided samples from the Cerro del Fraile area and some unpublished data including trace elements of clinopyroxenes and major elements for two host basalts and one websterite. Dr. J-P. Li provided four spinel standards which were used for calibrating spinel compositions in this research.

CHAPTER 1

Metasomatism of sub-arc mantle peridotites below southernmost South America: reduction of fO_2 by slab-melt

Manuscript published in ***Contributions to Mineralogy and Petrology***:

Wang J, Hattori KH, Kilian R, Stern CR (2007) Metasomatism of Sub-arc Mantle Peridotites below Southernmost South America: Reduction of fO_2 by Slab-melt. Contrib Mineral Petrol 153:607-624

Abstract

Quaternary basalts in the Cerro del Fraile area contain two types of mantle xenoliths; coarse-grained (2 - 5 mm) C-type spinel harzburgites and lherzolites, and fine-grained (0.5 - 2 mm) intensely metasomatized F-type spinel lherzolites. C-type xenoliths have high Mg in olivine (Fo = 90 - 91) and a range in Cr# [Cr/ (Cr + Al) = 0.17 - 0.34] in spinel. Two C-type samples contain websterite veinlets and solidified patches of melt that is now composed of minute quenched grains of plagioclase + Cr-spinel + clinopyroxene + olivine. These patches of quenched melts formed by decompression melting of pargasitic amphibole. High Ti contents and common occurrence of relic Cr- spinel in the quenched melts indicate that the amphibole formed from spinel by interaction with the Ti-rich parental magma of the websterite veinlets. The fO_2 values of these two C-type xenoliths range from ΔFMQ-0.2 to -0.4, which is consistent with their metasomatism by an asthenospheric mantle-derived melt. The rest of the C-type samples are free of "melt", but show cryptic metasomatism by slab-derived aqueous fluids, which produced high concentrations of fluid-mobile elements in clinopyroxenes, and higher fO_2 ranging from ΔFMQ +0.1 to +0.3.

F-type lherzolites are intensely metasomatized to form spinel with low Cr# (~ 0.13) and silicate minerals with low MgO; olivine (Fo = ~ 84), orthpyroxene [Mg# = Mg/(Mg + ∑Fe) = ~ 0.86] and clinopyroxene (Mg# = ~ 0.88). Patches of "melt" are common in all F-type samples and their compositions are similar to pargasitic amphibole with low TiO_2 (< 0.56 wt%), Cr_2O_3 (< 0.55 wt%) and MgO (< 16.3 wt%). Low Mg# values of silicate minerals including the amphibole suggest that the metasomatic agent is most likely a slab melt. This is supported by high ratios of Sr/Y and light rare earth elements (REE)/heavy REE in clinopyroxenes. F-type xenoliths show relatively low fO_2 (ΔFMQ-0.9 to -1.1) compared to C-type xenoliths and this is explained by the fusion of organic-rich sediments overlying the slab during the slab melt. Trench-fill sediments in the area are high in organic matter. The fusion of such wet sediments likely produced CH_4-rich fluids and reduced melts, that mixed with the slab melt. High U and Th in bulk rocks and clinopyroxene support the proposed interpretation.

Key words: mantle oxidation state, mantle wedges, subduction zone, adakites

1.1. Introduction

Most arc magmas are generated by partial melting of refractory mantle peridotites in the interior of mantle wedges in response to an influx of water, although the transfer mechanism of water from subducted slabs to the hot interior of the mantle wedge is still in debate (e.g. Mibe et al. 1999; Hattori and Guillot 2003). Mantle xenoliths from wedges overlying subduction zones are very rare, but studies of these xenoliths suggest that the sub-arc mantle is commonly hydrated and enriched in fluid-soluble alkali and alkali-earth elements (e.g. Brandon and Draper 1996; Arai et al. 2004; Lee 2005; Ishimaru et al. 2007). Metasomatism in the sub-arc mantle is commonly accompanied by oxidation, which probably reflects the oxidized nature of aqueous fluids released from subducted slab (e.g. Wood et al. 1990; Ionov and Wood 1992; Brandon and Draper 1996; Parkinson and Arculus 1999; Arai et al. 2003).

Subduction of young oceanic crust may result in partial melting of slabs themselves, producing adakitic arc magmas (e.g. Defant and Drummond 1990). Mantle wedges above such young hot slabs are metasomatized by slab melt (Rapp et al. 1999) and may have significantly different compositions compared to those overlying old slabs that dehydrate but do not melt. Mantle xenoliths from the Cerro del Fraile Quaternary basalts, in the southern Patagonia plateau lavas field (Fig. 1-1), provide samples for the study of the interaction of slab melt with mantle peridotites. Their host basalts formed in response to upwelling asthenospheric mantle through a slab window that developed due to the subduction of the Chile Ridge. Subduction of the young Nazca plate prior to the subduction of the Chile Ridge likely produced slab melt below the study area, similar to the current production of adakitic magmas in the AVZ by the subducted Antarctic plate (Stern and Kilian 1996).

This paper presents the mineralogy, mineral compositions and oxidation conditions of representative samples of mantle xenoliths from Cerro del Fraile, documents different styles of mantle metasomatism, and discusses the change in oxidation state during the metasomatism of

the underlying mantle.

1.2. Geological Setting

The late Cenozoic tectonic history of southernmost South America is explained by the subduction of the Nazca and Antarctic Plates and Chile Ridge beneath the South American Plate. Subduction of the Nazca plate resulted in the formation of a continental arc along the west coast of southernmost South America in Miocene time. This ended when the Chile Ridge collided with the trench at ~ 14 - 15 Ma (Cande and Leslie 1986), forming a triple junction between the South American, Nazca, and Antarctic plates near the southern tip of South America. The triple Junction has since migrated northwards to its present position, ~ 46 °S (Fig. 1-1a; Cande and Leslie 1986). Ridge subduction resulted in the formation of a slab window and the extensive eruption of plateau lavas from late Miocene to Recent (e.g. Ramos and Kay 1992; Gorring et al. 1997; D'Orazio et al. 2000).

In Miocene time, the subducted Nazca Plate became progressively younger as the Chile Ridge approached the trench, likely produced slab melt below the Cerro del Fraile area. Indeed, 13 Ma adakitic magmas produced by the subduction of young Nazca plate have been documented farther to the north at Cerro Pampa by Kay et al. (1993). This was followed by the arrival of the subducted Chile ridge, which resulted in the development of the slab window and allowed upwelling of asthenospheric mantle, producing Patagonian plateau alkali basalt in the area (Fig. 1-1). Subduction of young Antarctic plate west of the ridge now produces adakitic magmas in the Andean Austral Volcanic Zone (AVZ; Stern and Kilian 1996), located ~ 25 km west of the Cerro del Fraile area (Fig. 1-1).

1.3. Xenolith petrography and petrology

Mantle xenoliths of 2 to 30 cm in size occur in basaltic lava flows and diatreme breccias in the area of Cerro del Fraile. We selected nine representative samples similar to xenolith samples described in Kilian and Stern (2002). All are spinel-facies harzburgites and lherzolites, representing peridotites at relatively shallow depths in the underlying lithospheric mantle.

Adopting the classification of Arai et al. (2004), two types are recognized based on grain size and textures; coarse-grained (2-5 mm) C-type spinel lherzolite and harzburgite (samples Bxe32-I,-II,-III, Bxe11, Bxe11-I, Bxe31-I, Bxe35-I; Fig. 1-2a) and fine to medium-grained (0.5 - 2 mm) F-type spinel lherzolite (samples Bxe1, Bxe22; Fig. 1-2b). C-type xenoliths show protogranular to porphyroclastic textures with large subhedral grains of olivine and/or orthopyroxene. F-type shows a weak foliation due to elongated mineral grains. This likely reflects deformation associated with the re-crystallization of these fine-grained peridotites as has been suggested for fine-grained, foliated peridotites by Arai et al. (2004). Therefore, these two types of xenoliths probably represent different areas in the underlying mantle, consistent with different temperatures of equilibration and fO_2 as described below.

C-type spinel lherzolite (sample Bxe35-I) contains olivine (~ 70 vol%), orthopyroxene (~ 20 vol%), clinopyroxene (~ 5 vol%), and spinel (2 - 3 vol%). C-type harzburgites (samples Bxe32-I, -II, -III, Bxe11, Bxe11-I, and Bxe31-I), contain veins of websterite (Fig. 1-2a). The area free of websterite contains olivine (~ 80 vol%), orthopyroxene (10 - 15 vol%), clinopyroxene (0-5 vol%) and spinel (< 3 vol%). Websterite is coarse-grained (2 - 5 mm) and consists of clinopyroxene (60-70 vol%) and orthopyroxene (30 - 40 vol%) with minor spinel. Fine blobs and lamellae of spinel are common in pyroxenes in websterite. Patches of solidified "melt" are not common in C-type peridotites, but two samples (samples Bxe11 and Bxe11-I) contain solidified "melt" (~ 5 vol%), which forms patches (up to 2 mm), and discontinuous veinlets along grain boundaries (Fig. 1-2c). These "melt" patches are accompanied by abundant sulfides (10 to 20 grains/section) and secondary fluid inclusions in minerals adjacent to these patches.

F-type spinel lherzolites consist of olivine (55 - 60 vol%), orthopyroxene (~ 20 vol%), clinopyroxene (5 - 10 vol%), spinel (~ 5 vol%) and abundant solidified "melt" (~ 10 vol%). Solidified "melt" forms veinlets (< 0.2 mm) and large patches (up to 2 x 2 mm), which are commonly connected by veinlets (Figs. 1-2e, 1-2f).

1.4. Analytical methods

The compositions of minerals were determined using a JEOL 8900 Super Probe at McGill University in wavelength dispersive spectroscopy analysis, and X-ray intensities were simultaneously counted with four analyzers. The operating conditions were 20 kV acceleration voltage, 20 nA beam current, and 1 μm beam size. Counting times of 30 s were used for most elements, but 50 s was required for Ca in orthopyroxene and olivine. Due to heterogeneous distributions of minute crystals in "melt patches", the composition of an area 50 x 50 μm was calculated by dividing the area into four areas and determining the composition of each sub-square using a broad beam of 25 x 25 μm. The ZAF correction procedure by JEOL was applied to raw counts.

Attention was paid to accurate determination of Fe^{3+} contents of spinel because this is critical in calculation of fO_2. The Fe^{3+} contents are commonly calculated assuming the stoichiometric composition of spinel, but spinel may not be stoichiometric. In our study, four secondary spinel standards with known contents of Fe^{3+} were used to calibrate $Fe^{3+}/\Sigma Fe$ of samples (see Wood and Virgo 1989; Woodland et al. 1992). The inter-grain variation of the calibrated ratio was less than 10% based on analysis of 3 to 5 different grains in each sample (Table 1-5), and the repeated determination of $Fe^{3+}/\Sigma Fe$ ratios on one grain show a precision of < 5%. The calibrated ratios are slightly lower than those calculated based on stoichiometry (Fig. 1-3). The fO_2 values were calculated using the olivine-orthopyroxene-spinel oxybarometry of Nell and Wood (1991) and olivine-orthopyroxene-spinel oxybarometry by Ballhaus et al. (1991) (Table 1-5). Average compositions of the cores of grains were used for the fO_2 calculation for each sample. The fO_2 values are presented relative to the FMQ buffer because these values are not significantly affected by either temperatures or pressures. For example, a change in 100 °C or 1 GPa leads to the difference of only ± 0.2 or ± 0.3 in logarithmic unit of fO_2, respectively (Wood et al. 1990). We determined Fe^{3+} in the same way as Woodland et al. (1992), therefore we believe the uncertainty in the $Fe^{3+}/\Sigma Fe$ calculation is about ± 0.025, which also results in an uncertainty in fO_2 of 0.3-0.4 logarithmic units (Woodland et al. 1992). Assuming normal error propagation, the uncertainty in relative fO_2 remains only about ± 0.5 logarithmic units.

The major element compositions of bulk rock xenoliths were determined by X-ray fluorescence spectrometry at University of Heidelberg, Germany, and the trace element contents by inductively coupled plasma mass spectrometry (ICP-MS) at the Memorial University of Newfoundland, Canada. Trace element contents of clinopyroxene were determined by an ICP-MS equipped with a laser ablation system at the Memorial University of Newfoundland, Canada, using the technique described in Taylor et al. (1997).

1.5. Mineral chemistry

1.5.1. Olivine

Olivine grains in C-type lherzolites show Fo values ranging from 90 to 91 with moderate CaO (0.04 -0.08 wt%) and NiO (0.35 - 0.39 wt%), whereas olivine in F-type lherzolite shows lower Fo, ~ 84, and lower CaO (0.03 - 0.04 wt%) and NiO (0.19 - 0.20 wt%) than that in C-type lherzolites (Table 1-1).

1.5.2. Orthopyroxene

Orthopyroxene shows Mg# ranging from 0.91 to 0.92 in C-type and ~ 0.86 in F-type lherzolites (Table 1-1). The values are always higher than Fo of co-existing olivine in each sample, which is consistent with equilibrium Fe-Mg exchange between these phases, as observed in other mantle xenoliths (e.g. Qi et al. 1995; Conceição and Green 2004). Orthopyroxene contains moderate CaO (0.57 - 0.92 wt%) and Al_2O_3 (2.36 - 3.69 wt%) in both C- and F-type xenoliths. Orthopyroxene grains in F-type lherzolites contain higher TiO_2 (~ 0.11 wt%) and lower Cr_2O_3 (0.26-0.30 wt%) than those in C-type lherzolites (< 0.05 wt%TiO_2, 0.40-0.57 wt%Cr_2O_3). Rims (< 50 μm) of orthopyroxene in F-type peridotite have lower Al_2O_3, CaO, Cr_2O_3, and TiO_2, and higher MgO than cores, but the differences are very minor (Table 1-1). The narrow size of rims suggests that they likely formed during the ascent of the xenoliths to the surface. No zoning was found in orthopyroxene in C-type lherzolites (Table 1-1).

1.5.3. Clinopyroxene

Clinopyroxene shows different compositions in F- and C-type xenoliths. Clinopyroxene in

F-type samples have low-Mg# (~ 0.88) with relatively high Al_2O_3 (4.06 - 4.73 wt%), TiO_2 (0.34 - 0.57 wt%), and Na_2O (0.63 - 0.85 wt%), and low Cr_2O_3 (0.46 - 0.66 wt%). Similar to orthopyroxene, rims (< 50 μm) contain lower Al, Ti, Cr and Na, and higher Mg than cores (Table 1-1), but the differences are very minor. Clinopyroxene in C-type xenoliths shows high Mg# (0.91-0.93) with Al_2O_3 (2.97 - 4.09 wt%), TiO_2 (0.16 - 0.23 wt%), and Na_2O (0.51 - 0.89 wt%), and with no apparent compositionally distinct rims.

1.5.4. Spinel

In both C- and F-type xenoliths, spinel occurs as large semihedral grains (<1 mm in C-type; < 0.5 mm in F-type), small grains (<0.5 mm in C-type; <0.2 mm in F-type) along grain boundaries of silicate minerals (Fig. 1-2f), and small (<0.2 mm in C-type; <0.1 mm in F-type) rounded inclusions in olivine and pyroxene (Fig. 1-2f).

Spinel grains in both C- and F-type xenoliths contain low Fe_2O_3 (up to 3.7 wt%; Table 1-1; Fig. 1-5), which is consistent with their origin in mantle peridotites. Spinel in C-type lherzolites shows low Cr# (=Cr/(Cr+Al), 0.17 - 0.34), TiO_2 (< 0.2 wt%) and Fe_2O_3 (2.2 - 3.7 wt%), and a narrow range in the ratios of $Mg/(Mg+Fe^{2+})$ (0.74 - 0.81; Fig. 1-4), They plot in the field of abyssal peridotites on the binary diagram of Cr# and $Mg/(Mg+Fe^{2+})$ (Fig. 1-4) and ternary diagram of Fe^{3+}-Cr-Al (Fig. 1-5). Spinel grains in F-type peridotites show low Cr# (~ 0.13) and $Mg/(Mg+Fe^{2+})$ (~ 0.69). They have much lower TiO_2 (~ 0.07 wt%) and mostly lower Fe_2O_3 (2.5 - 2.8wt%) than those in C-type lherzolite xenoliths. They plot outside or at the margin of the field of abyssal peridotites on the binary and ternary diagrams (Figs. 1-4, 1-5). Spinel inclusions in olivine and pyroxenes are similar in composition to large intergranular grains in the same samples (Table 1-1), suggesting that the grains are all in equilibrium.

1.5.5. Solidified "melt" patches

Solidified patches of "melt" are common in F-type peridotites. Melt patches also occur in two C-type peridotites that contain abundant websterite veins. These "melt" patches in C-type and F-type peridotites show different textures. Patches in the two C-type xenoliths commonly contain coarse spinel grains with embayments (Fig. 1-2c). Patches in F-type xenoliths commonly

show clusters of different mineral assemblage with symplectic texture (Fig. 1-2h), such as clusters of clinopyroxene + spinel, orthopyroxene+ spinel, and plagioclase + spinel + slinopyroxene.

Melt patches in C- and F-type xenoliths contain different assemblages of quenched minute (< 10 μm) minerals. Those in C-type contain plagioclase (30 - 40 vol%), Cr-spinel (2 - 5 vol%), clinopyroxene (40 - 45 vol%) and olivine (10 - 20 vol%) (Figs. 1-2c, 1-2d), whereas the patches in F-type xenoliths contain these minerals plus orthopyroxene (Figs. 1-2g, 1-2h). Spinel grains in the two types show different compositions. Spinel grains in patches of C-type peridotites contain systematically higher Cr# (~ 0.57) than those (Cr# = 0.33 - 0.34) outside the patches, which is consistent with overall high Cr_2O_3 of the composition of patch melt (Table 1-2). On the other hand, spinel in patches of F-type peridotites contains low Cr_2O_3 (< 1 wt%).

Individual mineral phases show compositional variations even within a single patch in both C- and F-type peridotites. The ranges of compositional variation within a single patch are large for clinopyroxene and plagioclase and small for olivine and orthopyroxene. Furthermore, the compositions of pyroxenes and olivine are different from those outside these "melt" patches (Table 1-2) The evidence suggests that melt in patches was rapidly solidified without equilibration.

The compositions of patches of "melt" are different between C- and F-type xenoliths (Table 1-2). Patches in C-type have higher Mg# (~ 0.87), Cr_2O_3 (1.9 wt%) and TiO_2 (1.1 wt%) than those in F-type (Mg#= ~ 0.83, $Cr_2O_3 \leq 0.14$, $TiO_2 \leq 0.13$).

1.6. Equilibrium conditions

1.6.1. Thermobarometry

A good positive correlation between Mg# of cores of coexisting mineral phases outside of melt patches suggests equilibrium among these minerals. This is a valid basis for estimating equilibrium P-T conditions and fO_2 of these xenoliths (Table 1-5). The core compositions of silicate minerals of C-type xenoliths exhibit higher temperatures than those for F-type xenoliths

by 50-150 °C using a given geothermometer. The results support the suggestion that these two types of peridotites originated from different portions of the mantle. When three thermometers are compared, all yielded similar equilibrium temperatures for C-type xenoliths with differences less than 20 °C except for one sample (Bxe35-I). This one sample yielded unusually high temperature (~ 1460 °C) using the Ca-in-Opx thermometer (Table 1-5), a result that was discarded because the other two thermometers gave consistent temperatures of 980 - 1000 °C (Table 1-5). For F-type lherzolites, the two-pyroxene thermometer of Brey and Köhler (1990) yielded temperatures systematically lower by ~ 50 °C than the two-pyroxene thermometer of Wells (1977) and lower by ~ 100 °C than the Ca-in-Opx thermometer of Brey and Köhler (1990) (Table 1-5).

We also calculated temperatures based on the Fe-Mg exchange between olivine and spinel by Ballhaus et al. (1991), but the temperatures are lower by about 100 °C than other results. It is known that olivine-spinel Fe-Mg thermometry may provide unrealistically low temperatures due to low re-equlibration of Fe-Mg exchange at low temperatures (e.g. Sinigoi et al. 1980; De Hoog et al. 2004). These unusually low temperatures have been explained by the lower closure temperature for ion exchange between spinel and olivine than that between two pyroxenes.

The absence of garnet and plagioclase in these spinel peridotites limits their crystallization pressures to between 0.8 and 2 GPa (Qi et al. 1995). A pressure of 1.5 GPa was used in calculating the equilibrium temperatures using the two pyroxene thermometers of Brey and Köhler (1990). A difference of 0.5 GPa can result only in 5-10 °C and 20-30 °C temperature differences for Brey and Köhler's two-pyroxene thermometer and Ca-in-Opx thermometer, respectively.

1.6.2. Oxybarometry

The calculation of fO_2 used the temperature obtained by Wells' two pyroxene thermometer because it has been used for fO_2 calculations of mantle peridotites by many workers and this keeps our calculations consistent with their results. Although different thermometers yielded

different temperatures for F-type xenoliths (Table 1-5), these differences, of ~100 °C, only result in a negligible discrepancy in fO_2, of < 0.2 logarithmic unit. The pressure for the fO_2 calculations is assumed to be 1.5 GPa.

The values of fO_2 were calculated using the equations of Nell and Wood (1991) and Ballhaus et al. (1991) (Table 1-5). The two methods gave comparable fO_2 with differences of less than 0.33 logarithmic unit (Table 1-5), but the oxybarometry of Ballhaus et al. (1991) yielded systematically lower fO_2 for C-type xenoliths and higher values for F-type xenoliths than the oxybarometry of Nell and Wood (1991). This paper uses the fO_2 value based on the equation of Nell and Wood (1991).

C-type peridotite yielded fO_2 ranging from ΔFMQ -0.39 to +0.31 (average ΔFMQ-0.03 ± 0.28) and the values are not correlated with Cr# in spinel (Fig. 1-6; Table 1-5). Two samples with abundant patch "melt" show slightly reduced fO_2, ΔFMQ -0.37 to -0.18. Intensely metasomatized F-type peridotites yield relatively low fO_2 as low as ΔFMQ-1.1 (Fig. 1-6; Table 1-5).

1.7. Discussion

1.7.1. Parental magmas for websterite

Websterite veinlets in C-type peridotites consist of two pyroxenes, minor Al-rich spinel and abundant sulphides (10 grains/section). Abundant fluid inclusions along cracks in olivine and pyroxenes around the websterite veinlets suggest that the parental magmas to these websterite veins contained high concentrations of volatiles. The bulk composition of websterite is also high in TiO_2 (~ 1.1 wt%; Table 1-4) and shows an ocean island basalt-like geochemical signature (Fig. 1-8d) similar to the basalts hosting the xenoliths (Table 1-4). Therefore, the websterite is interpreted as a cumulate of melt derived from the asthenospheric mantle. The development of the slab window and asthenospheric melts that generated the host basalts in the area took place in the past 2 Ma. It is this young event, < 2 Ma, that produced websterite and associated Ti-rich metasomatism.

1.7.2. Origin of patch "melt"

The patches of solidified "melt" could be a melting product of pre-existing minerals or invaded melt from the parental magmas for the host volcanic rocks. The latter possibility is rejected because the compositions of the "melt" patches in both C- and F-type peridotites show high CaO and MgO and low K_2O, which is significantly different from the compositions of host basalts (Tables 1-2 and 1-4). Instead, the compositions of the "melt" patches in both types of xenoliths are similar to those of pargasitic amphibole (Table 1-3), suggesting that these "melt" patches are likely a breakdown product of amphibole. Pargasitic amphibole is common in hydrated peridotite xenoliths from sub-arc mantle, such as Nunivak Island, Alaska (Francis 1976), Megata, Japan (Abe et al. 1998), south Kamchatka, Russia (Arai et al. 2003), and Iraya, Philippines (Arai et al. 2004) (Table 1-3).

Pargasitic amphibole may melt during decompression or heating. Mantle peridotites in the area may have been heated by upwelling asthenospheric mantle during the development of a slab window, but this possibility is discounted because of disequilibrium mineral assemblages and compositions of minerals in individual patches. The melting must have occurred quickly with little re-equilibration time after melting and prior to quenching. Therefore we conclude that rapid rise of these xenoliths to the surface most likely led to decompression melting of the pargasitic amphibole in the xenoliths. Solidified "melt", that also has the compositions similar to pargasitic amphibole, has been reported in mantle xenoliths from other areas and has also been explained by decompressional melting of amphibole. Examples include melts in xenoliths from Nunivak Island, Alaska (Francis 1976), western Victoria, Australia (Yaxley et al. 1997), southeastern Australia (Yaxley and Kamenetsky 1999), and western Eifel, Germany (Shaw and Klügel 2002; Ban et al. 2005).

Kilian and Stern (2002) described veinlets of adakitic "melt" that contain high SiO_2 (> 60 wt%) and Na_2O (> 6 wt%), and low MgO and CaO in xenoliths from Cerro del Fraile (Table 1-4). We did not observe such "melt" in our samples.

1.7.3. Origin of amphibole

The inferred compositions of pargasitic amphiboles are different between F-type and C-type xenoliths (Table 1-2). The latter shows higher Cr_2O_3 (1.9 wt%) and TiO_2 (~ 1.1 wt%) than those in F-type peridotites (Table 1-2). Furthermore, patches in C-type contain relatively large spinel grains with embayment (Fig. 1-2c), suggesting that the pargasitic amphibole likely formed after spinel during their reaction with a metasomatizing agent. Spinel grains in C-type all contain low TiO_2, < 0.15-0.16 wt%, whereas the melt patches in these xenoliths contain high TiO_2, suggesting that the metasomatizing agent contained high TiO_2.

The metasomatizing agent may have been either an aqueous fluid or a melt. In the study area, aqueous fluids could be those released from the subducted slab. Melts may be arc magmas or melts from asthenospheric mantle formed during the development of the slab window that generated the host Cerro del Fraile basalts. Aqueous fluids released from slabs and arc magmas are both low in Ti. Therefore, we discount these possibilities. For example, amphiboles in mantle xenoliths from Nunivak Island are considered to have formed during the reaction of spinel with volatiles released from arc magmas (Francis 1976). These amphiboles show lower Ti contents than those in our C-type xenolith samples (Tables 1-2 and 1-3).

The contents of Ti are high in the websterite veins in amphibole-bearing C-type xenoliths (Table 1-4). Therefore, we suggest that the amphibole in C-type xenoliths formed by reactions with the asthenosphere-derived parental magma for these websterite veins during the development of a slab window. During the metasomatism, Al in pre-existing spinel is incorporated into newly formed amphibole, which resulted in high Cr# of the relict spinel grains.

Pargasitic amphiboles in F-type peridotites contained slightly higher CaO and lower Mg# and Ti compared to amphiboles in C-type (Table 1-2). Furthermore, there is no embayed spinel grain in patches of "melt" or no clinopyroxene grain around the patches. The evidence may suggest that pargasitic amphiboles may have formed at the expense of clinopyroxene. Low Mg# of the amphibole suggests that they likely formed together with other low Mg silicates. Furthermore, the amphibole compositions are similar to those in the xenoliths that were

metasomatized by slab-melt, such as those in Batan Island, Philippines (Schiano et al. 1995; Table 1-3) and Al-augite series xenoliths in north Kamchatka, Russia (Kepezhinskas et al. 1995; Table 1-3). Moreover, minute spinel grains in the "melt" patches are compositionally similar to the Al-Fe-Mg spinel in Al-augite series xenoliths from north Kamchatka arc. Remarkable similarities of amphiboles between Cerro del Fraile F-type samples and mantle xenoliths affected by slab melt suggest that the pargasitic amphiboles in these samples likely formed by similar processes, associated with metasomatism by slab-melt.

1.7.4. Origin of the two types of peridotites

1.7.4.1. C-type peridotites

The mineralogy and mineral compositions of the C-type xenoliths are similar to mantle peridotites from many parts of the world. This is supported by the plots of samples in the olivine-spinel mantle array of Arai (1994) (Fig. 1-7). The compositions of spinel overlap with the field of abyssal peridotites (Figs. 1-4, 1-5 and 1-7). The evidence supports the proposal that the subcontinental lithospheric mantle below southernmost South America increased its size by stacking of oceanic lithosphere (Stern et al. 1999; Carlson et al. 2005).

The modal metasomatism, the formation of websterite veins and high Ti pargasitic amphibole, in C-type peridotites was produced by interaction with Ti-rich asthenospheric melt, as described in the previous section. Cryptic metasomatism has also affected C-type peridotites. This metasomatism did not produce amphiboles or veins, but clinopyroxene grains have elevated contents of fluid-mobile elements and low Nb and Zr (Fig. 1-8a). The data suggest that they have undergone cryptic metasomatism by slab-derived aqueous fluids. Considering the tectonic history of the area, this metasomatism most likely took place in early-middle Miocene when the Nazca plate was being subducted beneath the area.

1.7.4.2. F-type peridotites

F-type xenoliths are very distinct from the C-type xenoliths. Olivine and pyroxenes are low

in Mg. Spinel contains low Cr (Figs. 1-4, 1-5), and they plot outside the olivine-spinel mantle array of Arai (1994) (Fig. 1-7), suggesting that they are not typical mantle peridotites. Low Mg in minerals suggest that F-type may be cumulates or the product of metasomatism by an agent with low Mg# and Cr. The first possibility is discounted because cumulates should have only one or two early crystallizing minerals that fractionated from parental magmas, such as websterite veins in C-type xenoliths. F-type peridotites contain olivine, two pyroxenes and large (up to 2 mm) patches of solidified "melt" (~ 10 vol%) that was once low Mg pargasitic amphibole (Fig. 1-2e). A rock with all these coarse crystalline minerals is not a cumulate because it requires a substantial evolution of parental melt. Second, spinel in F-type peridotites shows a restricted range in Cr# (~ 0.13) in different samples. Spinel in cumulates commonly shows a wide range in Cr# because Cr contents in melt rapidly change during the crystallization of spinel (Dick and Bullen 1984; Barnes and Roeder 2001). Third, spinel compositions show low Cr# and Mg#, far from the field of arc-cumulates in the diagram of Al_2O_3 -Cr_2O_3 (Fig. 1-9).

Therefore, we suggest the F-type peridotites are a product of metasomatism of mantle peridotites. Their low Cr# in spinel and low Mg# in silicate minerals reflect the character of the metasomatizing agent. Considering the compositional change in Cr and Al in spinel, we suggest that the metasomatizing agent was most likely melt instead of fluid alone. The nature of the metasomatizing melt is evaluated based on Mg# of olivine using the Fe-Mg exchange coefficient, K_d, between olivine and melt. The value of K_d is a function of temperature, pressure, and compositions of the olivine and melt (Toplis 2005). The effect of pressures on K_d is small (~ 0.01 per Gpa). However, the concentrations of silica and alkalis of melts and temperature of the melt may affect K_d under high pressures. Since high degrees of partial melting occurred at high temperature (increasing K_d), but such melt is generally poor in silica (lowering K_d), these affects canceling each other out, resulting in K_d value close to 0.30, which is commonly observed in natural systems (Roeder and Emslie 1970). Considering the above factors, we used K_d value of 0.30 for the calculation. The hypothetical melt that metasomatized the F-Type xenoliths thesefore has Mg# of ~ 0.60. This value is lower than the Mg# of normal mid-oceanic ridge

basalts, ~ 0.64 (Hofmann 1988). The low Mg# values of the hypothetical melt suggest that the metasomatizing melt for F-type xenoliths is most likely a slab melt.

Slab-derived melt is Si-rich compared to mantle derived melt. Therefore, the interaction of mantle peridotites with slab-melt commonly results in the formation of secondary orthopyroxene at the expense of olivine as described in metasomatized peridotites from Kamchatka (Arai et al. 2003) and Batan Island, Philippines (Schiano et al. 1995; Arai et al. 2004). Experimental results by Rapp et al. (1999) also suggest the formation of low Mg orthopyroxene after olivine in peridotites during the interactions with slab melt at high melt/rock ratios. We consider that orthopyroxene grains in our F-type peridotites most likely formed from olivine during the reactions with slab-melt because they show low Mg values and extensive re-crystallization texture. Furthermore, this is consistent with the relatively low abundance of olivine in F-type peridotites compared to C-type peridotites. The amount of orthopyroxene is expected to be high when peridotites underwent metasomatism, but the amount of orthopyroxene likely varies depending on the effective ratios of melt to peridotites. Rapp et al. (1999) suggest that peridotites show varying effects from hybridization of the melt to cryptic metasomatism depending on the effective melt/rock ratios. Considering the modification of mineral compositions and the formation of amphiboles, we suggest the F-type peridotites were metasomatized by slab melt at a moderately high melt/rock ratio.

The metasomatism of sub-arc mantle peridotites by slab-melt is documented in xenoliths in Batan Island, Philippines (Schiano et al. 1995). It produced polygonal low Mg olivine and orthopyroxene neoblasts with the development of mosaic textures, and pargasitic amphibole (Schiano et al. 1995). Another well-documented example is in the north Kamchatka arc (Kepezhinskas et al. 1995, 1996). The mantle xenoliths from the north Kamchatka arc are classified into Cr-diopside series and Al-augite series based on pyroxene compositions (Kepezhinskas et al. 1995). Cr-diopside series xenoliths represent peridotites that were metasomatized by fluids released from slabs. Their spinel is characterized by high Cr#, low Mg and slightly elevated Fe^{3+} common in sub-arc mantle peridotites (Figs. 1-5, 1-9). Al-augite series

xenoliths are interpreted to have formed during the interaction with Si-rich melt (Kepezhinskas et al. 1995). They contain green spinel with low Cr_2O_3 (< 2 wt%) (Figs. 1-5, 1-9), suggesting that spinel was enriched in Al and depleted in Cr during the metasomatism with a slab melt. In terms of the compositions of spinel and metasomatic agent, F-type peridotites in Cerro del Fraile are similar to the Al-augite series xenoliths from north Kamchatka arc (Figs. 1-5, 1-9). Furthermore, veins with high SiO_2 (67 wt%) and Al, low Ti and high Na/K ratios of 3-5 in Al-augite series xenoliths were interpreted as solidified slab "melt" (Kepezhinskas et al. 1995), which is comparable to the adakitic veins from Cerro del Fraile as described by Kilian and Stern (2002) (Table 1-4).

Our proposed interpretation is further supported by high Sr/Y in clinopyroxene and bulk composition of F-type peridotites (Figs. 1-8b, 1-8c and 1-8d). High Sr/Y ratios are one of characteristic features of a slab melt (Defant and Drummond, 1990).

Metasomatism of the mantle below Cerro del Fraile by slab-melt likely took place after the late Miocene as the Nazca Plate became younger during the time when the Chile Ridge was approaching the trench.

1.7.5. Oxidation state of C-type peridotites

Sub-arc mantle overlying subducted oceanic crust is generally considered to be oxidized, with ΔFMQ +0.3 to +2.0. Examples include Ichinomegata in Japan, Marelava in Vanuatu arc, Grenada in Lesser Antilles arc, Santa Isabel and San Jorge in Solomon islands and the Simcoe area in Cascade arc (Wood and Virgo 1989; Ballhaus et al. 1991; Brandon and Draper 1996; Parkinson and Arculus 1999; Parkinson et al. 2003) (Fig. 1-6). The oxidized condition of mantle wedges is explained by the introduction of oxidizing aqueous fluids liberated from down-going oceanic slabs (Arculus 1985; Wood and Virgo 1989; Brandon and Draper 1996; Parkinson and Arculus 1999). This is consistent with slightly elevated fO_2 values, ΔFMQ+0.1 to +0.3, of most anhydrous C-type peridotites without "melt" patches because these peridotites are interpreted to have undergone cryptic metasomatism by aqueous fluids released from slabs based on the

enrichment of fluid-mobile elements (Fig. 1-8a). The narrow spread in fO_2 of samples and the lack of correlation between Cr# of spinel and fO_2 (Fig. 1-6) may suggest that this cryptic metasomatism homogenized fO_2 values of the peridotites.

The two "melt"-bearing C-type samples that were metasomatized by an asthenospheric mantle-derived melt, show fO_2 slightly below FMQ. The results are consistent with the fO_2 of asthenospheric mantle near the FMQ buffer (Taylor and Green 1987; Ballhaus 1993).

1.7.6. Oxidation state of F-type peridotites metasomatized by slab melt

The F-type peridotites record low fO_2 values. The F-type xenolith has undergone extensive recrystallization and metasomatism by slab-melt. All silicate minerals contain low Mg# than usual mantle peridotites. Therefore it is reasonable to consider that low fO_2 values were acquired during the metasomatism and that the metasomatism by slab-melt was accompanied by lowering of fO_2. This proposed interpretation requires a reducing nature of this slab-melt. This appears to be in conflict with generally oxidized nature of oceanic crust which is weathered on the oxidizing sea floor and altered by interactions with oxidizing sea water. Subducted slab is overlain by wet sediments, which likely fuse during the slab melting of underlying oceanic crust. Sediments contain water, carbonate and organic matter and the fusion produces melt and aqueous fluids high in CO_2 and CH_4. The abundance of these volatiles in aquous fluids is controlled by the following reactions:

$C + O_2 = CO_2$ ---------- (1)

$C + 2\ H_2O = CH_4 + O_2$ ---------- (2)

The reaction (1) shows that the presence of organic matter imposes an upper limit of fO_2 of fluids. The upper stability field of graphite is estimated to be close to the FMQ buffer in natural systems because other volatile species may lower the activities of CO_2 and CO and allow the stable occurrence of graphite (Wood et al. 1990; Fig. 1-10). The reaction 2 shows the formation of CH_4 in aqueous fluids from graphite. The equation suggests that the heating and fusion of organic-rich wet sediments produce CH_4. The relationship between fO_2 and fraction of CH_4 in

the aqueous fluids coexisting with graphite is shown in Fig. 1-10. Fluids high in CO_2 occur at high fO_2, whereas fluids high in CH_4 at low fO_2. The diagram also shows that the hypothetical fluids in equilibrium with the F-type xenoliths must have contained CH_4.

The pelagic sediments in the Chile trench sediments contain little or no carbonates, but abundant bitumens and kerogen and the evidence of hydrocarbon formation at depths (Behrmann et al. 1992). This is in contrast with high carbonate contents of common oceanic pelagic sediments (Plank and Langmuir 1998). The evidence suggests that aqueous fluids released from sediments in the area likely contained CH_4 and the melt formed from the slab overlain by such sediments was most likely reducing in fO_2 because CH_4 from organic matter, which maintains low fO_2 in the fused sediment and slab melt. Reducing fluids together with the slab melt ascended into the overlying mantle and contributed to lowering fO_2 of the F-type Cerro del Fraile peridotites.

Sediments are generally high in U, especially organic-rich sediments because U^{6+} dissolved in sea water can be fixed as U^{4+} in the organic-rich, reduced sediments (Klinkhammer and Palmer 1991). Therefore, the fusion of sediments and subsequent mixing with a slab-melt produces a melt with elevated concentrations of U. The metasomatism of mantle peridotites by such a melt would produce high U. We consider that high content of U in clinopyroxene in F-type peridotites as another line of evidence for the contribution of sediments to the slab melt that metasomatized these xenoliths (Fig. 1-8c). For example, clinopyroxene in sample Bxe1 shows more than two times higher U content than that of U-rich C-type samples (Fig. 1-8c).

Average pelagic sediments on the ocean floor consist of 72 vol% carbonate ooze, 19 vol% red clay, and 9 vol% siliceous ooze, and they contain approximately 12wt% CO_2 and 5 wt% H_2O bound in mineral structures plus up to 50 vol% H_2O in pore spaces (Peacock 1990). Oceanic basalts that are altered on and near sea floor also contain abundant carbonates and hydrous minerals. Therefore, subducted slabs in many locations release CO_2 –H_2O fluids. This is consistent with overall oxidized nature, above FMQ, of mantle wedges. But subducted sediments vary depending on locations (Plank and Langmuir 1998). This suggests that sub-arc mantle

would have different fO_2 depending on the type of subducted sediments. This is further supported by recent finding of unusually oxidized nature of the mantle wedge in Himalayas where evaporitic sulphates are subducted (Hattori et al. 2005).

Our data suggest that subducted sediments may be important in controlling the redox condition of mantle wedges. In most subduction zones, fluids are released from slabs and sediments to overlying mantle wedges. CO_2 and H_2O are predominant species in the fluids and they maintain relatively high fO_2 of overlying mantle wedges. In subduction zones involving young slabs, partial melting of the slabs and fusion of overlying sediments takes place. When the sediments contain high contents of organic matter, the fluids and melt are reducing with high CH_4. The ascent of the slab melt and accompanying fluids could significantly lower fO_2 of the overlying mantle peridotites.

Acknowledgements

This work was supported by a NSERC Discovery grant to K. H. Hattori and an Ontario Graduate Scholarship in Science and Technology and the University of Ottawa Excellence Scholarship to J. Wang. We thank J-P. Li for allowing us to use the spinel standards prepared by B. J. Wood and D. Virgo. Thanks are also given to L. Shi for his help during the electron microprobe analysis at McGill University. The manuscript benefited from the constructive comments by J. Hoefs, S. Arai and an anonymous journal reviewer.

References

Abe N, Arai S, Yurimoto H (1998) Geochemical characteristics of the uppermost mantle beneath the Japan island arcs: Implications for upper mantle evolution. Phys Earth Planet Inter 107:233-248

Arai S (1994) Characterization of spinel peridotites by olivine-spinel compositional relationships: Review and interpretation. Chem Geol 111:191-204

Arai S, Ishimaru S, Okrugin VM (2003) Metasomatized harzburgite xenoliths from Avacha volcano as fragments of mantle wedge of the Kamchatka arc: implication for the metasomatic agent. The Island Arc 12:233-246

Arai S, Takada S, Michibayashi K, Kida M (2004) Petrology of peridotite xenoliths from Iraya volcano, Philippines, and its implication for dynamic mantle-wedge processes. J Petrol 45:369-389

Arculus RJ (1985) Oxidation status of the mantle: past and present. Ann Rev Earth Planet Sci 13:75-95

Ballhaus C, Berry RF, Green DH (1991) High pressure experiment calibration of the olivine – orthopyroxene – spinel oxygen barometer: implications for the oxidation state of the mantle. Contrib Mineral Petrol 107:27-40

Ballhaus C (1993) Redox states of lithospheric and asthenospheric upper mantle. Contrib Mineral Petrol 114:331-348

Ban M, Witt-Eickschen G, Klein M, Seck HA (2005) The origin of glasses in hydrous mantle xenoliths from the West Eifel, Germany: incongruent break down of amphibole. Contrib Mineral Petrol 148:511-523

Barnes SJ, Roeder PL (2001) The range of spinel compositions in terrestrial mafic and ultramafic rocks. J Petrol 42:2279-2302

Barsdell M, Smith IEM (1989) Petrology of recrystallized ultramafic xenoliths from Merelava volcano, Vanuatu. Contrib Mineral Petrol 102:230-241

Behrmann JH, Lewis SD et al (1992) Proceedings of the Ocean Drilling Program, Initial Reports, College Station, Texas (Ocean Drilling Program),141, 807 pp

Brandon AD, Draper DS (1996) Constraints on the origin of the oxidation state of the mantle overlying subduction zones: an example from Simcoe, Washington, USA. Geochim Cosmochim Acta 60:1739-1749

Brey GP, Köhler T (1990) Geothermobarometry in four-phase lherzolites II. New thermobarometers, and practical assessment of existing thermobarometers. J Petrol

31:1353-1378

Bryndzia LT, Wood BJ (1990) Oxygen thermobarometry of abyssal spinel peridotites: the redox state and the C-H-O volatile composition of the Earth's sub-oceanic mantle. Am J Sci 290:1093-1116

Cande SC, Leslie RB (1986) Late Cenozoic tectonics of the southern Chile Trench. J Geophys Res 91:471-496

Carlson RW, Pearson DG, James DE (2005) Physical, chemical, and chronological characteristics of continental mantle. Reviews of Geophysics 43:1-24

Conceição RV, Green DH (2004) Derivation of potassic (shoshonitic) magmas by decompression melting of phlogopite + pargasite lherzolite. Lithos 72:209-229

Defant MJ, Drummond MS (1990) Derivation of some modern arc magmas by melting of young subducted lithosphere. Nature 347:662-665

DeHoog JCM, Hattori KH, Hoblitt RP (2004) Oxidized sulfur-rich mafic magma at Mount Pinatubo, Philippines. Contrib Mineral Petrol 146:750-761

Dick HJB, Bullen T (1984) Chromian spinel as a petrogenetic indicator in abyssal and alpine-type peridotites and spatially associated lavas. Contrib Mineral Petrol 86:54-76

D'Orazio M, Agostini S, Mazzarini F, Innocenti F, Manetti P, Haller MJ, Lahsen A (2000) The Pali Aike Volcanic Field, Patagonia: slab-window magmatism near the tip of South America. Tectonophysics 321: 407-427

Francis DM (1976) The origin of amphibole in lherzolite xenoliths from Nunivak Island, Alaska. J Petrol 17:357-378

Gorring ML, Kays SM, Zeitler PK, Ramos VA, Rubiolo D, Fernandez MI, Panza JL (1997) Neogene Patagonian plateau lavas: Continental magmas associated with ridge collision at the Chile triple Junction. Tectonics 16:1-17

Hattori KH, Guillot S (2003) Volcanic fronts as a consequence of serpentinite dehydration in the mantle wedge. Geology 31:525-528

Hattori K, Takahashi Y, Guillot S, Johanson B (2005) Occurrence of arsenic (V) in forearc

mantle serpentinites based on X-ray absorption spectroscopy study. Geochim Cosmochim Acta 69:5585-5596

Hofmann AW (1988) Chemical differentiation of the Earth: the relationship between mantle, continental crustal, and oceanic crust. Earth Planet Sci Lett 90:297-314

Ionov DA, Wood BJ (1992) The oxidation state of subcontinental mantle: oxygen thermobarometry of mantle xenoliths from Central Asia. Contrib Mineral Petrol 11:179-193

Ishimaru S, Arai S, Ishida Y, Shirasaka M, Okrugin VM (2007) Melting and multi-stage metasomatism in the mantle wedge beneath a frontal arc inferred from highly depleted peridotite xenoliths from the Avacha Volcano, southern Kamchatka. J Petrol 48: 395-433

Kay SM, Ramos VA, Marquez M (1993) Evidence in Cerro Pampa volcanic rocks for slab-melting prior to ridge-trench collision in southern South America. J Geol 101:703-714

Kepezhinskas PK, Defant MJ, Drummond MS (1995) Na metasomatism in the island-arc mantle by slab melt-peridotite interaction: evidence from mantle xenoliths in the north Kamchatka arc. J Petrol 36:1505-1527

Kepezhinskas PK, Defant MJ, Drummond MS (1996) Progressive enrichment of island arc mantle by melt-peridotite interaction inferred from Kamchatka xenoliths. Geochim Cosmochim Acta 60:1217-1229

Kilian R, Stern CR (2002) Constraints on the interaction between slab melts and the mantle wedge from adakitic glass in peridotite xenoliths. Eur J Mineral 14:25-36

Klinkhammer GP, Palmer MR (1991) Uranium in the oceans: Where it goes and why. Geochim Cosmochim Acta 55:1799-1806

Lee C-TA (2005) Trace element evidence for hydrous metasomatism at the base of the North American lithosphere and possible association with Laramide low-angle subduction. J Geol 113: 673-685

McDonough WF, Sun SS (1995) The composition of the Earth. Chem Geol 120:223-253

Mibe K, Fujii T, Yasuda A (1999) Control of the location of the volcanic front in island arcs by aqueous fluid connectivity in the mantle wedge. Nature 401:259-262

Nell J, Wood BJ (1991) High-temperature electrical measurements and thermodynamic properties of Fe_3O_4-$FeCr_2O_4$-$MgCr_2O_4$-$FeAl_2O_4$ spinels. Am Mineral 76:406-426

Parkinson IJ, Arculus RJ (1999) The redox state of subduction zones: insights from arc-peridotites. Chem Geol 160:409-423

Parkinson IJ, Arculus RJ, Eggins SM (2003) Peridotite xenoliths from Grenada, Lesser Antilles Island arc. Contrib Mineral Petrol 146:241-262

Peacock SM (1990) Fluid processes in subduction zones. Science 248:329-336

Plank T, Langmuir CH (1998) The chemical composition of subducting sediment: implications for the crust and mantle. Chem Geol 145:325-394

Qi Q, Taylor LA, Zhou XM (1995) Petrology and geochemistry of mantle peridotite xenoliths from SE China. J Petrol 36:55-79

Rapp RP, Shimizu N, Norman MD, Applegate GS (1999) Reaction between slab-derived melts and peridotite in the mantle wedge: experimental constraints at 3.8 GPa. Chem Geol 160:335-356

Roeder PL, Emslie RF (1970) Olivine-Liquid equilibrium. Contrib Mineral Petrol 29:275-289

Schiano P, Clocchiatti R, Schimizu N, Maury RC, Jochum KP, Hofmann AW (1995) Hydrous, silica-rich melts in the sub-arc mantle and their relationship with erupted arc lavas. Nature 377:595-600

Shaw CSJ, Klügel A (2002) The pressure and temperature conditions and timing of glass formation in mantle-derived xenoliths from Baarley, Western Eifel, Germany: the case for amphibole breakdown, lava infiltration and mineral-melt reaction. Mineral Petrol 74:163-187

Sinigoi S, Comin-Chiaramonti P, Alberti AA (1980) Phase relations in the partial melting of the Baldissero spinel-lherzolite (Ivrea-Verbano Zone, Western Alps, Italy). Contrib Mineral Petrol 75:111-121

Stern CR, Kilian R (1996) Role of the subducted slab, mantle wedge and continental crust in the generation of adakites from the Andean Austral Volcanic zone. Contrib Mineral Petrol

123:263-281

Stern CR, Kilian R, Olker B, Hauri EH, Kyser TK (1999) Evidence from the mantle xenoliths for relatively thin (<100 km) continental lithosphere below the Phanerozoic crust of southernmost South America. Lithos 48:217-235

Taylor WR, Green DH (1987) Measurement of reduced peridotite-C-O-H solidus and implications for redox melting of the mantle. Nature 332:349-352

Taylor RP, Jackson SE, Longerich HP, Webster JD (1997) In situ trace-element analysis of individual silicate melt inclusions by laser ablation microprobe-inductively coupled plasma-mass spectrometry (LAM-ICP-MS). Geochim Cosmochim Acta 61:2559-2567

Toplis MJ (2005) The thermodynamics of iron and magnesium partitioning between olivine and liquid: criteria for assessing and predicting equilibrium in natural and experimental systems. Contrib Mineral Petrol 149:22-39

Wells PRA (1977) Pyroxene thermometry in simple and complex systems. Contrib Mineral Petrol 62:129-139

Wood BJ, Virgo D (1989) Upper mantle oxidation state: ferric iron contents of lherzolite spinels by 57Fe Mössbauer spectroscopy and resultant oxygen fugacities. Geochim Cosmochim Acta 53:1277-1291

Wood BJ, Bryndiza LT, Johnson KE (1990) Mantle oxidation state and its relationship to tectonic environment and fluid speciation. Science 248:337-345

Woodland AB, Kornprobst J, Wood BJ (1992) Oxygen thermobarometry of orogenic lherzolite massifs. J Petrol 33:203-230

Yaxley GM, Kamenetsky V, Green DH, Falloon TJ (1997) Glasses in mantle xenoliths from western Victoria, Australia, and their relevance to mantle processes. Earth Planet Sci Lett 148:433-446

Yaxley GM, Kamenetsky V (1999) In situ origin for glass in mantle xenoliths from southeastern Australia: insights from trace element compositions of glasses and metasomatic phases. Earth Planet Sci Lett 172:97-109

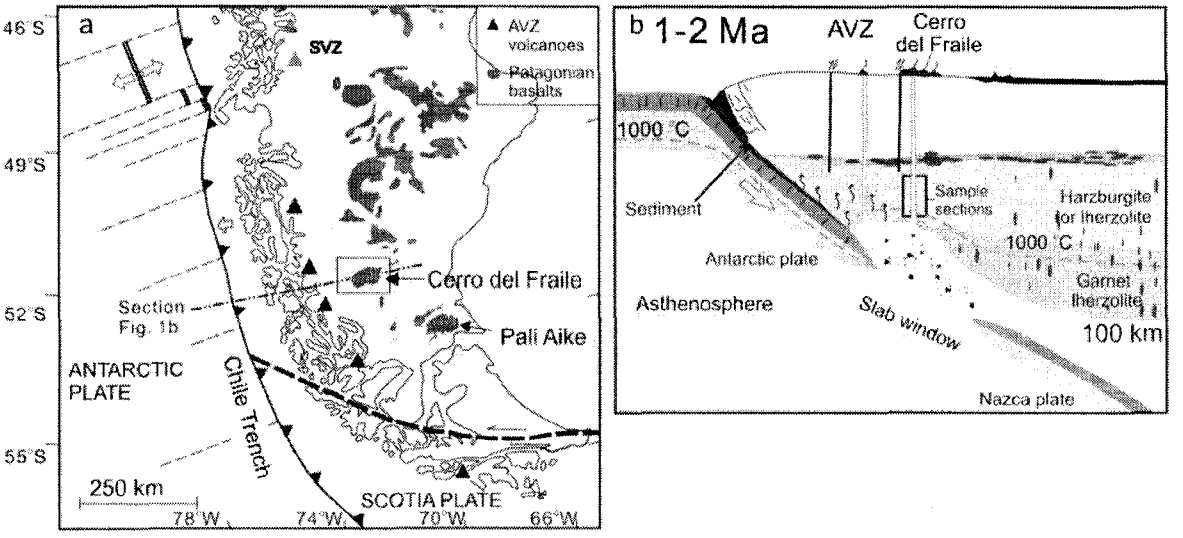

Figure 1-1 a) Map of southernmost South America showing the locations of the Quaternary alkali olivine basalt fields of Cerro del Fraile (CF), Pali-Aike (PA) and other late Cenozoic basalts of Patagonian plateau. Also shown are stratovolcanoes of the Andean Austral Zone (AVZ). **b)** Schematic section across Antarctic plate margin-AVZ arc-Cerro del Fraile-Patagonian plateau basalts, including the lithospheric structure below the South American craton (modified after Kilian and Stern 2002).

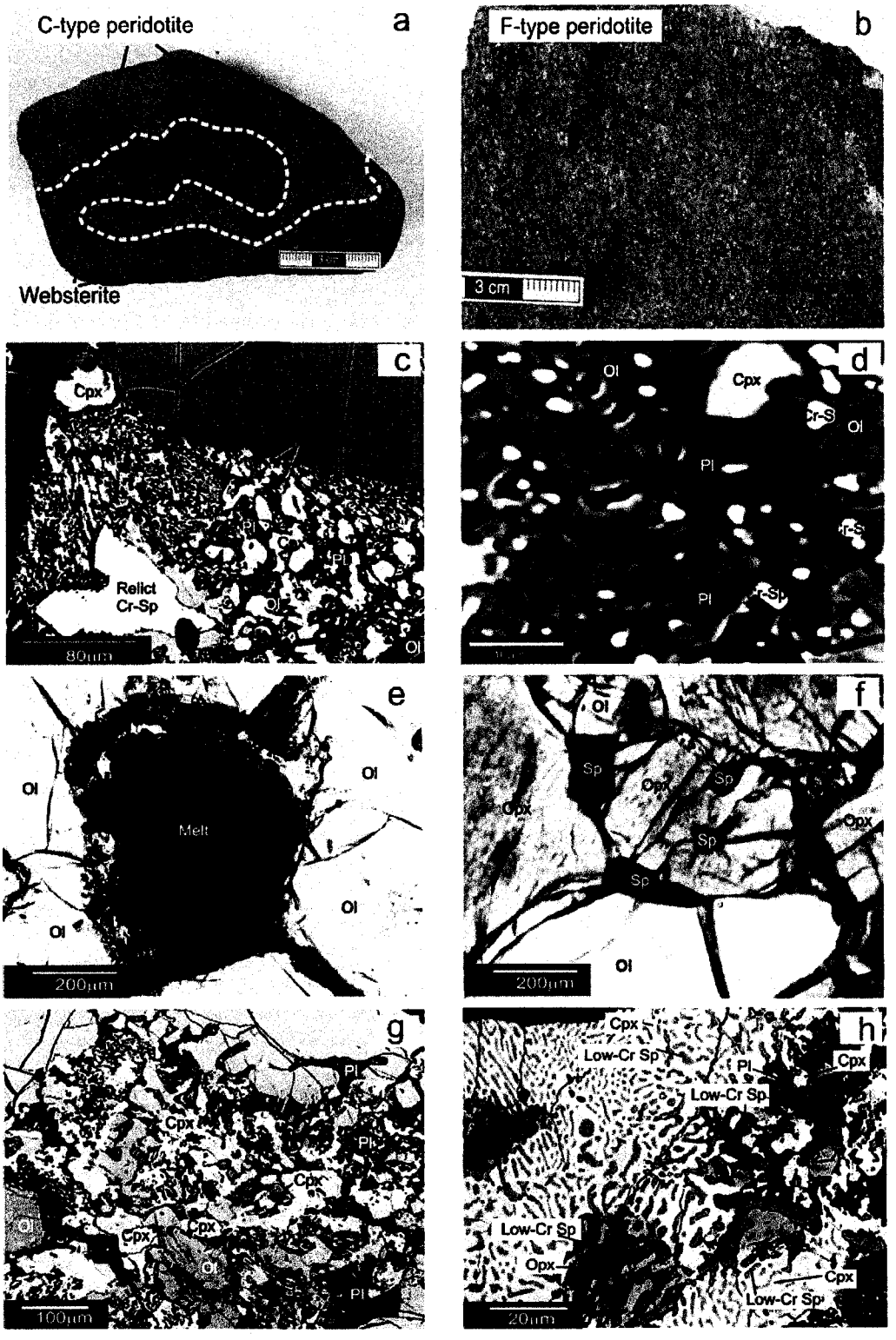
C-type peridotite
a
Websterite
F-type peridotite
b
3 cm
c
Cpx
Relict
Cr-Sp
Ol
80μm
d
Ol
Cpx
Pl
e
Ol
Melt
200μm
f
Sp
Opx
200μm
g
Pl
Cpx
100μm
h
Cpx
Low-Cr Sp
Pl
Opx
20μm

Figure 1-2 a) Photograph of a C-type lherzolite containing websterite vein. The boundary of websterite and perditotites are shown with thick dotted line. **b)** Photograph of a metasomatized F-type lherzolite xenolith. **c)** Back-scattered electron (BSE) image of a veinlet (0.2 mm in width and greater than 0.5mm in length) in C-type spinel peridotite (sample Bxe11-I). The veinlet is composed of mineral aggregates of plagioclase (Pl) + clinopyroxene (Cpx) + olivine (Ol)+ Cr-spinel (Cr-Sp). **d**) BSE image of minute mineral aggregate of solidified "patch" melt in C-type peridotite (sample Bxe11-I). **e**) Photomicrograph of patch "melt" in F-type lherzolite under plain polarized light (sample Bxe1). The patch represents a pseudomorph of pargasitic amphibole with narrow veinlets of solidified "melt" radiating from the patch. The patch "melt" is dark due to the desseminated grains of fine-grained spinel. **f)** Photomicrograph of F-type peridotite under plane polarized light (sample Bxe1). Spinel (Sp) grains occur along grain boundaries of orthopyroxene (Opx) and olivine (Ol) and as inclusions in orthopyroxene. These spinel grains have similar compositions, suggesting that they are equilibrated. **g)** BSE image of a solidified "melt" in F-type peridotite (sample Bxe22). The "melt" is composed of an aggregate of minute clinopyroxene (Cpx) + olivine (Ol) + plagioclase (Pl). Olivine contains dusty spinel inclusions (bright spots). **h**) Enlarged BSE image of portion of a patch "melt" in F-type peridotite (sample Bxe1). Heterogeneous distribution of quenched phases is apparent in enlarged images, showing different clusters of minerals; a cluster of orthopyroxene (Opx)+ low-Cr spinel (Sp) in the lower left, clusters of clinopyroxene (Cpx)+ low-Cr spinel in the centre top and centre bottom, and a cluster of clinopyroxene + plagioclase (Pl) + low-Cr spinel (Cr_2O_3 < 1 wt%) in the upper right.

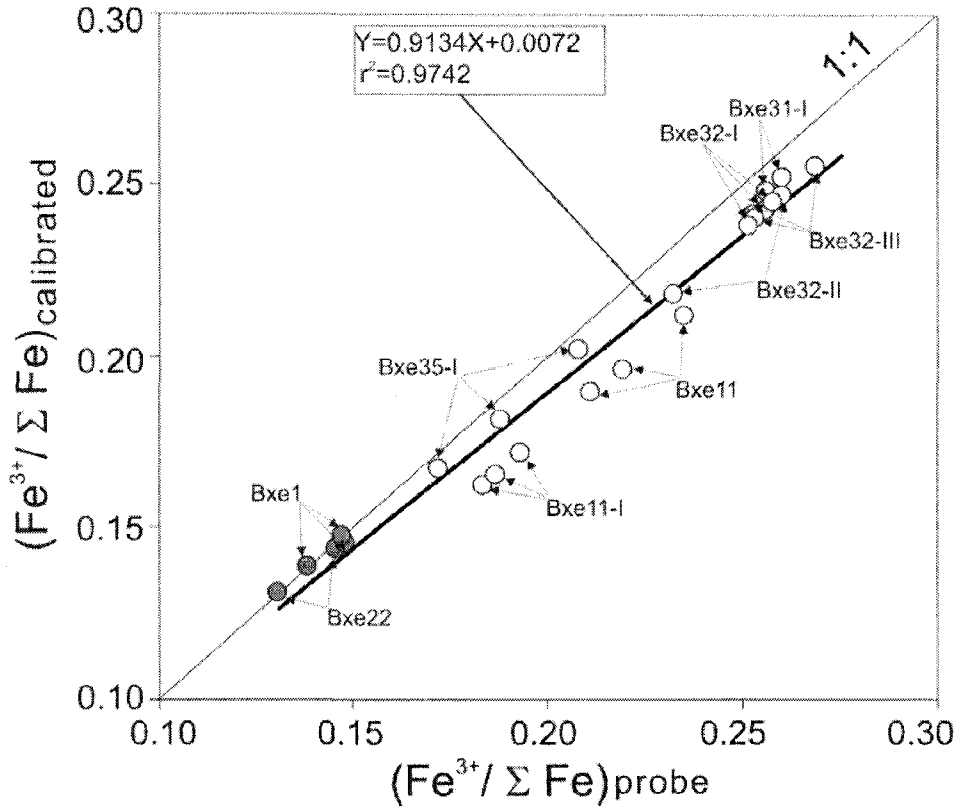

Figure 1-3 $Fe^{3+}/\Sigma Fe$ ratios calibrated using spinel standards, $(Fe^{3+}/\Sigma Fe)_{calibrated}$, are compared to those calculated assuming stoichiometric composition of spinel, $(Fe^{3+}/\Sigma Fe)_{probe}$ from Cerro del Fraile. Each point represents one spinel grain. Quenched spinel crystals in solidified "melt" show different compositions even within a single patch and these compositions are not plotted. Calibrated ratios, $(Fe^{3+}/\Sigma Fe)_{calibrated}$, were obtained using four spinel standard samples (KLB8304, KLB8311, MBR8305 and KLB8316) with known Fe^{3+} contents and the calculation method described by Wood and Virgo (1989) and Woodland et al. (1992).

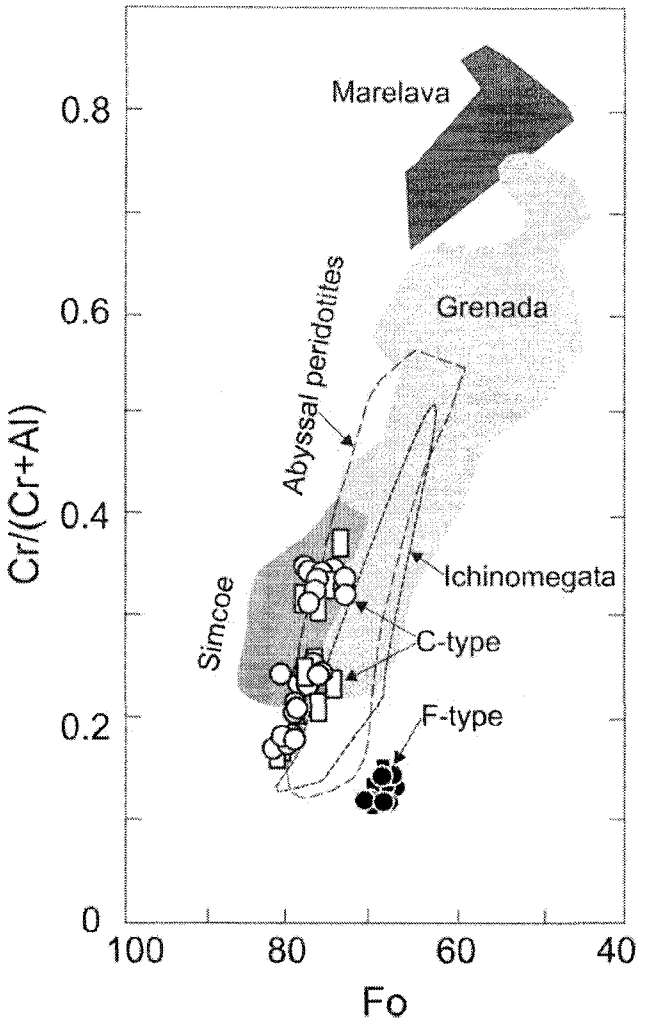

Figure 1-4 Plot of Cr# vs. Mg/ ($Mg+Fe^{2+}$) for spinel in peridotites from Cerro del Fraile, compared with the data for abyssal peridotites (Dick and Bullen 1984) and sub-arc mantle peridotites. Open circles= intergranular spinel in C-type; open rectangles= spinel inclusion in silicate minerals in C-type; filled circles= intergranular spinel in F-type; filled rectangles= spinel inclusions in silicate minerals in F-type lherzolite. Data sources of other sub-arc mantle peridotites: Simcoe, western US (Brandon and Draper 1996), Marelava, Vanuatu (Barsdell and Smith 1989), Ichinomegata, Japan (Wood and Virgo 1989; Parkinson and Arculus 1999), Grenada (Parkinson et al. 2003). Note that F-type xenoliths are plotted outside the fields for most mantle xenoliths and abyssal peridotites.

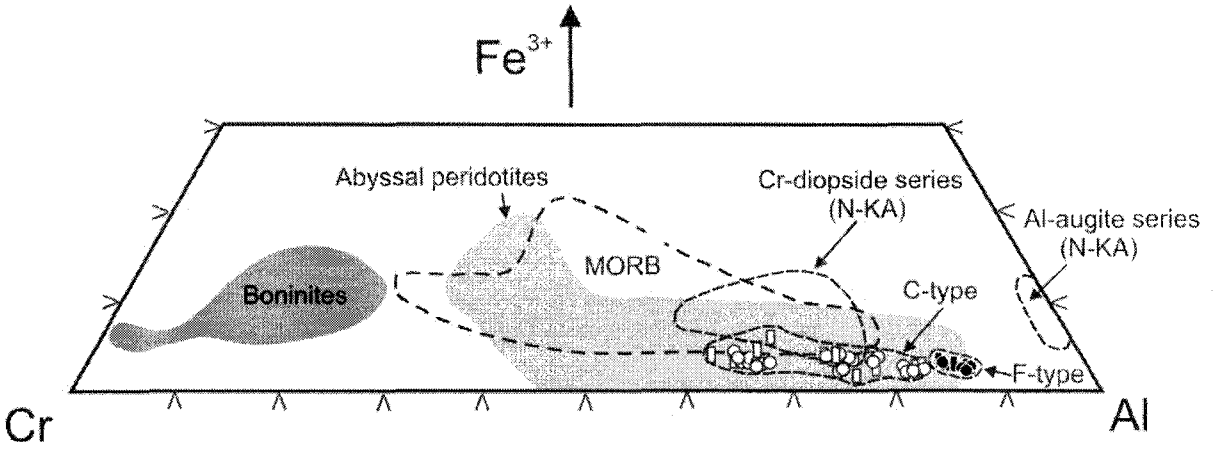

Figure 1-5 Ternary diagram of Fe^{3+}- Cr- Al for spinels in the peridotite xenoliths from Cerro del Fraile. Symbols are the same as in Fig. 1-4. Note that spinel in F-type has lower Cr# than that in C-type peridotites. Data sources: abyssal peridotite, MORB and boninite (Barnes and Roeder 2001); Cr-diopside series (N-KA) and Al-augite series (N-KA) are those series from north Kamchatka arc (N-KA) (Kepezhinskas et al.1995).

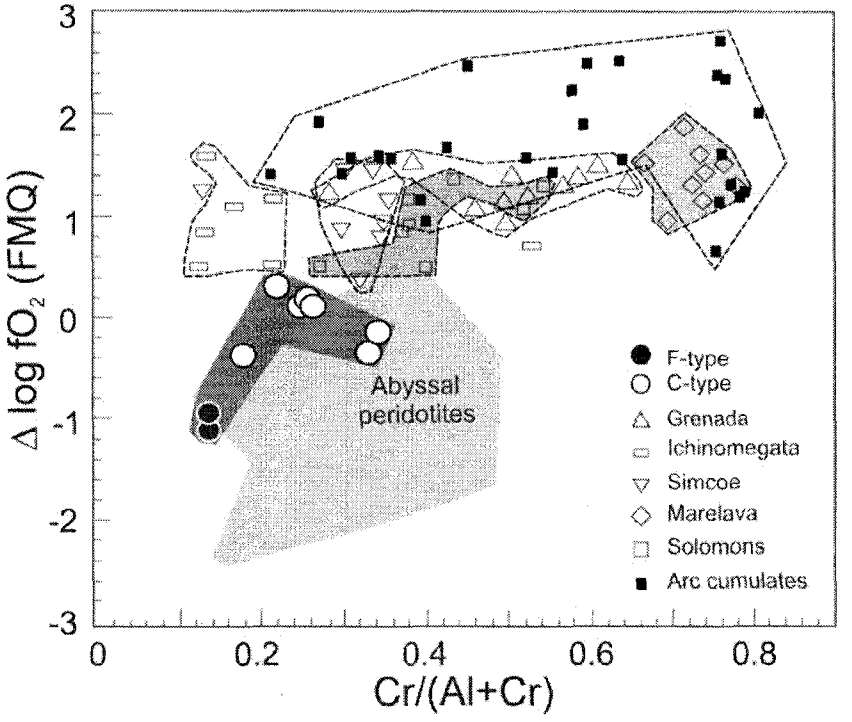

Figure 1-6 Values of fO_2 relative to FMQ buffer (ΔfO_2 (FMQ) vs. Cr# in spinel for peridotites from Cerro del Fraile compared with arc cumulates (Ballhaus, 1993), abyssal peridotites (Bryndzia and Wood 1990) and sub-arc mantle peridotites. Data source for sub-arc mantle peridotites: Simcoe (Brandon and Draper 1996), Ichinomegata, Japan (Wood and Virgo 1989; Parkinson and Arculus 1999), Grenada, Marelava, and Solomons (Parkinson and Arculus 1999; Parkinson et al. 2003).

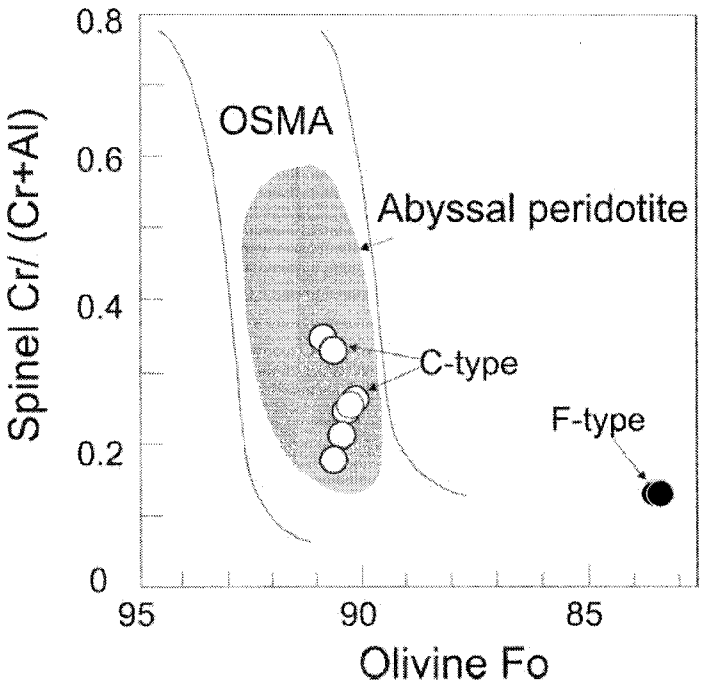

Figure 1-7 Relationships between the Fo contents of olivine and Cr# values of spinel in peridotite xenoliths from C-type (open circles) and F-type peridotites (solid circles) in Cerro del Fraile. Note the F-type peridotites plot outside the olivine-spinel mantle array (OSMA; Arai 1994), suggesting they are not primary mantle peridotites. It also shows the field of abyssal peridotite as a shaded area (Arai 1994).

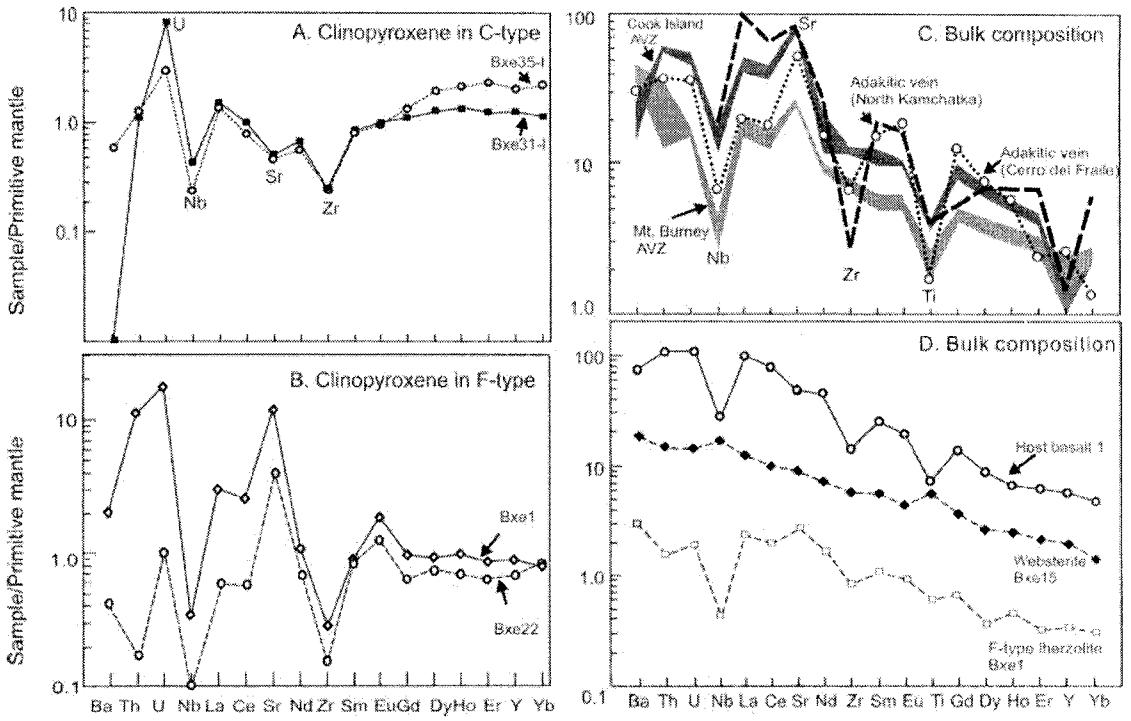

Figure 1-8 Primitive mantle-normalized element patterns of minerals, solidified melt, adakitic magmas and bulk rock compositions of host basalts and websterites; **(a)** representative clinopyroxene (Cpx) in samples Bxe35-I and Bxe31-I of C-type xenoliths; **(b)** representative clinopyroxene in samples Bxe22 and Bxe1 of F-type xenoliths; **(c)** adakitic melt in sub-arc mantle xenoliths from Cerro del Fraile xenoliths (Kilian and Stern 2002; Table 1-4) and north Kamchatka arc (Kepezhinskas et al. 1995), and adakitic volcanic rocks in Mt. Burney and Cook Island, AVZ (Stern and Kilian 1996); **(d)** bulk compositions of representative host basalts (host-1) (this study; Table 1-4), websterite (Bxe15) (this study; Table1- 4) and F-type lherzolite (Bxe1) (Kilian and Stern 2002). Primitive mantle values are from McDonough and Sun (1995).

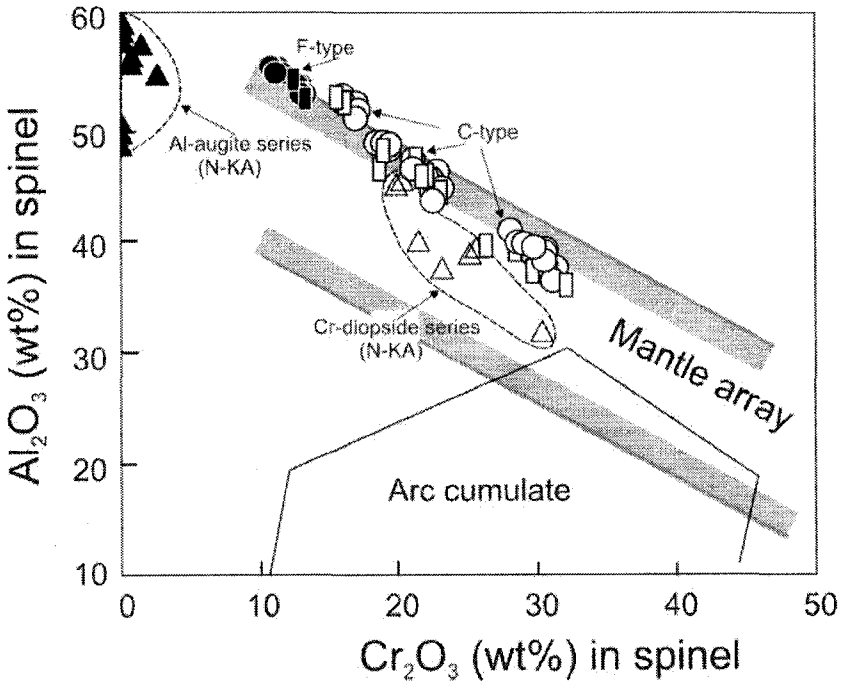

Figure 1-9 Al_2O_3 vs. Cr_2O_3 in spinel for mantle xenoliths from Cerro del Fraile. Symbols are the same as Fig. 1-4. Also shown are fields of sub-arc mantle xenoliths of Cr-diopside series and Al-augite series from north of Kamchatka arc (N-KA) (Kepezhinskas et al. 1995).

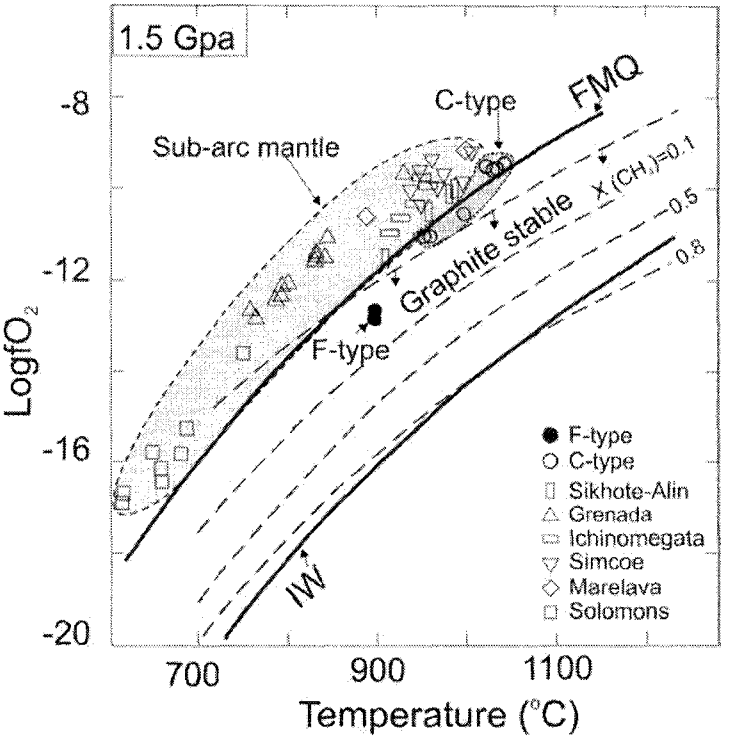

Figure 1-10 Fraction of CH_3 in C-H-O fluids on a diagram of fO_2 vs. temperatures (modified after Wood et al. 1990). The values for mantle xenoliths from Cerro del Fraile (this study) are compared to those from other sub-arc mantles; Sikhote-Alin, Russia (Ionov and Wood 1992), Simcoe (Brandon and Draper 1996), Ichinomegata, Japan (Wood and Virgo 1989), Grenada, Marelava, and Solomon islands (Parkinson and Arculus 1999; Parkinson et al. 2003). IW= iron-wustite buffer. Note that the F-type peridotites plot in the field of CH_4-bearing field.

Table 1-1 Average compositions of minerals in mantle xenoliths from Cerro del Fraile, southern South America

Olivine

Type	C-type							F-type	
Sample	Bxe32-I	Bxe32-II	Bxe32-III	Bxe11	Bxe11-I	Bxe31-I	Bxe35-I	Bxe1	Bxe22
SiO2	40.92	40.75	40.77	41.01	40.91	41.10	41.02	39.66	40.01
FeO	9.42	9.45	9.31	8.88	9.13	9.28	9.12	15.62	15.63
MgO	49.21	49.13	49.11	49.76	49.68	49.53	49.68	44.31	44.41
MnO	0.16	0.14	0.15	0.13	0.13	0.14	0.13	0.23	0.23
CaO	0.07	0.08	0.08	0.04	0.04	0.07	0.06	0.04	0.03
NiO	0.39	0.37	0.37	0.36	0.37	0.37	0.35	0.19	0.20
Total	99.77	99.54	99.42	99.82	99.88	100.12	100.00	99.85	100.32
Fo [a]	90	90	90	91	91	90	91	83	84

Orthopyroxene

Type	C-type														F-type			
Sample	Bxe32-I		Bxe32-II		Bxe32-III		Bxe11		Bxe11-I		Bxe31-I		Bxe35-I		Bxe1		Bxe22	
	core	rim	core	rim	core	rim	core	rim	core	rim	core	rim	core	rim	core	rim	core	rim
SiO_2	55.17	55.27	54.80	54.88	55.15	54.90	56.19	55.99	55.69	55.81	54.80	54.82	55.56	55.40	54.02	54.61	54.38	54.69
Al_2O_3	3.55	3.62	3.57	3.58	3.55	3.58	2.36	2.32	2.46	2.41	3.69	3.75	3.52	3.66	3.55	3.00	3.38	3.06
TiO_2	0.06	0.08	0.07	0.07	0.06	0.08	0.08	0.07	0.07	0.07	0.06	0.06	0.04	0.06	0.12	0.06	0.11	0.06
Cr_2O_3	0.52	0.52	0.57	0.55	0.51	0.53	0.46	0.40	0.45	0.41	0.51	0.49	0.39	0.40	0.30	0.22	0.26	0.20
FeO(t)[b]	6.04	6.01	6.26	6.19	6.01	5.97	5.82	5.75	5.92	5.87	6.10	6.11	5.88	5.89	9.91	9.82	9.62	9.79
MgO	32.92	33.08	32.87	32.86	32.93	32.97	34.18	34.03	33.68	33.67	32.82	32.84	33.32	33.30	30.64	30.94	30.70	31.15
MnO	0.15	0.15	0.15	0.15	0.14	0.15	0.14	0.14	0.15	0.14	0.14	0.14	0.14	0.13	0.24	0.23	0.22	0.24
CaO	0.91	0.94	0.92	0.93	0.92	0.95	0.63	0.67	0.65	0.64	0.86	0.87	0.72	0.72	0.57	0.53	0.71	0.56
Na_2O	0.02	0.03	0.04	0.04	0.03	0.05	0.04	0.05	0.03	0.02	0.03	0.03	0.03	0.04	0.03	0.02	0.03	0.01
Total	99.36	99.69	99.25	99.26	99.31	99.17	99.89	99.42	99.10	99.04	99.01	99.13	99.60	99.59	99.38	99.44	99.42	99.77
Mg# [c]	0.91	0.91	0.91	0.91	0.91	0.92	0.92	0.92	0.92	0.91	0.91	0.91	0.91	0.91	0.86	0.86	0.86	0.86

Clinopyroxene

Type	C-type														F-type			
Sample	Bxe32-I		Bxe32-II		Bxe32-III		Bxe11		Bxe11-I		Bxe31-I		Bxe35-I		Bxe1		Bxe22	
	core	rim	core	rim	core	rim	core	rim	core	rim	core	rim	core	rim	core	rim	core	rim
SiO_2	52.61	52.72	52.26	52.37	52.24	52.16	53.33	53.24	53.12	52.86	52.12	52.23	52.75	52.72	51.25	51.30	51.47	51.96
Al_2O_3	3.95	4.07	3.94	4.00	3.94	3.97	3.07	3.16	2.97	3.09	4.16	4.23	4.10	4.18	4.67	4.57	4.70	4.34
TiO_2	0.21	0.21	0.17	0.19	0.19	0.19	0.19	0.21	0.19	0.20	0.18	0.18	0.18	0.18	0.57	0.53	0.56	0.42
Cr_2O_3	0.78	0.79	0.79	0.84	0.79	0.83	0.78	0.80	0.68	0.78	0.82	0.77	0.72	0.66	0.64	0.62	0.59	0.53
FeO(t)[b]	2.80	2.89	2.90	2.96	2.79	2.84	2.27	2.34	2.31	2.31	2.84	2.88	2.54	2.53	3.78	3.75	3.81	3.80
MgO	17.34	17.44	17.16	17.29	17.32	17.32	17.17	17.11	17.19	16.98	16.96	16.99	17.07	17.08	15.28	15.45	15.31	15.70
MnO	0.10	0.10	0.09	0.10	0.10	0.10	0.08	0.08	0.07	0.08	0.09	0.08	0.09	0.09	0.12	0.12	0.12	0.12
CaO	21.66	21.50	21.56	21.51	21.59	21.58	22.16	22.08	22.12	22.07	21.49	21.45	21.87	21.91	22.11	22.28	22.23	22.30
Na_2O	0.55	0.63	0.56	0.59	0.53	0.54	0.84	0.85	0.74	0.80	0.63	0.62	0.72	0.71	0.81	0.73	0.78	0.72
Total	100.0	100.3	99.43	99.85	99.49	99.53	99.89	99.85	99.39	99.17	99.29	99.43	100.0	100.1	99.22	99.34	99.55	99.89
Mg# [c]	0.92	0.92	0.91	0.91	0.92	0.92	0.93	0.93	0.93	0.93	0.91	0.91	0.92	0.92	0.88	0.88	0.88	0.88

Table 1-1 Continued

Spinel

Type	C-type														F-type			
Sample	Bxe32-I		Bxe32-II		Bxe32-III		Bxe11		Bxe11-1		Bxe31-1		Bxe35-1		Bxe1		Bxe22	
	core	rim	core	rim	core	rim	core	rim	core	rim	core	rim	core	rim	core	rim	core	rim
Al_2O_3	44.92	45.44	44.54	44.81	45.30	45.39	38.56	38.05	39.43	38.93	48.13	48.34	51.77	51.65	54.07	54.27	54.44	54.16
TiO_2	0.16	0.15	0.14	0.15	0.15	0.15	0.15	0.15	0.16	0.16	0.11	0.12	0.08	0.07	0.08	0.09	0.06	0.08
Cr_2O_3	22.20	21.89	22.52	22.33	21.62	21.63	29.80	29.45	28.55	28.96	18.89	18.80	16.28	16.37	11.80	11.56	11.77	11.71
Fe_2O_3[a]	3.57	2.61	3.36	3.32	3.48	3.29	2.78	3.45	2.44	2.76	3.49	3.35	2.20	2.40	2.59	2.85	2.45	2.65
FeO[d]	9.97	9.57	9.94	10.07	9.68	9.90	9.90	9.94	10.91	10.69	9.36	9.18	8.70	8.56	13.84	13.37	13.79	13.46
MgO	18.99	19.09	18.88	18.86	19.12	19.00	18.46	18.29	17.82	17.95	19.61	19.75	20.33	20.42	17.27	17.62	17.39	17.51
MnO	0.15	0.17	0.17	0.15	0.16	0.15	0.19	0.19	0.18	0.18	0.14	0.14	0.13	0.12	0.17	0.16	0.15	0.15
NiO	0.30	0.28	0.31	0.30	0.31	0.29	0.19	0.20	0.21	0.23	0.29	0.30	0.32	0.28	0.20	0.21	0.20	0.22
Total	100.3	99.19	99.85	99.99	99.81	99.81	100.0	99.73	99.69	99.86	100.0	99.98	99.80	99.88	100.0	100.1	100.3	99.93
$Mg/(Mg+Fe^{2+})$	0.77	0.78	0.77	0.77	0.78	0.77	0.77	0.77	0.74	0.75	0.79	0.79	0.81	0.81	0.69	0.70	0.69	0.70
Cr#[e]	0.25	0.24	0.25	0.25	0.24	0.24	0.34	0.34	0.33	0.33	0.21	0.21	0.17	0.18	0.13	0.13	0.13	0.13

Spinel inclusions

Type	C-type														F-type	
Sample	Bxe32-I		Bxe32-II		Bxe32-III		Bxe11		Bxe11-I		Bxe31-I		Bxe35-I		Bxe22	
Host	Ol	Opx	Ol	Cpx	Ol	Opx	Ol	Opx	Ol	Cpx	Ol	Opx	Ol	Opx	Ol	Opx
Al_2O_3	46.59	44.89	44.02	45.48	44.99	44.89	35.63	37.02	38.81	39.14	47.66	46.10	52.05	52.37	53.97	52.06
TiO_2	0.16	0.17	0.15	0.15	0.15	0.16	0.17	0.16	0.19	0.17	0.12	0.10	0.05	0.07	0.06	0.09
Cr_2O_3	21.06	21.59	22.82	21.44	21.76	21.82	31.61	29.27	27.95	26.03	18.69	18.36	15.88	15.47	12.12	13.06
Fe_2O_3[a]	1.25	3.76	3.74	3.50	3.83	3.37	3.43	2.98	4.05	5.53	4.02	2.11	2.48	2.47	2.80	3.37
FeO[d]	11.21	9.46	9.69	9.71	9.35	9.61	10.86	10.85	9.71	10.17	8.92	10.40	8.43	8.21	13.22	13.54
MgO	18.05	19.10	18.97	19.12	19.32	19.02	17.36	17.56	18.55	18.10	19.69	19.54	20.55	20.70	17.71	17.22
MnO	0.15	0.15	0.16	0.15	0.14	0.17	0.17	0.17	0.17	0.18	0.15	0.13	0.11	0.11	0.15	0.17
NiO	0.30	0.29	0.29	0.29	0.31	0.29	0.18	0.22	0.20	0.37	0.30	0.30	0.32	0.32	0.22	0.20
Total	98.76	99.41	99.84	99.84	99.85	99.32	99.41	98.21	99.63	99.68	99.54	97.03	99.87	99.71	100.3	99.71
$Mg/(Mg+Fe^{2+})$	0.74	0.79	0.78	0.78	0.79	0.78	0.75	0.75	0.78	0.77	0.80	0.77	0.81	0.82	0.70	0.69
Cr#[e]	0.23	0.24	0.26	0.24	0.24	0.25	0.37	0.35	0.33	0.31	0.21	0.21	0.17	0.17	0.13	0.14

Ol olivine, *Opx* orthopyroxene, *Cpx* clinopyroxene

[a] Fo forsterite component, $100\times Mg/(Mg + Fe^{2+})$

[b] Total Fe as FeO

[c] Mg# =Mg/(Mg+ΣFe)

[d] Fe_2O_3 contents calibrated using four spinel standards with known $Fe^{3+}/\Sigma Fe$, FeO is the total Fe as FeO minus the calibrated amount of Fe_2O_3

[e] Cr# =Cr/(Cr+Al)

Table 1-2 Compositions of patch "melt" and quenched phases in the "melt" in xenoliths from Cerro del Fraile

Sample	Bxe11-I (C-type)					Bxe22 (F-type)						Bxe1(F-type)					
Phase [a]	Cpx	Sp	Ol	Pl	melt1	Cpx	Sp	Ol	Pl	melt1	melt2	Cpx	Sp	Pl	Ol	Opx	melt1
SiO2	43.72	0.41	41.11	52.58	45.45	52.54	0.21	39.71	51.24	44.10	41.71	53.34	0.40	51.19	39.77	54.60	39.01
TiO2	3.77	4.97	<0.04	0.17	1.09	0.72	0.08	<0.04	<0.05	0.13	0.08	0.00	0.08	<0.05	<0.04	<0.04	0.05
Al2O3	10.74	18.60	0.28	28.28	16.54	2.55	64.32	0.04	31.35	18.85	16.79	4.43	65.11	30.88	0.05	4.14	20.45
Cr2O3	2.66	37.00	0.08	0.22	1.90	0.23	0.72	<0.04	<0.02	0.38	0.14	0.01	0.02	<0.02	<0.04	0.05	0.05
FeO [b]	3.99	22.47	9.38	1.06	4.58	5.29	13.51	14.45	0.30	4.95	5.78	3.95	12.90	0.48	15.27	10.17	6.40
MnO	0.05	0.14	0.14	nd	0.06	0.19	0.12	0.27	nd	0.08	0.17	0.17	0.18	nd	0.29	0.20	0.13
MgO	11.61	12.75	48.34	1.78	17.25	16.31	20.14	44.73	0.06	14.10	16.10	15.37	19.85	0.07	44.38	30.22	16.30
CaO	22.83	0.30	0.27	11.83	10.03	21.30	0.27	0.21	14.07	12.96	16.96	22.50	0.09	14.36	0.18	0.62	15.47
Na2O	0.82	0.01	0.03	4.21	2.25	0.44	0.01	0.04	3.59	1.16	0.33	0.56	0.03	3.32	0.04	0.04	0.38
K2O	<0.02	nd	nd	0.21	0.11	<0.02	nd	nd	0.12	0.05	0.02	<0.02	nd	0.13	nd	<0.02	0.02
Total	100.21	96.67	99.70	100.34	99.28	99.58	99.37	99.48	100.73	96.77	98.10	100.33	98.65	100.46	100.05	100.05	98.25
Mg# [c]	0.84	0.50	0.90		0.87	0.85	0.73	0.85		0.84	0.83	0.87	0.73		0.84	0.84	0.82

nd not determined

Cpx clinopyroxene, *Ol* olivine, *Opx* orthopyroxene, *Pl* plagioclase

[a] "Melt" compositions are those of an area, 50 × 50 μm

[b] Total Fe as FeO

[c] Mg# = Mg/(Mg + ΣFe) except for spinel. Mg/(Mg + Fe^{2+}) is listed for spinel in which Fe^{2+} is calculated assuming stoichiometric composition

Table 1-3 Compositions of amphiboles in other sub-arc mantle peridotites

Area sample	Nunivak Island, Alaska						Megata, Japan		North-Kamchatka			Batan, Philippines	
Sample	10006	10013	10016	10050	10052	10067	I-610A	I-014A	val55/ 4-2	val55/ 4-4	Val55/12	A	B
SiO_2	45.99	44.54	46.75	43.57	44.04	43.85	43.80	44.44	43.11	42.86	42.96	42.20	48.96
TiO_2	0.08	0.38	0.11	0.95	0.43	0.37	0.85	0.79	2.11	2.10	2.91	1.85	0.30
Al_2O_3	12.91	13.42	11.51	14.18	14.64	14.54	14.67	12.63	12.18	12.83	11.44	12.87	12.90
Cr_2O_3	3.14	2.85	2.55	1.91	1.50	1.97	0.15	1.09	0.01	0.02	0.00	1.27	0.05
FeO (t)[a]	3.42	4.13	3.29	3.90	3.14	4.50	6.89	6.79	10.97	10.13	11.62	6.49	9.24
MnO	0.07	0.11	0.11	0.06	0.08	0.11	0.21	0.12	0.13	0.11	0.11	0.17	0.06
MgO	18.45	17.68	19.01	17.79	18.16	17.80	16.48	16.55	14.77	15.29	14.81	16.60	13.56
CaO	9.07	9.79	9.43	10.89	11.14	9.32	11.50	11.49	10.40	10.77	11.38	11.97	10.01
Na_2O	4.79	3.83	4.39	2.96	3.18	3.84	2.17	2.25	3.08	3.49	2.47	1.85	1.56
K_2O	0.92	1.31	0.72	1.63	1.09	1.24	0.65	0.78	0.51	0.45	0.66	1.10	1.18
Total	98.84	98.04	97.87	97.83	97.39	97.54	97.37	96.93	97.27	98.05	98.36	96.49	98.02
Mg#[b]	0.91	0.88	0.91	0.89	0.91	0.88	0.81	0.81	0.71	0.73	0.69	0.82	0.72
Reference	Francis (1976)						Abe et al. (1998)		Kepezhinskas et al. (1995)			Schiano et al. (1995)	

[a] Total Fe as FeO

[b] Mg# = Mg/(Mg + ΣFe)

Table 1-4 Compositions of host basalts, and veins of websterite and adakitic melt in xenoliths from Cerro del Fraile

Sample	Basalt 1	Basalt 2	Websterite	Adakitic vein [c]
SiO_2	48.35	48.78	40.3	60.30
TiO_2	1.51	1.57	1.06	0.21
Al_2O_3	16.9	16.67	7.9	20.30
Cr_2O_3	0.02	0.02	0.07	0.35
FeO (t)[a]	10.51	10.13	17.57	1.10
MnO	0.17	0.17	0.21	0.05
MgO	6.99	6.93	26.53	3.30
CaO	7.78	7.67	5.87	6.60
Na_2O	4.16	4.14	1.01	6.20
K_2O	1.02	1.14	0.22	0.65
P_2O_5	0.93	0.89	0.14	nd
Total	98.31	98.07	100.88	99.06
Mg#[b]	0.54	0.55	0.74	0.84

nd not determined

[a] Total Fe as FeO

[b] Mg# = Mg/(Mg+ΣFe)

[c] Average compositions (n = 800) of adakitic veinlets (Kilian and Stern 2002)

Table 1-5 Compositions of olivine, orthopyroxene and spinel and oxygen fugacity values for the mantle xenoliths from Cerro del Fraile, southernmost, South America

Type samples	C-type							F-type	
	Bxe32-I	Bxe32-II	Bxe32-III	Bxe11	Bxe11-I	Bxe31-I	Bxe35-I	Bxe1	Bxe22
Olivine									
X_{Fe}	0.097	0.097	0.096	0.091	0.093	0.095	0.093	0.165	0.165
X_{Mg}	0.903	0.903	0.904	0.909	0.907	0.905	0.907	0.835	0.835
Orthopyroxene									
Enstatite	0.889	0.885	0.889	0.900	0.897	0.889	0.895	0.834	0.836
Ferrosilite	0.094	0.097	0.093	0.088	0.091	0.095	0.091	0.155	0.150
M1(Fe) [a]	0.086	0.090	0.085	0.083	0.085	0.087	0.083	0.144	0.139
M2(Fe) [a]	0.089	0.092	0.089	0.085	0.087	0.091	0.087	0.149	0.144
Spinel									
Cr#	0.25	0.25	0.24	0.34	0.33	0.21	0.17	0.13	0.13
$(Fe^{3+}/\Sigma Fe)^{b}_{probe}$	0.26	0.25	0.26	0.22	0.19	0.26	0.19	0.14	0.14
$(Fe^{3+}/\Sigma Fe)^{c}_{calibrated}$	0.24	0.23	0.24	0.20	0.17	0.25	0.19	0.14	0.14
SD(%)[d] for $(Fe^{3+}/\Sigma Fe)_{calibrated}$	1.17	8.28	3.47	5.78	3.01	1.37	10.33	3.37	6.70
$Mg/(Mg+Fe^{2+})$	0.77	0.77	0.78	0.77	0.74	0.79	0.81	0.69	0.69
log a_{Fe3O4}	-2.07	-2.11	-2.09	-2.27	-2.34	-2.04	-2.36	-1.90	-1.95
Temperature and oxygen fugacity									
T °C (Wells)[e]	1036	1031	1041	955	963	1023	1000	901	901
T °C (BK)[f]	1029	1028	1028	925	932	1018	982	855	857
T °C (BK)[g]	1030	1035	1035	942	951	1018	1458	929	977
△log(fO2)FMQ[h]	-0.03	-0.15	-0.06	-0.45	-0.55	-0.01	-0.72	-0.80	-0.90
△log(fO2)FMQ[i]	0.14	0.12	0.14	-0.18	-0.37	0.31	-0.39	-0.92	-1.08

[a] M1(Fe), M2 (Fe) = Fractions of Fe at M1 and M2 sites, calculated following the method in Wood et al (1990)

[b] Calculated assuming stoichiometric composition of spinel

[c] Calibrated using the four spinel grains with known Fe^{3+} contents

[d] Standard deviation calculated based on cores of 3-5 grains in each sample

[e] Calculated based on two-pyroxene thermometer (Wells 1977)

[f] Calculated based on two-pyroxene thermometer (Brey and Köhler 1990)

[g] Calculated based on the Ca-in-OPX thermometer (Brey and Köhler 1990)

[h] Calculated following the method of Ballhaus et al (1991) using the Fe^{3+} contents of spinel assuming its stoichiometric composition

[i] Calculated following the method of Nell and Wood (1991) using the calibrated contents of Fe^{3+}

Addendum to Chapter 1

This addendum explains comments raised by the thesis examining board. Chapter 1 has been published as a paper in "Contributions to Mineralogy and Petrology" in 2007 and it was not modified during the revision.

Comment: Calculated logfO_2 has an uncertainty of ± 0.4 logarithmic units and the variation of fO_2 in samples is not discernible.

Response: C-type peridotites have average fO_2 around the FMQ buffer, and F-type has fO_2 at ~ FMQ-1.1. The two sets of samples show consistently different values and the difference is larger than the uncertainty of 0.4 logarithmic units.

Comment: No data were present for the trace element patterns of Fig. 8.

Response: The trace element patterns were provided by Dr. Rolf Kilian, a co-author of the paper.

Comment: H_2O-CO_2 fluids are very poor oxidants in the mantle (because their reaction is limited by low fH_2 attainable in the mantle).

Response: Fluids can move along grains boundaries and escape from a system. Therefore, CO_2-bearing fluid can be an oxidant or reducer depending on the oxidation condition of the rocks and composition of the fluids.

Comment: The nature of slab and asthenospheric melts are qualitatively inferred and their roles are essentially predicted by the starting assumptions of the paper, rather than being "tested" by the data.

Response: Previous researchers have documented asthenospheric origin for the basalts hosting the xenoliths (e.g. Stern et al. 1990, 1999; Gorring et al. 1997; D'Orazio et al. 2000), and the occurrence of slab melt in the area (e.g., Kilian and Stern 2002). I interpreted my new data in the framework of previous work. Regarding the presence of slab-melt in this area, I obtained the interpretation based on the data obtained during my PhD thesis project. The supporting data include low Mg# of silicate minerals and low Cr# of spinel.

Comment: The number of samples, nine, is not large with only two F-type samples and they may not represent peridotites underlying the study area.

Response: We are not suggesting that our data represent the entire subcontinental lithospheric mantle underlying the southern South America. The Chapter presents the mantle processes recorded in the xenoliths.

CHAPTER 2

Oxidation state of Paleozoic continental lithospheric mantle below southern South America

Jian Wang[1], Keiko H. Hattori[1], Jianping Li[1], Charles R. Stern[2]

Department of Earth Sciences, University of Ottawa,
Ottawa, Ontario, Canada, K1N 6N5
Corresponding author e-mail: jwang062@uottawa.ca
Tel: 1-613-562-5800 (X 6729), Fax: 1-613-562-5192

Manuscript in preparation for submission to a refereed journal

Abstract

Mantle xenoliths in the Quaternary Pali Aike alkaline basalts of southern Patagonia include lherzolites and harzburgites with and without garnet. The values of fO_2 for all xenoliths range from FMQ-0.33 to +0.75, which overlap those for abyssal peridotites. The fO_2 data, together with the bulk rock, major- and trace-element data, suggest that the Patagonian subcontinental mantle lithosphere (SCLM) formed through the accretion of oceanic lithosphere. Textural relations of garnet and spinel suggest that garnet facies xenoliths formed from spinel facies peridotites due to cooling and/or increasing pressure during or after stablization below the Paleozoic continental crust. The narrow range of fO_2 between garnet- and spinel-facies peridotites suggests this transformation process was not accompanied by changes of fO_2.

Modal and cryptic metasomatism of the xenoliths resulted in the formation of Ti-phlogopite, Ti-amphibole, and ilmenite, and lowering of Mg and enrichment of Ti in bulk rocks and minerals. Metasomatism led to the replacement of olivine by orthopyroxene, in some cases forming orthopyroxenites. The metasomatism observed in the xenoliths reflects relatively recent Neogene infiltration of asthenosphere-derived melt through a slab window in conjunction with the generation of the Pali Aike basalts. For the entire peridotite xenolith suite, fO_2 values are similar between non-metasomatized (FMQ-0.23 to +0.48) and metasomazied (FMQ-0.33 to +0.75) samples. This is explained by similar fO_2 of the asthenosphere-derived metasomatizing melt (~FMQ-0.50) and non-metasomatized samples of abyssal origin.

Key words: Patagonia, slab window, Fe- and Ti-rich melt, peridotite xenoliths, mantle oxidation condition

2.1. Introduction

Mantle oxidation state is important in controlling the composition and nature of partial melt. For example, oxidized sub-arc mantle is conducive to form high sulfur magmas (DeHoog et al. 2004) and giant Au and Cu deposits because metals can be effectively partitioned to partial melt under oxidized condition (Mungall 2002; Hattori and Keith 2001). A significant variation is observed in fO_2 in samples of the lithospheric upper mantle from different tectonic environments, but its causes are still not well understood. Partial melting is generally considered to result in low fO_2 in the residual mantle as Fe^{3+} is preferentially incorporated in melt (Arculus 1994; Canil et al. 1994; McCammon and Kopylova 2004). Lowering of fO_2 in refractory peridotites is supported by the data from sub-continental lithospheric mantle (SCLM) beneath old cratons (e.g. Kaapvaal, South Africa) where reduced fO_2 values are accompanied by high Cr# values (atomic ratio of Cr/[Cr+Al]) in spinel (e.g. Woodland and Koch 2003). However, a positive correlation between fO_2 and Cr# in spinel was observed in sub-arc mantle peridotites (e.g. Ballhaus 1993; Parkinson and Arculus 1999). Oxidized condition of refractory peridotites in sub-arc mantle has been explained by the infiltration of oxidized aqueous fluids released from down-going slabs (Arculus 1985; Wood and Virgo 1989; Brandon and Draper 1996; Parkinson and Arculus 1999), but in some other cases it has been demonstrated that slab-derived fluids and melts can also be reducing (Wang et al. 2007).

Abyssal peridotites, which likely reflect fO_2 of the upper asthenospheric mantle, are slightly reduced compared to the FMQ buffer (Christie et al. 1986; Bryndzia and Wood 1990; Bézos and Humler 2005). This is consistent with reduced oxidation state of mantle peridotites underlying continental rifts and hot spots that have been infiltrated by asthenosphere-derived melts and/or fluids (Ionov and Wood 1992).

Previous studies on oxidation state of SCLM focused on those underlying Archean continents, such as Kaapvaal craton (South Africa) and Slave province of the Canadian Shield (e.g. Daniels and Gurney 1991; Gudmundsson and Wood 1995; McCammon et al. 2001; Woodland and Koch 2003; McCammon and Kopylova 2004). Studies on Phanerozoic SCLM are

few. The Patagonian terrane in the southern part of South America is considered to have formed in the late Proterozoic to early Paleozoic and docked with the part of Gondwanaland that was later to become the South American continent in the late Paleozoic (e.g. Ramos 1988; Rapalini 2005). Therefore, mantle xenoliths from Patagonian basalts contain information relevant to the formation of the Phanerozoic Patagonian terrane SCLM. This paper reports the bulk rock compositions, mineral chemistry, and the oxidation condition of the representative mantle peridotite xenoliths from the Quaternary Pali Aike basalts, southern Patagonia (Fig. 2-1) and discusses the origin and evolution of this relatively young SCLM.

2.2. Tectonic Setting

The continental crust and SCLM of the Patagonian terrane of South America formed during late Proterozoic to middle Paleozoic time (e.g. Ramos 1988; Rapalini 2005), and collided with and was accreted to Gondwanaland in the late Paleozoic (Ramos 1988). Late Paleozoic calc-alkaline volcanic and plutonic rocks in northern Patagonia are interpreted as the products developed in an arc before the collision (Ramos 1988). During the late Jurassic break-up of Gondwanaland, a volcanic-tectonic rift zone, associated with voluminous rhyolitic volcanism forming the Chon Aike Formation (Bruhn et al. 1978; Kay et al. 1989), affected all of Patagonia. Since the late Jurassic or early Cretaceous, the area has been dominated by subsidence and sedimentation, forming the Magallanes basin, as well as the subduction of eastern Pacific oceanic plate below western South American.

In the Miocene, subduction of the Chile Rise produced strike-slip along the boundary between the Scotia Plate and the South American Plate (D'Orazio et al. 2000 ; Fig. 2-1). The Chile ridge between the Nazca and Antarctic Plates collided with the trench near the southern tip of South America at ~14-15 Ma, forming a triple junction (Cande and Leslie 1986) which has since migrated northward to its present position at 46.5 °S (Fig. 2-1). Ridge subduction was responsible for uplift of the southernmost sector of the Andes, formation of the Patagonian fold-thrust belt (Ramos 1989), and formation of a slab window, which produced extensive

plateau basaltic lavas (D'Orazio et al. 2000). The plateau basaltic lavas range from late Miocene to recent and systematically young to the northeast following the track of the subducted ridge. The Pali Aike volcanic field, which covers 4500 km^2, is the southernmost among the Patagonian plateau basalts (Skewes and Stern 1979; Stern et al. 1990; D'Orazio et al. 2000). Partial melting of the young Antarctic plate, west of the ridge, is producing adakitic melts erupted from the stratovolcanoes of the Andean Austral Volcanic Zone (Stern and Kilian 1996), ~ 250 km west of the Pali Aike area (Fig. 2-1).

2.3. Samples

We examined a total of thirty-two mantle xenoliths collected from the Pali Aike basalts. They range in size from 3 to 20 cm in the longest dimension. Samples are rounded and show no evidence of weathering and serpentinization, but the rims of several samples show the evidence of the infiltration of host basaltic magma. These parts were removed before preparing samples for bulk rock analysis. Six samples (LS33, BN50, TM15, TM0, TM2, and LS1) were described previously by Stern et al. (1999), but their bulk compositions and the compositions of minerals were re-determined together with the other twenty-six new samples.

The mantle xenoliths are divided into two types; peridotites and pyroxenites. Their mineralogy is listed in Table 1. Peridotites are lherzolites and harzburgites. They are further divided into five subtypes based on the presence of garnet and/or spinel: garnet lherzolite (n = 1), garnet-spinel lherzolite (n = 6), spinel lherzolite (n = 2), garnet-spinel harzburgite (n = 8), and spinel harzburgite (n = 7). Pyroxenite xenoliths are orthopyroxenites and minor websterites. This paper focuses on peridotite samples.

Garnet-bearing lherzolite consists mainly of olivine (50-70 vol%), orthopyroxene (15-30 vol%), clinopyroxene (5-20 vol%), garnet (5-15 vol%) and spinel ($\leq$ 2 vol.%). It shows coarse-grained (1- 4 mm) equigranular to porphyroblastic texture (Fig. 2-2a). Garnet-spinel harzburgite shows prophyroblastic to equigranular (1 - 4 mm) texture (Fig. 2-2b) and contains olivine (50-70 vol%), orthopyroxene (25-30 vol%), and garnet (5-10 vol%) with minor spinel ($\leq$

2 vol%) and clinopyroxene (≤ 0.5 vol%). Garnet is variable in size (1 - 6 mm) and shows a symplectic rim (>50 μm), a mixture of fine-grained pyroxenes and spinels, that was most likely formed during the ascent of the xenoliths. Relict grains of spinel (up to 2 mm) showing reaction rims are common in garnet (Fig. 2-2c), suggesting that garnet is a product of reaction involving spinel. Spinel inclusions (0.2-0.3 mm) and intergrowth with olivine and pyroxene (up to 2 mm) are also common in garnet-bearing peridotites. Spinel peridotites show same grain sizes and mineral assemblages similar as garnet-bearing peridotites except no garnet.

Orthopyroxenite (n = 8) occurs either as discrete xenoliths or veinlets (>5 mm) in garnet-bearing harzburgites (Fig. 2-2d). Discrete orthopyroxenite xenoliths commonly contain small angular dunite and/or harzburgite fragments (5-10 mm in size) with diffuse boundaries with orthopyroxenite host. Orthopyroxenites show equigranular and/or porphyroblastic texture with coarse garnet (up to 5 mm) and orthopyroxene (up to 4 mm). They are composed of orthopyroxene (≥85 vol%), garnet, olivine, Ti-phlogopite, Ti-amphibole, Mg-ilmenite, and minor sulphide minerals (pentlandite and pyrrhotite), with or without minor clinopyroxene. The veinlets of orthopyroxenite contain the same mineral assemblage as garnet orthopyroxenite xenoliths and are accompanied by halos of secondary orthopyroxene (Fig. 2-2d).

2.4. Analytical methods

Mineral compositions were determined using the Camebax MBX electron probe at Carleton University and the JEOL 8900 Super probe at McGill University. Camebax MBX electron probe was operated with 15 kV acceleration voltage, ~20 nA beam current, and focused beam size of <1 μm. Counting time was set up as 20s for all elements except Ca (50s) in olivine. JEOL 8900 Super Probe was operated with 20 kV acceleration voltage, 20 nA beam current, and 1 μm beam size. Counting time of 30s was used for most elements except 50s for Ca in olivine. Cameca PAP and ZAF correction procedures were applied to raw data for Camebax MBX and JEOL 8900 probes, respectively. A suite of well characterized natural and synthetic minerals were used as standards in both probes.

Sources of uncertainty in the calculation of fO_2 include analytical errors, mineral heterogeneity, and errors in P and T estimates. In practice, inaccurate Fe^{3+} contents in spinel contributes the greatest uncertainty in fO_2 calculations (O'Neill and Wall 1987; Wood and Virgo 1989). To circumvent this problem, four secondary spinel standards with known Fe^{3+} contents were used to calibrate $Fe^{3+}/\Sigma Fe$ of samples (see Wood and Virgo 1989; Woodland et al. 1992). The calibrated $Fe^{3+}/\Sigma Fe$ ratios are higher than those calculated assuming stoichiometry and charge balance (Fig. 2-3). Propagating counting errors through this calculation yields an uncertainty in $Fe^{3+}/\Sigma Fe$ of ± 0.025 which corresponds to 0.3-0.4 log units. The contribution to the fO_2 uncertainty from silicate phases is small. Standard errors in olivine composition are less than $\pm$ 0.003 in X_{Fe}, which translates into an uncertainty of ± 0.15 log units in fO_2. Orthopyroxene is more heterogeneous than olivine; however, propagated uncertainties from this heterogeneity are small, on the order of 0.1 log units in fO_2 or less. The equilibration P and T are subject to significant uncertainty. This is particularly the case for P as no accurate geobarometer is at present available for spinel peridotites. However, referencing fO_2 relative to FMQ buffer mitigates the effects of P and T uncertainties. Errors of $\pm$ 100 °C and $\pm$ 8Kb produce uncertainties of only ± 0.2 and ± 0.3 log units in $\Delta \log fO_2$ (FMQ), respectively. Considering a normal distribution of error, overall uncertainties of about ± 0.5 log units can be expected in $\Delta \log fO_2$ (FMQ).

For the bulk rock composition analysis, rims and veins were removed before grinding samples. Major and minor elements were determined using a Philips PW 2400 X-ray fluorescence spectrometer after fusing the sample powder with $LiBO_3$ at the University of Ottawa. Precision based on replicate runs of eleven samples is $\pm$ 0.35 % for Al_2O_3, $\pm$ 0.48 % for MgO, $\pm$ 1.3 % for Cr, and $\pm$ 9.2 % for Ni. The accuracy, which was monitored using references of MRG-1 and Sy-2, shows $\pm$ 0.039 % for Al_2O_3, 0.28 for MgO, 3.4 % for Cr, and 4.0 % for Ni. Accuracy is less than 1 % and 10 % for other major and minor elements, respectively. Loss of ignition was determined after heating samples at 1050 °C for 1.5 hrs.

2.5. Mineral chemistry and bulk compositions of xenoliths

2.5.1. Mineral chemistry

2.5.1.1. Olivine

Olivine in Grt-Spl lherzolite has higher Fo (89.1-90.6) than that in garnet-spinel harzburgites (87.1-89.3) (Table 2-2a). Olivine shows similar Fo in spinel lherzolite and spinel harzburgite, 89.5-90.6 and 86.0-91.6, respectively (Table 2-2b). The high Fo in Grt-Spl lherzolites relative to Grt-Spl harzburgites is not consistent with the generally conceived interpretation that harzburgite is refractory compared to lherzolite. Therefore, low Fo values in Grt-Spl harzburgites are attributed to metasomatism. Olivine occurs as a minor relict phase in orthopyroxenites and shows low Fo values, 83.3-87.3 (Table 2-2c).

2.5.1.2. Orthopyroxene

The values of Mg# (=Mg/(Mg + ΣFe)) are high in lherzolite, ranging from 0.895 to 0.910, but they are low (0.865-0.922) in harzburgites (Table 2-2a, 2-2b). TiO_2 contents of orthopyroxenes are higher in harzburgites (0.13-0.35 wt%), another indication that the harzburgites have been metasomatized. Orthopyroxenites contain orthopyroxene with low Mg# (0.845-0.892) and relatively high TiO_2 (0.20-0.59 wt%) (Table 2-2c). Mg# in orthopyroxenes are always higher than Fo in co-existing olivines in all samples, confirming that these phases are in Fe-Mg exchange equilibrium (e.g. Grove et al. 1992; Qi et al. 1995; Conceição and Green 2004).

2.5.1.3. Clinopyroxene

As in olivine and orthopyroxene, clinopyroxene in garnet-spinel harzburgites shows slightly lower Mg# (0.879-0.886), but significantly higher TiO_2 (0.90-1.26 wt%) than that of garnet-spinel lherzolites (Mg# = 0.892-0.908; 0.11-0.64 wt% TiO_2) (Table 2-2a), suggesting that the garnet-spinel harzburgites likely underwent metasomatism to be enriched in Fe and Ti. Clinopyroxene grains in spinel lherzolites and spinel harzburgites generally have higher Mg# than those in garnet-bearing xenoliths (Table 2-2b). Clinopyroxenes in orthopyroxenites are relict and contain high TiO_2 (0.65-1.59 wt%) and low Mg# (0.826-0.907 wt%) and Cr_2O_3 (0.25-1.16 wt%) compared to that in peridotites (Table 2-2c).

2.5.1.4. Oxides

Spinel

The compositions of intergranular grains of spinel and inclusions in silicate minerals are similar in individual samples (Table 2-2d), suggesting that spinel equilibrated. However, spinel grains in contact with host volcanic rocks developed symplectic rims (30-50 μm) with high Cr# (> 0.6) and the composition data of these rims were discarded. Spinel in most peridotites plot in the field for abyssal peridotites on the binary Cr#-Mg# diagram and ternary Fe^{3+}-Cr^{3+}-Al^{3+} diagram (Figs.2-4, 2-5). Similar compositions for spinel in garnet-bearing lherzolites (0.271-0.368; Table 2-5) and harzburgites (0.289-0.331; Table 2-5) suggest that harzburgites are not typical mantle residues because refractory harzburgites should have higher Cr# in spinel (Dick and Bullen 1984). Spinel in garnet-free peridotites shows variable compositions, low Cr# (~ 0.170) in lherzolites and high Cr# (0.361-0.504) in harzburgites (Table 2-5). Spinel in orthopyroxenite is rare and characterized by low Cr (Table 2-5).

Ilmenite

Ilmenite commonly occurs in orthopyroxenites. Ilmenites are also common in the veinlets of Ti-rich phlogopite in garnet-bearing peridotites. Ilmenite is characterized by high MgO (11.09-13.66 wt%) (Table 2-2c). The hematite components in ilmenite are low, 0.52- 4.07 mol%, and no exsolution lamellae of hematite were observed.

2.5.1.5. Garnet

Garnet in peridotites contains high Mg# (0.768-0.856) compared to that in orthopyroxenites (0.737-0.798) (Table 2-2a, c). Garnet in garnet-spinel harzburgite and garnet orthopyroxenite contains significantly higher TiO_2 (0.18-0.42 wt%) and lower Cr_2O_3 (0.39-1.63 wt%) compared to those in lherzolite, which have TiO_2 and Cr_2O_3 at 0.05-0.25 wt% and 1.21-1.93 wt%, respectively (Table 2-2a, 2-2c). There is no difference in composition between the garnets with and without spinel inclusions.

2.5.1.6. Hydrous minerals

Phlogopite and amphibole are high in Ti (Table 2-2c). They occur in orthopyroxenites and several harzburgites. Amphibole shows a large compositional variation in TiO_2 (3.38- 4.83 wt%), CaO (5.87-12.2 wt%), and K_2O+Na_2O (1.77-8.93 wt%). The compositional variation in individual samples suggest that amphibole formed late and was not equilibrated after crystallization.

2.5.2. Bulk rock compositions of xenoliths

All lherzolites contain lower CaO and Al_2O_3 and higher Mg# (Mg/(Mg + ΣFe)) than the estimated primitive mantle composition (McDonough and Sun 1995), confirming that they are residues of various degrees of partial melting (Table 2-3; Fig. 2-6). Most lherzolites and spinel harzburgites have similar compositions as abyssal peridotites (Fig. 2-6).

Most garnet-bearing harzburgites have higher Si, Al, Ti and lower Mg# than that of spinel harzburgites (Fig. 2-6). Furthermore, they contain higher Ti and lower Mg# than garnet-bearing lherzolites, suggesting they were enriched in Si, Al, Fe and Ti during later modification processes (Figs. 2-6a, 2-6c, 2-6d). Three spinel harzburgite samples also show higher Ti and lower Mg# than spinel lherzolites (Figs. 2-6c, 2-6d), suggesting that spinel harzburgites were also affected by similar modification processes as in garnet-bearing harzburgites.

Garnet orthopyroxenites contain high SiO_2 (48.8–53.95 wt%), Al_2O_3 (3.62–11.34 wt%) and TiO_2 (up to 2.0 wt%), and low Mg# (0.846–0.880) compared to peridotite xenoliths in the area (Fig. 2-6).

2.5.3. Metasomatism

Modal metasomatism resulted in the formation of Ti minerals (Ti-phlogopite, Ti-amphibole and Mg-ilmenite). Metasomatic minerals are common in garnet-bearing samples (samples TM14, TM15, BN92, BN45, PAK6) which are derived from the deepest part of the lithosphere. Several garnet-bearing harzburgites contain veinlets of orthopyroxenite with halos of Ti-phlogopite, Ti-amphibole and secondary orthopyroxenes (Fig. 2-2d). These veinlets have identical mineralogy and mineral chemistry as discrete garnet orthopyroxenite xenoliths. Cryptic

metasomatism without metasomatic minerals is expressed in some xenoliths as low Mg# and elevated TiO_2 in minerals and bulk rock compositions (Figs. 2-6c, 2-6d, 2-7).

Olivine and pyroxenes in harzburgites commonly show lower Mg# and higher TiO_2 than those in lherzolites, suggesting the metasomatism is more prevalent in harzburgites (Fig. 2-7). Low Mg# of olivine make most garnet-bearing harzburgites plot outside or on the margin of the olivine-spinel mantle array of Arai (1994) (Fig. 2-8).

Metasomatism in spinel peridotites from the shallower part of the lithosphere is not as common as in garnet-bearing peridotites. Only one lherzolite sample (PA64) contains a veinlet of websterite, and two harzburgites (PAK5 and LS100) show high TiO_2 and low Mg# in bulk rock and mineral compositions (Figs. 2-6, 2-7). The high Ti and low Mg# nature of metasomatism is similar to that in garnet-bearing peridotites, suggesting that a similar metasomatizing melt affected both garnet-bearing and garnet-free peridotites, but it preferentially affected the deeper part of the lithosphere (Stern et al. 1999).

Considering the formation of Ti-rich minerals and high Ti and low Mg# in bulk rocks, we suggest that the metasomatizing melt is an evolved alkali basaltic melt, similar to the Pali Aike alkali basalts, that originates from the asthenospheric mantle. Isotopic data for modally metasomatized garnet-spinel harzburgites reported by Stern et al. (1999) are similar to those of Pali Aike host basalts and other Patagonian plateau alkali basalts (Stern et al. 1990). As described before, the Patagonian basalts are derived from the asthenospheric mantle through a slab window (Stern et al. 1990; Gorring et al. 1997; D'Orazio et al. 2000). The orthopyroxenites are considered to be the products of extensive metasomatism of peridotites based on textures of relict grains of olivine, mineral chemistry and bulk compositions (see chapter 3).

2.6. Calculation of pressure, temperature and fO_2

There is a good positive correlation between Mg# of coexisting mineral phases in different samples except for two garnet bearing harzburgite (TM 14, TM 15) suggesting that most minerals were equilibrated. This is a valid basis for estimating equilibrium PT conditions and fO_2

of these xenoliths. Temperatures for peridotite xenoliths were determined using two-pyroxene thermometers (Wells 1977; Brey and Köhler 1990) and Ca-in-Opx thermometry (Brey and Köhler 1990) (Table 2-4). The two-pyroxene thermometry of Brey and Köhler (1990) yielded systematically higher temperatures by up to ~100 °C than the results using the Wells' thermometry. The Ca-in-Opx thermometry (Brey and Köhler 1990) gave similar temperatures as the two-pyroxene thermometry of Wells (1977) but the former gives slightly higher temperature by approximately 5 °C. The olivine-spinel Fe-Mg exchange thermometry of Ballhaus et al. (1991) gave systematically lower temperatures than others most likely due to lower closure temperature for ion exchange between spinel and olivine (e.g. De Hoog et al. 2004). Wells' thermometry was used for fO_2 calculations in this study because it has been used for fO_2 calculations of mantle peridotites by previous workers (e.g. Ionov and Wood 1992; Wood and Virgo 1989). For those samples without clinopyroxene, the temperatures using the Ca-in-Opx thermometry were used after subtracting the systematic difference of 5 °C between the two thermometers.

The Al-in-Opx barometry of Nickel and Green (1985) and Brey and Köhler (1990) yielded comparable values with discrepancies of 5-7 Kb in several samples. This paper used the pressures based on the barometry of Nickel and Green (1985) (Table 2-4). For the calculation of fO_2, we use 15 Kb for all spinel facies peridotites. The estimated PT are consistent with previous results (Stern et al. 1999).

The fO_2 values are calculated using the reaction equilibrium of olivine-orthopyroxene-spinel and the activities of Fe_3O_4 using the formula of Nell and Wood (1991). We report fO_2 values relative to the FMQ buffer ($\Delta \log fO_2$ (FMQ)) because this cancels out the uncertainties associated with estimates of temperatures and pressures. For comparison, fO_2 values calculated using the formula of Ballhaus et al. (1991) are listed in Table 2-5.

The calculated fO_2 values of peridotites range from FMQ-0.33 to FMQ+0.75 and the majority of samples are slightly more oxidized than the FMQ buffer, with the median value of FMQ +0.30 (n = 24) (Table 2-5). Garnet-bearing lherzolite and harzburgite show similar mean

fO_2 values of FMQ+0.13 ± 0.32 (n = 6) and FMQ+0.22 ± 0.19 (n = 8), respectively. Orthopyroxenite sample BNC2 shows relatively reduced fO_2 value of FMQ-0.50.

2.7. Discussion

2.7.1. Origin and evolution of the mantle below southern South America

Formation of SCLM below Pali Aike

Several possible processes have been proposed for the formation of SCLM, including; underplating of mantle plumes (Herzberg 1999), formation of highly refractory mantle in wedge mantle (Parman et al. 2004), and accretion of oceanic lithosphere (Boyd 1989; Niu and O'Hara 2003). The model of oceanic lithosphere accretion suggests that the lithosphere mantle thickens by stacking of oceanic lithosphere during subduction (Boyd 1989; Niu and O'Hara 2003). The mantle plume model involves upwelling of hot asthenospheric mantle plume followed by high degree of partial melting above plume heads to form buoyant refractory lithospheric mantle. The "mantle wedge" model suggests that continents and underlying lithospheric mantle may be formed in subduction zones where refractory wedge mantle eventually changed to cratonic lithospheric mantle (Parman et al. 2004). This model becomes increasingly popular because it provides an explanation for the occurrence of subduction-related igneous rocks in ancient continents (Canil 2004), the silica-enrichment in SCLM (Kelemen et al. 1998); and small volumes of komatiite to mass balance the composition of SCLM. The model also provides the mechanism for continental rocks to be enriched in incompatible trace elements (Carlson et al. 2005).

Both "hot plume" and "mantle wedge" models require partial melting to high degree to form refractory SCLM and the age of SCLM should be older than or similar to voluminous igneous rocks on the overlying continent. Our peridotites are only variably depleted compared to the primitive mantle composition (Fig. 2-6). Many samples are not as refractory as most ancient SCLM (Stern et al. 1999), such as Kaapvaal, Siberian, and Slave cratons, particularly when Mg# of bulk rocks and/or Cr# in spinel are considered (Boyd 1989; Boyd et al. 1997; Kopylova and

Russell 2000), suggesting that these two models may not be applicable to the formation of Pali Aike peridotites. The degrees of partial melting and origin of peridotites can be evaluated by examining the ratios of Mg/Si and Al/Si of bulk rock compositions. Overall, Pali Aike peridotites show lower Mg/Si and higher Al/Si than sub-arc peridotites and overlap with the field of off-craton peridotites (Fig. 2-9). The non-metasomatized peridotites plot in the field of abyssal peridotites (Fig. 2-9), suggesting they likely originated from oceanic mantle. The degree of depletion due to melt extraction in the residual mantle can also be illustrated in a diagram of Al_2O_3 in orthopyroxene vs Cr# in Spinel (Fig. 2-10) because Al is preferentially incorporated in melt and Al^{VI} in orthopyroxene lowers and Cr# of spinel increase in the residues during partial melting. Non-metasomatized garnet-bearing lherzolites and most spinel peridotites in Pali Aike show Al_2O_3 contents in Opx and Cr# in Spl overall overlapping with the field of abyssal peridotites, and notably higher Al (Opx) and lower Cr (Spl) than sub-arc peridotites, such as Mariana (Bloomer and Hawkins 1983; Shcherbakov and Savelyeva 1984; Parkinson and Pearce 1998), Tonga (Bloomer and Fisher 1987), and south Kamchatka (Arai et al. 2003). In addition, compositions of spinel in anhydrous peridotite xenoliths plot in the field of abyssal peridotites in both the binary (Mg#-Cr#) and ternary (Fe^{3+}-Cr^{3+}-Al^{3+}) diagrams (Figs. 2-4, 2-5).

Therefore our data support the accretion of oceanic lithosphere model proposed by Boyd (1989) and Niu and O'Hara (2003) for the SCLM beneath Pali Aike. This interpretation is also supported by low ratios of light to heavy rare-earth-elements and Sr, Nd, Pb, O and Os isotope compositions of garnet lherzolites which are similar to those of mid-oceanic ridge basalts (Stern et al. 1999).

Although there is some uncertainty surrounding the tectonic origin of the Patagonian terrane (e.g. Romos 1988; Gonzalez et al. 2002; Rapela et al. 1998; Rapela and Pankhurst 2002), the most accepted model is that it formed in late Proterozoic to early Paleozoic and collided with Gondwana in the late Paleozoic (Rapalini 2005). The tectonic history of the area suggests that oceanic lithosphere likely accreted to the margin of Patagonian terrane from the late Precambrian to early Paleozoic time, and with the margin of Gondwana from the early to late Paleozoic

accretion of the Patagonian terrane, and this formed the present lithospheric upper mantle in the area. This interpretation is also consistent with the Os model ages of 531 Ma (sample TM2) and 860 Ma (sample LS33) for Pali Aike garnet peridotites reported by Stern et al (1999).

Origin of garnet bearing peridotites

Two possible processes are proposed to explain the common occurrence of relict spinel in garnet (Fig 2-2c). Stern et al (1999) suggested that accreted oceanic lithosphere cooled significantly after accretion and this cooling process caused spinel to break down to form garnet and olivine. They documented over 175°C of cooling based on core-to-rim compositional difference in clinopyroxenes from Pali Aike spinel lherzolites, and suggested that this resulted from slow, long term cooling of the lithosphere, either since it was accreted or since the last major episode magmatism in the region which occurred in the Jurassic in association with the opening of the southern Atlantic ocean and the separation of South America from Gondwana (Bruhn et al. 1978; Selverstone and Stern 1983; Kay et al. 1989). Another possibility is that during accretion below the continental crust portions of oceanic lithosphere subducted to a deeper level where spinel became unstable forming garnet and olivine during the accretion process.

Both processes involve the following reaction spinel + orthopyroxene + clinopyroxene forming garnet + olivine, a temperature and pressure sensitive isochemical reaction (Obata and Morten 1987). The estimated PT conditions (P = 19-25 Kb and T = 960-1120 °C; Table 2-4) for the Pali Aike garnet-bearing xenoliths yield the geotherm lying close to oceanic geotherm and those of off-craton areas affected by upwelling asthenospheric mantle, such as Vitim, Russia (Ionov et al. 1993) and SE China (Qi et al. 1995) (Fig. 2-11), but much higher than that of ancient cratonic provinces, such as South Africa, Siberia and Namibia (Fig. 2-11). Therefore, the high geotherm in the area most likely is a recent feature which reflects the hot upwelling asthenospheric mantle through a slab window and the generation of the Pali Aike basalts as suggested by Stern et al. (1999).

2.7.2. Possible processes controlling the oxidation states of mantle rocks

The variable lithologies, a range in Cr# in spinel and the evidence of metasomatism in our samples suggest that the redox state may have been influenced by both partial melting in the original suboceanic lithosphere and the subsequent metasomatism associated with the generation of the Pali Aike basalts. Partial melting is considered to result in reduction of fO_2 in the residual mantle as Fe^{3+} is preferentially incorporated in partial melt (Arculus 1994). However, our spinel facies xenolith samples, which are in general free of metasomatism, do not show any correlation between fO_2 and Cr# of spinel in (Fig. 2-12), suggesting that their fO_2 did not change during partial melting. Our results are consistent with comparable fO_2 values between mid-oceanic ridge basalts and the residue of melting, abyssal peridotites (Bézos and Humler 2005). It is also supported by the experimental result of Amundsen and Neumann (1992), who showed that fertile garnet facies mantle peridotites produce a partial melt with comparable $Fe^{3+}/\Sigma Fe$ ratios.

Orthopyroxenites represent the products of metasomatism (see chapter 3), therefore, fO_2 value of orthopyroxenites likely reflects the oxidation state of the metasomatizing melt. One orthopyroxenite (BNC2) yielded fO_2 of FMQ-0.50 based on spinel + orthopyroxene + olivine oxybarometry. The mineral compositions of ilmenite and clinopyroxene also support reduced fO_2 for orthopyroxenites. Hematite components in ilmenite range from 0.01 to 0.024, suggesting a relatively reduced fO_2 below FMQ (Frost et al. 1988). Clinopyroxene contains low $Fe^{3+}/\Sigma Fe$ below 0.067. Recent experimental study shows low Fe^{3+} contents in clinopyroxene that crystallizes under fO_2 below the FMQ buffer (McCanta et al. 2004).

Low fO_2 value of the metasomatizing melt is consistent with relatively low fO_2 of abyssal peridotites. Abyssal peridotites, which likely reflect fO_2 of the upper asthenospheric mantle, are slightly reduced compared to the FMQ buffer (Christie et al. 1986; Bryndzia and Wood 1990; Bézos and Humler 2005). This is consistent with reduced oxidation state of mantle peridotites underlying continental rifts and hot spots that have been infiltrated by asthenosphere-derived melts and/or fluids (Ionov and Wood 1992).

No discernable variations (within uncertainty) of fO_2 were found between metasomatized (FMQ-0.33 to +0.75) and non-metasomatized (FMQ-0.23 to +0.48) samples, and between

spinel-facies (FMQ-0.23 to +0.75) and garnet-facies peridotites (FMQ-0.33 to +0.47), suggesting the early transformation process from spinel facies to garnet facies and later infiltration of asthenospheric melt were not accompanied by changes of fO_2 (Table 2-5; Fig. 2-12).

2.7.3. Implications for the oxidation state of SCLM beneath the Pali Aike area

Pali Aike xenoliths show fO_2 values slightly elevated, but comparable to abyssal peridotites and other continental lithspheric upper mantles affected by asthenospheric mantle, such as Baikal rift zone (Russia), Dariganga (Mongalia), Kilbourne Hole and San Carlos (USA), and western Victoria (Australia) (Wood and Virgo 1989; Chen et al. 1991; Ionov and Wood 1992) (Figs. 2-12, 2-13). The values are lower than most sub-arc mantle peridotites. The observed values are consistent with the history of the mantle in the area. They were abyssal peridotites before their accretion in late Proterozoic-Cambrian time. The subduction of the Nacza Plate led to the collision of Chile ridge with the trench at ~14 Ma (Gorring et al. 1997; Gorring and Kays 2001). Eastward migration of the subducted ridge produced a slab window in the area (D'Orazio et al. 2000) and allowed the infiltration of asthenosphere- derived melt, which has comparable fO_2 to MORB (Taylor and Green 1987, 1989; Ballhaus 1993, 1994) and would not be able to oxidize the overlying SCLM. Therefore this SCLM, which is of abyssal oceanic origin, preserves its original fO_2.

Conclusions

The values of fO_2, FMQ-0.33 to +0.75, for the entire peridotite sample are comparable to those for abyssal peridotites, and lower than fO_2 for many sub-arc mantles. Our data supports the formation of continental lithospheric mantle below southernmost South America through the accretion of oceanic lithosphere. The mantle peridotites, especially garnet-bearing harzburgites, in the area have undergone metasomatism by melt that was generated in association with the generation of the Pali Aike basalts in response to the development of a slab window overlying upwelling asthenospheric mantle. The metasomatizing melt is characterized by high contents of

Al, Si, Ti and Fe, and reduced in fO_2, ~ FMQ -0.50. The infiltration of the metasomatizing melt did not significantly change the oxidation state of garnet- and spinel- facies peridotites.

Acknowledgements

This work was supported by a NSERC Discovery grant to KHH and an Ontario Graduate Scholarship in Science and Technology and an PhD Admission Scholarship of the University of Ottawa to JW. We thank P. Jones at Carleton University and L. Shi at McGill University for their help during the electron microprobe analyses and B.J. Wood for allowing us to use his reference spinel with known Fe^{3+} contents. Thanks are also given to R. Hartree for his help with the XRF analysis at University of Ottawa.

References

Amundsen HEF, Neumann E-R (1992) Redox control during mantle/melt interaction. Geochimica et Cosmochimica Acta 56:2405-2416

Arai S (1994) Characterization of spinel peridotites by olivine-spinel compositional relationships: Review and interpretation. Chem Geol 111:191-204

Arai S, Ishimaru S, Okrugin VM (2003) Metasomatized harzburgite xenoliths from Avacha volcano as fragments of mantle wedge of the Kamchatka arc: implication for the metasomatic agent. The Island Arc 12:233-246

Arculus RJ (1985) Oxidation status of the mantle: past and present. Ann Rev Earth Planet Sci 13:75-95

Arculus RJ (1994) Aspects of magma genesis in arcs. Lithos 33:189-208

Ballhaus C, Berry RF, Green DH (1991) High pressure experimental calibration of the olivine-orthopyroxene-spinel oxygen geobarometer: implications for the oxidation state of the upper mantle. Contrib Mineral Petrol 107:27-40

Ballhaus C (1993) Redox states of lithospheric and asthenospheric upper mantle. Contrib Mineral Petrol 114:331-348

Ballhaus C, Frost BR (1994) The generation of oxidized CO_2-bearing basaltic melts from reduced CH_4-bearing upper mantle sources. Geochim Cosmochim Acta 58:4931-4940

Barnes SJ, Roeder PL (2001) The range of spinel compositions in terrestrial mafic and ultramafic rocks. J Petrol 42: 2279-2302

Bézos A, Humler E (2005) The $Fe^{3+}/\Sigma Fe$ ratios of MORB glasses and their implications for mantle melting. Geochim Cosmochim Acta 69:711-725

Bloomer SH, Hawkins JW (1983) Gabbroic and ultramafic rocks from Mariana Trench: an island arc ophiolite. In: Tectonic and Geological Evolution of the SE Asian Seas and Islands. AGU Geophys Monogr 27:234-316

Bloomer SH, Fisher RJ (1987) Petrology and geochemistry of igneous rocks from the Tonga Trench, a non-accreting plate boundary. J Geol 95:469- 495

Boyd FR (1989) Compositional distinction between oceanic and cratonic lithosphere. Earth Planet Sci Lett 96:15-26

Boyd FR, Pokhilenko NP, Pearson DG, Mertzman SA, Sobolev NV, Finger LW (1997) Composition of the Siberian cratonic mantle: Evidence from Udachnaya peridotite xenoliths. Contrib Mineral Petrol 128:228-248

Brandon AD, Draper DS (1996) Constraints on the origin of the oxidation state of mantle overlying subduction zones: an example from Simcoe, Washington, USA. Geochim Cosmochim Acta 60:1739-1749

Brey GP, Köhler T (1990) Geothermobarometry in four-phase lherzolites: II. New thermobarometers, and practical assessment of existing thermobarometers. J Petrol 31:1353-1378

Bruhn RL, Stern CR, de Wit MJ (1978) Field and geochemical data bearing on the development of a Mesozoic volcanic-tectonic rift zone and back arc basin in southernmost South America. Earth Planet Sci Lett 41: 32-46

Bryndzia LT, Wood BJ (1990) Oxygen thermobarometry of abyssal spinel peridotites: The redox state and C-H-O volatile composition of the Earth's sub-oceainc upper mantle. Amer. J Sci 290:1093-1116

Cande SC, Leslie RB (1986) Late Cenozoic tectonics of the Southern Chile Trench. J Geophys Res 91:471-496

Canil D, O'Neill HStC, Pearson DG, Rudnick RL, McDonough WF, Carswell DA (1994) Ferric iron in peridotites and mantle oxidation states. Earth Planet Sci Lett 13:205-220

Canil D (2004) Mildly incompatible elements in peridotites and the origins of mantle lithosphere. Lithos 77:375-393

Carlson RW, Pearson DG, James DE (2005) Physical, Chemical, and chronological characteristics of continental mantle. Reviews of Geophysics 43:1-24

Chen YD, Pearson NJ, O'Reilly SY, Griffin WL (1991) Applications of olivine–orthopyroxene-spinel oxygen geothermometers to the redox state of the upper mantle. J Petrol Special Volume 291-306

Christie DM, Carmichael ISE and Langmuir CH (1986) Oxidation states of mid-oceanic ridge basalt glasses. Earth Planet Sci Lett 79:397-411

Clark SP, Ringwood AE (1964) Density distribution and constitution of the mantle. Res Geophys 2:35-88

Conceição RV, Green DH (2004) Derivation of potassic (shoshonitic) magmas by decompression melting of phlogopite + pargasite lherzolite. Lithos 72:209-229

Daniels LRM, Gurney JJ (1991) Oxygen fugacity constraints on the southern African lithosphere. Contrib Mineral Petrol 108:154-161

DeHoog JCM, Hattori KH, Hoblitt RP (2004) Oxidized sulfur-rich mafic magma at Mount Pinatubo, Philippines. Contrib Mineral Petrol 146:750-761

Dick JJB, Bullen T (1984) Chromian spinel as a petrogenetic indicator in abyssal and alpine-type peridotites and spatially associated lavas. Contrib Mineral Petrol 86:54-76

D'Orazio M, Agostini S, Mazzarini F, Innocenti F, Manetti P, Haller MJ, Lahsen A (2000) The Pali Aike Volcanic Field, Patagonia: slab-window magmatism near the tip of South America. Tectonophysics 321:407-427

Embey-Isztin A, Scharbert HG, Dietrich H, Poultidis H (1989) Petrology and geochemistry of peridotite xenoliths in alkali basalts from the transdanubian volcanic region, west Hungary. J Petrol 30:79-105

Frey FA, Prinz M (1978) Ultramafic inclusions from San Carlos, Arizona: petrologic and geochemical data bearing on their petrogenesis. Earth Planet Sci Lett 38:129-176

Frost BR, Lindsley DH, Andersen DJ (1988) Fe-Ti oxide-silicate equilibria: Assemblages with fayalitic olivine. Am Mineral 73:727-740

Gonzalez PD, Poiré DG, Varela R (2002) Hallazgo de trazas fósiles en la Formació El Jaguelito y su relación con la edad de las metasedimentitas, Macizo Norpatagónico Oriental, provincial de Rio Negro. Revista de la Asociación Geológica Argentina 57:35-44

Gorring ML, Kays SM, Zeitler PK, Ramos VA, Rubiolo D, Fernandez MI, Panza JL (1997) Neogene Patagonian plateau lavas: Continental magmas associated with ridge collision at the Chile triple Junction. Tectonics 16:1-17

Gorring ML, Kays SM (2001) Mantle processes and sources of Neogene slab window magmas from Southern Patagonia, Argentina. J Petrol 42:1067-1094

Grove TL, Kinzler RJ, Bryan WB (1992) Fractionation of mid-ocean ridge basalts (MORB). Geophys Monogr 71:281-310

Gudmundsson G, Wood BJ (1995) Experimental tests of garnet peridotite oxygen barometry. Contrib Mineral Petrol 119:56-67

Hattori KH, Keith JD (2001) Contribution of mafic melt for porphyry deposits; evidence from Pinatubo and Bingham. Mineralium Deposits 36:799-806

Hattori KH, Guillot S (2007) Geochemical character of serpentinites associated with high- to ultrahigh- pressure metamorphic rocks in the Alps, Cuba and Himalayas: recycling of elements in subduction zones. Geochemistry Geophysics Geosystems (in press)

Herzberg C (1999) Formation of cratonic mantle as plume residues and cumulates. In: Fei Y, Bertka C, Mysen BO (ed) Mantle Petrology: Field Observations and high Pressure Experimentation, Geochem Soc Houston Tex, pp 241-257

Ionov DA, Wood BJ (1992) The oxidation state of subcontinental mantle: oxygen thermobarometry of mantle xenoliths from Central Asia. Contri Mineral Petrol 111:179-193

Ionov DA, Ashchepkov IV, Stosch H-G, Witt-Eickschen G, Seck HA (1993) Garnet Peridotite xenoliths from the Vitim volcanic field, Baikal region: the nature of the garnet-spinel peridotite transition zone in the continental mantle. J Petrol 34: 1141-1175

Ishii T, Robinson PT, Maekawa H, Fiske R (1992) Petrological studies of peridotites from diapiric serpentinites seamounts in the Izu-Ogasawara-Mariana forearc, Leg 125: Scientific Results, College Station, TX. 125, 445-463

Kay SM, Ramos VA, Mpodozis C, Sruoga P (1989) Late Paleozoic to Jurassic silicic magmatism at the Gondwanaland margin: analogy to the Middle Proterozoic in North America? Geology 17:324-328

Kennedy CS, Kennedy GC (1976) The equilibrium boundary between graphite and diamond. J Geophys Res 81:2467-2470

Kilian R, Stern CR (2002) Constraints on the interaction between slab melts and the mantle wedge from adakitic glass in peridotite xenoliths. Eur J Mineral 14:25-36

Kelemen PB, Hart SR, Bernstein S (1998) Silica enrichment in the continental upper mantle via melt/rock reaction. Earth Planet Sci Lett 164:387-406

Kopylova MG, Russell JK (2000) Chemical stratification of cratonic lithosphere: Constraints from the northern Slave craton, Canada. Earth Planet Sci Lett 181:71-87

McCammon CA, Griffin WL, Shee SR, O'Neill HStC (2001) Oxidation during metasomatism in ultramafic xenoliths from the Wesselton kimberlite, South Africa: implications from the survival of diamond. Contrib Mineral Petrol 141:287-296

McCammon C, Kopylova MG (2004) A redox profile of the Slave mantle and oxygen fugacity control in the cratonic mantle. Contrib Mineral Petrol 148: 55-68

McCanta MC, Dyar MD, Rutherford MJ, Delaney JS (2004) Iron partitioning between basaltic melts and clinopyroxene as a function of oxygen fugacity. Am Mineral 89:1685-1693

McDonough WF, Sun SS (1995) The composition of the Earth. Chem Geol 120:223-253=

Michael PJ, Bonatti E (1985) Peridotite composition from the North Atlantic: regional and tectonic variations and implications for partial melting. Earth Planet Sci Lett 73:91-104

Mungall JE (2002) Roasting the mantle: slab melting and the genesis of major Au and Au-rich Cu deposits. Geology 30:915-918

Nell J, Wood BJ (1991) High-temperature electrical measurements and thermodynamic properties of Fe_3O_4-$FeCr_2O_4$-$MgCr_2O_4$-$FeAl_2O_4$ spinels. Am Mineral 76:406-426

Nickel KG, Green DH (1985) Empirical geothermobarometry for garnet peridotites and implications for the nature of the lithosphere, kimberlites and diamonds. Earth Planet Sci Lett 73:158-170

Niu YL, O'Hara MJ (2003) The origin of ocean island basalts (OIB): A new perspective from petrology, geochemistry and mineral physics considerations. J Geophys Res 108, 10.1029/2002JB002048

Niu YL (2004) Bulk-rock major and trace element compositions of abyssal peridotites: implications for mantle melting, melt extraction and post-melting processes beneath mid-ocean ridges. J Petrol 45: 2423-2458

Obata M, Morten L (1987) Transformation of spinel lherzolite to garnet lherzolite in ultramafic lenses of the Austridic crystalline complex, northern Italy. J Petrol 28:599-623

O'Neill HStC, Wall VJ (1987) The olivine-orthopyroxene-spinel oxygen barometer, the nickel precipitation curve, and the oxygen fugacity of the Earth's upper mantle. J Petrol 28:1169-1191

Parker RL, Oldenburg DW (1973) Thermal modal of ocean ridges. Nature 242:137-139

Parkinson IJ, Pearce JA (1998) Peridotites from the Izu-Bonin-Mariana Forearc (ODP Leg 125): evidence for mantle melting and melt-mantle interaction in a supra-subduction zone setting. J Petrol 39:1577-1608

Parkinson IJ, Arculus RJ (1999) The redox state of subduction zones: Insights from arc-peridotites. Chem Geol 160: 409-423

Parman SW, Grove TL, Dann JC, del Wit MJ (2004) A subduction origin for komatiitees and cratonic lithospheric mantle. S Africa J Geol 107:107-118

Preb S, Witt G, Seck HA, Eonov D, Kovalenko VI (1986) Spinel peridotite xenoliths from the Tariat depression, Mongolia. I: major element chemistry and mineralogy of a primitive mantle xenolith suite. Geochim Cosmochim Acta 50: 2587-2599

Qi Q, Taylor LA, Zhou XM (1995) Petrology and geochemistry of mantle peridotite xenoliths from SE China. J Petrol 36:55-79

Ramos VA (1988) Late Proterozoic-Early Paleozoic of South America- a collisional history. Episode 11: 168-174

Ramos VA (1989) Foodhills structures in Northern Magallanes Basin, Argentina. AAPG Bull 73: 887-903

Ramos VA, Dallmeyer R, Vujovich G (1998) Time constraints in the Early Paleozoic docking of the Precordillera, Central Argentina. In: Pankhurst R, Rapela C (Eds) The Proto-Andean Margin of Gondwana. Spec Publ Geol Soc Lond 142:143-158

Rapalini AE (2005) The accretionary history of southern South America from the latest Proterozoic to the late Paleozoic: some palaeomagnetic constraints. Spec Publ Geol Soc Lond. 246: 305-328

Rapela C, Pankhurst R, Casquet C, Baldo E, Saavedra J, Galindo C (1998) Early evolution of the proto-Andean margin of South America. Geology 26 (8):707-710

Rapela CW, Pankhurst RJ (2002) Eventos tectonomagmáticos del Paleozoico Inferior en el márgen proto-atlántico del sur de Sudamérica. 15th Congreso Geológico Argentino, El Calafate, 1, Asociación Geológica Argentina, Buenos Aires 24-29

Selverstone MA, Stern CR (1983) Petrochemistry and recrystallization history of granulite xenoliths from the Pali Aike volcanic field, Chile. Am Mineral 68:1102-1112

Shcherbakov SA, Savelyeva GN (1984) Structures of ultramafic rocks of the Mariana Trench and the Owen Fracture Zone. Geotectonics 18:159-167

Skewes MA, Stern CR (1979) Petrology and geo chemistry of alkali basalts and ultramafic inclusions from the Pali Aike volcanic field in southern Chile and the origin of the Patagonian plateau lavas. J Volcanol Geotherm Res 6:3-25

Stern CR, Frey FA, Futa K, Zartman RE, Peng Z, Kyser TK (1990) Trace-element and Sr, Nd, Pb, and O isotopic compositions of Pliocene and Quaternary alkali basalts of the Patagonian plateau lavas of southernmost South America. Contrib Mineral Petrol 104:294-308

Stern CR, Kilian R (1996) Role of the subducted slab, mantle wedge and continental crust in the generation of adakites from the Andean Austral Volcanic zone. Contrib Mineral Petrol 123:263-281

Stern CR, Kilian R, Olker B, Hauri EH, Kyser TK (1999) Evidence from mantle xenoliths for relatively thin (< 100km) continental lithosphere below the Phanerozoic crust of southernmost South America. Lithos 48:217-235

Taylor WR, Green DH (1987) Measurement of reduced peridotite-C-O-H solidus and implications for redox melting of the mantle. Nature 332:349-352

Taylor WR, Green DH (1989) The role of reduced C-O-H fluids in mantle partial melting. Spec Publ Geol Soc Aust 14 vol 1:592-602

Wang J, Hattori KH, Kilian R, Stern CR (2007) Metasomatism of sub-arc mantle peridotites below southernmost South America reduction of fO_2 by slab-melt. Contrib Mineral Petrol 153: 607-624

Wells PRA (1977) Pyroxene thermometry in simple and complex systems. Contrib Mineral Petrol 62:119-139

Wood BJ, Bryndzia LT, Johnson KE (1990) Mantle oxidation state and its relationship to tectonic environment and fluid speciation. Sciences 248:337-345

Wood BJ, Virgo D (1989) Upper mantle oxidation state: Ferric iron content of lherzolite spinels by 57Fe Mössbauer spectroscopy and resultant oxygen fugacities. Geochim Cosmochim Acta 53:1277-1291

Woodland AB, Kornprobst J, Wood BJ (1992) Oxygen thermobarometry of orogenic lherzolite massifs. J Petrol 33:203-230

Woodland AB, Koch M (2003) Variation in oxygen fugacity with depth in the upper mantle beneath the Kaapvaal craton, southern Africa. Earth Planet Sci Lett 214:295-310

Yamamoto K, Matsutani N, Nakamura N, Ishii T (1992) REE characteristics of mafic rocks from a fore-arc seamount in the Izu-Ogasawara region, western Pacific, Geochem J. 26:411-423

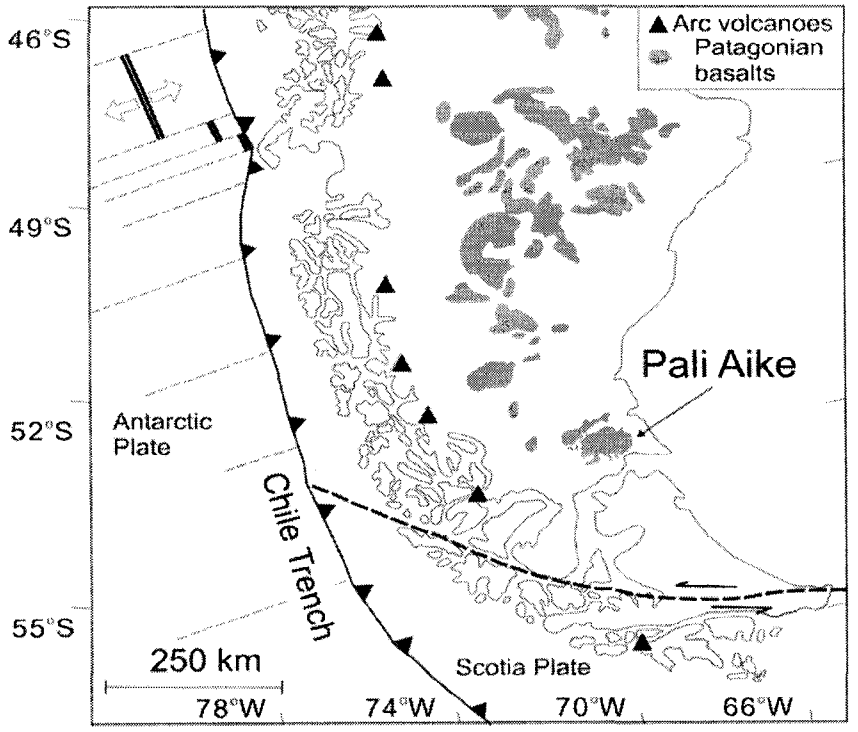

Figure 2-1 The location of the study area and the distribution of the alkaline basalt fields of Pali Aike, and other late Cenozoic basalts of Patagonian plateau. Also shown are volcanoes of the Andean Austral Zone (AVZ) (modified after Kilian and Stern 2002).

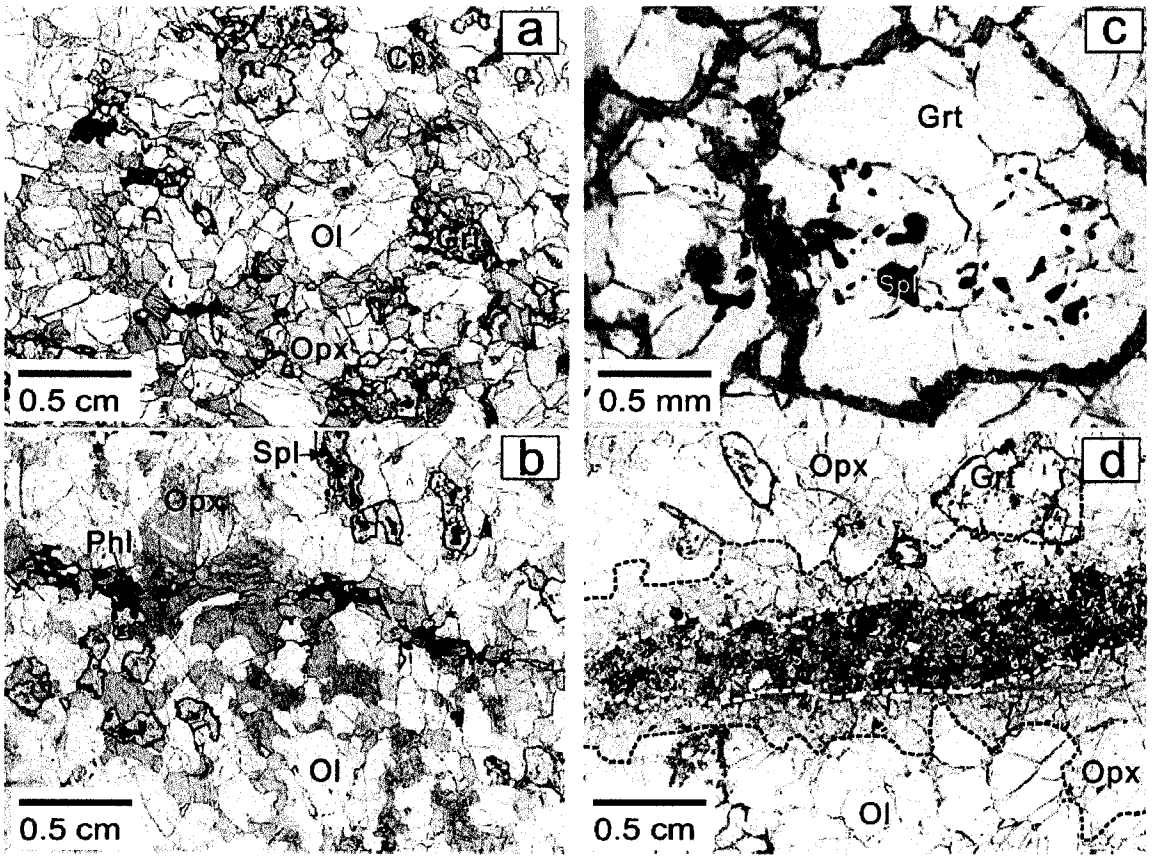

Figure 2-2 a Photograph of a Grt-Spl lherzolite (sample TM2). **b** Photograph of a metasomatized Grt-Spl harzburgite (sample TM15). Note that discontinuous phlogopite veinlet cuts across the host harzburgite. Also shown in 2-2b is the relict spinel enclosed in large garnet. **c** Photomicrograph of coarse garnet (Grt) enclosing relict spinel (Spl) grain in Grt-Spl harzburgite (sample BN32) under plane polarized light. Note that there is a reaction rim between relict Spl and host Grt. **d** Photograph of an orthopyroxenite veinlet in Grt-Spl harzburgite (sample BN92). The veinlet (shown with white dashed lines) is accompanied by metasomatic halos (shown with black dashed lines). Red = garnet, opaque minerals = ilmenite, yellow green = orthopyroxene, and transparent = olivine.

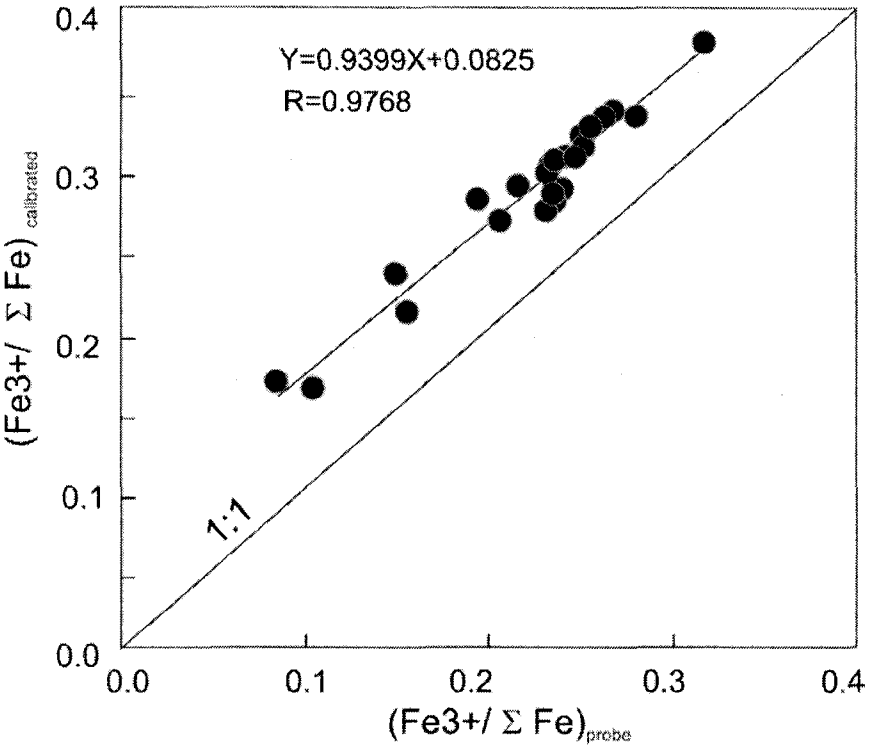

Figure 2-3 Comparison between the ratios of $(Fe^{3+}/\Sigma Fe)_{probe}$ and $(Fe^{3+}/\Sigma Fe)_{calibrated}$ of spinel samples in mantle peridotites from Pali Aike. Ratios of $(Fe^{3+}/\Sigma Fe)_{probe}$ are calculated assuming stoichiometry of spinel compositions and each point represent an average of 5-8 grains in each sample. Calibrated ratios, $(Fe^{3+}/\Sigma Fe)_{calibrated}$, were obtained using four spinel standard samples (KLB8304, KLB8311, MBR8305 and KLB8316) with known Fe^{3+} contents following the method described by Wood and Virgo (1989).

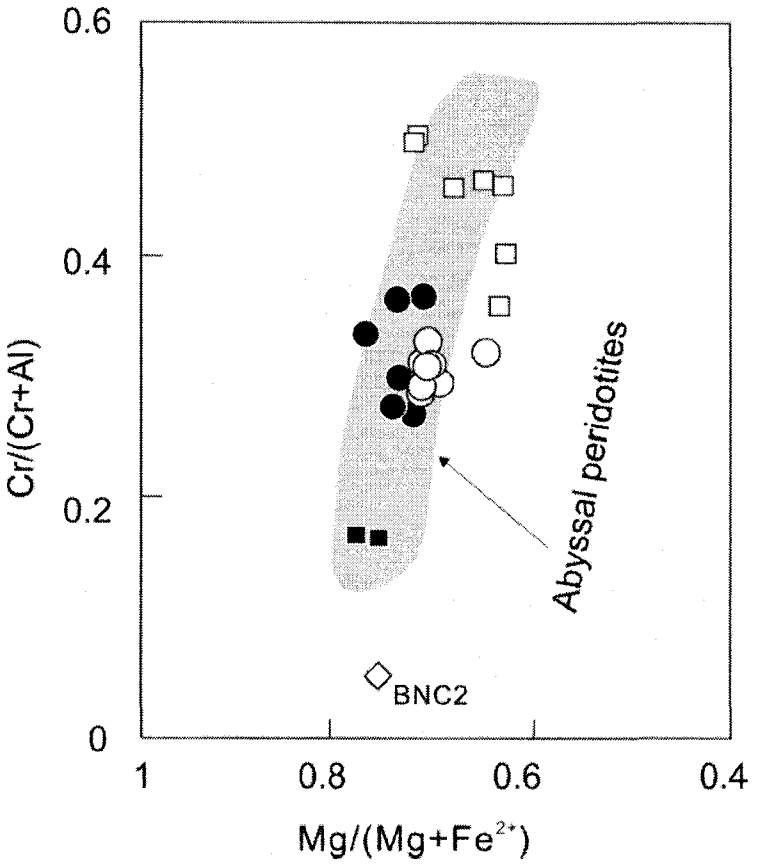

Figure 2-4 Plot of Cr# vs. Mg/ ($Mg+Fe^{2+}$) for spinel in peridotites from Pali Aike, compared with the data for abyssal peridotites (Dick and Bullen 1984). Filled circles = garnet lherzolites, open circles = garnet harzburgites, filled squares= spinel lherzolites, open squares = spinel harzburgites, diamond = orthopyroxenite. Each point represents an average of 5 to 8 grains of spinel in each section.

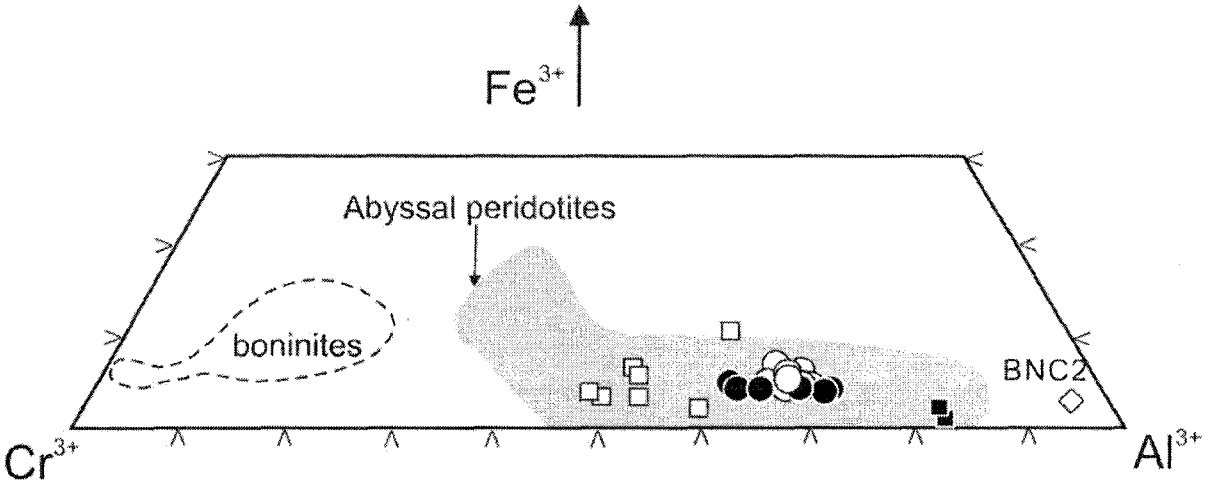

Figure 2-5 Ternary diagram of Fe^{3+}-Cr^{3+}-Al^{3+} for spinel in the peridotite xenoliths from Pali Aike. Symbols are the same as in Fig. 2-4. Note that spinel grains in Pali-Aike mantle xenoliths are generally low in Fe^{3+} and that their compositions overlap with the field of abyssal peridotites except for garnet orthopyroxenite. Field for abyssal peridotites is after Dick and Bullen (1984) and Barnes and Roeder (2001), and field for boninite is after Barnes and Roeder (2001).

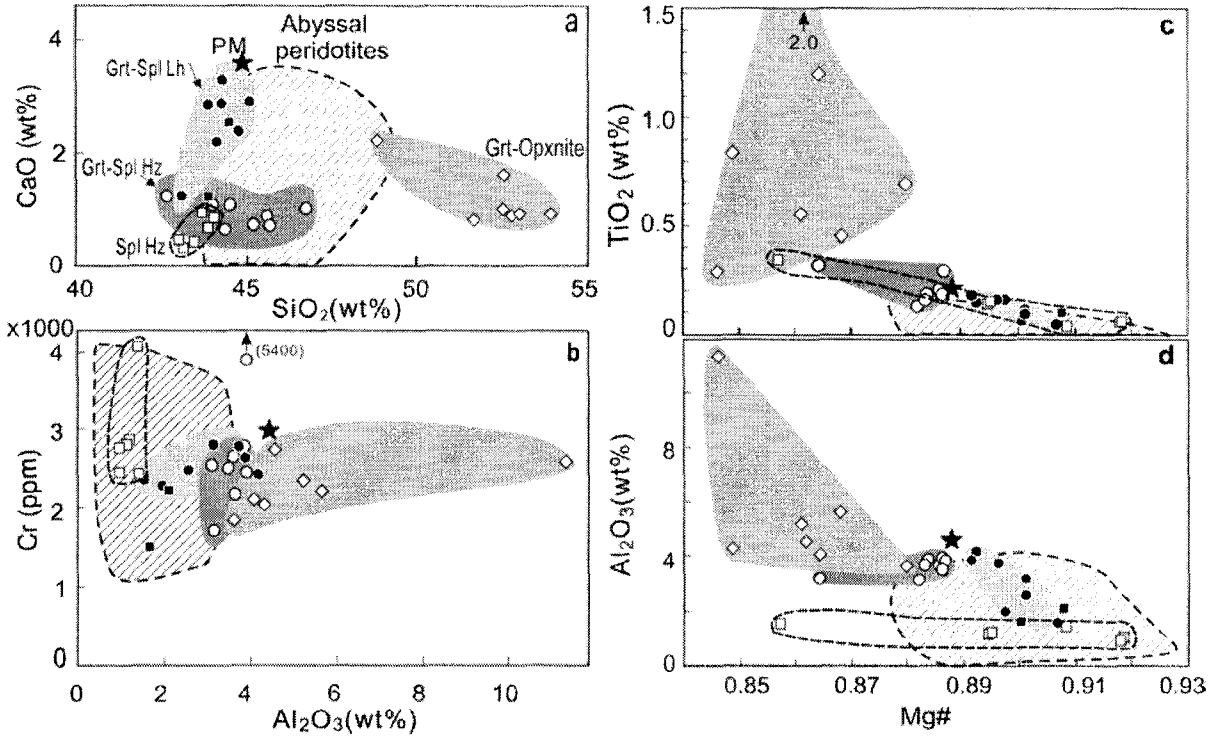

Figure 2-6 Bulk chemical compositions of mantle xenoliths from the Pali-Aike area. Plots of (a) CaO vs. SiO_2, (b) Cr vs. Al_2O_3, (c) TiO_2 vs. Mg# and (d) Al_2O_3 vs. Mg# for bulk compositions of mantle xenoliths from Pali-Aike. Filled star depicted with PM refers to the primitive mantle composition (McDonough and Sun 1995). Oblique hatching areas circled with dash line are abyssal peridotites (data source: Niu 2004). Filled circles in shaded area = garnet-spinel lherzolites (Grt-Spl Lh), open circles in dark shaded area= garnet-spinel harzburgites (Grt-Spl Hz), filled squares enclosed by dashed line = spinel lherzolites (Spl Lh), open squares enclosed by dashed line = spinel harzburgites (Spl Hz), open diamond in shaded area = garnet orthopyroxenites. Note that garnet orthopyroxenites show a wide compositional variation; Spl Hz shows a wide compositional variation in 2-6c and 2-6d.

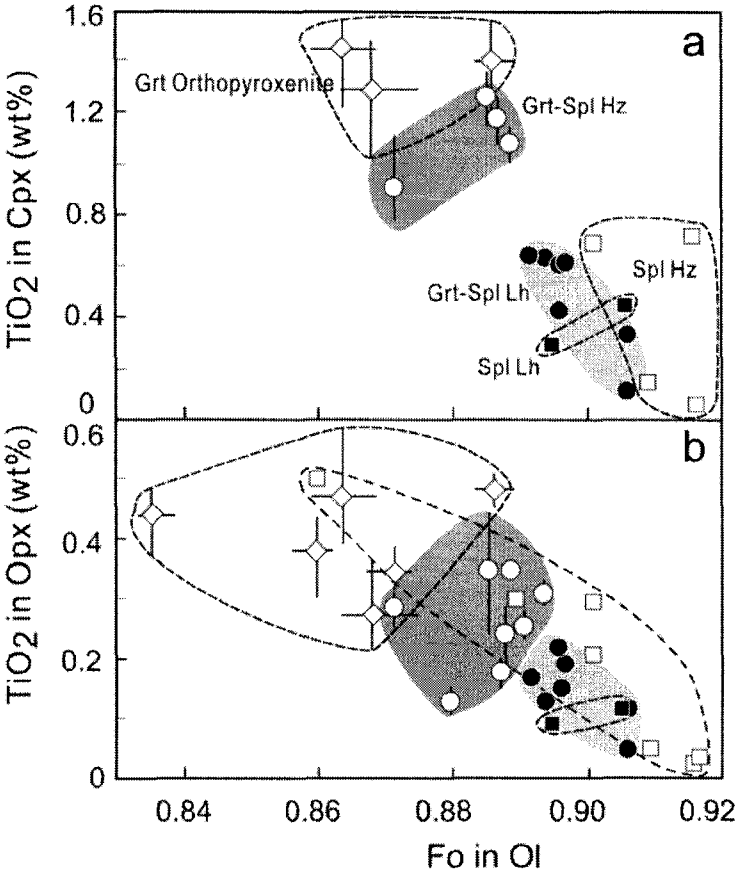

Figure 2-7 Plots of TiO_2 in pyroxenes and Fo in olivine (Ol) in mantle xenoliths from the Pali Aike area. Symbols for samples are the same as in Fig. 2-4. Note that orthopyroxenites, Grt-Spl harzburgites and several Spl harzburgites show low Fo in olivine and high TiO_2 contents in clinopyroxene and orthopyroxene compared with their lherzolites counterparts. The variation bars shown in orthopyroxenites and Grt-Spl harzburgites are based on 3-5 analyses.

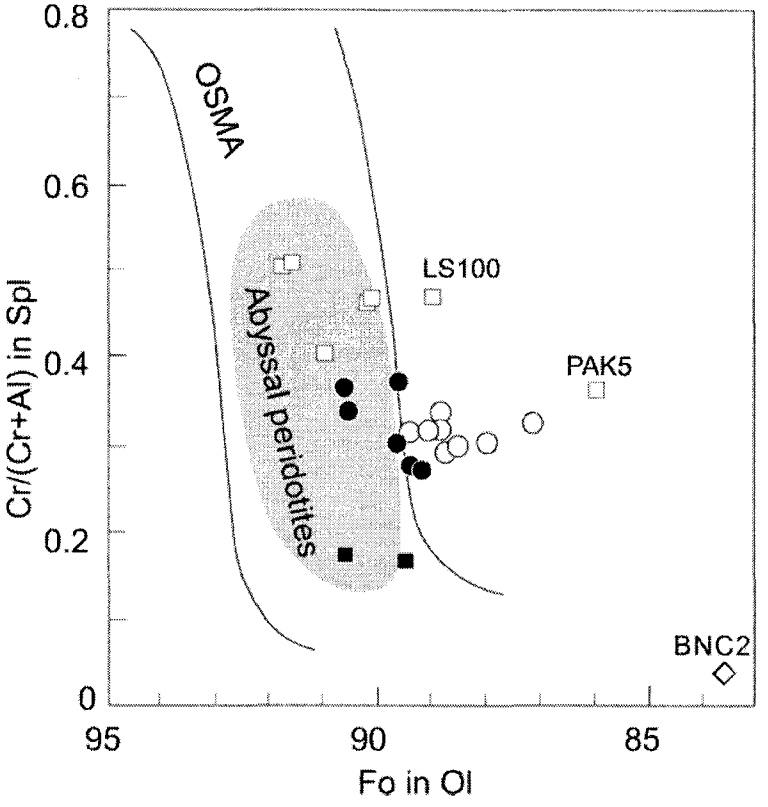

Figure 2-8 Relationships between the Fo component of olivine and Cr# of spinel in peridotite xenoliths from Pali Aike. Symbols are the same as Fig. 2-4. Note that all Grt-Spl harzburgites, two Spl harzburgites and one orthopyroxenite (BNC2) plot outside the olivine-spinel mantle array (OSMA) defined by Arai (1994), suggesting that they are not primary mantle peridotites. It also shows the field of abyssal peridotite as a shaded area (Arai 1994).

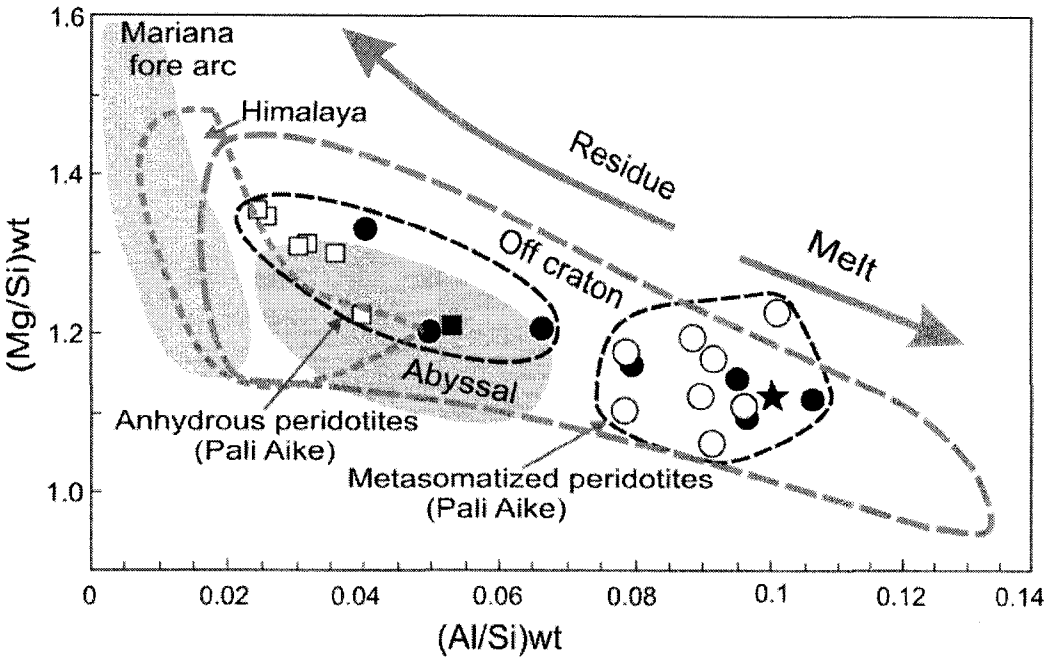

Figure 2-9 Weight ratio of Mg/Si vs. Al/Si of peridotites in Pali Aike area. The large solid star represents primitive mantle value from McDonough and Sun (1995). The field for abyssal peridotites is based on 10^{th} and 90^{th} percentile values of 126 samples by Niu (2004). Himalaya peridotites are from Hattori and Guillot (2007). Mariana fore-arc peridotites are from Ishii et al.(1992), Yamamoto et al.(1992), and Parkinson and Pearce (1998). The field for off-craton is based on the data from Vitim volcanic field, Russia (Ionov et al. 1993), Tariat, Mongolia (Preb et al. 1986), San Carlos, US (Frey and Prinz 1978), Transdanubian volcanic region, west Hungary (Embey-Isztin et al. 1989), and SE China (Qi et al. 1995). The compositional variation expected during partial melting is shown with arrows. Residues have higher Mg/Si and lower Al/Si, whereas melt has a lower Mg/Si and higher Al/Si. Symbols are the same as in Fig. 2-4. Note that all Pali Aike peridotites overlap with off-craton, and the non-metasomatized peridotites overall overlap with the field of abyssal peridotites.

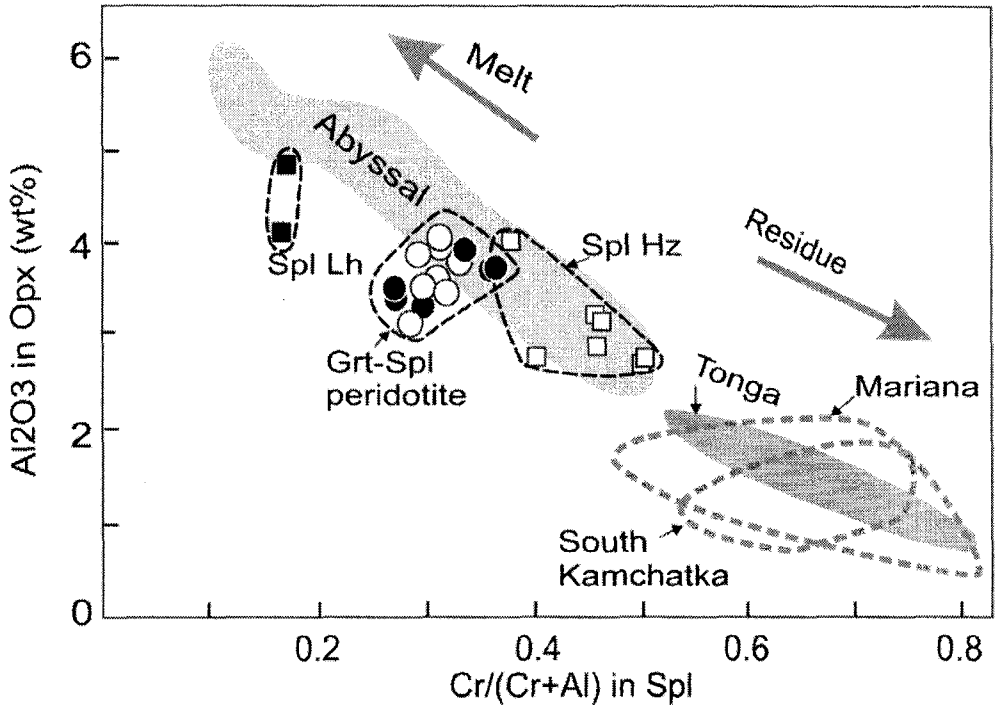

Figure 2-10 Plot of Al_2O_3 in Opx (wt%) vs. Cr# in Spl for peridotites in Pali Aike area. The field for abyssal peridotites is based on the samples from North Atlantic oceanic peridotites by Michael and Bonatti (1985). Data source for arc mantle peridotites includes Mariana (Bloomer and Hawkins 1983; Shcherbakov and Savelyeva 1984; Parkinson and Pearce 1998), Tonga (Bloomer and Fisher 1987), and south Kamchatka (Arai et al. 2003). The mineral compositional variation expected during partial melting is shown with arrows. Residues have higher Cr# in Spl and lower Al_2O_3 in Opx. Symbols are the same as in Fig. 2-4. Note the Spl peridotites and non-metasomatized Grt-Spl peridotites in Pali Aike overall overlap with the field of abyssal peridotites, and show notable high Al in Opx and low Cr in Spl compared with mantle wedge peridotites.

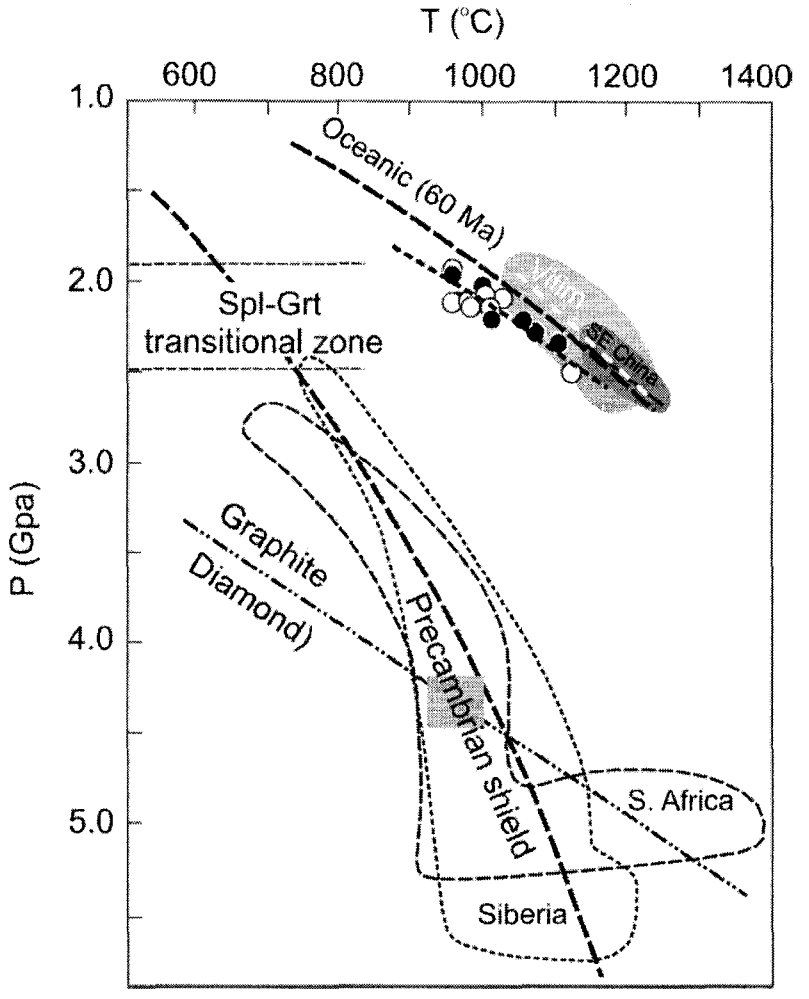

Figure 2-11 Results of thermobarometries of the xenoliths in this study. Symbols are the same as in Fig. 2-4. Our data of garnet-bearing xenoliths define a continuous geotherm, close to the oceanic geotherm of Parker and Oldenburg (1973) for 60 Ma old plate. Precambrian shield represents the geotherm of Precambrian shield by Clark and Ringwood (1964). Reference regions, S. Africa, Siberia and Namibia, are after Nickel and Green (1985); Vitim, Russia and SE China are after Ionov et al. (1993) and Qi et al. (1995), respectively. The location of graphite-diamond inversion is from Kennedy and Kennedy (1976). The Spl-Grt transitional zone is based on this study.

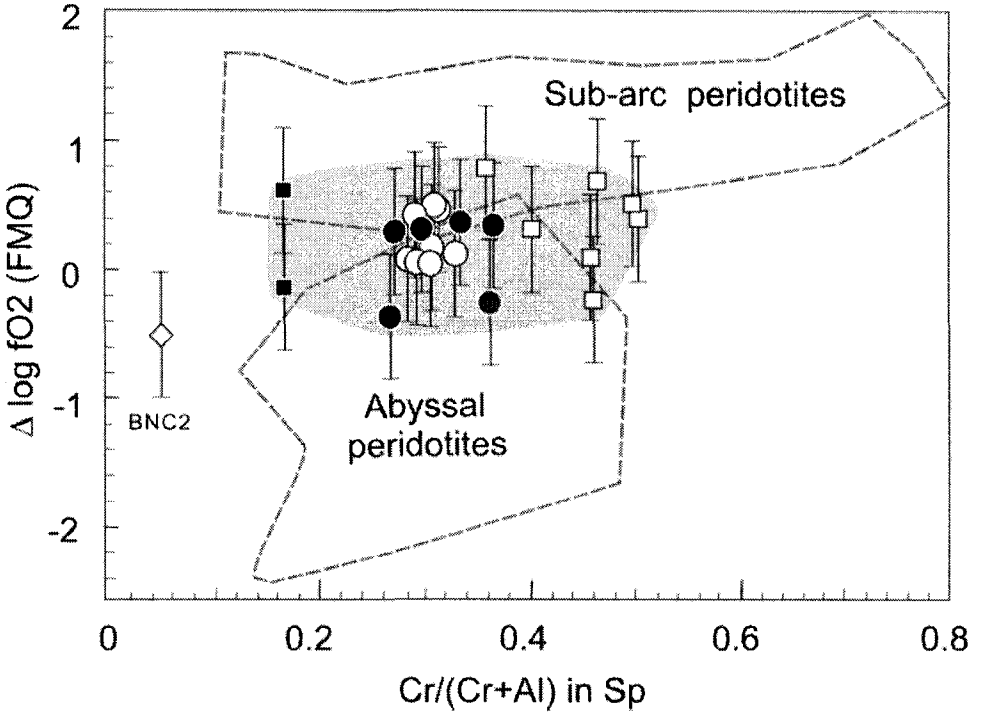

Figure 2-12 Values of fO_2 relative to FMQ buffer (ΔfO_2 (FMQ)) vs. Cr# in spinel for peridotites from Pali Aike compared with abyssal peridotites (Bryndzia and Wood 1990) and sub-arc mantle peridotites. Symbols are the same as Fig. 2-4. Sub-arc mantle peridotites include those from Ichinomegata in Japan, Marelava in Vanuatu arc, Grenada in Lesser Antilles arc, Santa Isabel and San Jorge in Solomon islands and the Simcoe area in Cascade arc (Wood and Virgo 1989; Ballhaus et al. 1991; Brandon and Draper 1996; Parkinson and Arculus 1999; Parkinson et al. 2003).

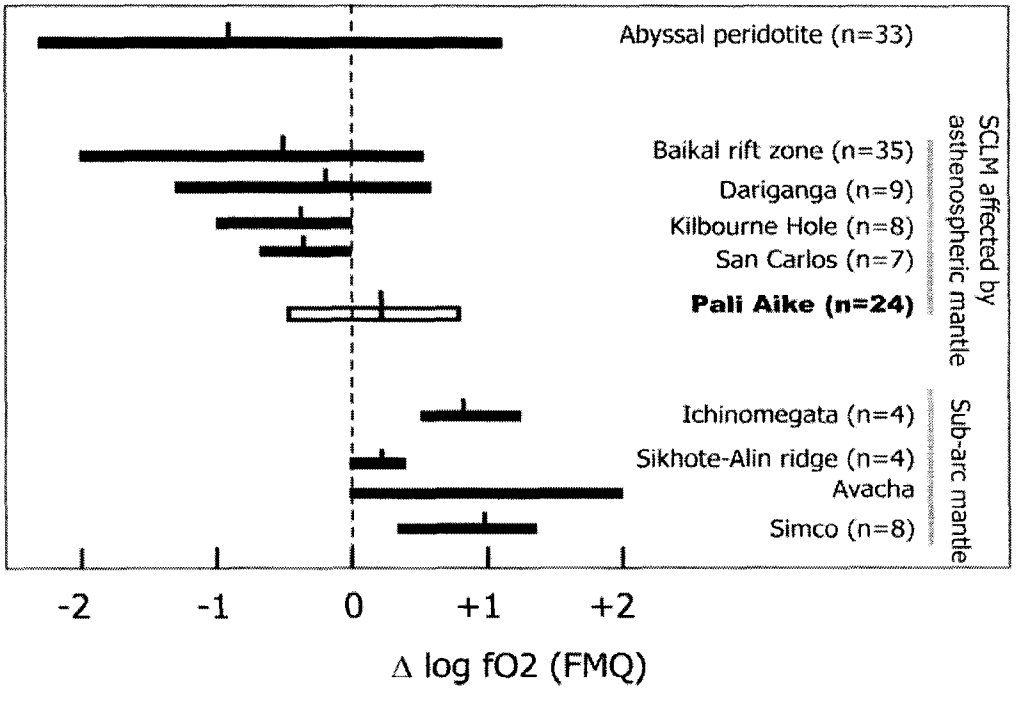

Figure 2-13 Oxidation state for mantle xenoliths from Pali Aike in comparison with those for other mantle peridotites. Data source: abyssal peridotite (Bryndzia and Wood 1990); Baikal rift zone, Dariganga, and Sikhote-Alin ridge (Ionov and Wood 1992); Kilbourne Hole, San Carlos and Ichinomegata (Wood and Virgo 1989); Avacha (Arai et al. 2003); Simcoe (Parkinson and Arculus 1999). The vertical bar indicates the mean $\Delta \log fO_2$ (FMQ) value for a particular region.

Table 2-1 Mantle xenoliths from the Pali Aike area, southern South America

Xenolith group	Rock type	Assemblage	Samples
Peridotites	Grt lherzolite	Ol+Opx+Cpx+Grt	**LS33**
	Grt-Spl lherzolite	Ol+Opx+Cpx+Grt+Spl	**TM0, TM2**, LS50, BN73, LS1, **BN32**
	Grt-Spl harzburgite	Ol+Opx+Grt+Spl±Cpx	**TM14, TM15, BN92, BN50, PAK6, PAHK1, BN45, BN31**
	Spl lherzolite	Ol+Opx+Cpx+Spl	**PA64**, PAK1
	Spl harzburgite	Ol+Opx+Spl±Cpx	LS5, PAK2, PAK3, 01BN, BNH11, **LS100, PAK5**
Pyroxenite	Grt orthopyroxenite	Opx+Grt+Mg-ilm+Ti-Phl+Ti-Amp±Ol±Cpx	BNH13, BNC2, BNC1, BN43, BNO5, BNC3, BNH5, BN46
	Ol websterite	Cpx+Opx+Ol±Grt±Spl	BNH7, BNC4, BN31x, LLS3

Abbreviations: Cpx=clinopyroxene, Grt=garnet, Ol=olivine, Opx=orthopyroxene, Spl=spinel, Ti-Phl=Ti-phlogopite, Ti-Amp=Ti-amphibole, Mg-Ilm=magnesium ilmenite, Sul=sulfide

Bold=samples affected by cryptic metasomatism showing low Mg# and high Ti in minerals and bulk rock compositions

Underlined bold=modally metasomatized samples containing any one of Ti-amphibole, Ti-phlogopite, and Mg ilmenite

Table 2-2a Average compositions of minerals in garnet-bearing peridotites from Pali Aike, southern South America

Lithology	Grt-Spl lherzolite							Grt-Spl harzburgite							
Sample	LS33[a]	TM0	TM2	LS50	BN73	LS1	BN32	TM14	TM15	BN92	BN50	PAHK1	PAK6	BN45	BN31
Olivine															
Number of grains	2	2	2	3	3	3	2	2	2	2	2	3	3	3	3
SiO_2	40.63	40.64	40.02	40.64	41.05	40.88	40.93	40.89	40.54	39.92	40.38	40.74	40.41	40.81	40.16
Al_2O_3	0.05	<0.04	<0.04	<0.04	0.04	<0.04	<0.04	<0.04	<0.04	<0.04	<0.04	<0.04	<0.04	<0.04	<0.04
FeO(t)[b]	9.66	10.33	9.88	10.05	9.18	9.12	10.55	11.02	11.65	11.05	10.73	10.64	12.41	10.31	10.83
MgO	49.55	48.70	48.17	48.43	49.33	49.33	48.62	48.40	47.78	47.85	48.11	48.48	47.15	48.43	47.98
MnO	0.10	0.12	0.14	0.11	0.12	0.12	0.11	0.13	0.09	0.14	0.14	0.15	0.13	0.12	0.08
CaO	0.11	0.06	0.05	0.06	0.09	0.06	0.05	0.07	0.05	0.06	0.07	0.04	0.05	0.07	0.06
NiO	0.36	0.36	0.37	0.32	0.33	0.38	0.41	0.39	0.38	0.48	0.39	0.45	0.44	0.44	0.47
Total	100.4	100.2	98.64	99.63	100.1	99.95	100.7	100.9	100.5	99.51	99.81	100.5	100.7	100.2	99.61
Fo	90.1	89.4	89.7	89.6	90.6	90.6	89.1	88.7	88.0	88.5	88.9	89.0	87.1	89.3	88.8
SD[d] (±) of Fo	0.10	0.01	0.14	0.16	0.31	0.01	0.05	0.14	0.17	0.07	0.09	0.63	0.02	0.04	0.06
Orthopyroxene															
Number of grains	2	2	2	3	2	3	4	2	2	3	2	2	3	3	3
SiO_2	54.72	55.93	54.88	55.46	55.20	54.79	54.82	55.72	55.79	54.17	54.43	54.76	54.36	54.17	55.41
Al_2O_3	4.31	3.44	3.34	3.73	3.91	3.69	3.51	3.15	3.51	3.88	3.80	4.02	3.50	3.91	3.58
TiO_2	0.15	0.13	0.19	0.22	0.05	0.12	0.17	0.18	0.13	0.35	0.35	0.26	0.29	0.31	0.24
Cr_2O_3	0.65	0.42	0.43	0.62	0.82	0.66	0.40	0.36	0.35	0.55	0.67	0.68	0.43	0.50	0.45
FeO(t)[b]	6.15	6.48	6.37	6.47	5.88	5.87	6.72	6.74	7.00	6.97	6.66	7.03	7.91	6.71	6.89
MgO	32.31	32.95	32.72	32.63	32.71	33.15	33.07	32.91	32.78	31.79	32.25	32.10	31.03	32.56	32.79
MnO	0.15	0.11	0.11	0.12	0.12	0.12	0.12	0.10	0.06	0.11	0.11	0.15	0.12	0.12	0.13
CaO	1.16	0.68	0.62	0.83	0.98	0.85	0.69	0.66	0.63	0.73	0.78	0.75	0.66	0.82	0.71
Na_2O	0.24	0.14	0.06	0.11	0.14	0.17	0.13	0.17	0.13	0.12	0.14	0.19	0.13	0.12	0.12
Total	99.82	100.3	98.71	100.2	99.82	99.41	99.61	99.98	100.4	98.67	99.16	99.92	98.41	99.22	100.3
Mg#[c]	0.904	0.901	0.902	0.900	0.908	0.910	0.898	0.897	0.893	0.891	0.896	0.891	0.875	0.896	0.895
SD[d] (±) of Mg#	0.002	0.001	0.002	0.003	0.001	0.000	0.002	0.000	0.001	0.001	0.002	0.000	0.001	0.001	0.002
Spinel															
Number of grains		3	2	3	7	3	6	3	2	3	4	2	4	2	6
SiO_2		0.09	0.10	0.11	0.11	0.10	0.06	0.08	0.05	0.14	0.07	0.24	0.02	0.13	0.12
Al_2O_3		41.17	40.47	34.61	37.98	35.64	41.77	40.52	40.72	37.81	36.46	37.72	35.77	37.44	37.79
TiO_2		0.52	0.59	0.94	0.16	0.49	0.66	1.10	1.03	1.89	1.43	1.22	1.69	1.47	1.51
Cr_2O_3		25.01	25.52	30.01	28.78	30.47	23.14	24.36	24.00	24.40	26.99	26.07	25.10	25.15	24.98
FeO(t)[b]		15.54	15.33	16.71	14.16	15.39	16.27	16.97	17.50	18.04	17.91	18.16	21.16	18.11	17.52
MgO		17.25	16.89	16.38	17.94	17.01	17.03	16.98	16.59	16.50	16.59	16.93	14.89	16.74	16.84
MnO		0.12	0.11	0.07	0.08	0.06	0.05	0.11	0.10	0.14	0.11	0.09	0.15	0.07	0.07
NiO		0.24	nd	0.30	0.28	0.25	0.32	nd	0.29	nd	nd	nd	0.35	0.35	0.39
Total		99.96	99.01	99.18	99.51	99.45	99.31	100.1	100.3	98.95	99.56	100.4	99.14	99.50	99.23

Table 2-2a Continued

Lithology	Grt-Spl lherzolite							Grt-Spl harzburgite							
Sample	LS33[a]	TM0	TM2	LS50	BN73	LS1	BN32	TM14	TM15	BN92	BN50	PAHK1	PAK6	BN45	BN31
Garnet															
Number of grains	2	2	2	4	3	3	3	3	2	2	2	2	3	3	3
SiO_2	42.54	42.15	41.66	42.20	46.88	41.92	41.94	42.11	42.36	41.74	42.02	42.26	41.47	41.90	42.23
Al_2O_3	23.00	23.55	23.23	22.47	17.88	22.97	23.21	23.51	23.66	23.11	23.10	23.02	22.98	23.20	22.62
TiO_2	0.25	0.16	0.20	0.21	0.05	0.13	0.18	0.22	0.27	0.33	0.29	0.25	0.28	0.32	0.34
Cr_2O_3	1.93	1.32	1.40	1.81	1.92	1.86	1.21	1.20	1.14	1.19	1.63	1.59	1.38	1.30	1.31
FeO(t)[b]	7.03	8.09	7.75	7.72	6.38	7.48	8.85	8.67	8.79	8.21	8.39	8.32	10.21	8.36	8.30
MgO	21.39	20.48	20.23	20.54	21.21	20.25	19.72	20.44	19.87	20.50	20.36	20.98	18.96	20.08	20.63
MnO	0.29	0.33	0.37	0.26	0.36	0.31	0.32	0.34	0.36	0.31	0.34	0.32	0.33	0.30	0.30
CaO	4.98	4.92	4.87	5.04	5.48	5.09	5.01	4.77	4.78	4.53	5.07	4.44	4.71	4.95	4.52
Total	101.4	101.0	99.7	100.3	100.2	100.0	100.4	101.3	101.2	99.9	101.2	101.2	100.3	100.4	100.2
Mg#[c]	0.84	0.82	0.82	0.83	0.86	0.83	0.80	0.81	0.80	0.82	0.81	0.82	0.77	0.81	0.82
Clinopyroxene															
Number of grains	2	2	2	4	3	3	4	2		1	2		1		
SiO_2	52.19	52.47	52.52	52.72	53.03	52.85	52.42	51.44		50.58	51.70		51.77		
Al_2O_3	5.93	6.22	5.73	5.42	5.00	5.13	5.64	6.02		6.19	5.55		5.83		
TiO_2	0.43	0.63	0.61	0.60	0.11	0.33	0.64	1.17		1.26	1.08		0.90		
Cr_2O_3	1.26	0.84	0.89	1.52	1.46	1.43	0.90	1.21		1.26	1.40		2.39		
FeO(t)[b]	3.55	3.13	3.05	3.33	2.98	3.00	3.30	3.47		3.58	3.41		3.96		
MgO	16.48	14.81	14.83	15.36	16.25	16.56	15.58	14.62		14.85	14.89		16.20		
MnO	0.13	0.06	0.07	0.09	0.07	0.09	0.07	0.11		0.06	0.10		0.11		
CaO	17.71	19.39	19.22	18.55	18.55	18.80	19.23	19.31		18.89	19.24		16.72		
Na_2O	1.75	2.09	1.92	2.02	1.61	1.91	2.07	1.95		1.72	1.77		2.31		
Total	99.41	99.62	98.83	99.60	99.05	100.1	99.85	99.29		98.39	99.12		100.2		
Mg#[c]	0.892	0.894	0.897	0.892	0.907	0.908	0.894	0.883		0.881	0.886		0.879		
SD[d] (±) of Mg#	0.002	0.005	0.001	0.003	0.002	0.001	0.003	0.001			0.001				

nd not determined

[a] Grt lherzolite

[b] Total Fe as FeO

[c] Mg#=Mg/(Mg+ΣFe)

[d] SD = Standard deviation

Table 2-2b Average compositions of minerals in spinel peridotites from Pali Aike

Lithology	Spl lherzolite		Spl harzburgite						
Sample	PA64	PAK1	LS5	PAK2	PAK3	LS100	PAK5	01BN	BNH11
Olivine									
Number of grains	2	3	3	3	4	5	3	3	3
SiO_2	40.74	41.17	40.97	41.20	40.86	40.58	39.90	40.87	40.89
Al_2O_3	0.01	0.01	0.03	0.02	0.02	0.03	0.06	0.01	0.02
FeO(t)[b]	10.34	9.18	9.71	8.23	8.11	10.66	13.36	8.86	9.64
MgO	49.31	49.36	49.41	50.17	49.89	48.20	46.03	49.98	49.12
MnO	0.14	0.13	0.11	0.12	0.10	0.10	0.12	0.18	0.13
CaO	<0.05	<0.05	0.07	0.07	0.06	0.08	0.08	<0.05	0.05
NiO	0.37	0.38	0.40	0.41	0.40	0.36	0.44	0.39	0.41
Total	100.9	100.2	100.8	100.2	99.44	100.0	99.99	100.3	100.3
Fo	89.5	90.6	90.1	91.6	91.6	88.9	86.0	90.9	90.1
SD[d] (±) of Fo	0.48	0.15	0.01	0.06	0.15	0.12	0.19	0.02	0.02
Orthopyroxene									
Number of grains	3	6	3	3	3	7	2	2	3
SiO_2	55.21	55.24	54.72	56.19	56.13	55.45	54.15	56.25	54.93
Al_2O_3	4.11	4.82	3.21	2.77	2.70	3.17	4.03	2.77	2.89
TiO_2	0.09	0.12	0.30	<0.04	0.04	0.30	0.50	0.05	0.21
Cr_2O_3	0.53	0.63	0.72	0.73	0.72	0.67	0.68	0.62	0.41
FeO(t)[b]	6.89	5.95	6.24	5.10	5.16	6.77	8.56	5.98	6.29
MgO	32.82	32.66	33.14	33.90	33.82	32.38	30.71	33.74	33.22
MnO	0.18	0.14	0.11	0.15	0.13	0.14	0.13	0.09	0.12
CaO	0.49	0.66	0.78	0.88	0.83	0.85	0.87	0.45	0.74
Na_2O	<0.05	<0.05	0.15	0.05	0.05	0.20	0.14	<0.05	0.10
Total	100.4	100.2	99.37	99.81	99.58	99.93	99.75	99.95	98.92
Mg#[c]	0.895	0.907	0.904	0.922	0.921	0.895	0.865	0.910	0.904
SD[d](±) of Mg#	0.007	0.001	0.001	0.002	0.000	0.002	0.001	0.002	0.001
Spinel									
Number of grains	2	6	6	2	4	8	6	5	2
SiO_2	0.03	<0.03	0.09	0.07	0.06	0.08	0.13	<0.03	0.08
Al_2O_3	50.29	52.57	27.42	27.31	27.36	26.45	29.44	33.57	27.79
TiO_2	0.06	0.12	2.36	0.16	0.18	2.57	3.85	0.10	1.88
Cr_2O_3	17.14	15.82	34.91	41.35	40.81	34.39	25.48	33.77	35.04
FeO(t)[b]	13.74	11.52	18.80	14.49	14.39	20.53	24.99	17.15	19.12
MgO	18.54	19.27	15.76	16.26	16.17	14.88	14.96	14.46	15.00
MnO	0.07	0.08	0.07	0.04	0.07	0.09	0.07	0.12	0.12
NiO	nd.	0.33	0.25	0.23	0.20	0.27	0.39	0.13	0.28
Total	99.85	99.73	99.68	99.93	99.26	99.26	99.31	99.31	99.34
Clinopyroxene									
Number of grains	3	5		3	3			3	3
SiO_2	52.01	52.52		52.84	53.41			53.42	52.47
Al_2O_3	4.77	6.21		3.62	3.51			3.36	4.58
TiO_2	0.29	0.44		0.72	0.06			0.14	0.69
Cr_2O_3	0.94	1.17		1.50	1.49			1.24	1.02
FeO(t)[b]	2.29	2.10		2.58	2.44			1.87	3.37
MgO	15.20	14.20		16.53	16.75			15.80	16.57
MnO	0.09	0.06		0.08	0.09			0.07	0.10
CaO	23.61	21.14		20.87	20.13			22.39	19.22
Na_2O	0.58	1.72		1.07	1.24			0.72	1.61
Total	99.78	99.56		99.80	99.13			99.01	99.62
Mg#[c]	0.922	0.923		0.919	0.924			0.938	0.898
SD[d] (±) of Mg#	0.001	0.003		0.011	0.003			0.002	0.011

[b] Total Fe as FeO; [c] Mg#=Mg/(Mg+ΣFe); [d] SD = Standard deviation.

Table 2-2c Representative compositions of minerals in garnet-bearing orthopyroxenites from Pali Aike*

Sample	BN46				BNH5				BN43			BNO5			BNC1				
Phase [a]	Opx	Grt	Cpx	Ti-Phl	Opx	Cpx	Grt	Spl	Ol	Ol-f	Opx	Ol	Opx	Grt	Ol	Ol-f	Opx	Cpx-f	Mg-Ilm
Host of inclusions			Opx			Opx		Grt	Opx			Opx			Opx				
SiO_2	56.25	41.94	52.45	38.68	55.89	52.62	41.99	0.02	40.03	39.96	54.25	40.91	55.52	42.45	40.81	40.97	55.19	51.60	0.03
TiO_2	0.37	0.20	1.07	5.23	0.26	0.65	0.18	0.48	0.06	0.00	0.31	0.01	0.30	0.42	0.07	0.08	0.44	1.42	54.63
Al_2O_3	3.17	23.27	5.73	16.21	3.64	5.51	23.89	57.82	0.03	0.06	3.64	0.04	3.77	23.36	0.06	0.07	4.01	6.60	0.90
Cr_2O_3	0.15	0.46	0.31	0.33	0.35	0.39	0.39	7.29	<0.03	<0.03	0.28	<0.03	0.48	0.97	<0.03	<0.03	0.33	1.01	1.80
FeO(t)[c]	9.51	11.84	5.12	6.19	7.69	3.96	9.61	14.18	12.20	12.99	7.77	13.24	8.29	9.19	13.11	13.61	8.45	4.58	30.14
MnO	0.13	0.38	0.11	<0.03	0.06	0.06	0.30	<0.03	0.13	0.14	0.14	0.09	0.12	0.32	0.14	0.05	0.24	0.06	0.21
MgO	30.73	18.58	14.67	18.99	31.75	15.12	20.11	19.69	47.05	47.36	32.11	46.27	31.41	20.32	46.76	46.08	31.79	14.83	12.02
CaO	0.81	4.82	18.51	0.07	0.56	17.32	4.03	<0.01	0.06	0.08	0.58	0.11	0.78	3.99	0.09	0.10	0.72	17.37	0.03
Na_2O	0.13	0.03	2.19	0.75	0.12	1.86	0.05	0.02	<0.02	0.04	0.17	<0.02	0.12	0.10	0.04	0.03	0.20	2.18	0.06
NiO	0.08	0.02	0.03	<0.01	0.16	<0.03	0.03	0.44	0.33	0.34	0.22	0.41	0.15	<0.02	0.47	0.33	0.06	0.17	0.25
K_2O				9.17															
Cl				0.02															
F				0.18															
Total	101.3	101.5	100.2	95.81	100.5	97.48	100.6	99.94	99.91	101.0	99.46	101.1	100.9	101.1	101.6	101.4	101.4	99.83	100.1
Mg# [d]	0.852	0.737	0.836	0.846	0.880	0.872	0.789	0.760	0.873	0.867	0.881	0.862	0.871	0.798	0.864	0.858	0.870	0.852	0.435
Cr# [e]								0.078											

Table 2-2c Continued

Sample	BNC2						BN92 [b]				BNH13				
Phase [a]	Ol-f	Opx	Mg-Ilm	Spl	Ti-Amp	Ti-Phl	Ol-f	Opx-f	Cpx-f	Mg-Ilm	Ol	Ol-f	Cpx-f	Opx	Ti-Amp
Host of inclusions											Opx				
SiO_2	39.92	54.34	0.02	0.16	54.07	37.38	41.12	54.93	52.03	<0.04	40.53	40.66	51.13	56.41	56.04
TiO_2	0.12	0.43	55.09	0.76	4.83	7.13	<0.04	0.45	1.59	55.09	<0.04	<0.04	1.42	0.23	3.38
Al_2O_3	0.06	3.80	0.24	59.43	15.38	15.18	0.02	4.18	6.33	1.38	<0.02	0.02	7.55	3.27	19.24
Cr_2O_3	0.00	0.30	1.10	4.23	<0.04	0.60	<0.03	0.42	0.34	1.84	<0.03	<0.03	0.72	0.31	<0.04
FeO(t) [c]	15.42	9.71	32.24	14.71	5.24	6.69	11.13	7.12	3.96	26.89	12.95	12.19	4.04	8.06	5.04
MnO	0.19	0.17	0.26	0.14	0.06	0.04	0.13	0.12	0.07	0.34	0.13	0.09	0.06	0.10	0.12
MgO	44.11	30.17	11.09	19.87	3.58	17.37	47.20	31.74	14.58	13.66	45.94	46.12	14.18	31.10	3.23
CaO	0.09	0.76	0.04	0.01	5.87	0.04	0.08	0.73	19.44	0.02	0.05	0.08	18.79	0.66	7.31
Na_2O	<0.02	0.23	<0.04	0.03	3.28	0.59	<0.02	0.11	1.73	<0.04	<0.02	<0.02	1.84	0.15	0.98
NiO	0.36	0.09	0.19	0.33	0.15	0.20	0.34	0.11	0.17	0.24	0.44	0.41	0.05	0.13	<0.04
K_2O					5.65	9.85									1.53
Cl					<0.02	<0.02									0.10
F					0.04	0.28									0.16
Total	100.3	99.99	100.3	99.66	98.18	95.49	100.0	99.91	100.2	99.46	100.0	99.63	99.77	100.4	97.13
Mg# [d]	0.836	0.847	0.399	0.760	0.550	0.822	0.883	0.888	0.868	0.492	0.863	0.871	0.862	0.873	0.533
Cr# [e]				0.046											

* Different grains for the same mineral show a narrow range in composition in each sample, therefore representative analyses are listed

[a] *Ol* olivine, *Opx* orthopyroxene, *Cpx* clinopyroxene, *Ilm* ilmenite, *Grt* garnet, *Phl* phlogopite, *Amp* amphibole, *Spl* spinel
f = fine-grain along grain boundaries or forming aggregates

[b] Veinlet of garnet-bearing orthopyroxenite in BN92

[c] Total Fe as FeO

[d] *Mg#* = Mg/(Mg + total Fe) for all minerals except for spinel. Mg# =Mg/(Mg + Fe^{2+}) is listed for spinel and ilmenite in which Fe^{2+} is calculated assuming stoichiometric composition

[e] Cr# = Cr/(Cr + Al)

Table 2-2d Compositions of spinel with different occurrences in one garnet-bearing peridotite

Rock type/sample	Grt-Spl harzburgite (BN50)				
Spinel occurrence	in Grt1	in Grt2	in Opx	int	ave
Al_2O_3	36.36	36.50	36.56	36.41	36.46
TiO_2	1.41	1.48	1.41	1.42	1.43
Cr_2O_3	27.04	27.52	26.54	26.87	26.99
FeO (t)[a]	17.80	18.06	17.75	18.02	17.91
MgO	16.49	16.77	16.61	16.47	16.59
MnO	0.11	0.12	0.12	0.10	0.11
Total	99.21	100.45	98.99	99.29	99.49

In Grt = enclosed in garnet; in Opx= inclusion in Opx; int= intergranular

Table 2-3 Major element and selected trace element (Ni and Cr)contents of mantle xenoliths from Pali Aike area

Rock type	Grt-Spl lherzolite							Grt-Spl harzburgite							
Sample	LS-33[a]	TM-0	TM-2	LS50	BN73	LS1	BN32	TM14	TM15	BN92	BN50	PAHK1	PAK6	BN45	BN31
Major (wt%)															
SiO_2	44.69	44.24	44.20	43.87	43.04	44.02	45.00	44.01	44.49	46.74	42.76	44.38	45.18	45.58	45.62
TiO_2	0.12	0.14	0.16	0.16	0.05	0.10	0.18	0.17	0.13	0.29	0.18	0.15	0.32	0.18	0.20
Al_2O_3	3.14	4.18	3.73	1.97	1.53	2.57	3.86	3.47	3.12	3.80	3.84	3.62	3.16	3.89	3.64
Fe_2O_3 (t)[b]	8.78	9.17	9.02	9.30	9.10	8.95	9.21	10.35	10.73	9.70	10.59	10.52	11.98	9.93	10.11
MnO	0.13	0.14	0.14	0.12	0.12	0.13	0.13	0.14	0.14	0.13	0.14	0.14	0.14	0.14	0.13
MgO	40.41	38.35	39.25	41.02	44.54	41.13	38.19	40.75	40.52	38.40	40.65	40.20	38.57	39.13	39.60
CaO	2.43	3.33	2.86	2.83	1.24	2.29	2.97	1.09	0.99	1.04	1.21	0.68	0.66	0.87	0.75
K_2O	<0.02	<0.02	<0.02	<0.02	<0.02	<0.02	0.04	0.02	<0.02	<0.02	<0.02	<0.02	<0.02	<0.02	<0.02
Total	99.70	99.55	99.36	99.27	99.62	99.18	99.58	99.99	100.1	100.1	99.37	99.69	100.0	99.72	100.0
Mg# [c]	0.90	0.89	0.90	0.90	0.91	0.90	0.89	0.89	0.88	0.89	0.88	0.88	0.86	0.89	0.89
Minor (ppm)															
Cr	2800	2416	2778	2264	2355	2467	2623	2509	2541	2680	5437	2645	1732	2450	2174
Ni	1720	1740	1410	2370	2460	2250	1930	1700	1970	1550	1510	2190	2340	2330	2370

Table 2-3 Continued

Rock type	Spl-lherzolite		Spl-harzburgite						Grt orthopyroxenite						
Sample	PA64	PAK1	LS5	PAK2	PAK3	LS100	PAK5	01BN	BNH13	BNC2	BNC1	BN43	BNO5	BNC3	BNH5
Major (wt%)															
SiO_2	43.82	44.36	43.14	43.65	43.84	43.42	43.00	44.04	52.58	53.02	52.76	53.95	52.53	51.74	48.80
TiO_2	0.05	0.10	0.14	0.05	0.05	0.14	0.34	<0.05	0.46	0.84	1.20	0.70	0.55	2.00	0.29
Al_2O_3	1.64	2.09	1.22	0.98	0.95	1.15	1.51	1.40	5.65	4.28	4.05	3.62	5.22	4.57	11.34
Fe_2O_3 (t)[b]	9.53	8.40	10.21	8.03	8.13	10.32	13.52	8.88	9.07	10.56	9.53	8.64	9.69	9.74	9.66
MnO	0.14	0.12	0.12	0.11	0.11	0.12	0.13	0.13	0.14	0.13	0.11	0.12	0.13	0.12	0.19
MgO	43.52	41.69	43.95	45.59	46.05	44.08	40.92	44.47	30.24	29.93	30.71	31.93	30.34	30.68	26.80
CaO	1.23	2.56	0.31	0.94	0.67	0.41	0.46	0.85	1.54	0.92	0.93	0.91	1.04	0.78	2.19
K_2O	<0.02	<0.02	<0.02	<0.02	<0.02	<0.02	<0.02	<0.02	0.27	0.14	0.02	0.02	0.02	0.03	0.01
Total	99.94	99.32	99.09	99.36	99.80	99.64	99.88	99.77	99.95	99.82	99.31	99.89	99.52	99.66	99.28
Mg# [c]	0.90	0.91	0.90	0.92	0.92	0.89	0.86	0.91	0.87	0.85	0.86	0.88	0.86	0.86	0.85
Minor (ppm)															
Cr	1521	2233	2841	2759	2470	2765	2388	4078	2215	2061	2125	1843	2348	2735	2576
Ni	2190	2275	2500	2510	2590	2320	2720	2450	761	971	991	743	1110	1290	698

[a] Grt lherzolite

[b] Total Fe reported as Fe_2O_3

[c] Mg# =Mg/(Mg + total Fe)

Table 2-4 Temperature and pressure estimates for the peridotite xenoliths from Pali Aik earea

		Temperature (°C)				Pressure (Kbar)	
Sample	Rock type	Wells (77)[a]	B&K-2Px (90)[b]	B&K-Ca(90)[c]	Ballhaus (91)[d]	B&K Al-in Opx(90)[e]	N&G Al-in Opx(85)[f]
LS33	Grt-Spl lherzolite	1110	1209	1121		24.5	23.2
TM0		959	1011	984	922	17.8	19.6
TM2		964	1040	965	915	19.0	20.8
LS50		1015	1099	1035	945	20.0	22.0
BN73		1055	1133	1073	1020	20.7	22.1
LS1		1074	1127	1043	940	28.1	22.7
BN32		1001	1051	993	875	27.3	20.1
TM14	Grt-Spl harzburgite	959	1027	993	917	20.7	21.1
TM15				965	902	17.7	19.3
BN92		1006	1073	1010	986	20.2	21.4
BN50		980	1061	1019	951	20.9	20.9
PAHK1				1010	938	21.2	20.8
PAK6		1125	1165	984	895	25.2	24.9
BN45				1035	900	26.7	20.8
BN31				993	933	21.1	21.4
PA64	Spl-lherzolite	777	685	891	801		
PAK1		849	836	951	784		
LS5	Spl harzburgite			994	977		
PAK2		997	1030	1018	959		
PAK3		1024	1066	1010	952		
LS100				1018	975		
PAK5				1025	1057		
01BN		909	882	880	672		
BNH11		1055	1103	986	831		

[a] Wells (1977) two-pyroxene thermoter

[b] Brey and Kohler (1990) two-pyroxene thermometer

[c] Brey and Kohler (1990) Ca-in-Opx thermoter

[d] Ballhaus (1991) Mg-Fe exchange thermometer in olivine-spinel

[e] Brey and Kohler (1990) Al-in-Opx barometer

[f] Nickel and Green (1985) Al-in-Opx barometer

Table 2-5 Summary of the compositions of olivine, orthopyroxene and spinel and oxygen fugacity values for the mantle xenoliths from Pali Aike southern South America

Lithology	Grt-Spl lherzolite						Grt-Spl harzburgite							
Sample	TM0	TM2	LS50	BN73	LS1	BN32	TM14	TM15	BN92	BN50	PAHK	PAK6	BN45	BN31
Olivine														
X_{Fe}	0.11	0.10	0.10	0.09	0.09	0.11	0.11	0.12	0.11	0.11	0.11	0.13	0.11	0.11
X_{Mg}	0.89	0.90	0.90	0.91	0.91	0.89	0.89	0.88	0.89	0.89	0.89	0.87	0.89	0.89
Orthopyroxene														
$M1_{(Fe)}$ [a]	0.09	0.09	0.09	0.08	0.06	0.07	0.09	0.10	0.10	0.09	0.09	0.11	0.07	0.09
$M2_{(Fe)}$ [a]	0.10	0.10	0.10	0.09	0.07	0.08	0.09	0.10	0.10	0.09	0.10	0.12	0.08	0.10
Spinel														
Cr#	0.28	0.30	0.37	0.34	0.36	0.27	0.29	0.30	0.29	0.33	0.31	0.32	0.31	0.31
$Fe^{3+}/\Sigma Fe$ [b]	0.29	0.29	0.30	0.34	0.31	0.29	0.29	0.28	0.34	0.31	0.34	0.33	0.32	0.31
$Mg/(Mg+Fe^{2+})$	0.75	0.74	0.72	0.77	0.74	0.73	0.72	0.70	0.72	0.71	0.71	0.65	0.71	0.71
$\log a_{Fe3O4}^{Sp}$	-1.74	-1.77	-1.76	-1.86	-1.87	-1.70	-1.67	-1.65	-1.59	-1.65	-1.58	-1.55	-1.63	-1.65
P (Kbar) [c]	19.6	20.8	22.0	22.1	22.7	20.1	21.1	19.3	21.4	20.9	20.8	24.9	20.8	21.4
T °C (wells) [d]	959	964	1015	1060	1074	1000	959	960	1010	980	1010	1130	1030	988
T(°C) [e]	922	915	945	1020	940	875	917	902	986	951	938	895	900	933
△log(fO2)FMQ [f]	0.11	0.10	0.22	0.15	0.21	0.28	0.19	0.20	0.56	0.35	0.56	0.52	0.61	0.33
△log(fO2)FMQ [g]	0.27	0.32	0.35	0.39	-0.23	-0.33	0.05	0.03	0.41	0.13	0.47	0.44	0.04	0.17

Table 2-5 Continued

Lithology	Spl lherzolite		Spl harzburgite							Grt orthopyroxenite
Sample	PA64	PAK1	LS5	PAK2	PAK3	LS100	PAK5	01BN	BNH11	BNC2
Olivine										
X_{Fe}	0.11	0.09	0.10	0.08	0.08	0.11	0.14	0.09	0.10	0.16
X_{Mg}	0.89	0.91	0.90	0.92	0.92	0.89	0.86	0.91	0.90	0.84
Orthopyroxene										
$M1_{(Fe)}$ [a]	0.09	0.08	0.07	0.07	0.07	0.10	0.12	0.08	0.07	0.14
$M2_{(Fe)}$ [a]	0.10	0.09	0.07	0.07	0.08	0.10	0.13	0.09	0.08	0.15
Spinel										
Cr#	0.17	0.17	0.46	0.50	0.50	0.47	0.36	0.40	0.46	0.05
$Fe^{3+}/\Sigma Fe$ [b]	0.24	0.17	0.31	0.27	0.27	0.32	0.39	0.17	0.22	0.24
$Mg/(Mg+Fe^{2+})$	0.76	0.78	0.69	0.73	0.73	0.65	0.64	0.63	0.64	0.76
$\log a_{Fe3O4}^{Sp}$	-1.56	-2.09	-1.66	-2.02	-2.04	-1.62	-1.32	-2.02	-1.99	-1.65
P (Kbar) [c]	15.0	15.0	15.0	15.0	15.0	15.0	15.0	15.0	15.0	21.3
T °C (wells) [d]	777	849	946	997	1020	1010	1020	909	1060	994
T(°C) [e]	801	784	977	959	952	975	1057	672	831	1000
$\triangle\log(fO2)FMQ$ [f]	0.05	-0.59	0.77	0.15	0.17	0.81	1.19	0.01	0.36	-0.58
$\triangle\log(fO2)FMQ$ [g]	0.59	-0.13	0.11	0.41	0.48	0.66	0.75	0.32	-0.23	-0.50

[a] M1(Fe), M2 (Fe) = Fractions of Fe at M1 and M2 sites, calculated following the method in Wood et al (1990)

[b] Calibrated using the four spinel grains with known Fe^{3+} contents

[c] For garnet-bearing xenoliths, pressures were calculated based on Al-in-Opx barometer of Nickel and Green (1985) and for those garnet-free xenoliths pressures were assumed as 1.5 Gpa in fO_2 calculation

[d] For xenoliths containning both Opx and Cpx, T were calculated based on two-pyroxene thermometer (Wells 1977), and for those samples without Cpx, T were calculated based on Ca-in-Opx thermometery (Brey and Köhler 1990)

[e] Calculated based on Fe-Mg exchange (in Ol-Spl) thermometer of Ballhaus (1991)

[f] Calculated following the method of Ballhaus et al (1991) using the Fe^{3+} contents of spinel assuming its stoichiometric composition

[g] Calculated following the method of Nell and Wood (1991) using the calibrated contents of Fe^{3+}

CHAPTER 3

Metasomatic origin of garnet orthopyroxenites and mobility of siderophile and chalcophile elements in the subcontinental lithospheric mantle underlying southern South America

Jian Wang and Keiko H. Hattori

Department of Earth Sciences, University of Ottawa,
Ottawa, Ontario, Canada, K1N 6N5
Corresponding author e-mail: jwang062@uottawa.ca
Tel: 1-613-562-5800 (X 6729), Fax: 1-613-562-5192

Manuscript submitted to ***Contribution to Mineralogy and Petrology***

Abstract

Garnet-bearing orthopyroxenite occurs as discrete mantle xenoliths and veinlets in peridotite xenoliths that were brought to the surface by the Quaternary volcanic rocks in Pali Aike, one of the Patagonian plateau basalt fields in southern South America. Orthopyroxenites commonly contain Ti-rich minerals and relict grains of olivine (Ol) and clinopyroxene (Cpx) occurring as inclusions in secondary orthopyroxene (Opx). The secondary Opx contains high TiO_2 (0.20-0.59 wt%), moderate Al_2O_3 (2.87-5.10 wt%) and low magnesium numbers (Mg#, 0.845-0.892) compared with Opx in garnet-bearing peridotites in the area. This evidence suggests that secondary Opx formed at the expense of Ol and Cpx during metasomatism by a Ti-rich evolved melt. The orthopyroxenites contain similar bulk-rock concentrations of Cr, Ni and platinum group elements (PGE) as do peridotites, suggesting that these metals were essentially immobile during metasomatism, and that the metasomatizing melt did not introduce these elements. Instead, the metasomatizing melt contributed alkalis, Ti, Si, Cu, and S to the orthopyroxenites based on increased concentrations of these elements and mineralogy. The evolved metasomatising melt was saturated with S and introduced immiscible sulphide liquid containing Cu and S to the orthopyroxenites.

Secondary Opx has been documented in sub-arc mantle peridotites. In comparison with such Opx in sub arc mantle samples, our secondary Opx contains high Ti and Al and low Mg. High Ti and low Mg in our samples reflect the evolved nature of the metasomazing melt that originated from the underlying asthenospheric mantle. This new type of secondary Opx, typified by our samples, may be common in the SCLM elsewhere, affected by asthenospheric upwelling.

Keywords: Orthopyroxenite, mantle metasomatism, silica enrichment, PGE, siderophile elements, chalcophile elements, sulphur, asthenospheric melt, southern South America

3.1. Introduction

The occurrence of secondary orthopyroxene (Opx) has been documented in mantle wedges and has been interpreted as Si enrichment by aqueous fluids and melt derived from subducting slabs (e.g. Smith et al. 1999; Arai et al. 2004). A similar process produced the garnet (Grt) orthopyroxenites beneath the North China craton during subduction of the Yangtze craton, after the collision of the two cratons (Liu et al. 2005; Malaspina et al. 2006). The high modal abundance of Opx in ancient SCLM underlying Archean cratons can also be explained by infiltration of Si-rich melt (Kesson and Ringwood 1989; Kelemen et al. 1998).

An alkali-rich melt has a low activity of SiO_2 and is not expected to cause Si enrichment in mantle peridotites. However, a recent study of xenoliths in western Japan by Arai et al (2006) suggests that evolved alkali-rich melt is in fact capable of producing Si enrichment in such peridotites. Ertan and Leeman (1996) also documented the formation of phlogopite-bearing orthopyroxenite in harzburgites during the metasomatism by high-K melt in the Cascades sub-arc mantle.

This paper reports the bulk-rock compositions, mineralogy and mineral chemistry of Grt-bearing orthopyroxenites in Quaternary alkali basalts in the Pali Aike area, southern South America (Fig. 3-1). The data, combined with the textures of rocks and minerals, indicate that orthopyroxenites formed from Grt peridotites during the injection of asthenospheric mantle-derived, Ti-rich melt.

3.2. Geological Background and Petrological Description of the Xenoliths from Pali Aike

The modern geological framework of South America resulted mainly from the subduction of the Nazca and Antarctic plates beneath the South American continent (Fig. 3-1) (D'Orazio et al. 2000). The Chile ridge between the Nazca and Antarctic plates collided with the trench near the southern tip of South America at ~14-15 Ma (Cande and Leslie 1986), and then subducted beneath the South American continent. This ridge subduction was responsible for the formation of a slab window, which produced the extensive Patagonian plateau basalts in the interior of

southern South America (e.g. Ramos and Kay 1992; Gorring et al. 1997; Gorring and Kays 2001). The basalts are considered to have originated from the underlying asthenospheric mantle through a slab window (e.g. Gorring et al. 1997) and are systematically younger to the northeast, with ages ranging from ~12 Ma to recent, following the track of the subducted ridge. Pali Aike volcanic field represents the southernmost plateau basalt field, covering 45×100 km^2 (Fig. 3-1), but it is young in age (≤4 Ma). This time delay has been explained with the hypothesis that an extensional tectonic regime, favorable to the ascent of the magmas, was present in Pali Aike area only after 6 Ma (D'Orazio et al. 2000). The volcanic field contains extensive basaltic lavas and pyroclastic rocks, and includes tuff breccias and spatter and scoria cones. Pyroclastic rocks contain abundant xenoliths (D'Orazio et al. 2000), which are the focus of this study.

3.3. Petrography of Samples

The xenolith samples are divided into two types based on their mineralogy and textures; peridotites and pyroxenites. The peridotites are spinel-bearing lherzolites and harzburgites and further divided into four subtypes based on the presence of Grt: Grt-spinel lherzolite, spinel lherzolite, Grt-spinel harzburgite, and spinel harzburgite. They commonly show modal and cryptic metasomatism, especially in Grt-bearing samples. Modal metasomatism produced Ti-rich phlogopite, Ti-rich amphibole (Ti-Amp), Mg-rich ilmenite (Mg-Ilm) and minor sulphides. Discontinuous narrow veinlets (<3 mm) composed of Ti-phlogopite and/or Mg-Ilm are common in Grt-bearing harzburgites.

Pyroxenite xenoliths are mainly orthopyroxenites with minor olivine (Ol) websterites. Olivine websterites are free of apparent metasomatism. Garnet is lacking in several Ol websterite samples, suggesting their formation at relatively shallow levels. All orthopyroxenite samples contain Grt.

3.4. Analytical Method

Mineral compositions were determined by a Camebax MBX microprobe at Carleton University using 15 kV accelerating voltage, 20 nA beam current, focused beam size (<1 μm), and natural and synthetic mineral standards. A counting time of 20 s was used for all elements except 50 s for Ca in Ol and 60s for F in phlogopite. Compositions for a certain mineral in individual samples show a narrow range, therefore only representative analyses of minerals are listed in Table 3-1.

For bulk-rock analysis, the rims of xenoliths that have been affected by host volcanic rocks and weathering were removed. Major and minor elements were determined using a Philips PW 2400 X-ray fluorescence spectrometer after fusing the sample powder with $LiBO_3$ at the University of Ottawa. Precision based on replicate runs of eleven samples is ± 0.35 % for Al_2O_3, ± 0.48 % for MgO, ± 1.3 % for Cr, ± 9.2 % for Ni. The accuracy, which was monitored using references of MRG-1 and Sy-2, shows ± 0.039 % for Al_2O_3, 0.28 % for MgO, 3.4 % for Cr, 4.0 % for Ni. Accuracy is less than 1 % and 10 % for other major and minor elements, respectively.

Platinum group elements (PGE) were determined by isotopic dilution using a mixed spike of ^{190}Os, ^{191}Ir, ^{99}Ru, ^{194}Pt and ^{105}Pd. Platinum group elements with a spike were pre-concentrated into a Ni bead and dissolved in concentrated HNO_3. The analytical procedures are similar to those by Ravizza and Pyle (1997). Mass ratios were determined using an Agilent HP-4500 ICP-MS at the University of Ottawa. Blank contributions were 0.002-0.006 ng Os/g flux, 0.002-0.007 ng Ir/g flux, 0.02 ng Ru/g flux, 0.07-0.16 ng Pt/g flux and 0.03-0.12 ng Pd/g flux. The blanks are negligible compared to the amounts in samples; thus, blank corrections were not applied to the results. Precisions of PGE determination are < 15% for Os, < 14% for Ir, < 12% for Ru, < 11% for Pt and < 19% for Pd based on repeat analyses of five samples.

The contents of S and Cu were determined using a Varian Vista-Pro inductively coupled plasma atomic emission spectrometer after digestion of ~0.2 g power sample with aqua regia in a screw-top Teflon vial at ~130 °C for 48 hrs. Precision based on replicate runs of five samples is < 8 % for Cu and < 5 % for S. The detection limit for Cu is 0.2 ppm and 4.5 ppm for S.

3.5. Garnet Orthopyroxenite

3.5.1. Petrography

Garnet orthopyroxenites are dark brown in hand specimens and are different from light colored peridotites. They occur either as discrete xenoliths or veinlets (>5 mm) in harzburgites (BN92)(Fig. 3-2a). Orthopyroxenite xenoliths contain small angular peridotite fragments (5-10 mm in size) and these fragments show diffuse boundaries with an orthopyroxenite host. Orthopyroxenites show equigranular and/or porphyroblastic texture with coarse Grt (up to 5 mm) and Opx (up to 4 mm). They are composed of Opx (≥85 vol%), Grt (1-5 vol%), Ol (≤1 vol%), Cpx (≤1 vol%), Ti-phlogopite, Ti-Amp, Mg-Ilm, and minor sulphide minerals (Ni-bearing pyrrhotite, pentlandite, cubanite, and chalcopyrite) by visual estimation under microscope.

Olivine, Cpx, and spinel are interpreted as the primary minerals and are commonly enclosed by poikilitic Opx and Grt. Olivine occurs as inclusions within coarse Opx (Fig. 3-2d) and as interstitial grains along boundaries of minerals (Figs. 3-2b, 3-2c). Clinopyroxene is minor (<5 vol %) and found only in four samples (BNH5, BNH13, BNC1 and BN46). Optically continuous relict Cpx grains occur as inclusions in secondary Opx (Fig. 3-2e) and Grt. It also forms narrow (<200 μm) bands along secondary Opx (Fig. 3-2f).

Secondary Opx is fine (<0.3 mm) to coarse (>2 mm) and characterized by variable shape, no cleavages, and abundant fluid inclusions (Fig. 3-2d). Fine-grained Opx forms aggregates in coarse-grained Opx, and bands along boundaries of other minerals. In some cases, secondary Opx shows re-crystallization texture with ~120° triple junctions (Fig. 3-2e). Clear Opx without fluid inclusions are considered as primary. They are tabular in form and coarse-grained (>2 mm), and display well developed cleavages. The compositions of primary and secondary Opx are similar in individual samples, suggesting that Opx grains have chemically re-equilibrated.

Garnet usually occurs as isolated large grains (up to 5 mm) and commonly contains inclusions of rounded spinel and corroded Cpx. Ti-phlogopite and Mg-Ilm are minor to rare, but occur in all Grt orthopyroxenites. They commonly form discontinuous and irregular narrow (<2

mm) veinlets. Coarse-grained phlogopite commonly enclose rounded secondary Opx. Ti-Amp is rare and locally occurs as thin veinlets surrounding Ol, Cpx or spinel, and it is commonly associated with fine-grained Mg-Ilm.

Spinel occurs either as inclusions in Grt with narrow reaction rims (less than 5μm) or as individual grains surrounded by Ti-Amp and Opx (Fig. 3-2g). Sulphides are minor, but present in all orthopyroxenite samples. Sulphides form spherical to globular grains (up to 200 μm) and are commonly associated with phlogopite or Amp and enclosed by Opx and Ol (Fig. 3-2h). The globular shape of sulphides suggests that sulphides were once liquid and that immiscible sulphide liquid was likely present in the metasomatizing agent. Most sulphide grains are homogeneous Ni-bearing pyrrhotite ($Fe_{1-x}S$, <20 wt% Ni). Several pyrrhotite grains contain exsolved phase of pentlandite ($(Ni, Fe, Co)_9S_8$) or cubanite ($CuFe_2S_3$). These exsolved phases form flames, lamellae and bands close to the margins of sulphide grains (Fig. 3-2h). Sulphide grains commonly contain minor (<5 vol%) oxide with Fe and minor Cu in their margins (Fig. 3-2h). A similar occurrence of oxides has been reported within globular sulphide grains in volcanic rocks and mantle peridotites, and has been interpreted as an exsolution product of sulphide liquid (e.g. Francis 1990; Hattori et al. 2002), since O may replace up to 50 % of S in sulphide liquid (Gaetani and Grove 1997; Rose and Brenan 2001).

Orthopyroxenite veinlets contain the same mineral assemblage as orthopyroxenite xenoliths, but grain size is smaller (<0.5 mm) in veinlets. The veinlets have diffuse boundaries with the host peridotites and are accompanied by halos of secondary Opx (Fig. 3-2a). These secondary Opx grains are distinctly different from primary Opx because the secondary Opx is cloudy due to abundant fluid inclusions (Fig. 3-2d). Relict grains of Ol are common in veinlets and some are optically continuous with Ol grains outside the veinlets (Figs. 3-2b, 3-2c).

3.5.2. Mineral Chemistry of Orthopyroxenites

Olivine compositions are similar within and between grains in individual samples (Table 3-1), suggesting that Ol has generally attained equilibration excluding one case described below. Olivine is characterized by low Mg (Fo = 83.3-87.3) and high NiO contents (0.33-0.53 wt%) compared with Ol in peridotite samples; Fo 87.1-89.3 and 0.38-0.48 wt% NiO for Ol in Grt-spinel harzburgite, and Fo 89.1-90.6 and 0.32-0.41 wt% NiO for Ol in Grt-spinel lherzolite (Table 3-1, Fig. 3-3). One Ol inclusion in Opx in sample BNH13 contains high Fo, 90.1, which is higher than other grains (Fo, ~87) in the same sample, implying this grain keeps the original composition and was not in equilibrium with other relict Ol and secondary Opx.

Clinopyroxene is interpreted as a relict mineral, but it is variably enriched in TiO_2 (0.65-1.59 wt%), lowered in Mg# (Mg/[Mg + total Fe] = 0.826-0.907) and Cr_2O_3 (0.25-1.16 wt%) compared to Cpx in peridotites. Furthermore, single grains of Cpx shows compositional variations in Ti and MgO content, suggesting that the Cpx compositions are not in equilibrium.

Spinel grains show small compositional variations of Cr and Al within individual grains. X_{Mg} (= Mg/[Mg + Fe^{2+}]) of spinel inclusions in Grt in sample BNH5 range from 0.705 to 0.761, and individual grains of BNC2 from 0.745 to 0.773. The values of Cr# (= Cr/[Al + Cr]) range from 0.077 to 0.187 in BNH 5 and from 0.035 to 0.049 in BNC2 (Fig. 4). Furthermore, spinel grains in BNC2 show compositional zoning with rims (~30 μm) high in Mg and low in Cr (Table 3-1; Fig. 3-2g). Spinel contains lower Cr# than that of peridotites in the area.

Secondary Opx grains are texturally distinct from the primary Opx because of their shape and abundant fluid inclusions, but their compositions are similar in individual samples, suggesting that equilibration was attained among grains (Table 3-1). Orthopyroxene does not exhibit compositional zoning in grains (Table 3-1), which is consistent with equilibration among Opx grains, which have low Cr_2O_3 (0.09-0.48 wt%) and Mg# (0.845-0.892), similar Al_2O_3 (2.87-5.10 wt%), and high TiO_2 (0.20-0.59 wt%) compared to Opx in peridotites (Fig. 3-5).

Amphiboles contain overall high TiO_2 (3.38-4.83 wt%) and alkalis (K_2O+Na_2O = 2.50-8.93 wt%) and low Mg# (0.533-0.713). Their compositions suggest that they are sodic-calcic Amp, such as richterite, magnesio-katophorite, and winchite based on the amphibole-classification of

Leake et al. (1997), but their phases were not identified due to their large compositional variation within grains and small sizes. The compositional variation suggests that Amp did not equilibrate after crystallization.

Phlogopite is characterized by high TiO_2 (5.18-7.13 wt%) and Mg# ranging from 0.822 to 0.847 (Table 3-1). The compositions are similar within grains and samples, and their occurrences are spatially associated with Ti-Amp.

3.5.3. Major, Minor and Platinum-group Elements in Bulk Samples

Garnet orthopyroxenites contain high SiO_2 (48.8–54 wt%), Al_2O_3 (3.62–11.3 wt%) and TiO_2 (up to 2.0 wt%), and low Mg# (0.846–0.880) compared to Grt-bearing peridotites in the area (SiO_2<47 wt%; Al_2O_3< 4 wt%; TiO_2 <0.4 wt%; Mg# >0.87) (Fig. 3-6), but their compositions are distinctly different from those of host basalts and Ol websterite in the study area (Fig. 3-7b). Olivine websterite has low total PGE contents and fractionated primitive mantle-normalized PGE pattern. The data support that Ol websterites are cumulates of melt.

Garnet orthopyroxenites contain high contents of PGE (12.9 to 29.8 ppb in total), comparable to the primitive mantle values, and they have nearly flat primitive mantle-normalized PGE patterns (Fig. 3-7a). In terms of absolute and relative PGE abundances, the Grt orthopyroxenites are comparable to Grt-bearing peridotites in the study area (Fig. 3-7a; Table 3-2). Furthermore, the data from orthopyroxenites are similar to mantle peridotites from many other areas, such as Ronda in Spain and Beni Bousera in Morocco (e.g. Gueddari et al. 1996).

Orthopyroxenites contain greater concentrations of S (10-140 ppm) and Cu (3-14 ppm) compared to Grt-Spl harzburgites (5-25 ppm S; 1-5 ppm Cu) (Table 3-2; Fig. 3-9a). Garnet-Spl lherzolites contain slightly higher S (10-50 ppm) and much higher Cu (3-25 ppm) compared to the Grt-spinel harzburgites (Fig. 3-9a). Their lower concentrations in harzburgites are consistent with their incorporation into melt during partial melting.

3.6. Discussion

3.6.1. Relationships Between Peridotites and Orthopyroxenites

Orthopyroxenites are commonly considered to be cumulates of melt (e.g. Anhaeusser 2001; Maaløe 2005). We discount this possibility here based on the texture of Opx replacing Ol and Cpx described in the previous sections. The original rocks were either harzburgite or lherzolite and metasomatized to form orthopyroxenites. This metasomatic origin of orthopyroxenite is further supported by the finding of a high Mg Ol (Fo=90.4) inclusion in Opx. The Mg content is similar to that of peridotites and this Ol grain totally enclosed by a coarse-grained Opx apparently escaped equilibration with Ol outside the Opx. A metasomatic origin is also supported by high concentrations of refractory elements, such as Cr and Ir-type PGE. Cumulates should contain low Ir-type PGE and high ratios of Pt-type PGE/Ir-type PGE compared to mantle residues, because refractory Ir-type PGE remain in mantle residue during partial melting (e.g. Brenan et al. 2005). Chromium is also highly compatible and remains in the residual peridotites during partial melting. Indeed, cumulates of Ol websterites in our samples contain low Cr (<1600 ppm) and high Pt-type PGE (Pt-type PGE/Ir-type PGE = ~ 4). Similar Cr and PGE contents and unfractionated PGE patterns of orthopyroxentes and peridotites suggest that the orthopyroxenites are unlikely to be cumulates, but rather formed from Grt-bearing peridotites by metasomatism.

3.6.2. Mg# in Opx and Ol

At equilibrium, the Mg# of Opx positively correlates with Mg# of Ol, and the values of the former are always higher than that of the latter (e.g. Grove et al. 1992). This equilibrium relationship is observed in most peridotites and orthopyroxenites, suggesting that Ol and Opx are equilibrated (Fig. 3-10). Several Grt-bearing harzburgites show different Fo at the same Mg# of Opx, suggesting that the two minerals are not in equilibrium even though each mineral shows similar compositions within individual samples. The Mg# of Opx in Grt-bearing harzburgites range between those of other peridotites and orthopyoxenites. Similarly, the Fo values of Ol range from 89.3 to 87.1; the high value is similar to those of other anhydrous peridotites and the

low value is similar to orthopyroxenites. The evidence suggests that Grt-bearing harzburgites contain Ol and Opx of two different origins; primary and metasomatic products.

3.6.3. Nature of Metasomatizing Agent

Garnet orthopyroxenites contain higher SiO_2, Al_2O_3, TiO_2, and lower Mg# in bulk rocks compared to Grt-bearing peridotites in the area (Table 3-2; Fig. 3-6), suggesting that the metasomatizing agent is likely to be rich in Si, Al, Ti and Fe. Therefore, the metasomatizing agent is most likely melt rather than fluid because Ti and Al are relatively immobile in aqueous fluids. The proposed interpretation is supported by the high F/Cl ratios in Ti-phlogopite and Ti-Amp in our samples (Table 3-1), because F is preferentially retained in melt and Cl in aqueous fluids (e.g. Willmore et al. 2000). High Ti in the metasomatizing melt is supported by high Ti contents in secondary Opx, as well as in phlogopite and Amp, whereas high Al contents in melt are reflected in the rims of individual spinel grains (Table 3-1). Furthermore, the common existence of Ti-phlogopite and Ti-Amp and high alkali contents (K_2O+Na_2O, up to 9 wt%) in Amp suggest that the melt was also rich in alkalis.

The low Mg# values of secondary Opx likely reflect the character of the metasomatizing melt. The Mg# of the metasomatizing melt was evaluated using the composition of Ol and the Fe-Mg exchange coefficient (see chapter 1). Olivine is a relict phase but it equilibrated with Opx in orthopyroxenites, based on the positive correlation of Mg# between Ol and Opx (Fig. 3-10). The calculated Mg# of the melt is 0.560-0.637, lower than that of the host basalts (0.618-0.728). The host basalts in the area contain high contents of MgO, Ni and Cr up to 17.1 wt%, 650 ppm, and 500 ppm (Table 3-2), representing rather primary basaltic magmatic melts. Therefore, the low Mg# value of the hypothetical melt indicates that it was evolved.

The evolved nature of the metasomatizing melt explains the variable and low Cr# of spinel (0.035-0.019) in orthopyroxenites. The Cr content of a melt decreases quickly during solidification of the melt, and the spinel formed during such crystallization shows a highly variable Cr# (Barnes and Roeder 2001). The preservation of a compositional variation in spinel

grains in our samples suggests that orthopyroxenites were brought to the surface not long after metasomatism, since spinel easily equilibrates with melt at high temperatures (e.g. Hammond and Taylor 1982).

3.6.4. Origin of Metasomatizing Melt

There are two possible origins of the metasomatizing melt that we argue was responsible for the formation of the orthopyroxenites: 1) a slab-melt and/or arc-related magma, and 2) melt unrelated to subduction. The first possibility is rejected because slab-melt and arc magmas contain low Ti (e.g. Prouteau et al. 1999), whereas the melt responsible for the formation of Grt orthopyroxenite was rich in Ti. In addition, the Pali Aike area is over 100 km from an identified arc (Fig. 3-1). Furthermore, the Al_2O_3 content in secondary Opx in our samples is high (2.87-5.10 wt%), whereas secondary Opx formed in sub-arc mantle peridotites has a low Al_2O_3 content (< 2 wt% in most cases; Fig. 3-5) (Arai et al. 2003, 2004). Instead, we suggest that the metasomatizing melt for formation of Grt orthopyroxenite in Pali Aike was an alkali basaltic melt that originated from asthenospheric mantle, because such a melt is commonly high in Ti (Gibson et al. 1995). Second, Sr and Nd isotopic data for modally metasomatized Grt-bearing harzburgites (Stern et al. 1999) are similar to the Pali Aike host basalts (D'Orazio et al. 2000) and other Patagonian Quaternary alkali basalts, which show trace element patterns similar to oceanic island basalts and have a well-established asthenospheric origin (Gorring et al. 1997). The subduction of the Chile ridge since the mid-Miocene (~14 Ma) resulted in the formation of a slab window which allowed upwelling of asthenospheic melt to form the voluminous plateau basalts (Gorring et al. 1997).

Our xenolith samples are hosted by Ol basalts that are rich in Ti and alkalis; therefore, the host basalt is potentially responsible for the metasomatizing event. However, we discount this possibility because the host basalts are primitive, with high Mg# and relatively low SiO_2 contents, even lower than peridotites. To enrich the peridotites with Si, an evolved melt is required.

Therefore, we consider that the metasomatizing melt has the same affinity as and is co-genetic with the host alkali basalt, but the two are different.

A Si-poor alkali melt may evolve to become a Si-saturated magma. Most plateau basalts in Pali Aike contain Ol and hypersthene (D'Orazio et al. 2000). The existence of these minerals indicates that the composition of the parental magmas plots in the inner tetrahedron of Ol-diopside- enstatite- albite in the system of nepheline- diopside- quartz- Ol (Yoder and Tilley 1962). At great depths, Ol and diopside would crystallize from the magmas without plagioclase because plagioclase is not stable under high pressures. The fractional crystallization of Ol and diopside results in the composition of the residual melt migrating towards the quartz apex, causing an enrichment of Si. The evolved Si-rich melt is not equilibrium with Ol and Cpx and may react with earlier formed Ol or Cpx. Therefore, it is not surprising to observe Si-saturated melt replacing Ol during its infiltration through mantle peridotites to form secondary Opx. A similar process of replacement of Ol by Opx was proposed by Arai et al. (2006) in explaining the generation of the Si-saturated evolved alkali basalts that were responsible for Fe-rich orthopyroxenite xenoliths in Takashima, southwestern Japan.

3.6.5. Formation of Grt Orthopyroxenites in the Pali Aike Area

Textural evidence suggests that secondary Opx in our samples formed mostly at the expense of Ol via the reaction:

Ol + melt 1 = Opx + melt 2 (1)

The secondary Opx contains more Fe, Si, Ti, and Al than Ol, and these components were supplied from the melt. Therefore, the protolith of orthopyxroxenites is most likely Grt-bearing harzburgites.

Our proposed interpretation is consistent with microscopic evidence from the orthopyroxenites. They commonly contain small irregularly shaped fragments of harzburgites, which most likely represent a remnant of the original harzburgites.

Orthopyroxenite samples BNH5 and BNH 13 contain relatively high CaO (2.19 and 1.54 wt%, respectively) and relict Cpx and Ol in secondary Opx; the secondary Opx is commonly associated with Ti-Amp. These orthopyroxenites likely formed from Grt-bearing lherzolites. In addition to reaction (1), Cpx in these samples also reacted with the metasomatizing melt, forming Opx:

Cpx + melt 1 = Opx + melt 2 (2)

BN46 contains relict grains of Cpx associated with secondary Opx, but the Opx contains distinctly lower Cr contents (~0.15 wt%) and Mg# (~0.85) than in other samples (Table 3-1; Fig. 3-5). Therefore, BN46 is most likely a metasomatic product of cumulate websterites. Unfortunately, the sample was barely sufficient for thin-section observation and too small to obtain a bulk-rock composition to verify our interpretation.

3.6.6. Mobility of Chalcophile, Siderophile and Other Elements During Metasomatism

Our orthopyroxenite samples show an enrichment of alkalis, Si, Al, Ti, Fe, and H_2O, a minor depletion of Ni, and an essential immobility of Cr and PGE during metasomatism. The enrichment of Si and Al, based on bulk-rock compositions (Fig. 3-6), is reflected by an increased modal abundance of Opx, whereas the enrichment of Ti and Fe is well illustrated by the mineral compositions, since the metasomatic products contain high Ti and Fe, and the rims of relict Cpx are enriched in Ti.

Nickel contents in bulk rock of orthopyroxenites are slightly low compared to peridotites (Fig. 3-7; Table 3-2), but NiO contents in Ol in orthopyroxenites are high, ranging from 0.33 to 0.53 wt% (Fig. 3-3). High NiO in Ol is explained as being due to the high distribution coefficient of Ni between Ol and Opx (Kennedy et al. 1993; Kelemen et al. 1998). During metasomatism, the volume of Ol decreased (<1 vol%), which resulted in a high Ni content in the remaining Ol. Nickel is also present in sulphides, but the amounts of Ni hosted by sulphides are estimated using Ni/S ratios in sulphide grains and the total S contents in the rocks and they are low, 5-70 ppm out of 700-1290 ppm Ni in the bulk rocks. Therefore, the majority of Ni in the rocks is hosted by

silicate minerals. The minor role of sulphides as the host of Ni is consistent with the lack of a positive correlation between S and Ni (Fig. 3-8b).

To evaluate the degree of equilibrium of Ni between sulphides and Ol, apparent distribution coefficients ($D= (Ni/Fe)_{Sulphide}/(Ni/Fe)_{Ol}$) were calculated using the concentrations of Ni in sulphide and Ol, and compared to the equilibrium D value. The sulphides in our samples are predominantly homogeneous Ni-bearing pyrrhotite with minor exsolved phase of either pentlandite (<5 vol% of the total sulphide) or cubanite (<5 vol%). Using the estimated volumes of different phases (observation under microscope) and their Ni contents (microprobe analyses), the Ni content in entire sulphide is estimated to be 13.3-21.6 wt%, which correspond to atomic ratio of 0.26-0.50 Ni/Fe. The atomic Ni/Fe ratios in Ol range from 0.026 to 0.033, which yielded apparent D values of 10-15.2 in our samples.

The equilibrium D for our sample is evaluated using the experimental results by Brenan and Caciagli (2000). The values vary widely, from 8.2 to 73.3, depending on the Ni contents in sulphide and the fO_2. Our samples yielded an equilibrium temperature of 1100 °C and an fO_2 near the FMQ buffer (Wang et al. 2006). Under the given fO_2 and the Ni contents (13-22 wt%) in sulphides, the equilibrium D is estimated to be 9.9-16. The values are similar to the estimated apparent D values and this excellent agreement between apparent and equilibrium D values for Ni between sulphides and Ol suggests that sulphide liquid was in fact in equilibrium with relict Ol.

The concentrations of PGE and their primitive mantle-normalized patterns of PGE for orthopyroxenites are similar to those of anhydrous Grt-spinel lherzolite samples (e.g. BN73 and LS1) and other metasomatized Grt-bearing samples (Fig. 3-7). Furthermore, the PGE abundance and patterns are also comparable with mantle peridotites in other areas, e.g. lherzolitic massifs from Ronda and Beni Bousera (Gueddari et al. 1996; Fig. 3-7b, 3-7c). The data suggest that metasomatism did not greatly modify the abundance of PGE, particularly Ir-type PGE. Palladium shows minor scatter in its concentrations in several samples (Fig. 3-7), consistent with the high

mobility of PGE in aqueous fluids (e.g. Hinchey and Hattori 2005). The immobility of Ir-type PGE suggests that they are useful to evaluate the protoliths of metasomatized ultramafic rocks.

In mantle peridotites, sulphides are considered to be the host of PGE (e.g. Hart and Ravizza 1996) because of the extremely high partition coefficients, > 1000, for PGE between sulphide and silicate melt (e.g. Crocket et al. 1997; Fleet et al. 1996). This interpretation is not applicable to our rocks because several Grt-bearing peridotite samples (e.g. LS50, PAHK1 and BN45) contain very low contents of S (<10 ppm), yet high total PGE (>20 ppb) (Fig. 3-8a), and PGE contents are independent of S. For example, samples BNH13 and BNH5 contain high S (144 and 138 ppm S, respectively) yet are relatively low in total PGE, 15.8 and 12.9 ppb, respectively, compared with the PGE content of other low S samples. The PGE may occur (a) in platinum group minerals (PGM), such as Ru-Os ± Ir sulfides and Pt-Ir ± Os alloys (Ballhaus et al. 2006; Luguet et al. 2007), and/or (b) in silicate and oxide minerals. Although no direct evidence is available for the first possibility, it was evidenced by a recent sudy that micron to submicron PGM grains located in the intergranular spaces of the base-metal sulfide-free mantle residues (e.g. harzburgites) and accounted for 50-100% of the PGE budget (Luguet et al. 2007).

For the second possibility, it is well known that Ir-type PGE may be incorporated into oxides (e.g. Capobianco et al. 1994; Righter et al. 2004), and also into silicate minerals, particularly under low fO_2, where Ir is mostly Ir^{2+} (Brenan et al. 2005). Since Ir^{2+} has seven electrons in the 5d shell, similar to the electron configuration of Co^{2+}, the two have similar crystal field stabilization energies in the octahedral site of silicate minerals. In addition, Ir^{2+} and Co^{2+} have similar ionic radii (~0.74 Å). Therefore, Ir^{2+} should have a similar compatibility as Co^{2+} with Ol and Opx. In addition, Ni^{2+} (0.69 Å) and Mg^{2+} (0.72 Å) have similar radii to Co^{2+}, and should also have similar compatibilities as Co in the octahedral site. This is confirmed by the experimental work by Brenan et al (2005), which yielded a partition coefficient of ~2 for Ir^{2+} between Ol and silicate melt at fO_2 of FMQ+2.5. The Grt-bearing peridotites in Pali Aike have fO_2 values near FMQ (Wang et al. 2006), which is more reduced than the experimental conditions used by Brenan et al. (2005). Therefore, we can safely conclude that Ir is divalent. Other Ir-type PGE,

such as Os and Ru, are considered to behave like Ir, given the close correlation among Ir-type PGE (Fig. 3-7).

Our interpretation, that PGE resides in silicate and oxide minerals, is consistent with the lack of a significant change in PGE abundances and pattern during metasomatism. Olivine is replaced by Opx during metasomatism and PGE in Ol are likely retained in secondary Opx, which also contains an octahedral site for Mg. Furthermore, a plot of ionic radii and partition coefficients for Opx indicates a broad peak for the octahedral site in "Onuma diagram" (Onuma et al.1968), suggesting that the partition coefficient of Ir^{2+} between Opx and melt is probably high, comparable to that for Mg^{2+}. Melt extraction would preferentially remove Pt-PGE from the mantle residues, whereas later melt infiltration would tend to enrich the depleted harzburgites with Pt-PGE. The two effects may cancel each other, resulting in relatively flat patterns of Pt-type PGE. For example, most Grt orthopyroxenites originated from harzburgites and retained low Pt-type PGE/Ir-type PGE ratios of harzburgites, whereas orthopyroxenite samples BNH5 and BNH13, which originated from lherzolites, show relatively elevated Pt-type PGE/Ir-type PGE ratios (Fig. 3-7a).

Copper is incompatible with mantle minerals and is removed from the residual peridotites during partial melting (e.g. Shirey and Walker 1998). This is confirmed by the low Cu contents in refractory peridotites and a positive correlation between CaO and Cu; peridotites with lower CaO contain lower Cu (e.g. Gueddari et al. 1996; Orberger et al. 1998). Copper contents are mostly about 0.1 to 1 ppm in peridotites containing less than 2 wt % CaO in Beni Bousera, Morocco, and Ronda, Spain (Gueddari et al. 1996). Our Grt-spinel harzburgites contain low CaO, <1.2 wt%, and low Cu, ranging from 1 to 5 ppm (Fig. 3-9b), which is nevertheless greater than the Cu contents of anhydrous harzburgites in Beni Bousera and Ronda. Furthermore, no positive correlation was observed between Cu and CaO in our Grt-spinel harzburgites (Fig. 3-9b), suggesting the Cu contents were brought in after the partial melting process.

Sulfur is also incompatible with mantle minerals and is removed from mantle residual peridotites during partial melting. Not metasomatized Spl harzburgites in Pali Aike area contain

very low S, <8.5 ppm because they were removed during partial melting (Appendix F). On the other hand, metasomatized Grt-Spl harzburgites contain significant amounts of S, 5-25 ppm (Appendix F), suggesting that the contents of S were brought in during the metasomatism.

A weak positive correlation between Cu and S was observed in our Grt orthopyroxenites, and overall their contents are higher than that of Grt-bearing harzburgites, suggesting the two are in the same phase, sulphide, and were introduced during metasomatism (Fig. 3-9a). The correlation between Cu and S is evidenced by exsolution lamellae of cubanite in Ni-bearing pyrrhotite in Grt orthopyroxenite (Fig. 3-2h).

3.6.7. Comparison With Orthopyroxenites in Other Regions

Peridotites in sub-arc mantle are refractory due to partial melting to high degree; Ol in such refractory peridotites contains low Al and high Mg, Fo > 90. Slab-derived melt and aqueous fluids are generally high in Si and low in Cr and Ti. Therefore, secondary Opx formed from Ol by reacting with a slab-derived fluid/melt usually contains low contents of Al_2O_3 (<2 wt%), TiO_2 (<0.1 wt%) and Cr_2O_3 (<0.4 wt%), and has a high Mg# (0.90-0.94), as documented in the Colorado Plateau (Smith and Riter 1997; Smith et al. 1999), Avacha in Russia (Arai et al. 2003) and Iraya in the Philippines (Arai et al. 2004) (Fig. 3-5). Secondary Opx in a phlogopite-bearing orthopyroxenite (Ertan and Leeman 1996) from the Cascades has a lower Mg#, ~ 0.87, comparable to our Opx, but still contains low TiO_2 (~0.06 wt%) and moderate Al_2O_3 (~2.36 wt%); the composition is similar to that of secondary Opx in mantle wedges (Fig. 3-5).

Secondary Opx from Takashima is interpreted to be formed from peridotites through reaction with an evolved alkali basaltic melt (Arai et al. 2006). The participation of such melt is suggested from the high contents of TiO_2 (0.37-0.57 wt%) and Al_2O_3 (5-6 wt%), and the low Mg# (0.73-0.88) and Cr_2O_3 (<0.08 wt%) in Opx (Fig. 3-5).

Our Opx contains relatively high Mg# and low Cr_2O_3, similar to that expected for secondary Opx formed during reaction with slab-derived fluid and/or melt (Fig. 3-5), but our Opx contains

high Ti and Al. The latter feature is similar to Opx formed during the reaction with evolved alkali melt in Takashima.

Peridotites in SCLM in continental rifts and hotspot areas are commonly affected by the upwelling sethenospheric mantle melt. In these tectonic settings, alkali basaltic melt commonly ascended from the asthenospheric mantle to the overlying SCLM. Pervasive infiltration of melt may have resulted in the formation of orthopyroxenites at depth in the SCLM if this melt experienced the similar evolution process as discussed in this study, and these orthopyroxenites may resemble our samples.

3.7. Conclusion

Garnet orthopyroxenite xenoliths are common in the Quaternary Pali Aike volcanic rocks, and contain minor Ti-rich Amp and phlogopite, and abundant relict Ol grains in Opx. The xenoliths were likely produced from Grt-bearing harzburgites during metasomatic replacement of Ol by Opx during reaction with a Ti-rich alkali melt. Injection of the melt also produced veinlets of Grt-bearing orthopyroxenite with diffuse boundaries in harzburgite xenoliths.

The Opx in Grt orthopyroxenites contains relatively high TiO_2 (0.20-0.59 wt%), moderate Al_2O_3 (3.27-5.10 wt%) and Cr_2O_3 (0.15-0.48 wt%), and low MgO (Mg# 0.85-0.88) compared to Grt-bearing peridotites. The compositions are distinctly different from secondary Opx formed from Ol through reaction with slab-fluid and/or melt that was generated in mantle wedges. The metasomatizing agent is most likely an evolved alkali melt that was derived from the underlying asthenospheric mantle.

The orthopyroxenites contain high concentrations of Cr, Ni, and PGE comparable to peridotites, suggesting that these elements were essentially immobile during metasomatism by the evolved asthenospheric melt. The contents of PGE are independent of S and they are most likely present in PGM, silicate and oxide minerals. The evolved asthenospheric melt was saturated with S and brought immiscible sulphide liquid, which resulted in elevated Cu and S in orthopyroxenites.

Acknowledgements

This work is part of the senior author's Ph.D. thesis project, and was financially supported by a NSERC Discovery Grant to KHH and an Ontario Graduate Scholarship in Science and Technology and the University of Ottawa Excellence Scholarship to JW. We thank Charles Stern for providing samples, M. Wilk-Alemany for help of PGE analyses, R. Hartree for XRF analysis, and G. Mrazek for the preparation of sections. Thanks are also given to P. Jones at Carleton University for his help with the electron microprobe analyses.

References

Anhaeusser CR (2001) The anatomy of an extrusive-intrusive Archean mafic-ultramafic sequence: the Nelshoogte schist belt and Stolzburg layered ultramafic complex, Barberton Greenstone belt, South Africa. South Africa J Geol 104:167-204

Arai S, Ishimaru S, Okrugin VM (2003) Metasomatized harzburgite xenoliths from Avacha volcano as fragments of mantle wedge of the Kamchatka arc: an implication for the metasomatic agent. The Island Arc 12:233-246

Arai S, Takada S, Michibayashi K, Kida M (2004) Petrology of peridotite xenoliths from Iraya Volcano, Philippines, and its implication for dynamic mantle-wedge processes. J Petrol 45:369-389

Arai S, Shimizu Y, Morishita T, Ishida Y (2006) A new type of orthopyroxenite xenolith from Takashima, Southwest Japan: silica enrichment of the mantle by evolved alkali basalt. Contrib Mineral Petrol 152:387-398

Ballhaus C, Bockrath C, Wohlgemuth-Ueberwasser C, Laurenz V, Berndt J (2006) Fractionation of the noble metals by physical processes. Contrib Mineral Petrol 152:667-684

Barnes SJ, Roeder PL (2001) The range of spinel compositions in terrestrial mafic and ultramafic rocks. J Petrol 42:2279-2302

Brenan JM, McDonough WF, Ash R (2005): An experimental study of the solubility and

partitioning of iridium, osmium and gold between olivine and silicate melt. Earth Planet Sci Lett 237:855-872

Brenan JM, Caciagli NC (2000) Fe-Ni exchange between olivine and sulphide liquid: Impliations for oxygen barometry in sulphide-saturated magmas. Geochim Cosmochim Acta 64:307-320

Capobianco CJ, Hervig RL, Drake MJ (1994) Experiments on crystal/liquid partitioning of Ru, Rh and Pd for magnetite and hematite solid solutions crystallized from silicate melt. Chem Geol 113:23-43

Cande SC, Leslie RB (1986) Late Cenozoic tectonics of the southern Chile Trench. J Geophys Res 91:471-496

Crocket JH, Fleeet ME, Stone WE (1997) Implications of composition for experimental partitioning of platinum-group elements and gold between sulfide liquid and basalt melt: the significance of nickel content. Geochim Cosmochim Acta 61:4139-4149

Dick HJB, Bullen T (1984) Chromian spinel as a petrogenetic indicator in abyssal and alpine-type peridotites and spatially associated lavas. Contrib Mineral Petrol 86:54-76

D'Orazio M, Agostini S, Mazzarini F, Innocenti F, Manetti P, Haller MJ, Lashsen A (2000) The Pali Aike Volcanic Field, Patagonia: slab-window magmatism near the tip of South America. Tectonophysics 321:407-427

Ertan IE, Leeman WP (1996) Metasomatism of Cascades subarc mantle: evidence from a rare phlogopite orthopyroxenite xenolith. Geology 24:451-454

Fleet ME, Crocket JH, Stone WE (1996) Partitioning of platinum-group elements (Os, Ir, Ru, Pt, Pd) and gold between sulfide liquid and basalt melt. Geochim Cosmochim Acta 60:2397-2412

Fleet ME, Crocket JH, Menghua L, Stone WE (1999) Laboratory partitioning of platinum-group elements (PGE) and gold with application to magmatic sulfide-PGE deposits. Lithos 47:127-144

Francis RD (1990) Sulfide globules in mid-ocean ridge basalts (MORB), and the effect of oxygen abundance in Fe-S-O liquids on the ability of those liquids to partition metals from MORB and komatiite magmas. Chem Geol 85:199-213

Gaetani GA, Grove TL (1997) Partitioning of moderately siderophile elements among olivine, silicate melt, and sulfide melt; constraints on core formation in the Earth and Mars. Geochim Cosmochim Acta 61:1829-1846

Gibson SA, Thompson RN, Dickin AP, Leonardos OH (1995) High-Ti and low-Ti mafic potassic magmas: Key to plume-lithosphere interactions and continental flood-basalt genesis. Earth Planet Sci Lett 136:149-165

Gorring ML, Kays SM, Zeitler PK, Ramos VA, Rubiolo D, Fernandez MI, Panza JL (1997) Neogene Patagonian plateau lavas: Continental magmas associated with ridge collision at the Chile triple Junction. Tectonics 16:1-17

Gorring ML, Kays SM (2001) Mantle processes and sources of Neogene slab window magmas from Southern Patagonia, Argentina. J Petrol 42:1067-1094

Grove TL, Kinzler RJ, Bryan WB (1992) Fractionation of mid-ocean ridge basalts (MORB). Geophys Monogr 71:281-310

Gueddari K, Piboule M, Amossé J (1996) Differentiation of platinum-group elements (PGE) and of gold during partial melting of peridotites in the lherzolitic massifs of the Betico-Rifean range (Ronda and Beni Bousera). Chem Geol 134:181-197

Hart SR, Ravizza G (1996) Os partitioning between phases in lherzolite and basalt, in: Basu A, Hart SR (Eds), Earth Processes: Reading the Isotopic Code. Am Geophys Union Geophys Monogr 95:123-134

Hammond PA, Taylor LA (1982) The ilmenite/titano-magnetite assemblage: Kinetics of re-equilibration. Earth Planet Sci Lett 61:143-150

Hattori KH, Arai S, Clarke DB (2002): Selenium, tellurium, arsenic and antimony contents of primary mantle sulfides. Can Mineral 40:637-650

Hinchey JG, Hattori KH (2005) Magmatic mineralization and hydrothermal enrichment of the High Grade Zone at Las des Iles palladium mine, northern Ontario, Canada. Mineralium Deposita 40:13-23

Kelemen PB, Hart SR, Bernstein S (1998) Silica enrichment in the continental upper mantle via melt/rock reaction. Earth Planet Sci Lett 164:387-406

Kennedy AK, Lofgren GE, Wasserburg GJ (1993) An experimental-study of trace-element partitioning between olivine, orthopyroxene and melt in chondrules - equilibrium values and kinetic effects. Earth Planet Sci Lett 115:177-195

Kesson SE, Ringwood AE (1989) Slab-mantle interactions: 2. The formation of diamonds. Chem Geol 78: 97-118

Kilian R, Stern CR (2002) Constraints on the interaction between slab melts and the mantle wedge from adakitic glass in peridotite xenoliths. Eur J Mineral 14: 25-36

Leake BE et al (1997) Nomenclature of amphiboles: report of the subcommittee on amphiboles of the international mineralogical association, commission on new minerals and mineral names. Can Mineral 35:219-246

Liu YS, Gao S, Lee CTA, Liu XM, Yuan HL (2005) Melt-peridotite interactions: Links between garnet pyroxenite and high-Mg# signature of continental crust: Earth Planet Sci Lett 234:39-57

Luguet A, Shirey SB, Lorand J-P, Horan MF, Carlson RW (2007) Residual platinum-group minerals from highly depleted harzburgites of the Lherz massif (France) and their role in HSE fractionation of the mantle. Geochim Cosmochim Acta 71:3082-3095

Maaløe S (2005) The dunite bodies, websterite and orthopyroxenite dikes of the Leka ophiolite complex, Norway. Mineral Petrol 85:163-204

Malaspina N, Hermann J, Scambelluri M, Compagnoni R (2006) Polyphase inclusions in garnet-orthopyroxenite (Dabie Shan, China) as monitors for metasomatism and fluid-related trace element transfer in subduction zone peridotite. Earth Planet Sci Lett 249:173-187

McDonough WF, Sun SS (1995) The composition of the Earth. Chem Geol 120:223-253

McInnes BIA, Gregoire M, Binns RA, Herzig PM, Hannington MD (2001) Hydrous metasoamtism of oceanic sub-arc mantle, Lihir, Papua New Guinea: Petrology and geochemistry of fluid-metasomatised mantle wedge xenoliths. Earth Planet Sci Lett 188:169-183

Niu YL (2004) Bulk-rock major and trace element compositions of abyssal peridotites: implications for mantle melting, melt extraction and post-melting processes beneath mid-ocean ridges. J Petrol 45: 2423-2458

Orberger B, Xu Y, Reeves SJ (1998) Platinum group elements in mantle xenoliths from eastern China. Tectonophysics 296:87-101

Onuma N, Higuchi H, Wakita H (1968) Trace element partition between two pyroxenes and the host lava. Earth Planet Sci Lett 5:47-51.

Prouteau G, Scaillet B, Pichavant M, Maury RC (1999) Fluid-present melting of ocean crust in subduction zones. Geology 27:1111-1114

Ramos VA, Kay SM (1992) Southern Patagonian plateau basalts and deformation: backarc testimony of ridge collision. Tectonophysics 205:261-282

Ravizza G, Pyle D (1997) PGEs and Os isotopic analyses of single sample aliquots with NiS fire assay preconcentration. Chem Geol 141:251-268

Righter K, Campbell M, Humayun M, Hervig MRL (2004) Partitioning of Ru, Rh, Pd, Re, Ir and Au between Cr-bearing spinel, olivine, pyroxene and silicate melts. Geochim Cosmochim Acta 68:867-880

Roeder PL, Emslie RF (1970) Olivine-liquid equilibrium. Contrib Mineral Petrol 29:275-289

Rose LA, Brenan JM (2001) Wetting properties of Fe-Ni-Co-Cu-O-S melts against olivine; implications for sulfide melt mobility. Econ Geol 96:145-157

Shirey SB, Walker RJ (1998) The Re-Os isotope system in cosmochemistry and high temperature geochemistry. Annu Rev Earth Planet Sci 26:423-500

Smith D, Riter JCA (1997) Genesis and evolution of low-Al orthopyroxenite in spinel peridotite xenoliths, Grand Canyon field, Arizona, USA. Contrib Mineral Petrol 127:391-404

Smith D, Riter JCA, Mertzman SA (1999) Water-rock interactions, orthopyroxene growth and Si-enrichment in the mantle: evidence in xenoliths from the Colorado Plateau, southwestern United States. Earth Planet Sci Lett 165:45-54

Stern CR, Kilian R, Olker B, Hauri EH, Kyser TK (1999) Evidence from the mantle xenoliths for relatively thin (<100 km) continental lithosphere below the Phanerozoic crust of southernmost South America. Lithos 48:217-235

Toplis MJ (2005) The thermodynamics of iron and magnesium partitioning between olivine and liquid: criteria for assessing and predicting equilibrium in natural and experimental systems. Contrib Mineral Petrol 149:22-39

Wang J, Hattori K, Li J-P (2006) Oxidation state of subcontinental lithospheric mantle below the southern South America. Eos Trans AGU 87(36), Western Pacific Geophys Meet Suppl Abstract V41B-0196

Wang J, Hattori KH, Kilian R, Stern CR (2007) Metasomatism of sub-arc mantle peridotites below southernmost South America: reduction of fO2 by slab-melt. Contrib Mineral Petrol 153:607-624

Willmore CC, Boudreau AE, Kruger FJ (2000) The halogen geochemistry of the Bushveld Complex, Republic of South Africa: Implications for chalcophile element distribution in the Lower and Critical Zones. J Petrol 41:1517-1539

Yoder HS, Tilley CE (1962) Origin of basalt magmas: an experimental study of natural and synthetic rock system. J Petrol 3:342-532

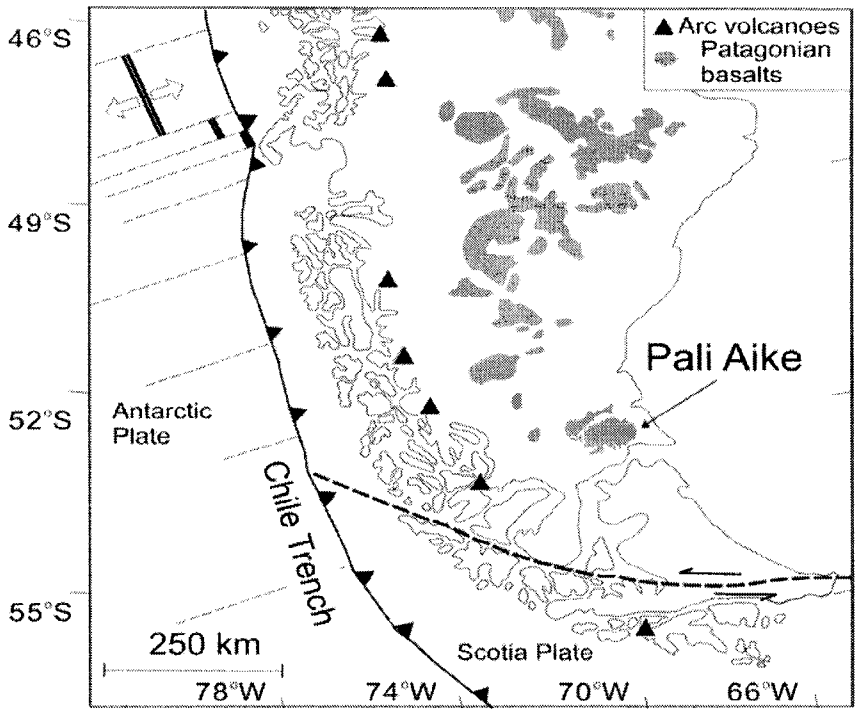

Figure 3-1 Map of southern South America, showing the locations of the Quaternary alkali basalt fields of Pali Aike and other late Cenozoic basalts of Patagonian plateau. Also shown are volcanoes of the Andean Austral Zone (AVZ) (modified after Kilian and Stern 2002)

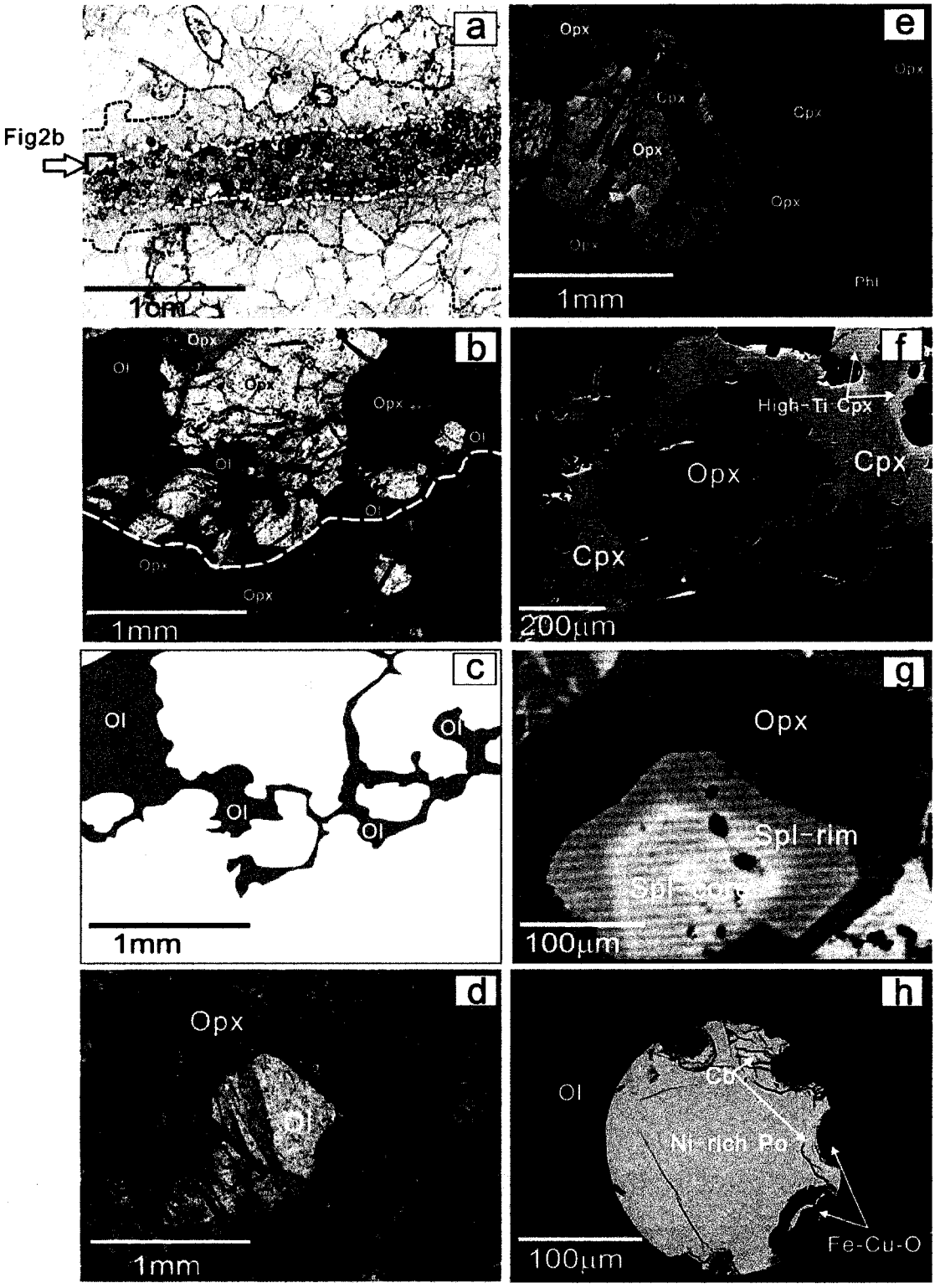
Fig2b
a
1cm
b
Opx
Ol
1mm
c
Ol
1mm
d
Opx
Ol
1mm
e
Opx
Cpx
Phl
1mm
f
High-Ti Cpx
Opx
Cpx
200μm
g
Opx
Spl-rim
100μm
h
Ol
Ni-rich Po
Fe-Cu-O
100μm

Figure 3-2 a Photograph of an orthopyroxenite veinlet in Grt-spinel harzburgite (sample BN92). The veinlet (shown with white dashed lines) is accompanied by metasomatic halos (outer margins shown with black dashed lines). Red = garnet, opaque minerals = ilmenite, yellow green = orthopyroxene, and transparent = olivine. Square in the middle left, at the contact between veinlet and halo, is shown in Fig. 3-2b. **b** Photomicrograph of the square in Fig. 3-2a under cross polarized light. Optically continuous relict olivine (Ol) grains occur in and along Opx grains and across the boundary of veinlet. The boundary of the veinlet and the metasomatic halo is shown with a thick white dashed line. Note the texture suggests that the veinlets were the foci of the injection of a metasomatic agent that resulted in the replacement of Ol by Opx.
c The outlines of the relict Ol grains shown in Fig. 3-2b. **d** Photomicrograph of orthopyroxene (Opx) enclosing a relict Ol grain in orthopyroxenite (sample BNC1). Note cloudy secondary Opx with abundant fluid inclusions. **e** Photomicrograph of secondary Opx enclosing relict clinopyroxene (Cpx) in orthopyroxenite under cross polarized light (sample BN46). Note the ~ 120 ° angle at triple junctions of grain boundaries of the secondary Opx in the upper part of the photograph. **f** Back-scattered electron image of a narrow (<200 μm) band of relict Cpx along newly formed Opx. Note the bright parts in the Cpx are high in Ti and low in Mg compared to darker parts. **g** Back-scattered electron image of a zoned spinel enclosed in secondary Opx in orthopyroxenite (sample BNC2). The rim is rich in Al (darker, Cr# = 0.035) compared to Cr-rich core (Cr# = 0.048). **h** Back-scattered electron image of a sulphide bleb in Opx in the veinlet of orthopyroxenite (sample BN92). Note cubanite (Cb) exsolutions at the margin areas of Ni-bearing pyrrothite (Po). The dark areas on the margin of the sulphide grain are Fe-Cu oxides.

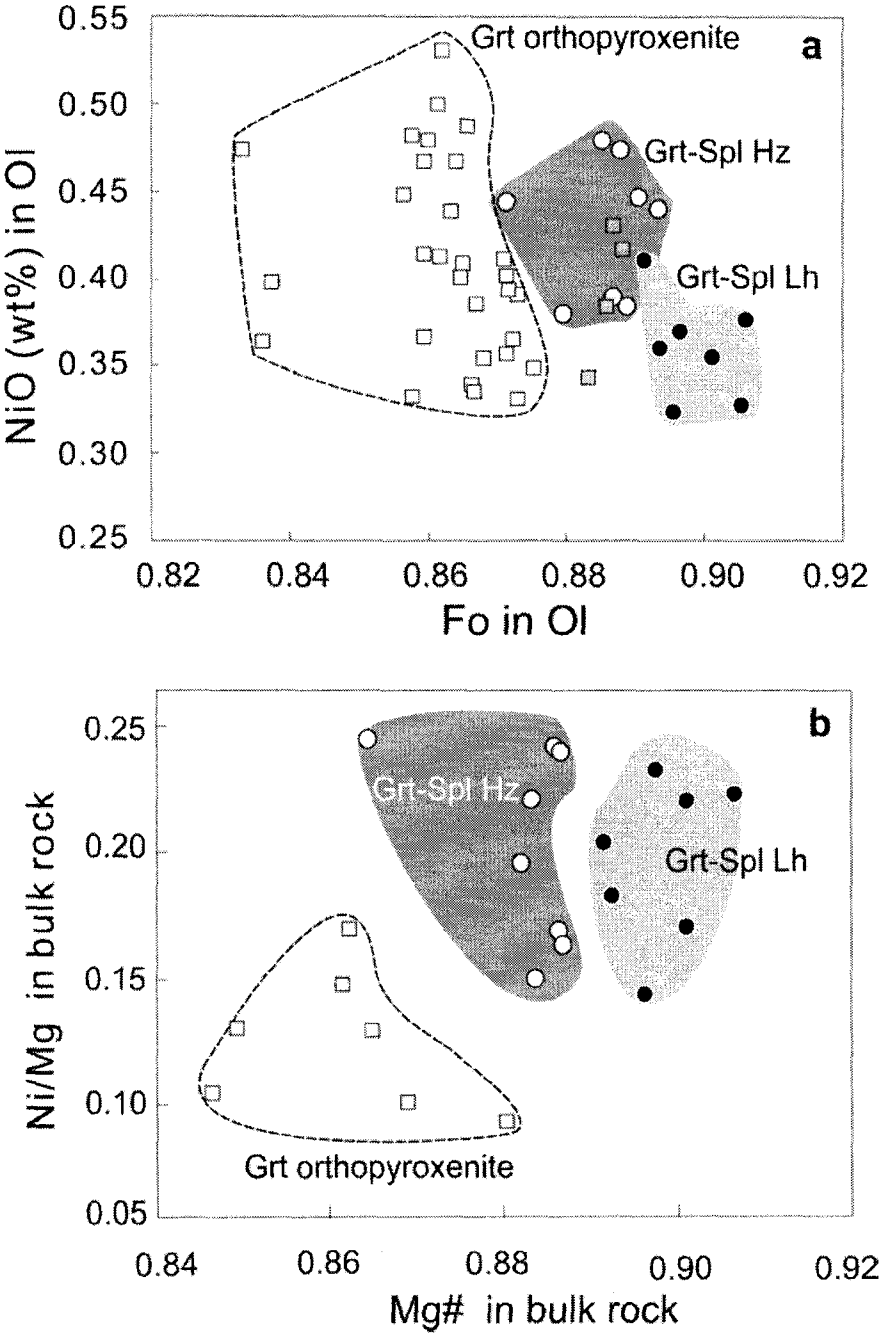

Figure 3-3 Plot of (a) NiO (wt%) in Ol vs. Fo for olivines and (b) Ni/Mg vs. Mg# for bulk rocks. Filled circles = garnet-spinel lherzolites (Grt-Spl Lh), open circles = garnet-spinel harzburgites (Grt-Spl Hz), open squares = Grt orthopyroxenites, filled squres = veinlet of Grt orthopyroxenites.

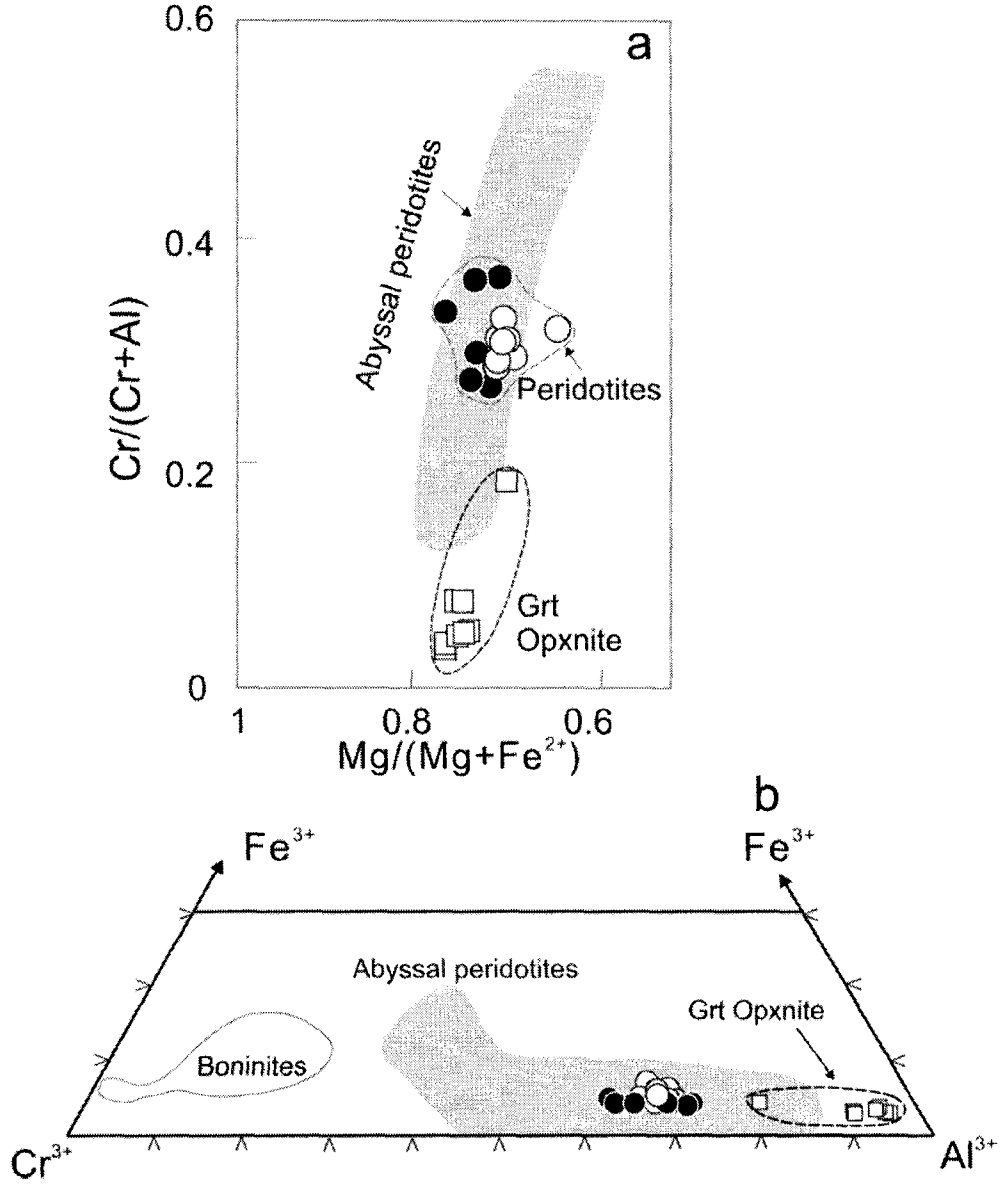

Figure 3-4 Binary (Cr# vs. X_{Mg}) and ternary (Fe^{3+}- Cr^{3+} - Al^{3+}) diagrams for chromite in the Grt orthopyroxenites (Grt Opxnite) and other Grt-bearing peridotites xenoliths from Pali Aike. Symbols are the same as in Fig. 3-3. Each data point represents one grain. Chromite grains are rare in Grt orthopyroxenites and found only in two samples (BNH 5, BNC2). These grains in orthopyroxenites show compositional variations, same as in Fig. 3-2g, but the differences between cores and rims are too small to be shown in the diagram. Note that these chromite grains in Grt orthopyroxenites contain low Cr^{3+} and Fe^{3+}. Data sources: abyssal peridotites (Dick and Bullen 1984; Barnes and Roeder 2001), boninite (Barnes and Roeder 2001).

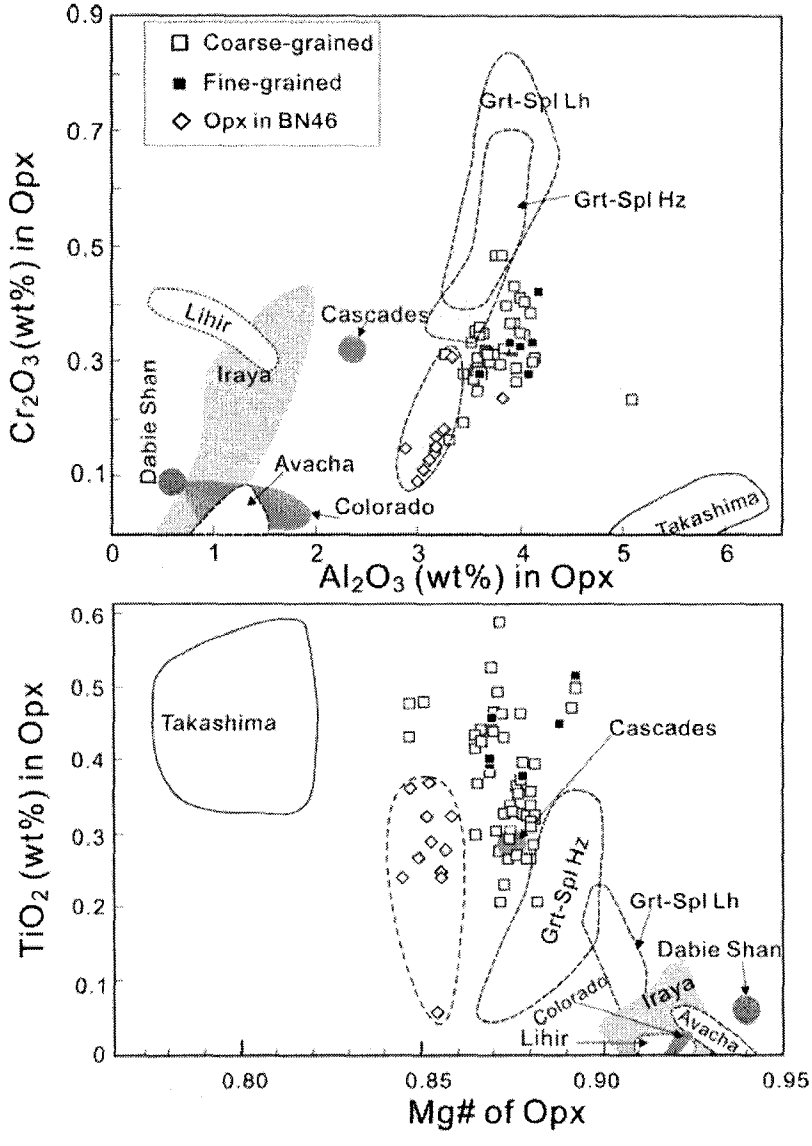

Figure 3-5 Relationships between Al_2O_3 vs. Cr_2O_3 and TiO_2 versus Mg# of secondary orthopyroxene in peridotites and orthopyroxenites. Open squares = coarse grains, filled squares = fine grains, and diamonds = grains in sample BN46. Note that orthopyroxene in Grt orthopyroxenite has a different composition from orthopyroxenes in Grt-bearing peridotites from the area, and secondary orthopyroxenes replacing olivine in mantle wedges. Data source Avacha, Russia (Arai et al. 2003), Iraya, Philippines (Arai et al. 2004), Takashima, Japan (Arai et al. 2006), Cascades, USA (Ertan and Leeman 1996), Colorado Plateau, USA (Smith et al. 1999), Dabie Shan, China (Malaspina et al. 2006) and Lihir, Papua New Guinea (McInnes et al. 2001). Orthopyroxenites in Dabie Shan formed in mantle wedge below the North China craton during the subduction of the Yangtze craton (Malaspina et al. 2006). Symbols are the same as in Fig. 3-3.

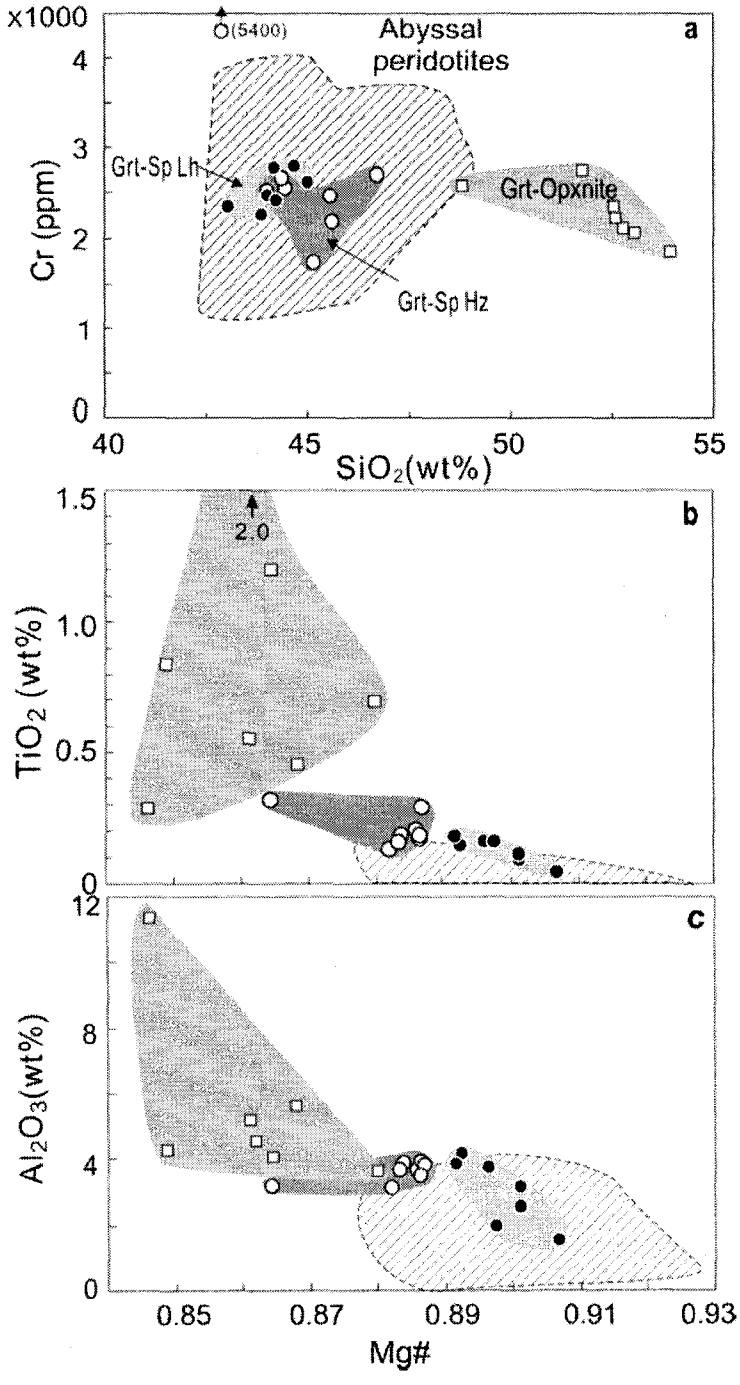

Figure 3-6 Bulk chemical compositions of mantle xenoliths from the Pali Aike area. (a) Cr vs. SiO_2, (b) TiO_2 vs. Mg#, and (c) Al_2O_3 vs. Mg# (= Mg/(Mg + total Fe). Oblique hatched areas are abyssal peridotites (Niu 2004). Symbols are the same as in Fig. 3-3.

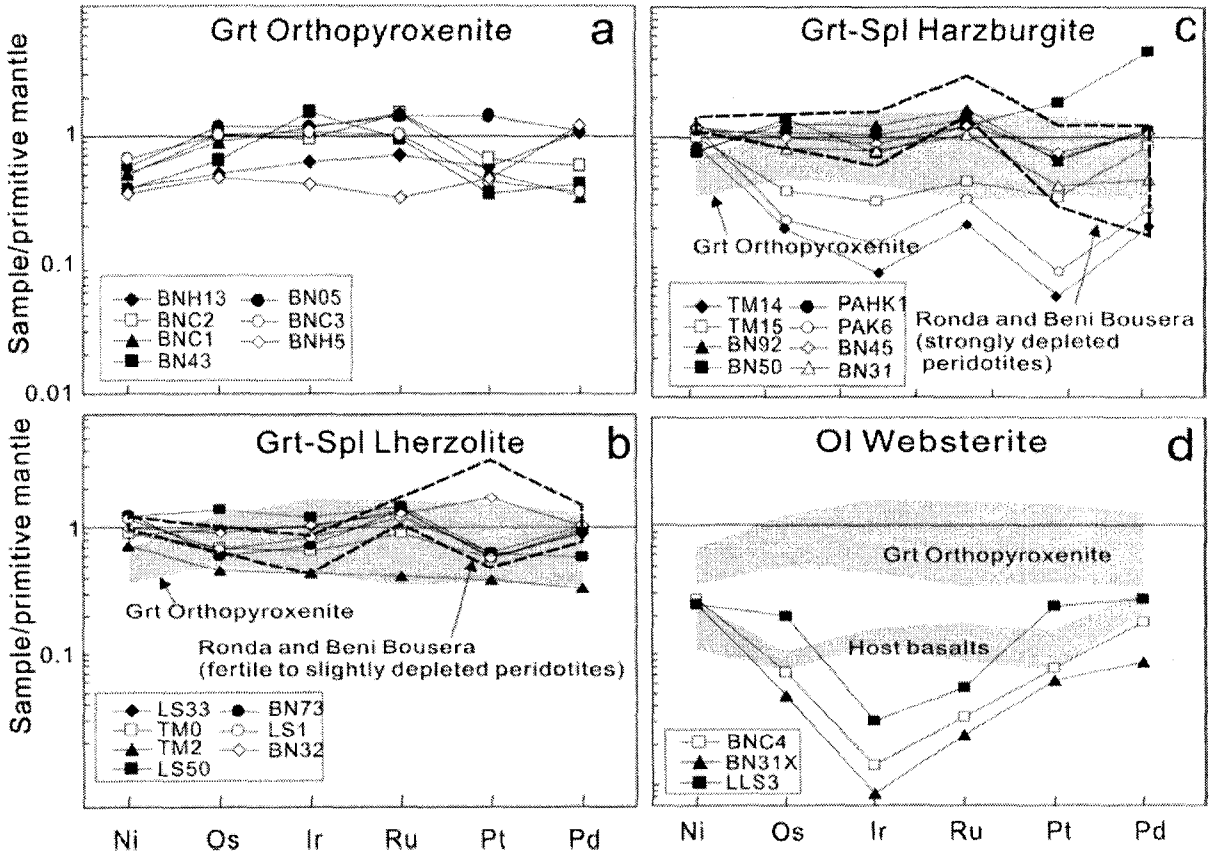

Figure 3-7 Primitive mantle-normalized platinum-group elements of mantle xenoliths. (a) Grt orthopyroxenite; (b) Grt-Spl lherzolite; (c) Grt-Spl harzburgite; (d) Ol websterite. Note that shaded area in (b) and (c) is the field of Grt orthopyroxenite, and that shaded areas in (d) are the fields for Grt orthopyroxenites and host basalts. The data of peridotites from Ronda and Beni Bousera are from Gueddari et al. (1996). Primitive mantle values are from McDonough and Sun (1995).

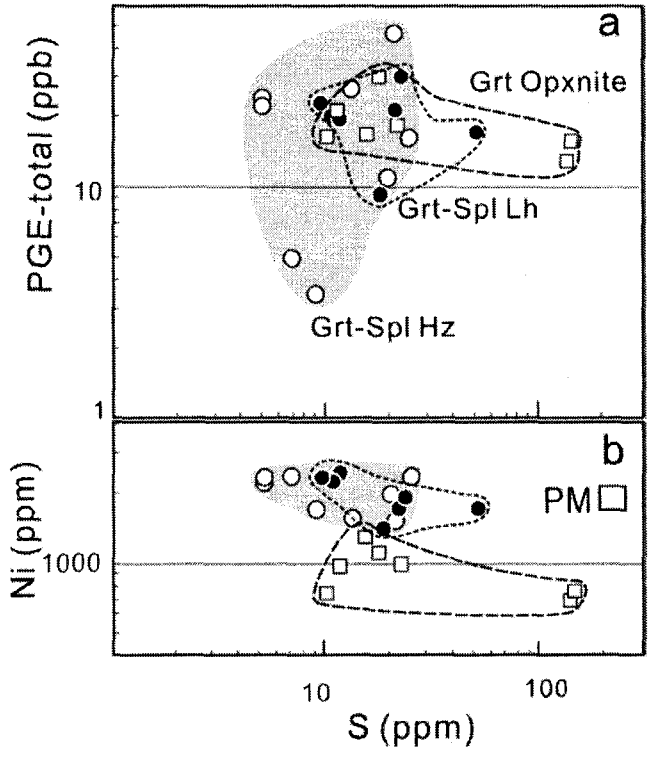

Figure 3-8 Plot of (a) PGE-total vs. S, and (b) Ni vs. S. Symbols are the same as in Fig. 3-3 Primitive mantle values are from McDonough and Sun (1995). Data for Grt-Spl Lh and Grt-Spl Hz are from this study.

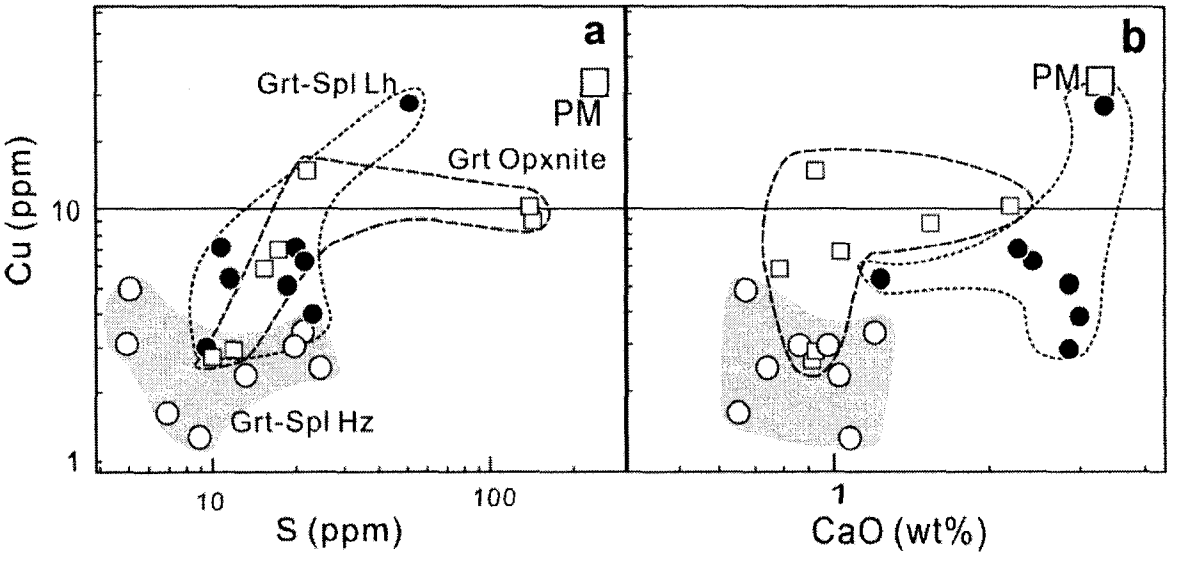

Figure 3-9 Plot of (a) Cu vs. S, and (b) Cu vs. CaO. Symbols are the same as in Fig. 3-3. Primitive mantle values are from McDonough and Sun (1995). Data for Grt-Spl Lh and Grt-Spl Hz are from this study.

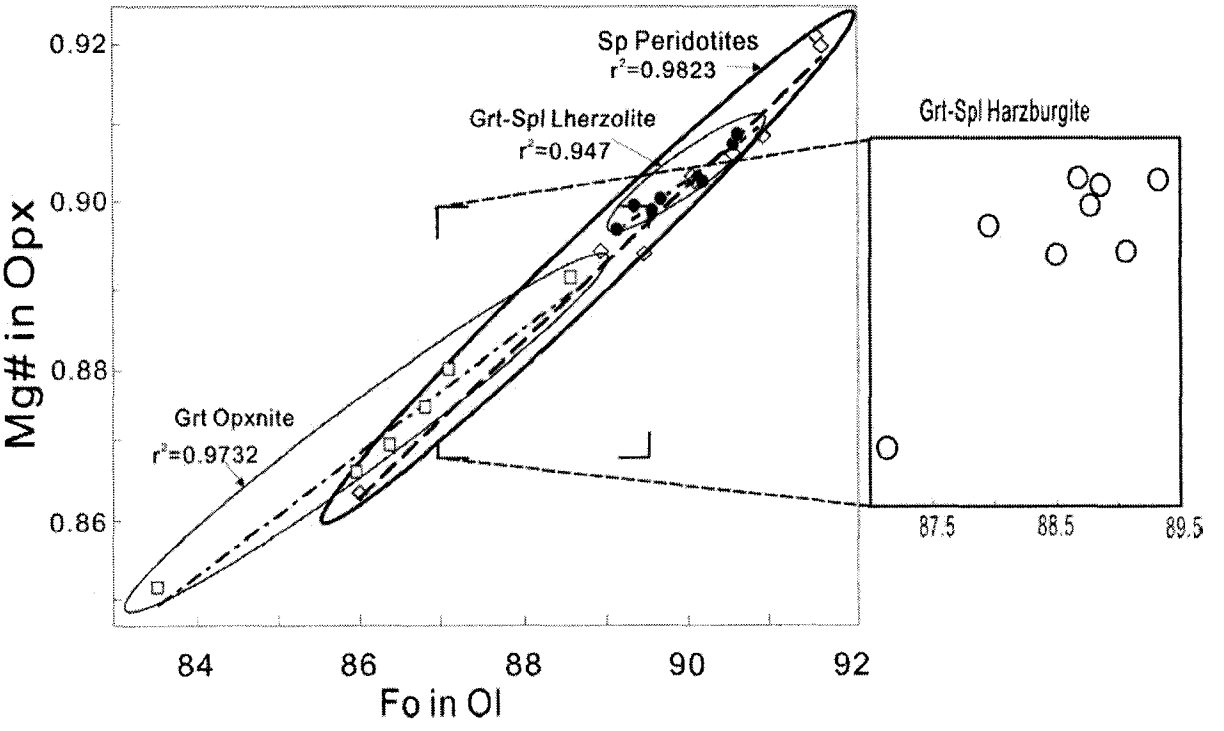

Figure 3-10 Mg# in Opx vs. Fo in Ol for mantle xenoliths from Pali Aike. Data for Grt-Spl lherzolite, Grt-Spl harzburgite ans Sp peridotite are from this study. Note that different lithologies in Pali Aike show a good positive correlation ranging from r^2=0.947 to r^2=0.9823 between Mg# in Opx and Fo in Ol except several samples in Grt-Spl harzburgites. This positive correlation suggests that minerals are in equilibrium within orthopyroxenites and most other lithologies and provides the basis for calculating Mg# of the metasomatizing agent.

Table 3-1 Representative compositions of minerals in garnet orthopyroxenites from Pali Aike

Sample	BN46						BNH5							BN43				
Phase [a]	Opx-C	Opx-R	Opx-f	Grt	Cpx	Ti-Phl	Opx-C	Opx-R	Opx-f	Cpx-C	Cpx-R	Grt	Spl	Ol-C	Ol-R	Ol-f	Opx-C	Opx-R
Host					Opx					Opx			Grt	Opx				
SiO_2	56.25	56.62	56.21	41.94	52.45	38.68	55.89	56.08	55.58	52.62	53.26	41.99	0.02	40.03	39.99	39.96	54.25	55.33
TiO_2	0.37	0.32	0.36	0.20	1.07	5.23	0.26	0.40	0.38	0.65	1.04	0.18	0.48	0.06	<0.04	<0.04	0.31	0.36
Al_2O_3	3.17	3.12	3.00	23.27	5.73	16.21	3.64	3.62	3.61	5.51	5.77	23.89	57.82	0.03	0.04	0.06	3.64	3.75
Cr_2O_3	0.15	0.13	0.09	0.46	0.31	0.33	0.35	0.30	0.28	0.39	0.44	0.39	7.29	<0.03	0.05	<0.03	0.28	0.31
FeO(t)[c]	9.51	9.04	9.84	11.84	5.12	6.19	7.69	7.83	8.02	3.96	4.02	9.61	14.18	12.20	12.33	12.99	7.77	7.83
MnO	0.13	0.13	0.18	0.38	0.11	<0.03	0.06	0.08	0.11	0.06	0.06	0.30	<0.03	0.13	0.10	0.14	0.14	0.13
MgO	30.73	30.81	30.55	18.58	14.67	18.99	31.75	31.76	32.39	15.12	14.84	20.11	19.69	47.05	46.85	47.36	32.11	32.33
CaO	0.81	0.82	0.83	4.82	18.51	0.07	0.56	0.58	0.54	17.32	17.57	4.03	<0.01	0.06	0.10	0.08	0.58	0.61
Na_2O	0.13	0.11	0.15	0.03	2.19	0.75	0.12	0.12	0.19	1.86	1.83	0.05	0.02	0.02	0.03	0.04	0.17	0.16
NiO	0.08	0.11	0.03	0.02	0.03	<0.01	0.16	0.14	0.27	<0.03	0.05	0.03	0.44	0.33	0.40	0.34	0.22	0.22
K_2O						9.17												
Cl						0.02												
F						0.18												
Total	101.3	101.2	101.2	101.5	100.2	95.81	100.5	100.9	101.4	97.48	98.87	100.6	99.94	99.91	99.90	101.0	99.46	101.0
Mg# [d]	0.852	0.859	0.847	0.737	0.836	0.846	0.880	0.879	0.878	0.872	0.868	0.789	0.760	0.873	0.871	0.867	0.881	0.880
Cr# [e]													0.078					

Table 3-1 Continued

Sample	BNO5					BNC1							BNC2					
Phase [a]	Ol-C	Ol-R	Grt	Opx-C	Opx-R	Ol-C	Ol-R	Ol-f	Opx-C	Opx-R	Opx-f	Cpx-f	Ol-f	Opx	Spl-C	Spl-R	Ti-Amp	Ti-Phl
Host	Opx					Opx												
SiO_2	40.91	41.05	42.45	55.52	55.40	40.81	40.97	40.97	55.19	54.84	55.38	51.60	39.92	54.34	0.15	0.17	54.07	37.38
TiO_2	<0.04	0.07	0.42	0.30	0.42	0.07	0.06	0.08	0.44	0.43	0.46	1.42	0.12	0.43	0.73	0.74	4.83	7.13
Al_2O_3	0.04	0.04	23.36	3.77	4.10	0.06	0.04	0.07	4.01	4.01	4.00	6.60	0.06	3.80	59.42	61.57	15.38	15.18
Cr_2O_3	<0.03	0.03	0.97	0.48	0.38	<0.03	<0.03	0.03	0.33	0.35	0.33	1.01	<0.03	0.30	4.43	3.30	0.03	0.60
FeO(t)[c]	13.24	13.44	9.19	8.29	8.69	13.11	13.55	13.61	8.45	8.56	8.43	4.58	15.42	9.71	15.42	13.92	5.24	6.69
MnO	0.09	0.13	0.32	0.12	0.11	0.14	0.15	0.05	0.24	0.23	0.20	0.06	0.19	0.17	0.17	0.09	0.06	0.04
MgO	46.27	46.35	20.32	31.41	31.34	46.76	46.48	46.08	31.79	31.34	31.66	14.83	44.11	30.17	19.59	20.64	3.58	17.37
CaO	0.11	0.17	3.99	0.78	0.78	0.09	0.10	0.10	0.72	0.82	0.81	17.37	0.09	0.76	0.01	0.02	5.87	0.04
Na_2O	<0.02	0.03	0.10	0.12	0.16	0.04	<0.02	0.03	0.20	0.20	0.22	2.18	<0.02	0.23	0.01	0.02	3.28	0.59
NiO	0.41	0.48	<0.02	0.15	0.09	0.47	0.37	0.33	0.06	0.14	0.17	0.17	0.36	0.09	0.35	0.30	0.15	0.20
K_2O																	5.65	9.85
Cl																	<0.02	<0.02
F																	0.04	0.28
Total	101.1	101.8	101.1	100.9	101.5	101.6	101.7	101.4	101.4	100.9	101.7	99.83	100.3	99.99	100.3	100.8	98.18	95.49
Mg# [d]	0.862	0.860	0.798	0.871	0.865	0.864	0.859	0.858	0.870	0.867	0.870	0.852	0.836	0.847	0.745	0.771	0.550	0.822
Cr# [e]															0.048	0.035		

Table 3-1 Continued

Sample	BN92[b]				BNH13						
Phase [a]	Ol-f	Opx-f	Cpx-f	Mg-Ilm	Ol-C	Ol-R	Ol-f	Cpx-f	Opx-C	Opx-R	Ti-Amp
Host					Opx						
SiO_2	41.12	54.93	52.03	<0.04	40.53	41.41	40.66	51.13	56.41	55.50	56.04
TiO_2	<0.04	0.45	1.59	55.09	<0.04	<0.04	<0.04	1.42	0.23	0.20	3.38
Al_2O_3	0.02	4.18	6.33	1.38	<0.02	0.02	0.02	7.55	3.27	3.61	19.24
Cr_2O_3	<0.03	0.42	0.34	1.84	<0.03	<0.03	<0.03	0.72	0.31	0.36	0.01
FeO(t) [c]	11.13	7.12	3.96	26.89	12.95	12.96	12.19	4.04	8.06	8.16	5.04
MnO	0.13	0.12	0.07	0.34	0.13	0.10	0.09	0.06	0.10	0.13	0.12
MgO	47.20	31.74	14.58	13.66	45.94	46.54	46.12	14.18	31.10	31.24	3.23
CaO	0.08	0.73	19.44	0.02	0.05	0.05	0.08	18.79	0.66	0.64	7.31
Na_2O	<0.02	0.11	1.73	0.01	<0.02	0.02	0.02	1.84	0.15	0.16	0.98
NiO	0.34	0.11	0.17	0.24	0.44	0.41	0.41	0.05	0.13	0.11	0.01
K_2O											1.53
Cl											0.10
F											0.16
Total	100.0	99.91	100.2	99.46	100.0	101.5	99.63	99.77	100.4	100.1	97.13
Mg# [d]	0.883	0.888	0.868	0.475	0.863	0.865	0.871	0.862	0.873	0.872	0.533
Cr# [e]											

[a] Ol= olivine, Opx =orthopyroxene, Cpx= clinopyroxene, Ilm=ilmenite, Grt =garnet, Phl=phlogopite, Amp= amphibole, Spl= spinel
C =core of coarse grain, R= rim of coarse grain, f= fine-grain along grain boundaries.

[b] Garnet-bearing orthopyroxenite veinlet in BN92

[c] Total Fe as FeO

[d] Mg# = Mg/(Mg + total Fe) for all minerals except for spinel. Mg# for spinel is $Mg/(Mg + Fe^{2+})$ in which Fe^{2+} is calculated assuming stoichiometric composition

[e] Cr# = Cr/(Cr + Al)

Table 3-2 Major elements and selected trace elements abundances of selected samples of Grt orthopyroxenites and host basalts

Rock type	Grt orthopyroxenite							Basalt	
Sample	BN43	BNC1	BNC2	BNC3	BNO5	BNH5	BNH13	LLS-1(v)	TM-15(v)
Major elements in wt%									
SiO_2	53.95	52.76	53.02	51.74	52.53	48.80	52.58	44.59	41.72
TiO_2	0.70	1.20	0.84	2.00	0.55	0.29	0.46	3.46	2.60
Al_2O_3	3.62	4.05	4.28	4.57	5.22	11.34	5.65	11.32	9.06
$Fe_2O_3(t)$[a]	8.64	9.53	10.56	9.74	9.69	9.66	9.07	13.29	12.63
MnO	0.12	0.11	0.13	0.12	0.13	0.19	0.14	0.17	0.18
MgO	31.93	30.71	29.93	30.68	30.34	26.80	30.24	10.85	17.10
CaO	0.91	0.93	0.92	0.78	1.04	2.19	1.54	8.74	9.06
Na_2O	<0.05	<0.05	<0.05	<0.05	<0.05	<0.05	<0.05	3.05	2.96
K_2O	0.02	0.02	0.14	0.03	0.02	<0.02	0.27	1.95	1.66
P_2O_5	0.02	0.02	0.02	0.02	0.01	0.05	0.03	0.75	0.99
Total	100.1	99.64	100.2	100.0	99.87	99.61	100.2	98.44	98.31
Mg# [b]	0.880	0.865	0.849	0.862	0.861	0.846	0.868	0.618	0.728
Trace elements in ppm									
Cr	1840	2130	2060	2740	2350	2580	2220	313	650
Ni	743	991	971	1292	1114	698	761	204	497
S	10.12	22.10	11.53	15.19	17.41	138.1	144.0	nd	nd
Cu	2.74	14.05	2.88	5.95	6.93	10.26	8.95	nd	nd
Platinum-group elements in ppb									
Os	2.30	3.17	3.62	3.57	4.17	1.69	1.79	0.27	0.37
Ir	4.99	3.78	3.07	3.53	3.81	1.37	2.07	0.38	0.52
Ru	4.82	7.61	7.59	5.23	7.22	1.70	3.63	0.45	0.88
Pt	2.60	3.77	4.78	3.25	10.25	3.41	4.13	0.55	1.13
Pd	1.68	1.36	2.35	1.44	4.31	4.76	4.22	0.86	1.27
Ru/Ir	0.97	2.01	2.47	1.48	1.89	1.24	1.76	1.18	1.69
Pd/Ir	0.34	0.36	0.77	0.41	1.13	3.49	2.04	2.25	2.45
(Pt+Pd)/(Os+Ir)	0.59	0.74	1.07	0.66	1.83	2.67	2.17	2.17	2.70
PGE-total	16.38	19.69	21.41	17.01	29.76	12.92	15.84	2.51	4.18

nd not determined

[a] Total Fe as Fe_2O_3

[b] Mg# = Mg/(Mg+ΣFe)

CHAPTER 4

Conclusions

Conclusions (I): Cerro del Fraile area

a) Mantle peridotites from Cerro del Fraile were classified into C- and F-types according to grain size and texture. Both C- and F-type xenoliths contain patch "melt" with pargasitic amphibole compositions. Amphibole in C-type xenoliths contain high Ti and originated from spinel by reacting with an asthenosphere-derived high Ti melt. Amphibole in F-type xenoliths contain high Ca, low Mg and Ti, and formed from clinopyroxene by reacting with a slab-melt.

b) C-type xenoliths formed at mantle wedge environment and suffered cryptic metasomatism by aqueous fluids released from the subducted Nazca slab; F-type formed from mantle wedge peridotites by reacting with slab-melt during late Miocene when Chile ridge arrived and Nazca plate was young and hot.

e) C-type xenoliths are slightly oxidized at above FMQ; F-type xenoliths are relatively reduced (FMQ-1.1). The relatively low fO_2 in F-type xenoliths is explained by the fusion of organic-rich sediments overlying the slab during the slab melt. The fusion of such wet sediments produced CH_4-rich fluids and reduced melts, that mixed with the slab melt.

Conclusions (II): Pali Aike area

a) The values of fO_2, FMQ-0.33 to +0.75, for the entire peridotite samples are comparable to those for abyssal peridotites. The fO_2 data, together with the bulk rock, major- and trace-element data, suggest that the Patagonian subcontinental mantle lithosphere formed through the accretion of oceanic lithosphere.

b) Garnet facies xenoliths formed from spinel facies peridotites due to cooling and/or increasing pressure during or after stablization below the Paleozoic continental crust.

c) Asthenosphere-derived Ti-rich melt was responsible for the metasomatism of garnet-bearing and –free peridotites and the formation of orthopyroxenites. The metasomatizing melt is characterized by high Al, Si, Ti and Fe, and low fO_2, FMQ-0.50.

d) The transformation processes from spinel facies to garnet facies and the infiltration of metasomatizing agent were not accompanied by significant change of oxidation state.

e) The orthopyroxene in orthopyroxenites contains high Ti and low Mg compared with garnet-bearing peridotites in the area. They are high in Al and low in Mg when compared with secondary orthopyroxene formed in other mantle wedges.

f) The Orthopyroxenites contain high Cr, Ni, and PGE. Their PGE patterns are similar to those of the peridotites in this area, as well as typical peridotites in other areas, suggesting essential immobility of these elements during metasomatism. The contents of Ni and PGEs are independent of S. They most likely present in metals and/or silicates. Copper and S show positive correlations in orthopyroxenites and were likely introduced during the metasomatism.

Appendix A

Calibration methods of spinel:

Four artificial spinel reference grains (KLB8304, KLB8311, MBR8305, KLB8316) were used to obtain Fe^{3+} contents in spinel samples. The reference grains were provided by B. J. Wood through JianPing Li. Fe^{3+} contents in reference grains were measured by Mössbauer spectroscopy by Wood and Virgo (1989)

These reference grains were analyzed by electron microprobe (EMP) together with each batch of samples. Each batch contains 3-4 samples and 2-8 grains were determined in each sample. The $Fe^{3+}/\Sigma Fe$ ratios, $(Fe^{3+}/\Sigma Fe)_{probe}$, of references and samples were then calculated assuming stoichiometric compositions of spinel, AB_2O_4. References yield a correction factor X, $(Fe^{3+}/\Sigma Fe)_{moss} - (Fe^{3+}/\Sigma Fe)_{probe}$, where $(Fe^{3+}/\Sigma Fe)_{moss}$ is the value obtained from Mossbauer spectroscopy data. The values of X are correlated with Al/Cr ratio of the spinel (see Wood and Virgo 1989):

$[(Fe^{3+}/\Sigma Fe)_{moss} - (Fe^{3+}/\Sigma Fe)_{probe}]_{standard} = a + b\,[Al/(Al+Cr)]$ ---------- (1)

where [Al/(Al+Cr)] are atomic ratios of Al/(Al+Cr). Four reference grains yielded the constants of a and b. The values may vary in different sessions. The values of a and b were used to correct the, $(Fe^{3+}/\Sigma Fe)_{probe}$ in samples of the same batch:

$[(Fe^{3+}/\Sigma Fe)_{corrected}]_{\text{in samples}} = (Fe^{3+}/\Sigma Fe)_{probe}]_{\text{in samples}} + a + b\,[Al/(Al+Cr)]$ ------- (2)

The differences between $(Fe^{3+}/\Sigma Fe)_{corrected}$ and $(Fe^{3+}/\Sigma Fe)_{probe}$ are illustrated in Figs 1-3, 2-3.

Calculation of fO_2 :

The fO_2 values are calculated using the following reaction equilibrium;

$6\,Fe_2SiO_4$ (in olivine) + $O_2 = 3\,Fe_2Si_2O_6$ (in orthopyroxene) + $2\,Fe_3O_4$ (in spinel) ---------- (1)

The Fe^{3+} contents in spinel were converted to activities of magnetite (Fe_3O_4) in spinel using the formula below by Nell and Wood (1991);

$\text{Log } a(Fe_3O_4 \text{ in Sp}) = \log((Fe^{2+})*(Fe^{3+})^2/4) + 1/T[406(Al)^2 + 653(Mg)*(Al) + 299\,(Cr)^2 + 199\,(Al)*(Cr) + 346(Mg)*(Cr)]$ ---------- (2)

The term in parentheses refers to total atomic concentration of Mg, Fe^{2+}, Fe^{3+}, Cr and Al in spinel on a four oxygen basis. K is Kelvin.

Therefore, $\Delta \log fO_2(FMQ)$ at a given pressure (in bar) and temperature (in K) is given by the following equation;

$\Delta \log fO_2(FMQ) = \log(fO_2) - \log(fO_2)FMQ = +220/T + 0.35 - 0.0369P/T - 12\log X_{Fe}Ol - 2620(X_{Mg}Ol)^2/T + 3\log[(X_{Fe}M1)Opx * (X_{Fe}M2)Opx] + 2\log a(Fe_3O_4 \text{ in Sp})$ ---- (3)

$(fO_2)FMQ$ is fO_2 relative to FMQ buffer, P in bar, T in Kelvin, $X_{Fe}Ol$ and $X_{Mg}Ol$ refer to the atomic ratios of $Fe^{2+}/(Mg + Fe^{2+})$ and $Mg/(Mg + Fe^{2+})$ in olivine, and $(X_{Fe}M1)$ Opx and $(X_{Fe}M2)$ Opx refer to the atomic fractions of Fe in M1 and M2 sites of orthopyroxene. $a(Fe_3O_4 \text{ in Sp})$ is activity of magnetite, Fe_3O_4, in spinel.

Appendix B

Sample Descriptions

Pali Aike area

Grt-bearing Lherzolite

LS33: Fresh, coarse - grained (2 - 4 mm), garnet lherzolite consisting of Ol (~ 65 vol%), Opx (~ 20 vol%), Cpx (~ 10 vol%), and Grt (~ 3 vol%) with minor sulfides (>10 grains/section). Some Opx grains contain trails of fluid inclusions.

TM0: Fresh, coarse - grained (2 - 4 mm), garnet-spinel lherzolite consisting of Ol (30 - 35 vol%), Opx (15 - 20 vol%), Cpx (~ 30 vol%), Grt (~ 20 vol%), and Spl (≤2 vol%) with abundant sulfides (>20 grains/section). Most Spl grains are enclosed in Grt. Trails of fluid inclusions are common in sample.

TM2: Fresh, coarse - grained (2 - 4 mm), garnet-spinel lherzolite consisting of Ol (~ 50 vol%), Opx (25 - 30 vol%), Cpx (~15 vol%), Grt (8 - 10 vol%), and Spl (≤2 vol%) with abundant sulfides (>20 grains/section). Trails of fluid inclusions are common in sample.

LS50: Fresh, medium - grained (1 - 3 mm), garnet lherzolite consisting of Ol (65 - 70 vol%), Opx (~ 15 vol%), Cpx (~ 15 vol%), and Grt (~ 5 vol%) with minor spinels and sulfides (<5 grains/section). Two small Spl grains enclosed in Opx. There is a narrow symplectic rim (<0.1 mm) surrounding Cpx grains. Trails of fluid inclusions are common in sample.

BN73: Fresh, medium - grained (1 - 3 mm), garnet lherzolite consisting of Ol (65 - 70 vol%), Opx (25 - 30 vol%), Cpx (~ 5 vol%), Grt (~ 3 vol%) and minor Spl (≤0.5 vol%).

LS1: Fresh, medium - grained (2 - 3 mm), garnet lherzolite consisting of Ol (70 - 75 vol%), Opx (~ 15 vol%), Cpx (~ 10 vol%), Grt (~ 5 vol%) and minor Spl (≤0.5 vol%).

BN32: Fresh, coarse - grained (1- 4 mm), garnet-spinel lherzolite consisting of Ol (~ 50 vol%), Opx (~ 30 vol%), Grt (~ 15 vol%), Cpx (~ 5 vol%), Spl (≤2 vol%), and minor brown Amp and sulfides (>5 grains/section). Spinel occurs both as relict grains in garnet and as individual grains intergrowth with silicate minerals. Trails of fluid inclusions are common in sample.

Grt-bearing Harzburgite

TM14: Fresh, medium - grained (1 - 3 mm), garnet-spinel harzburgite consisting of Ol (50 - 55 vol%), Opx (25 - 30 vol%), Grt (~ 10 vol%), Cpx (~ 5 vol%), and Spl (<5 vol%) with minor Amp. Spinel occurs as relict grains in Grt. A veinlet (~ 3 mm) of Phl cuts across the sample.

TM15: Fresh, coarse - grained (1 - 4 mm), garnet-spinel harzburgite consisting of Ol (~ 70 vol%), Opx (20 - 30 vol%), Grt (~ 8 vol%), Spl (≤2 vol%), and minor Cpx (≤0.5 vol%). Spinel occurs as relict grains in Grt. A veinlet (~ 3 mm) of Phl cuts across the sample. Trails of fluid inclusions are common in sample.

BN92: Fresh, coarse - grained (2 - 5 mm), garnet-spinel harzburgite consisting of Ol (55 - 60 vol%), Opx (25 - 30 vol%), Grt (~ 10 vol%), Spl (≤1 vol%), and Cpx (≤0.5 vol%) with minor sulfides (<5 grains/section). Spinel occurs both as relict grains in garnet and as individual grains intergrowth with silicate minerals. A veinlet of orthopyroxenite (~ 5 mm) cuts across the sample.

BN50: Fresh, coarse - grained (2 - 5 mm), garnet-spinel harzburgite consisting of Ol (55 - 60 vol%), Opx (25 - 30 vol%), Grt (~ 10 vol%), Spl (<5 vol%), and Cpx (≤0.5 vol%) with abundant sulfides (>10 grains/section). Spinel occurs both as relict grains in garnet and as individual grains intergrowth with silicate minerals.

PAHK1: Fresh, medium - grained (1 - 3 mm), garnet-spinel harzburgite consisting of Ol (~ 50 vol%), Opx (~ 40 vol%), Grt (~ 9 vol%), and Spl (≤1 vol%) with minor Cpx (≤0.5 vol%). Trails of fluid inclusions are common in sample.

PAK6: Fresh, coarse-grained (1 - 5 mm), garnet-spinel harzburgite consisting of Ol (~ 50 vol%), Opx (35 - 40 vol%), Grt (~ 10 vol%), Spl (~ 3 vol%), Mg-Ilm (~ 1vol%) and minor Cpx (≤0.5 vol%).

BN45: Fresh, coarse - grained (1 - 4 mm), garnet-spinel harzburgite consisting of Ol (~ 40 vol%), Opx (~ 50 vol%), Grt (~ 9 vol%), Phl (≤1 vol%), and Cpx (≤0.5 vol%) with minor Spl (1 grain).

BN31: Fresh, coarse -grained (1 - 4 mm), garnet-spinel harzburgite consisting of Ol (50 - 55 vol%), Opx (~ 35 vol%), Grt (~ 10 vol%), and Spl (≤2 vol%) with minor Cpx (≤0.5 vol%). A thin veinlet (<0.2 mm) of Amp occurs along grain boundaries.

Spl Lherzolite

PA64: Fresh, coarse-grained (2 - 4 mm), spinel lherzolite consisting of Ol (~ 80 vol%), Opx (~ 15 vol%), Cpx (~ 3 vol%) and Spl (~2 vol%) with abundant sulfides (>10 grains/section). A veinlet (>5 mm) of websterite cuts across the sample.

PAK1: Fresh, coarse-grained (3 - 4 mm), spinel lherzolite consisting of Ol (~ 70 vol%), Opx (~15 vol%), Cpx (~ 10 vol%) and Spl (~ 5 vol%) with minor sulfide (1 grain).

Spl Harzburgite

LS5: Fresh, coarse -grained (3 - 4 mm), spinel harzburgite consisting of Ol (~ 65 vol%), Opx (~ 30 vol%) and Spl (~ 5 vol%) with minor Cpx (≤0.5 vol%).

PAK2: Fresh, coarse-grained (3 - 4 mm), spinel harzburgite consisting of Ol (~80 vol%), Opx (~ 14 vol%), and Cpx (~ 5 vol%) with minor Spl (≤1 vol%). Spinel occurs both as small inclusions in Ol and Opx and as coarse grains intergrowth with silicate grains.

PAK3: Fresh, coarse-grained (3 - 4 mm), spinel harzburgite consisting of Ol (~ 70 vol%), Opx (~ 26 vol%), Cpx (≤2 vol%), and Spl (≤2 vol%). Spinel occurs both as small inclusions in Ol and Opx and as coarse grains intergrowth with silicate grains.

LS100: Fresh, coarse-grained (3 - 4 mm), spinel harzburgite consisting of Ol (~ 68 vol%), Opx (~30 vol%), and Spl (~2 vol%) with minor Cpx (≤0.5vol%). Trails of fluid inclusions are common in grains.

PAK5: Fresh, coarse -grained (3 - 4 mm), spinel harzburgite consisting of Ol (~ 67 vol%), Opx (~ 30 vol%), and Spl (~ 3 vol%) with minor Cpx (≤0.5vol%). Trails of fluid inclusions are common in grains.

01BN: Fresh, coarse-grained (3 - 4 mm), spinel harzburgite consisting of Ol (~70 vol%), Opx (~ 20 vol%), Spl (~ 6 vol%) and Cpx (~ 4 vol%). Spinel occurs both as small inclusions in Ol and Opx and as coarse grains intergrowth with silicate grains.

BNH11: Fresh, coarse-grained (3 - 4 mm), spinel harzburgite consisting of Ol (~70 vol%), Opx (~ 20 vol%), Spl (~ 2 vol%) and Cpx (~ 1 ol%).

Grt Orthopyroxenite

BNH13: Fresh, coarse-grained (1 - 5 mm), blown Grt orthopyroxenite. It shows porphyroblastic texture and consists of Opx (~ 75 vol%), Grt (~ 20 vol%), Cpx (3 - 5 vol%), and minor Ol (≤1 vol%) with abundant sulfide (>20 grains/section). Olivine and Cpx occur as relict grains in secondary Opx or along mineral boundaries. Orthopyroxene contains abundant fluid inclusions.

BNC2: Weakly altered, medium-grained (1 - 3 mm), blown orthopyroxenite. It shows porphyroblastic texture and consists of Opx (80 - 90 vol%), Grt (~ 5 vol%), Ol (2 - 3 vol%), Mg-Ilm (~ 5 vol%), Phl (≤2 vol%), Spl (≤0.5 vol%), and Amp (≤0.2 vol%) with minor sulfides (<5 grains/section). Olivine occurs as relict inclusions in secondary Opx which contains abundant fluid inclusions. Garnet grains decomposed and changed into fine-grained aggregates of other mineral.

BNC1: Weakly altered, medium-grained (1 - 3 mm), blown orthopyroxenite. It shows porphyroblastic texture and consists of Opx (80 - 90 vol%), Grt (~ 2 vol%), Ol (2 - 3 vol%), Mg-Ilm (~ 5 vol%), and Phl (≤2 vol%) with minor sulfides (>5 grains/section). Olivine

occurs as relict inclusions in secondary Opx which contains abundant fluid inclusions. Garnet grains decomposed and changed into fine-grained aggregates of other mineral.

BN43: Fresh, medium-grained (1 - 3 mm), blown orthopyroxenite. It shows porphyroblastic texture and consists of Opx (~ 85 vol%), Ol (8 - 10 vol%), Grt (2- 3 vol%), and Mg-Ilm (≤5 vol%) with minor Phl (≤1 vol%) and sulfide (>5 grains/section). A fragment of harzburgite present in this samples. Ol occurs as inclusions in secondary Opx which contains abundant fluid inclusions.

BNO5: Fresh, medium-grained (1 - 3 mm), blown orthopyroxenite. It shows porphyroblastic texture and consists of Opx (~ 90vol%), Ol (≤5 vol%), Grt (~ 5 vol%), and Mg-Ilm (≤0.5 vol%) with minor sulfide (<5 grains/section). Relict Ol occurs as inclusions in secondary Opx and along grain boundaries.

BNC3: Weakly altered, medium -grained (1 - 3 mm), blown orthopyroxenite. It shows porphyroblastic texture and consists of Opx (80 - 90 vol%), Grt (2- 3 vol%), Ol (2 - 3 vol%), Mg-Ilm (~ 5 vol%), and Phl (≤2 vol%) with minor sulfide (>5 grains/section). Olivine occurs as inclusions in secondary Opx which contains abundant fluid inclusions. Garnet grains decomposed and changed into fine-grained aggregates of other mineral.

BNH5: Fresh, coarse-grained (1 - 5 mm), blown Grt orthopyroxenite. It shows porphyroblastic texture and consists of Opx (~ 75 vol%), Grt (~ 20 vol%), Cpx (3 - 5 vol%), and Spl (≤2 vol%) with abundant sulfide (>20 grains/section). Clinopyroxene occurs as relict grains in secondary Opx. Orthopyroxene occurs both as coarse-grained (2 – 4 mm) individual grains, and as fine-grained (<0.3 mm) aligned aggregates. Spinel occurs as relict grains in garnet.

BN42: Fresh, medium-grained (2 - 3 mm), blown Grt orthopyroxenite. It shows equigranular texture and consists of Opx (60 - 65 vol%), Grt (25 - 30 vol%), Mg-Ilm (~ 5 vol%), Phl (≤1 vol%), Cpx (≤1 vol%), and minor Amp (≤0.5 vol%) with abundant sulfides (>20 grains/section). Clinopyroxene occurs as relict grains in secondary Opx.

BN46: Fresh, medium-grained (2 - 3 mm), blown Grt orthopyroxenite. It shows equigranular to porphyroblastic texture and consists of Opx (85- 90 vol%), Grt (~ 5 vol%), Phl (~ 5 vol%), Cpx (2 - 3 vol%), Mg-Ilm (≤0.5 vol%), and minor Amp (≤0.2 vol%) with abundant sulfides (>20 grains/section). Clinopyroxene occurs as relict grains in secondary Opx.

Ol Websterite

BNH7: Fresh, coarse-grained (2 - 5 mm), blown Ol websterite. It shows porphyroblastic texture and consists of Cpx (~ 50 vol%), Opx (~ 40 vol%), Grt (~ 5 vol%), Ol (~ 5 vol%), and Spl (≤3 vol%) with abundant sulfides (>10 grains/section). Relict Spl are enclosed in garnet.

BNC4: Fresh, coarse-grained (3 - 4 mm), blown Ol websterite. It shows equigranular texture and consists of Cpx (~ 40 vol%), Opx (~ 40 vol%), Ol (~ 20 vol%) and Mg-Ilm (≤0.5 vol%) with minor sulfides (<5 grains/section). Relict Ol are commonly surrounded by Opx grains.

BN31x: Fresh, medium-grained (1 - 3 mm), blown Ol websterite. It shows equigranular or granoclastic texture and consists of Cpx (~ 50 vol%), Opx (~ 30 vol%), and Ol (~ 20 vol%) with minor sulfides (<5 grains/section). Some small (≤0.2 mm) rounded Opx grains in coarse-grained Ol and Cpx were formed by replacing host Ol and Cpx.

LLS3: Fresh, medium-grained (2 - 3 mm), blown Ol websterite. It shows equigranular texture and consists of Cpx (~ 45 vol%), Opx (~ 35 vol%), and Ol (~ 20 vol%) with abundant sulfides (>10 grains/section). Some small (≤0.2 mm) rounded Opx grains in coarse-grained Ol and Cpx were formed by replacing host Ol and Cpx.

Cerro del Fraile area

Bxe32-I, II, III, and Bxe31-I: Coarse-grained (2 - 5 mm) spinel harzburgites containing veins of websterite. The area free of websterite contains olivine (~ 80 vol%), orthopyroxene (10 - 15 vol%), clinopyroxene (0-5 vol%) and spinel (< 3 vol%). They show protogranular to porphyroclastic textures with large subhedral grains of olivine and/or orthopyroxene.

Bxe11 and Bxe11-I: Coarse-grained (2 - 5 mm) spinel harzburgites containing veins of websterite. The area free of websterite contains olivine (~ 80 vol%), orthopyroxene (10 - 15 vol%), clinopyroxene (0-5 vol%) and spinel (< 3 vol%). They contain solidified "melt" (~ 5 vol%), which forms patches (up to 2 mm), and discontinuous veinlets along grain boundaries.

Bxe35-I: Coarse-grained (2 - 5 mm) spinel lherzolite consisting of olivine (~ 70 vol%), orthopyroxene (~ 20 vol%), clinopyroxene (~ 5 vol%), and spinel (2 - 3 vol%). It shows protogranular texture with large subhedral grains of olivine and/or orthopyroxene.

Bxe1 and Bxe22: Fine to medium-grained (0.5 - 2 mm) and weakly foliated spinel lherzolites consisting of olivine (55 - 60 vol%), orthopyroxene (~ 20 vol%), clinopyroxene (5 - 10 vol%), spinel (~ 5 vol%) and abundant solidified "melt" (~ 10 vol%). The samples show equigranular texture. Solidified "melt" forms veinlets (< 0.2 mm) and large patches (up to 2 x 2 mm), which are commonly connected by veinlets.

Appendix C

Mineral compositions in mantle peridotite xenoliths from Pali Aike area determined with an electrom microprobe

Appendix C-1 Olivine

Lithology	Grt-Spl Lherzolite																
Sample	LS33		TM0		TM2		LS50			BN73			LS1			BN32	
Grains [a]	Ol-1	Ol-2	Ol-1	Ol-2	Ol-1	Ol-2	Ol-1	Ol-2	Ol-3	Ol-1	Ol-2	Ol-3	Ol-1	Ol-2	Ol-3	Ol-1	Ol-2
SiO_2	40.74	40.51	40.72	40.55	39.92	40.11	40.50	40.55	40.86	41.07	41.45	40.63	40.93	40.87	40.86	40.81	41.04
Al_2O_3	0.06	<0.04	<0.04	<0.04	<0.04	<0.04	<0.04	<0.04	<0.04	0.05	<0.04	<0.04	<0.04	<0.04	<0.04	<0.04	<0.04
FeO (t) [b]	9.59	9.73	10.40	10.25	9.86	9.89	9.86	10.16	10.13	9.57	9.05	8.93	9.13	9.11	9.12	10.57	10.54
MgO	49.59	49.50	49.03	48.36	48.61	47.72	48.43	48.49	48.35	49.38	49.57	49.04	49.38	49.35	49.27	48.51	48.73
MnO	0.10	0.10	0.09	0.15	0.10	0.17	0.11	0.12	0.09	0.14	0.11	0.10	0.12	0.12	0.12	0.10	0.12
CaO	0.10	0.11	0.06	0.06	0.05	0.05	0.06	0.07	0.06	0.09	0.08	0.09	0.06	0.06	0.07	0.06	0.05
NiO	0.36	0.35	0.36	0.36	0.36	0.38	0.31	0.30	0.35	0.35	0.31	0.32	0.38	0.37	0.37	0.42	0.40
Fo	90.2	90.1	89.4	89.4	89.8	89.6	89.8	89.5	89.5	90.2	90.7	90.7	90.6	90.6	90.6	89.1	89.2
Total	100.5	100.3	100.7	99.76	98.92	98.35	99.28	99.70	99.84	100.7	100.6	99.11	100.0	99.89	99.81	100.5	100.9

Appendix C-1 Olivine continued

Lithology	Grt-Spl Harzburgite																			
Sample	TM14		TM15		BN92		BN50		PAHK1			PAK6			BN45			BN31		
Grains [a]	Ol-1	Ol-2	Ol-1	Ol-2	Ol-1	Ol-2	Ol-1	Ol-2	Ol-1	Ol-2	Ol-3	Ol-1	Ol-2	Ol-3	Ol-1	Ol-2	Ol-3	Ol-1	Ol-2	Ol-3
SiO_2	41.15	40.63	40.68	40.40	39.76	40.07	40.28	40.48	40.84	40.65	40.72	40.48	40.41	40.35	40.78	40.84	40.81	40.04	40.31	40.13
Al_2O_3	<0.04	<0.04	<0.04	<0.04	<0.04	<0.04	<0.04	<0.04	<0.04	<0.04	<0.04	<0.04	<0.04	<0.04	<0.04	<0.04	<0.04	<0.04	<0.04	<0.04
FeO (t) [b]	10.92	11.12	11.54	11.75	10.99	11.11	10.71	10.74	11.05	10.95	9.91	12.43	12.41	12.39	10.33	10.27	10.33	10.94	10.75	10.80
MgO	48.44	48.35	47.89	47.66	47.35	48.35	48.34	47.87	48.36	48.34	48.75	47.33	47.09	47.02	48.32	48.42	48.55	48.16	47.88	47.90
MnO	0.13	0.12	0.07	0.11	0.16	0.12	0.15	0.12	0.15	0.09	0.21	0.12	0.13	0.13	0.12	0.12	0.12	0.11	0.06	0.08
CaO	0.06	0.07	0.05	0.05	0.06	0.05	0.07	0.06	0.06	<0.05	<0.05	<0.05	<0.05	0.05	0.07	0.08	0.07	0.06	0.05	0.05
NiO	0.39	0.39	0.38	0.38	0.48	0.48	0.38	0.39	0.47	0.45	0.42	0.44	0.45	0.44	0.43	0.44	0.45	0.46	0.50	0.46
Fo	88.8	88.6	88.1	87.9	88.5	88.6	88.9	88.8	88.6	88.7	89.8	87.2	87.1	87.1	89.3	89.4	89.3	88.7	88.8	88.8
Total	101.1	100.7	100.6	100.4	98.83	100.2	99.95	99.67	101.0	100.5	100.1	100.8	100.5	100.4	100.0	100.2	100.3	99.78	99.55	99.42

Appendix C-1 Olivine continued

Lithology	Spl Lherzolite					Spl Harzburgite														
Sample	PA64		PAK1			LS5			PAK2			PAK3				LS100				
Grains [a]	Ol-1	Ol-2	Ol-1	Ol-2	Ol-3	Ol-1	Ol-2	Ol-3	Ol-1	Ol-2	Ol-3	Ol-1	Ol-2	Ol-3	Ol-4	Ol-1	Ol-2	Ol-3	Ol-4	Ol-5
SiO_2	40.71	40.76	41.06	41.44	41.01	41.08	40.89	40.94	41.19	41.21	41.21	40.78	41.13	40.76	40.77	40.51	40.67	40.56	40.54	40.45
Al_2O_3	<0.04	<0.04	<0.04	<0.04	<0.04	<0.04	<0.04	<0.04	<0.04	<0.04	<0.04	<0.04	<0.04	<0.04	<0.04	<0.04	<0.04	<0.04	<0.04	<0.04
FeO (t) [b]	9.95	10.72	9.11	9.29	9.15	9.73	9.71	9.71	8.30	8.16	8.24	8.24	7.95	8.04	8.23	10.52	10.82	10.63	10.60	10.53
MgO	49.26	49.35	49.61	48.98	49.49	49.43	49.35	49.45	50.22	50.14	50.16	50.03	50.07	49.70	49.76	48.35	48.13	48.10	47.88	47.89
MnO	0.15	0.12	0.12	0.15	0.12	0.11	0.12	0.11	0.13	0.11	0.12	0.10	0.09	0.10	0.10	0.11	0.10	0.09	0.11	0.11
CaO	<0.05	<0.05	<0.05	<0.05	<0.05	0.07	0.07	0.07	0.07	0.07	0.07	0.06	0.06	0.06	0.07	0.08	0.07	0.10	0.07	0.06
NiO	0.40	0.34	0.36	0.38	0.39	0.40	0.39	0.40	0.41	0.42	0.39	0.43	0.38	0.39	0.40	0.32	0.39	0.37	0.42	0.44
Fo	89.8	89.1	90.7	90.4	90.6	90.1	90.1	90.1	91.5	91.6	91.6	91.5	91.8	91.7	91.5	89.1	88.8	89.0	89.0	89.0
Total	100.5	101.3	100.3	100.2	100.2	100.8	100.5	100.7	100.3	100.1	100.2	99.63	99.68	99.04	99.33	99.88	100.2	99.86	99.62	99.48

Appendix C-1 Olivine continued

Lithology	Spl Harzburgite									Grt-Spl Websterite		
Sample	PAK5			01BN			BNH11			BNH7		
Grains [a]	Ol-1	Ol-2	Ol-3	Ol-1	Ol-2	Ol-3	Ol-1	Ol-2	Ol-3	Ol-1	Ol-2	Ol-3
SiO_2	40.34	39.64	39.72	40.81	40.73	41.08	40.82	40.95	40.90	40.80	40.71	40.42
Al_2O_3	0.06	0.05	0.05	<0.04	<0.04	<0.04	<0.04	<0.04	<0.04	<0.04	<0.04	<0.04
FeO (t) [b]	13.16	13.46	13.47	8.89	8.88	8.82	9.64	9.61	9.67	10.89	10.89	11.33
MgO	46.18	46.07	45.86	50.05	50.08	49.80	49.08	49.07	49.21	48.09	48.15	47.91
MnO	0.12	0.12	0.10	0.15	0.20	0.19	0.11	0.15	0.13	0.13	0.13	0.12
CaO	0.08	0.08	0.09	<0.05	<0.05	<0.05	0.05	0.06	0.05	0.06	<0.05	0.05
NiO	0.44	0.45	0.43	0.38	0.38	0.40	0.41	0.40	0.42	0.47	0.47	0.45
Fo	86.2	85.9	85.9	90.9	91.0	91.0	90.1	90.1	90.1	88.7	88.7	88.3
Total	100.4	99.87	99.72	100.3	100.3	100.3	100.1	100.2	100.4	100.4	100.4	100.3

[a] Different numbers denote different grains

[b] Total Fe as FeO

Appendix C-2 Orthopyroxene

Lithology	Grt-Spl Lherzolite																	
Sample	LS33		TM0		TM2		LS50			BN73		LS1			BN32			
Grains [a]	Opx1	Opx2	Opx1	Opx2	Opx1	Opx2	Opx1	Opx2	Opx3	Opx1	Opx2	Opx1	Opx2	Opx3	Opx1	Opx2	Opx3	Opx4
SiO_2	54.96	54.47	55.99	55.86	55.30	54.45	55.44	55.05	55.90	54.95	55.45	54.51	54.88	54.99	54.16	54.77	55.28	55.06
Al_2O_3	4.32	4.30	3.25	3.63	3.12	3.56	3.70	3.69	3.81	3.87	3.96	3.63	3.66	3.79	3.50	3.49	3.52	3.52
TiO_2	0.15	0.14	0.12	0.14	0.18	0.20	0.22	0.21	0.22	<0.04	0.06	0.11	0.12	0.12	0.18	0.18	0.17	0.14
Cr_2O_3	0.66	0.63	0.37	0.46	0.41	0.45	0.63	0.62	0.61	0.82	0.82	0.67	0.67	0.65	0.45	0.39	0.43	0.35
FeO (t) [b]	6.27	6.03	6.49	6.47	6.32	6.41	6.74	6.41	6.24	5.83	5.92	5.83	5.93	5.85	6.84	6.75	6.62	6.65
MgO	32.50	32.11	33.33	32.57	32.89	32.55	32.80	32.81	32.28	32.80	32.63	33.12	33.30	33.02	32.82	32.99	33.09	33.38
MnO	0.15	0.15	0.13	0.08	0.12	0.10	0.11	0.14	0.11	0.11	0.13	0.12	0.12	0.11	0.11	0.12	0.11	0.12
CaO	1.11	1.21	0.63	0.72	0.60	0.64	0.84	0.81	0.83	0.96	1.01	0.87	0.84	0.84	0.72	0.71	0.70	0.63
Na_2O	0.23	0.24	0.15	0.13	0.11	0.00	0.14	0.11	0.08	0.15	0.14	0.17	0.19	0.14	0.13	0.12	0.13	0.13
NiO	nd	nd	nd	nd	nd	nd	0.10	0.09	0.12	0.09	0.07	nd	nd	nd	nd	nd	nd	nd
Mg#	0.902	0.905	0.902	0.900	0.903	0.901	0.897	0.901	0.902	0.909	0.908	0.910	0.909	0.910	0.895	0.897	0.899	0.900
Total	100.4	99.28	100.5	100.1	99.05	98.36	100.7	99.95	100.2	99.60	100.2	99.02	99.70	99.51	98.92	99.51	100.0	99.98

Appendix C-2 Orthopyroxene continued

Lithology	Grt-Spl Harzburgite																			
Sample	TM14		TM15		BN92			BN50		PAHK1		PAK6			BN45			BN31		
Grains [a]	Opx1	Opx2	Opx1	Opx2	Opx1	Opx2	Opx3	Opx1	Opx2	Opx1	Opx2	Opx1	Opx2	Opx3	Opx1	Opx2	Opx3	Opx1	Opx2	Opx3
SiO_2	55.58	55.85	55.72	55.85	54.39	54.25	53.86	54.55	54.30	54.94	54.58	54.45	54.18	54.45	54.12	54.49	53.89	55.29	55.29	55.64
Al_2O_3	3.08	3.22	3.51	3.50	3.64	4.01	3.98	3.84	3.75	3.97	4.07	3.48	3.53	3.48	3.81	3.94	3.99	3.66	3.56	3.53
TiO_2	0.20	0.15	0.15	0.11	0.23	0.44	0.37	0.35	0.34	0.27	0.24	0.30	0.29	0.26	0.30	0.32	0.31	0.29	0.26	0.17
Cr_2O_3	0.36	0.36	0.32	0.38	0.48	0.55	0.63	0.65	0.69	0.68	0.68	0.44	0.42	0.42	0.50	0.52	0.50	0.44	0.45	0.47
FeO (t) [b]	6.71	6.77	6.92	7.08	7.05	6.93	6.93	6.77	6.54	7.08	6.97	7.89	7.90	7.94	6.65	6.71	6.76	6.94	6.96	6.77
MgO	32.83	32.98	32.76	32.79	31.78	31.81	31.79	32.23	32.26	32.35	31.84	31.16	30.82	31.10	32.45	32.61	32.62	32.70	32.77	32.89
MnO	0.12	0.08	0.08	0.03	0.13	0.09	0.12	0.12	0.10	0.18	0.11	0.13	0.13	0.11	0.12	0.11	0.12	0.12	0.16	0.12
CaO	0.67	0.65	0.62	0.63	0.75	0.75	0.69	0.74	0.81	0.74	0.76	0.64	0.69	0.64	0.83	0.83	0.81	0.69	0.71	0.71
Na_2O	0.16	0.18	0.12	0.14	0.13	0.11	0.12	0.12	0.15	0.16	0.22	0.13	0.14	0.12	0.12	0.11	0.13	0.11	0.12	0.12
NiO	nd	nd	nd	nd	nd	nd	nd	nd	nd	nd	nd	nd	nd	nd	nd	nd	nd	0.14	0.13	0.14
Mg#	0.897	0.897	0.894	0.892	0.889	0.891	0.891	0.895	0.898	0.891	0.891	0.876	0.874	0.875	0.897	0.896	0.896	0.894	0.894	0.896
Total	99.71	100.2	100.2	100.5	98.58	98.94	98.49	99.37	98.94	100.4	99.47	98.61	98.10	98.53	98.89	99.65	99.14	100.4	100.4	100.6

Appendix C-2 Orthopyroxene continued

Lithology	Spl Lherzolite									Spl Harzburgite								
Sample	PA64			PAK1						LS5			PAK2			PAK3		
Grains [a]	Opx1	Opx2	Opx3	Opx1	Opx2	Opx3	Opx4	Opx5	Opx6	Opx1	Opx2	Opx3	Opx1	Opx2	Opx3	Opx1	Opx2	Opx3
SiO_2	55.49	55.07	55.06	55.13	55.40	54.90	54.97	55.64	55.41	54.89	54.82	54.45	56.28	56.33	55.96	56.11	56.11	56.17
Al_2O_3	3.90	3.83	4.60	4.63	5.09	4.99	4.94	4.86	4.39	3.21	3.25	3.18	2.79	2.76	2.76	2.68	2.74	2.67
TiO_2	0.10	0.08	0.09	0.10	0.14	0.11	0.11	0.11	0.12	0.29	0.28	0.32	<0.04	<0.04	<0.04	<0.04	0.05	<0.04
Cr_2O_3	0.47	0.50	0.62	0.58	0.71	0.68	0.64	0.61	0.59	0.70	0.74	0.73	0.72	0.76	0.71	0.73	0.74	0.70
FeO (t) [b]	6.46	6.90	7.30	5.97	5.90	5.94	5.78	5.98	6.12	6.22	6.24	6.26	4.99	5.12	5.20	5.16	5.12	5.20
MgO	33.19	32.72	32.56	32.88	32.47	32.70	32.21	33.12	32.56	33.30	33.25	32.86	34.05	33.66	34.00	33.90	33.63	33.93
MnO	0.14	0.16	0.24	0.16	0.14	0.17	0.12	0.10	0.17	0.10	0.11	0.12	0.17	0.16	0.12	0.12	0.13	0.15
CaO	0.68	0.40	0.39	0.33	0.98	0.62	1.11	0.33	0.57	0.79	0.77	0.78	0.89	0.92	0.85	0.87	0.82	0.81
Na_2O	0.03	0.05	0.02	0.00	0.10	0.01	0.05	0.01	0.03	0.14	0.14	0.16	0.04	0.05	0.06	0.06	0.06	0.02
NiO	nd	nd	nd	0.08	0.07	0.08	0.07	0.06	0.12	nd	nd	nd	0.10	0.11	0.11	0.13	0.16	0.11
Mg#	0.902	0.894	0.888	0.908	0.908	0.908	0.909	0.908	0.905	0.905	0.905	0.903	0.924	0.921	0.921	0.921	0.921	0.921
Total	100.5	99.71	100.9	99.87	101.0	100.2	100.0	100.8	100.1	99.64	99.60	98.86	100.1	99.89	99.79	99.77	99.57	99.80

Appendix C-2 Orthopyroxene continued

Lithology	Spl Harzburgite														Grt-Spl Websterite		
Sample	LS100							PAK5		01BN		BNH11			BNH7		
Grains [a]	Opx1	Opx2	Opx3	Opx4	Opx5	Opx6	Opx7	Opx1	Opx2	Opx1	Opx2	Opx1	Opx2	Opx3	Opx1	Opx2	Opx3
SiO_2	55.19	55.33	55.59	55.71	55.01	55.33	55.19	54.30	53.99	56.00	56.49	54.65	54.91	55.22	54.97	55.44	54.91
Al_2O_3	3.16	3.14	3.16	3.21	3.13	3.24	3.14	3.95	4.10	2.79	2.74	3.30	2.68	2.70	3.24	3.22	3.20
TiO_2	0.30	0.28	0.33	0.28	0.33	0.36	0.33	0.50	0.50	<0.04	0.06	0.30	0.17	0.16	0.11	0.13	0.10
Cr_2O_3	0.68	0.69	0.65	0.68	0.76	0.74	0.70	0.68	0.68	0.67	0.58	0.14	0.54	0.56	0.18	0.15	0.13
FeO (t) [b]	6.59	6.84	6.83	6.82	6.96	6.75	6.66	8.60	8.51	6.06	5.90	6.34	6.26	6.28	6.73	6.52	6.93
MgO	32.33	32.28	32.49	32.43	32.07	32.04	32.12	30.71	30.71	33.71	33.78	33.08	33.19	33.38	33.18	33.39	32.91
MnO	0.15	0.13	0.18	0.09	0.09	0.10	0.13	0.14	0.11	0.07	0.11	0.12	0.12	0.12	0.12	0.11	0.12
CaO	0.86	0.86	0.85	0.83	0.83	0.84	0.80	0.84	0.89	0.40	0.50	0.67	0.77	0.80	0.63	0.60	0.64
Na_2O	0.16	0.21	0.22	0.22	0.15	0.15	0.14	0.13	0.15	0.00	0.01	0.11	0.10	0.10	0.07	0.11	0.08
NiO	0.12	0.09	0.11	0.11	0.14	0.13	0.12	0.11	0.13	0.07	0.05	nd	nd	nd	nd	nd	nd
Mg#	0.897	0.894	0.895	0.894	0.892	0.894	0.896	0.864	0.865	0.908	0.911	0.903	0.904	0.905	0.898	0.901	0.894
Total	99.55	99.84	100.4	100.4	99.46	99.67	99.32	99.97	99.78	99.80	100.2	98.70	98.74	99.32	99.23	99.68	99.03

nd not determined; [a] Different numbers denote different grains; [b] Total Fe as FeO

Appendix C-3 Clinopyroxene

Lithology	Grt-Spl Lherzolite																			
Sample	LS33		TM0		TM2		LS50				BN73			LS1			BN32			
Grains [a]	Cpx1	Cpx2	Cpx1	Cpx2	Cpx1	Cpx2	Cpx1	Cpx2	Cpx3	Cpx4	Cpx1	Cpx2	Cpx3	Cpx1	Cpx2	Cpx3	Cpx1	Cpx2	Cpx3	Cpx4
SiO_2	52.49	51.89	52.22	52.71	52.04	52.99	52.97	52.64	52.42	52.85	52.57	53.47	53.03	52.80	52.94	52.82	52.68	52.44	52.27	52.28
Al_2O_3	5.95	5.90	6.10	6.34	5.70	5.76	5.40	5.44	5.70	5.12	5.04	5.08	4.87	4.98	5.17	5.25	5.48	6.16	5.44	5.48
TiO_2	0.46	0.39	0.64	0.62	0.60	0.62	0.59	0.61	0.61	0.58	0.12	0.09	0.11	0.33	0.34	0.33	0.57	0.59	0.70	0.70
Cr_2O_3	1.23	1.29	0.74	0.93	0.88	0.90	1.50	1.57	1.49	1.53	1.47	1.50	1.43	1.40	1.46	1.41	0.89	0.74	1.01	0.97
FeO (t) [b]	3.50	3.60	3.26	2.99	3.07	3.02	3.27	3.41	3.41	3.21	2.89	3.09	2.95	2.96	3.00	3.04	3.24	3.13	3.44	3.38
MgO	16.49	16.47	14.94	14.67	14.82	14.84	15.21	15.53	15.20	15.48	16.04	16.48	16.24	16.50	16.66	16.53	15.65	15.35	15.63	15.69
MnO	0.14	0.11	0.05	0.07	0.06	0.08	0.08	0.13	0.08	0.06	0.06	0.06	0.10	0.07	0.09	0.09	0.07	0.06	0.08	0.07
CaO	17.75	17.66	19.18	19.60	19.27	19.17	18.52	18.96	18.54	18.20	18.46	18.81	18.37	18.85	18.82	18.74	19.32	19.16	19.14	19.32
Na2O	1.76	1.74	2.05	2.13	1.90	1.93	2.05	2.02	2.01	2.01	1.62	1.56	1.65	1.87	1.95	1.91	2.02	2.14	2.07	2.06
Mg#	0.894	0.891	0.891	0.897	0.896	0.898	0.892	0.890	0.888	0.896	0.908	0.905	0.908	0.909	0.908	0.907	0.896	0.897	0.890	0.892
Total	99.77	99.05	99.18	100.1	98.34	99.31	99.59	100.3	99.48	99.04	98.27	100.1	98.75	99.76	100.4	100.1	99.92	99.77	99.78	99.93

Appendix C-3 Clinopyroxene continued

Lithology	Grt-Spl Harzburgite						Spl Lherzolite							
Sample	TM14		BN92	BN50		PAK6	PA64			PAK1				
Grains [a]	Cpx1	Cpx2	Cpx1	Cpx1	Cpx2	Cpx1	Cpx1	Cpx2	Cpx3	Cpx1	Cpx2	Cpx3	Cpx4	Cpx5
SiO_2	51.07	51.81	50.58	51.77	51.62	51.77	51.87	52.10	52.07	51.95	52.41	53.02	52.68	52.55
Al_2O_3	6.05	5.99	6.19	5.50	5.60	5.83	4.70	4.74	4.87	6.05	6.30	6.24	6.26	6.23
TiO_2	1.26	1.08	1.26	1.00	1.15	0.90	0.27	0.31	0.29	0.44	0.44	0.45	0.43	0.45
Cr_2O_3	1.24	1.18	1.26	1.42	1.37	2.39	0.91	0.94	0.96	1.12	1.17	1.22	1.20	1.12
FeO (t) [b]	3.40	3.53	3.58	3.42	3.40	3.96	2.37	2.22	2.27	1.98	2.12	2.06	2.12	2.20
MgO	14.42	14.82	14.85	14.86	14.92	16.20	15.53	15.08	14.99	14.22	14.10	14.33	14.03	14.31
MnO	0.08	0.13	0.06	0.09	0.10	0.11	0.10	0.07	0.09	0.08	0.07	0.01	0.06	0.08
CaO	19.20	19.42	18.89	19.12	19.35	16.72	23.49	23.69	23.65	20.99	21.26	21.05	21.17	21.24
Na2O	1.94	1.95	1.72	1.78	1.76	2.31	0.58	0.59	0.58	1.76	1.77	1.66	1.75	1.65
Mg#	0.883	0.882	0.881	0.886	0.887	0.879	0.921	0.924	0.922	0.928	0.922	0.925	0.922	0.920
Total	98.66	99.91	98.39	98.96	99.27	100.19	99.82	99.74	99.77	98.59	99.63	100.05	99.69	99.82

Appendix C-3 Clinopyroxene continued

Lithology	Spl Harzburgite												Grt-Spl Websterite		
Sample	PAk2			PAK3			01BN			BNH11			BNH7		
Grains [a]	Cpx1	Cpx2	Cpx3	Cpx1	Cpx2	Cpx3	Cpx1	Cpx2	Cpx3	Cpx1	Cpx2	Cpx3	Cpx1	Cpx2	Cpx3
SiO_2	53.85	54.04	50.62	53.86	53.07	53.31	53.02	53.16	54.07	52.64	53.04	51.74	53.01	52.85	52.65
Al_2O_3	3.43	3.47	3.97	3.45	3.55	3.54	3.39	3.39	3.29	3.98	3.87	5.89	4.93	5.12	4.87
TiO_2	0.09	0.06	2.00	0.07	0.05	0.06	0.14	0.15	0.13	0.41	0.41	1.25	0.37	0.42	0.35
Cr_2O_3	1.44	1.52	1.52	1.46	1.47	1.54	1.28	1.24	1.20	1.38	1.35	0.32	0.36	0.35	0.34
FeO (t) [b]	2.44	2.38	2.93	2.57	2.37	2.39	1.87	1.79	1.95	3.13	3.17	3.81	3.14	2.98	3.29
MgO	16.86	16.79	15.94	16.85	16.68	16.72	15.77	15.69	15.93	16.48	16.71	16.51	16.06	15.84	15.92
MnO	0.10	0.09	0.07	0.10	0.09	0.09	0.09	0.06	0.07	0.09	0.10	0.11	0.08	0.07	0.09
CaO	20.20	20.58	21.82	20.25	19.60	20.54	22.42	22.50	22.26	19.63	19.84	18.18	20.29	20.18	20.21
Na2O	1.16	1.27	0.77	1.25	1.28	1.21	0.74	0.71	0.71	1.59	1.53	1.72	1.71	1.76	1.64
Mg#	0.925	0.926	0.907	0.921	0.926	0.926	0.938	0.940	0.936	0.904	0.904	0.885	0.901	0.905	0.896
Total	99.57	100.20	99.63	99.86	98.15	99.39	98.79	98.72	99.67	99.33	100.00	99.54	99.95	99.57	99.35

[a] Different numbers denote different grains

[b] Total Fe as FeO

Appendix C-4 Spinel

Lithology	Grt-Spl Lherzolite																	
Sample	TM0			TM2		LS50			BN73							LS1		
Grains [a]	Spl-1	Spl-2	Spl-3	Spl-1	Spl-2	Spl-1	Spl-2	Spl-3	Spl-1	Spl-2	Spl-3	Spl-4	Spl-5	Spl-6	Spl-7	Spl-1	Spl-2	Spl-3
SiO_2	0.11	0.06	0.10	0.09	0.11	0.10	0.10	0.11	0.10	0.11	0.12	0.12	0.12	0.12	0.11	0.09	0.08	0.12
Al_2O_3	40.89	41.05	41.58	40.55	40.38	34.35	34.79	34.68	37.96	37.53	38.16	37.86	37.97	38.30	38.09	36.16	35.70	35.07
TiO_2	0.50	0.57	0.49	0.64	0.53	0.96	0.94	0.93	0.16	0.16	0.14	0.16	0.15	0.18	0.14	0.47	0.50	0.50
Cr_2O_3	24.95	25.24	24.84	25.35	25.68	30.43	29.89	29.72	28.44	29.04	29.08	28.15	29.04	28.79	28.91	30.13	30.51	30.78
FeO (t) [b]	15.91	15.49	15.23	15.37	15.29	16.95	16.73	16.44	14.24	14.40	14.18	14.14	13.96	13.89	14.34	15.37	15.30	15.49
MgO	17.17	17.24	17.34	16.89	16.89	16.23	16.42	16.49	17.78	17.95	18.07	17.89	17.88	17.92	18.08	17.05	17.06	16.92
MnO	0.11	0.12	0.14	0.05	0.17	0.06	0.08	0.06	0.08	0.08	0.09	0.07	0.10	0.07	0.07	0.06	0.06	0.06
NiO	0.21	0.29	0.23	nd	nd	0.30	0.30	0.30	0.23	0.29	0.27	0.28	0.30	0.31	0.25	0.26	0.22	0.27
Total	99.87	100.1	99.95	98.95	99.06	99.41	99.32	98.81	99.01	99.58	100.1	98.69	99.54	99.60	100.0	99.59	99.44	99.32

Appendix C-4 Spinel continued

Lithology	Grt-Spl Lherzolite						Grt-Spl Harzburgite													
Sample	BN32						TM14			TM15		BN92			BN50				PAHK1	
Grains [a]	Spl-1	Spl-2	Spl-3	Spl-4	Spl-5	Spl-6	Spl-1	Spl-2	Spl-3	Spl-1	Spl-2	Spl-1	Spl-2	Spl-3	Spl-1	Spl-2	Spl-3	Spl-4	Spl-1	Spl-2
SiO_2	0.06	0.07	0.06	0.06	0.04	0.06	0.08	0.07	0.10	0.06	<0.03	0.12	0.14	0.17	0.06	0.06	0.08	0.06	0.34	0.14
Al_2O_3	40.39	40.75	42.10	40.96	47.60	38.79	39.46	41.93	40.17	42.44	38.99	37.96	36.87	38.61	36.36	36.56	36.41	36.50	37.11	38.32
TiO_2	0.64	0.61	0.65	0.85	0.47	0.77	1.10	1.02	1.17	0.86	1.19	1.95	1.90	1.83	1.41	1.41	1.42	1.48	1.28	1.15
Cr_2O_3	24.32	24.42	22.88	23.27	18.18	25.77	24.79	23.62	24.68	22.67	25.33	23.95	25.54	23.72	27.04	26.54	26.87	27.52	26.20	25.93
FeO (t) [b]	16.27	16.35	16.01	16.83	15.06	17.13	17.30	16.66	16.95	16.74	18.26	18.15	18.05	17.92	17.80	17.75	18.02	18.06	18.43	17.88
MgO	16.83	16.83	17.22	16.66	18.20	16.43	16.70	17.30	16.94	16.92	16.26	16.43	16.18	16.90	16.49	16.61	16.47	16.77	16.88	16.98
MnO	0.05	0.04	0.07	0.06	0.02	0.06	0.09	0.12	0.13	0.10	0.09	0.17	0.13	0.13	0.11	0.12	0.10	0.12	0.13	0.05
NiO	0.25	0.29	0.35	0.36	0.33	0.32	<0.02	<0.02	<0.02	0.25	0.33	nd	nd	nd	nd	nd	nd	nd	nd	nd
Total	98.82	99.38	99.34	99.05	99.90	99.34	99.54	100.7	100.1	100.0	100.5	98.73	98.83	99.28	99.28	99.06	99.39	100.5	100.4	100.5

Appendix C-4 Spinel continued

Lithology	Grt-Spl Harzburgite												Spl Lherzolite							
Sample	PAK6				BN45		BN31						PA64		PAK1					
Grains [a]	Spl-1	Spl-2	Spl-3	Spl-4	Spl-1	Spl-2	Spl-1	Spl-2	Spl-3	Spl-4	Spl-5	Spl-6	Spl-1	Spl-2	Spl-1	Spl-2	Spl-3	Spl-4	Spl-5	spl-6
SiO_2	<0.03	<0.03	<0.03	<0.03	0.11	0.15	0.10	0.21	0.09	0.13	0.12	0.09	<0.03	0.04	<0.03	<0.03	<0.03	<0.03	<0.03	0.04
Al_2O_3	35.99	35.10	35.98	36.02	37.51	37.37	37.03	36.70	39.62	37.61	37.16	38.59	49.31	51.27	52.32	52.30	52.85	52.31	52.63	52.98
TiO_2	1.71	1.69	1.67	1.68	1.47	1.47	1.70	1.56	1.01	1.67	1.56	1.56	0.05	0.06	0.11	0.10	0.11	0.13	0.13	0.14
Cr_2O_3	24.94	25.41	25.57	24.50	25.34	24.97	25.33	25.93	24.49	24.52	25.45	24.14	18.19	16.08	15.96	16.01	15.43	16.15	16.05	15.29
FeO (t) [b]	21.19	21.18	21.02	21.27	18.28	17.95	17.92	17.82	16.94	17.43	17.61	17.39	14.17	13.31	11.75	11.70	11.19	11.51	11.35	11.63
MgO	14.81	14.74	14.93	15.08	16.65	16.83	16.66	16.66	16.98	16.85	16.78	17.12	17.97	19.10	19.21	19.00	19.83	18.97	19.24	19.34
MnO	0.12	0.17	0.12	0.18	0.06	0.09	0.06	0.09	0.09	0.05	0.05	0.06	0.10	0.03	0.07	0.08	0.04	0.08	0.13	0.10
NiO	0.38	0.34	0.34	0.33	0.34	0.37	0.45	0.39	0.32	0.38	0.37	0.43	nd	nd	0.32	0.31	0.35	0.33	0.30	0.34
Total	99.15	98.65	99.65	99.09	99.78	99.22	99.27	99.41	99.54	98.66	99.10	99.39	99.80	99.90	99.78	99.54	99.82	99.51	99.84	99.86

Appendix C-4 Spinel continued

Lithology	Spl Harzburgite																			
Sample	LS5						PAK2		PAK3				LS100							
Grains [a]	Spl-1	Spl-2	Spl-3	Spl-4	Spl-5	Spl-6	Spl-1	Spl-2	Spl-1	Spl-2	Spl-3	Spl-4	Spl-1	Spl-2	Spl-3	Spl-4	Spl-5	Spl-6	Spl-7	Spl-8
SiO_2	0.08	0.09	0.09	0.09	0.10	0.11	0.06	0.08	0.06	0.07	0.05	0.07	0.09	0.08	0.08	0.07	0.09	0.07	0.07	0.08
Al_2O_3	27.47	27.35	27.31	27.25	27.66	27.47	27.40	27.23	26.98	27.71	27.64	27.10	26.56	26.47	26.14	26.22	26.38	26.64	26.75	26.47
TiO_2	2.50	2.55	2.28	2.34	2.22	2.29	0.16	0.15	0.18	0.18	0.17	0.18	2.49	2.47	2.67	2.68	2.61	2.59	2.53	2.53
Cr_2O_3	34.87	34.53	34.91	34.72	35.37	35.09	41.37	41.32	40.89	40.57	40.80	40.99	35.10	34.37	34.38	34.03	34.35	34.16	34.38	34.36
FeO (t) [b]	18.99	18.93	18.97	18.43	18.93	18.52	14.50	14.49	14.64	14.45	14.17	14.31	20.30	20.67	20.81	20.46	20.76	20.60	20.24	20.36
MgO	15.65	15.49	15.72	15.82	15.75	16.14	16.07	16.45	15.98	16.26	16.37	16.07	14.93	14.87	14.92	14.82	14.94	14.86	14.97	14.74
MnO	0.11	0.10	0.07	0.07	0.06	0.02	0.06	0.02	0.07	0.06	0.09	0.06	0.10	0.09	0.10	0.10	0.08	0.09	0.09	0.05
NiO	0.27	0.25	0.22	0.25	0.27	0.25	0.22	0.24	0.22	0.17	0.19	0.22	0.32	0.28	0.26	0.25	0.26	0.29	0.25	0.28
Total	99.96	99.30	99.59	98.97	100.4	99.91	99.85	100.0	99.04	99.50	99.49	99.01	99.89	99.30	99.37	98.62	99.46	99.30	99.28	98.88

Appendix C-4 Spinel continued

Lithology	Spl Harzburgite													Grt-Spl Websterite					
Sample	PAK5						01BN					BNH11		BNH7					
Grains [a]	Spl-1	Spl-2	Spl-3	Spl-4	Spl-5	Spl-6	Spl-1	Spl-2	Spl-3	Spl-4	Spl-5	Spl-1	Spl-2	Spl-1	Spl-2	Spl-3	Spl-4	Spl-5	Spl-6
SiO_2	0.15	0.12	0.12	0.15	0.14	0.12	<0.03	<0.03	<0.03	<0.03	<0.03	0.07	0.09	0.04	0.07	0.04	0.04	<0.03	<0.03
Al_2O_3	29.61	29.21	29.78	29.39	29.28	29.33	33.19	33.27	33.41	33.63	34.32	27.84	27.74	52.43	58.38	60.31	60.13	58.61	60.51
TiO_2	3.66	3.74	3.66	3.97	4.34	3.72	0.11	0.10	0.11	0.08	0.10	1.90	1.87	0.21	0.18	0.14	0.14	0.14	0.14
Cr_2O_3	25.44	25.08	25.76	25.03	25.32	26.27	34.03	34.49	33.83	33.58	32.93	35.39	34.70	11.84	7.81	5.99	5.95	6.82	5.83
FeO (t) [b]	24.37	25.33	24.44	26.17	25.06	24.55	17.63	17.57	17.21	16.39	16.96	19.16	19.09	14.67	13.65	12.68	12.59	13.21	12.06
MgO	15.03	15.03	14.84	14.86	14.91	15.11	13.92	14.23	14.23	15.10	14.81	14.86	15.15	18.53	19.76	20.24	20.26	19.95	20.57
MnO	0.06	0.06	0.07	0.08	0.06	0.07	0.13	0.13	0.13	0.11	0.12	0.14	0.10	0.09	0.11	0.06	0.05	0.07	0.06
NiO	0.41	0.38	0.39	0.38	0.39	0.38	0.14	0.11	0.11	0.13	0.13	0.27	0.30	0.48	0.46	0.55	0.50	0.53	0.51
Total	98.73	98.95	99.08	100.0	99.52	99.55	99.16	99.93	99.06	99.03	99.39	99.64	99.04	98.29	100.4	100.0	99.66	99.36	99.71

nd not determined

[a] Different numbers denote different grains

[b] Total Fe as FeO

Appendix C-5 Garnet

Lithology	Grt-Spl Lherzolite																		
Sample	LS33		TM0		TM2		LS50				BN73			LS1			BN32		
Grains [a]	Grt1	Grt2	Grt1	Grt2	Grt1	Grt2	Grt1	Grt2	Grt3	Grt4	Grt1	Grt2	Grt3	Grt1	Grt2	Grt3	Grt1	Grt2	Grt3
SiO_2	42.5	42.57	42.14	42.16	41.56	41.75	42.28	42.06	42.02	42.43	49.27	42.13	49.24	41.92	41.94	41.90	41.86	41.94	42.01
Al_2O_3	23.07	22.92	23.4	23.69	23.25	23.2	22.63	22.43	22.30	22.53	16.82	20.76	16.08	23.04	22.99	22.89	23.21	23.23	23.19
TiO_2	0.25	0.25	0.15	0.17	0.19	0.2	0.18	0.19	0.26	0.20	0.05	0.05	0.05	0.11	0.14	0.13	0.19	0.18	0.17
Cr_2O_3	1.86	1.99	1.36	1.27	1.28	1.51	1.76	1.86	1.86	1.78	1.29	2.91	1.56	1.87	1.88	1.85	1.28	1.18	1.16
FeO (t) [b]	6.92	7.13	8.09	8.08	7.63	7.87	7.70	7.79	7.76	7.63	6.16	6.84	6.13	7.54	7.39	7.51	8.89	8.77	8.88
MgO	21.33	21.45	20.4	20.56	20.08	20.38	20.57	20.43	20.62	20.54	20.20	21.23	22.20	20.23	20.17	20.36	19.73	19.76	19.66
MnO	0.29	0.28	0.33	0.32	0.37	0.36	0.28	0.29	0.20	0.27	0.35	0.32	0.40	0.32	0.30	0.32	0.34	0.33	0.31
CaO	4.86	5.09	5	4.83	4.76	4.98	5.03	5.11	5.01	5.02	6.26	4.54	5.64	5.15	5.03	5.11	5.03	4.99	5.01
Total	101.1	101.7	100.9	101.1	99.12	100.3	100.4	100.1	100.0	100.4	100.4	98.78	101.3	100.2	99.83	100.0	100.5	100.4	100.4

Appendix C-5 Garnet continued

Lithology	Grt-Spl Harzburgite																				Grt-Spl Websterite		
Sample	TM14			TM15		BN92		BN50		PAHK1		PAK6			BN45			BN31			BNH7		
Grains [a]	Grt1	Grt2	Grt3	Grt1	Grt2	Grt1	Grt2	Grt1	Grt2	Grt1	Grt2	Grt1	Grt2	Grt3	Grt1	Grt2	Grt3	Grt1	Grt2	Grt3	Grt1	Grt2	Grt3
SiO_2	42.12	42.16	42.04	42.45	42.27	41.36	42.12	41.76	42.27	42.24	42.28	41.51	41.48	41.44	41.92	41.82	41.96	42.35	42.42	41.94	41.77	41.66	41.90
Al_2O_3	23.52	23.36	23.64	23.7	23.61	22.82	23.4	23.01	23.18	22.87	23.17	22.76	23.08	23.10	23.44	23.13	23.04	22.72	22.56	22.59	23.67	23.85	24.00
TiO_2	0.3	0.18	0.17	0.26	0.28	0.44	0.22	0.3	0.27	0.3	0.2	0.27	0.19	0.37	0.30	0.32	0.34	0.32	0.34	0.37	0.10	0.10	0.09
Cr_2O_3	1.21	1.31	1.09	1.1	1.17	1.52	0.85	1.73	1.53	1.67	1.51	1.55	1.43	1.18	1.24	1.28	1.39	1.27	1.32	1.32	0.39	0.45	0.46
FeO (t) [b]	8.66	8.63	8.72	8.87	8.7	8.33	8.09	8.43	8.35	8.33	8.31	10.16	10.14	10.32	8.37	8.35	8.36	8.31	8.45	8.14	9.72	8.55	8.51
MgO	20.42	20.47	20.43	19.94	19.79	20.32	20.67	20.35	20.37	20.94	21.02	18.97	18.83	19.08	20.14	20.05	20.05	20.77	20.60	20.53	19.22	19.90	20.11
MnO	0.34	0.33	0.35	0.38	0.33	0.24	0.38	0.33	0.34	0.31	0.33	0.33	0.34	0.32	0.30	0.32	0.30	0.29	0.32	0.28	0.38	0.32	0.32
CaO	4.65	4.89	4.77	4.88	4.68	4.45	4.6	5.2	4.94	4.46	4.41	4.69	4.78	4.67	4.93	5.01	4.91	4.53	4.47	4.55	5.02	4.96	4.85
Total	101.2	101.3	101.2	101.6	100.8	99.48	100.3	101.1	101.3	101.1	101.2	100.2	100.3	100.5	100.6	100.3	100.3	100.6	100.5	99.71	100.3	99.80	100.2

[a] Different numbers denote different grains

[b] Total Fe as FeO

Appendix D

Mineral compositions in mantle Grt orthopyroxenite xenoliths from Pali Aike area determined with an electrom microprobe

Appendix D-1 Olivine

Sample	BN43							BNO5									BNC2			
Grains [a]	Ol-1	Ol-2	Ol-3	Ol-4	Ol-5	Ol-6	SD[c](±)	Ol-1	Ol-2	Ol-3	Ol-4	Ol-5	Ol-6	Ol-7	Ol-8	SD[c](±)	Ol-1	Ol-2	Ol-3	SD[c](±)
SiO_2	40.03	39.99	39.87	40.51	40.37	39.96	0.26	40.77	41.29	41.21	41.28	40.91	41.05	40.74	40.84	0.23	39.92	39.98	40.02	0.05
TiO_2	0.06	<0.04	0.05	<0.04	<0.04	<0.04	0.01	<0.04	<0.04	0.04	0.06	<0.04	0.07	0.05	0.10	0.02	0.12	0.07	<0.04	0.04
Al_2O_3	0.03	0.04	<0.02	0.03	0.06	0.06	0.01	0.08	0.06	0.04	0.06	0.04	0.04	0.04	0.05	0.01	0.06	0.05	0.06	0.01
Cr_2O_3	<0.03	0.05	<0.03	0.03	<0.03	<0.03	0.02	0.05	0.03	0.04	<0.03	<0.03	0.03	0.03	0.07	0.01	<0.03	0.03	<0.03	
FeO (t)[b]	12.20	12.33	12.37	12.43	12.47	12.99	0.27	13.60	13.17	13.43	13.23	13.24	13.44	13.73	13.43	0.19	15.42	15.61	15.16	0.23
MnO	0.13	0.10	0.12	0.14	0.11	0.14	0.02	0.11	0.13	0.14	0.14	0.09	0.13	0.09	0.14	0.02	0.19	0.19	0.10	0.05
MgO	47.05	46.85	47.41	47.19	47.44	47.36	0.23	46.00	45.94	46.13	46.37	46.27	46.35	45.94	46.08	0.18	44.11	43.70	43.83	0.21
CaO	0.06	0.10	0.05	0.01	0.03	0.08	0.03	0.09	0.11	0.06	0.11	0.11	0.17	0.04	0.09	0.04	0.09	0.10	0.10	0.01
Na_2O	0.02	0.03	0.03	0.06	0.09	0.04	0.03	0.05	0.02	0.03	<0.02	<0.02	0.03	0.03	0.03	0.01	<0.02	<0.02	<0.02	
NiO	0.33	0.40	0.37	0.36	0.39	0.34	0.03	0.48	0.50	0.47	0.53	0.41	0.48	0.45	0.41	0.04	0.36	0.47	0.40	0.06
Fo	87.3	87.1	87.2	87.1	87.1	86.7	0.22	85.8	86.2	86.0	86.2	86.2	86.0	85.6	86.0	0.20	83.6	83.3	83.8	0.23
Total	99.91	99.90	100.3	100.8	101.0	101.0		101.3	101.2	101.6	101.8	101.1	101.8	101.1	101.2		100.3	100.2	99.85	

Appendix D-1 Olivine continued

Sample	BNC1									BN92 (veinlet of orthopyroxenite)					BNH13								
Grains [a]	Ol-1	Ol-2	Ol-3	Ol-4	Ol-5	Ol-6	Ol-7	Ol-8	SD[c](±)	Ol-1	Ol-2	Ol-3	Ol-4	SD[c](±)	Ol-1	Ol-2	Ol-3	Ol-4	Ol-5	Ol-6	Ol-7	Ol-8	SD[c](±)
SiO_2	40.69	40.85	40.94	40.81	40.97	40.97	40.20	40.68	0.25	40.40	40.70	41.12	41.15	0.36	40.53	41.41	40.66	40.00	39.98	40.22	40.64	40.90	0.48
TiO_2	0.04	<0.04	0.09	0.07	0.06	0.08	0.13	0.12	0.03	0.08	0.06	<0.04	<0.04	0.01	<0.04	<0.04	<0.04	0.05	0.07	<0.04	<0.04	0.06	0.01
Al_2O_3	0.03	0.05	0.05	0.06	0.04	0.07	0.10	0.13	0.03	0.03	<0.02	<0.02	0.03	0.00	<0.02	<0.02	<0.02	<0.02	<0.02	0.05	0.05	0.07	0.01
Cr_2O_3	0.07	<0.03	0.08	<0.03	<0.03	0.03	<0.03	0.10	0.03	<0.03	<0.03	<0.03	<0.03		<0.03	<0.03	<0.03	<0.03	<0.03	<0.03	0.03	0.03	0.00
FeO (t)[b]	13.06	12.76	12.90	13.11	13.55	13.61	12.85	12.95	0.32	10.63	10.88	11.13	10.83	0.21	12.95	12.96	12.19	12.79	12.87	12.15	11.97	9.49	1.15
MnO	0.11	0.21	0.09	0.14	0.15	0.05	0.09	0.17	0.05	0.04	0.04	0.13	0.09	0.04	0.13	0.10	0.09	0.06	0.10	0.15	0.11	0.10	0.03
MgO	47.18	47.10	47.19	46.76	46.48	46.08	46.78	45.62	0.56	47.24	47.39	47.20	47.55	0.16	45.94	46.54	46.12	45.97	46.17	46.87	47.08	48.39	0.83
CaO	0.11	0.10	0.09	0.09	0.10	0.10	0.11	0.51	0.15	0.06	0.06	0.08	0.07	0.01	0.05	0.05	0.08	0.04	0.07	0.13	0.07	0.14	0.04
Na_2O	0.07	0.03	0.03	0.04	<0.02	0.03	0.03	0.05	0.01	<0.02	<0.02	<0.02	<0.02		<0.02	<0.02	<0.02	<0.02	0.04	<0.02	<0.02	<0.02	
NiO	0.49	0.36	0.39	0.47	0.37	0.33	0.34	0.18	0.09	0.42	0.38	0.34	0.43	0.04	0.44	0.41	0.41	0.41	0.40	0.39	0.35	0.39	0.03
Fo	86.6	86.8	86.7	86.4	85.9	85.8	86.6	86.3	0.37	88.8	88.6	88.3	88.7	0.20	86.3	86.5	87.1	86.5	86.5	87.3	87.5	90.1	1.24
Total	101.8	101.5	101.8	101.6	101.7	101.4	100.6	100.5		98.91	99.54	100.0	100.1		100.0	101.5	99.63	99.33	99.73	100.0	100.3	99.60	

[a] Different numbers denote different grains; [b] Total Fe as FeO; [c] SD = Standard deviation

Appendix D-2 Clinopyroxene

Sample	BN46						BNH5			BN92			BNH13							BNC1	BN42		
Grains [a]	Cpx1	Cpx2	Cpx3	Cpx1	Cpx2	SD[c] (±)	Cpx1	Cpx2	SD[c] (±)	Cpx1	Cpx2	SD[c] (±)	Cpx1	Cpx2	Cpx3	Cpx4	Cpx5	Cpx6	SD[c] (±)	Cpx1	Cpx1	Cpx2	SD[c] (±)
SiO_2	52.30	52.45	52.87	52.36	52.67	0.24	52.62	53.26	0.45	52.03	51.83	0.14	51.13	50.91	50.34	50.52	52.75	50.29	0.92	51.60	51.85	51.83	0.02
TiO_2	0.89	1.07	0.93	1.20	0.94	0.13	0.65	1.04	0.28	1.59	1.16	0.30	1.42	1.49	1.46	1.03	0.92	1.92	0.36	1.42	1.26	1.46	0.14
Al_2O_3	5.79	5.73	5.69	5.74	5.78	0.04	5.51	5.77	0.18	6.33	5.73	0.43	7.55	6.82	6.65	6.55	4.98	7.87	1.01	6.60	6.02	5.91	0.08
Cr_2O_3	0.50	0.31	0.25	0.31	0.23	0.10	0.39	0.44	0.03	0.34	1.13	0.56	0.72	0.65	1.16	0.40	0.49	0.51	0.27	1.01	0.45	0.29	0.11
FeO (t) [b]	5.21	5.12	5.41	5.25	5.13	0.12	3.96	4.02	0.04	3.96	3.47	0.35	4.04	3.19	3.67	3.83	4.90	4.41	0.60	4.58	3.91	4.27	0.25
MnO	0.11	0.11	0.09	0.09	0.05	0.03	0.06	0.06	0.00	0.07	0.13	0.04	0.06	0.03	0.06	0.09	0.17	0.08	0.05	0.06	0.04	0.10	0.05
MgO	14.74	14.67	14.41	14.31	13.70	0.41	15.12	14.84	0.20	14.58	15.04	0.32	14.18	17.38	16.59	14.77	17.17	14.13	1.51	14.83	15.25	15.04	0.15
CaO	18.60	18.51	18.61	18.44	17.29	0.56	17.32	17.57	0.18	19.44	18.96	0.34	18.79	17.27	17.71	19.20	17.26	19.36	0.96	17.37	18.76	19.08	0.23
Na_2O	2.13	2.19	2.01	1.99	2.05	0.08	1.86	1.83	0.02	1.73	1.75	0.02	1.84	1.32	1.21	1.67	1.66	1.68	0.24	2.18	1.84	1.67	0.12
NiO	0.05	0.03	0.03	nd	nd	0.01	<0.03	0.05		0.17	0.02	0.10	0.05	0.24	0.04	0.03	0.09	nd	0.09	0.17	0.09	nd	
Mg#	0.835	0.836	0.826	0.829	0.826	0.005	0.872	0.868	0.003	0.868	0.885	0.012	0.862	0.907	0.890	0.873	0.862	0.851	0.021	0.852	0.874	0.863	0.008
Total	100.3	100.2	100.3	99.69	97.84		97.48	98.87		100.2	99.22		99.77	99.29	98.88	98.11	100.4	100.3		99.83	99.47	99.65	

nd not determined

[a] Different numbers denote different grains

[b] Total Fe as FeO

[c] SD = Standard deviation

Appendix D-3 Orthopyroxene

Sample	BNH5																			
Grains [a]	Opx1	Opx2	Opx3	Opx4	Opx5	Opx6	Opx7	Opx8	Opx9	Opx10	Opx11	Opx12	Opx13	Opx14	Opx15	Opx16	Opx17	Opx18	Opx19	SD[c] (±)
SiO_2	55.91	56.14	55.65	56.28	55.04	55.98	55.59	55.97	55.59	55.81	55.89	56.08	55.44	55.64	55.92	56.08	55.41	54.37	55.58	0.44
TiO_2	0.30	0.34	0.28	0.33	0.46	0.33	0.29	0.27	0.36	0.20	0.26	0.40	0.28	0.33	0.26	0.26	0.37	0.32	0.38	0.06
Al_2O_3	3.60	3.55	3.56	3.61	3.61	3.69	3.59	3.71	3.59	3.31	3.64	3.62	3.57	3.58	3.16	3.45	3.58	3.69	3.61	0.13
Cr_2O_3	0.25	0.27	0.28	0.29	0.29	0.32	0.29	0.30	0.31	0.16	0.35	0.30	0.35	0.30	0.15	0.19	0.30	0.32	0.28	0.06
FeO (t) [b]	8.08	8.10	8.08	8.22	7.81	7.90	8.04	8.02	7.95	7.72	7.69	7.83	7.70	8.12	7.86	8.10	7.82	7.69	8.02	0.17
MnO	0.15	0.14	0.21	0.17	0.14	0.13	0.14	0.13	0.12	0.16	0.06	0.08	0.17	0.14	0.13	0.17	0.10	0.14	0.11	0.03
MgO	31.62	31.77	31.23	31.69	31.47	31.98	31.88	32.00	31.73	32.39	31.75	31.76	31.93	31.97	32.12	31.65	31.54	32.09	32.39	0.29
CaO	0.60	0.60	0.60	0.65	0.60	0.55	0.61	0.55	0.63	0.61	0.56	0.58	0.63	0.60	0.64	0.57	0.61	0.68	0.54	0.04
Na_2O	0.17	0.15	0.13	0.17	0.17	0.11	0.12	0.11	0.11	0.31	0.12	0.12	0.17	0.13	0.17	0.14	0.20	0.21	0.19	0.05
NiO	0.13	0.12	0.13	0.18	0.16	0.14	0.10	0.13	0.13	0.13	0.16	0.14	0.14	0.16	0.15	0.14	0.12	0.16	0.27	0.03
Mg#	0.875	0.875	0.873	0.873	0.878	0.878	0.876	0.877	0.877	0.882	0.880	0.879	0.881	0.875	0.879	0.875	0.878	0.882	0.878	0.003
Total	100.8	101.2	100.2	101.6	99.74	101.1	100.7	101.2	100.5	100.8	100.5	100.9	100.4	101.0	100.6	100.7	100.0	99.66	101.4	

Appendix D-3 Orthopyroxene continued

Sample	BN43									BNO5							BN92				
Grains [a]	Opx1	Opx2	Opx3	Opx4	Opx5	Opx6	Opx7	Opx8	SD[c] (±)	Opx1	Opx2	Opx3	Opx4	Opx5	Opx6	SD[c] (±)	Opx1	Opx2	Opx3	Opx4	SD[c] (±)
SiO_2	55.16	54.86	55.35	54.25	55.33	55.06	55.92	55.11	0.47	55.72	56.13	55.52	55.40	56.01	55.20	0.36	55.45	54.93	56.07	55.97	0.53
TiO_2	0.32	0.34	0.35	0.31	0.36	0.39	0.32	0.32	0.03	0.38	0.44	0.30	0.42	0.30	0.43	0.07	0.51	0.45	0.47	0.50	0.03
Al_2O_3	3.66	3.67	3.60	3.64	3.75	3.53	3.45	3.70	0.10	3.97	4.04	3.77	4.10	3.84	4.14	0.15	3.91	4.18	4.00	4.04	0.11
Cr_2O_3	0.32	0.31	0.34	0.28	0.31	0.33	0.28	0.31	0.02	0.29	0.34	0.48	0.38	0.48	0.31	0.09	0.33	0.42	0.41	0.40	0.04
FeO (t) [b]	7.91	7.79	8.13	7.77	7.83	7.70	7.77	7.90	0.13	8.41	8.55	8.29	8.69	8.75	8.60	0.17	6.86	7.12	6.93	6.78	0.15
MnO	0.11	0.17	0.17	0.14	0.13	0.11	0.13	0.10	0.03	0.13	0.14	0.12	0.11	0.12	0.12	0.01	0.14	0.12	0.13	0.16	0.02
MgO	32.37	32.23	32.52	32.11	32.33	32.23	32.42	32.57	0.16	31.28	31.21	31.41	31.34	31.50	30.95	0.19	32.13	31.74	32.11	31.75	0.22
CaO	0.51	0.63	0.60	0.58	0.61	0.58	0.59	0.68	0.05	0.74	0.74	0.78	0.78	0.80	0.74	0.03	0.74	0.73	0.73	0.71	0.01
Na_2O	0.14	0.13	0.14	0.17	0.16	0.14	0.17	0.14	0.02	0.19	0.15	0.12	0.16	0.15	0.16	0.02	0.14	0.11	0.15	0.14	0.02
NiO	0.21	0.24	0.25	0.22	0.22	0.14	0.11	0.13	0.05	0.17	0.13	0.15	0.09	0.12	0.09	0.03	0.15	0.11	0.11	0.14	0.02
Mg#	0.880	0.881	0.877	0.881	0.880	0.882	0.881	0.880	0.001	0.869	0.867	0.871	0.865	0.865	0.865	0.002	0.893	0.888	0.892	0.893	0.002
Total	100.7	100.4	101.4	99.46	101.0	100.2	101.2	101.0		101.3	101.9	100.9	101.5	102.1	100.7		100.4	99.91	101.1	100.6	

Appendix D-3 Orthopyroxene continued

Sample	BNC1													BNC2					
Grains [a]	Opx1	Opx2	Opx3	Opx4	Opx5	Opx6	Opx7	Opx8	Opx9	Opx10	Opx11	Opx12	SD[c] (±)	Opx1	Opx2	Opx3	Opx4	Opx5	SD[c] (±)
SiO_2	55.31	55.62	55.88	55.48	55.76	55.63	55.36	55.66	55.19	54.84	55.50	55.38	0.28	54.34	55.23	54.29	55.07	54.73	0.42
TiO_2	0.45	0.53	0.47	0.39	0.40	0.46	0.49	0.43	0.44	0.43	0.59	0.46	0.05	0.43	0.48	0.48	0.37	0.44	0.05
Al_2O_3	3.93	3.90	4.13	4.08	4.13	3.94	3.95	3.87	4.01	4.01	3.97	4.00	0.08	3.80	3.90	3.85	5.10	4.16	0.54
Cr_2O_3	0.32	0.32	0.30	0.28	0.33	0.36	0.43	0.39	0.33	0.35	0.26	0.33	0.05	0.30	0.37	0.32	0.23	0.30	0.05
FeO (t) [b]	8.43	8.43	8.38	8.49	8.44	8.23	8.38	8.20	8.45	8.56	8.20	8.43	0.12	9.71	9.75	9.54	8.35	9.34	0.58
MnO	0.10	0.10	0.10	0.10	0.13	0.10	0.12	0.09	0.24	0.23	0.15	0.20	0.05	0.17	0.14	0.14	0.18	0.16	0.02
MgO	31.55	31.56	31.57	31.58	31.45	31.65	31.84	31.68	31.79	31.34	31.39	31.66	0.15	30.17	30.27	30.58	30.18	30.30	0.16
CaO	0.81	0.74	0.85	0.81	0.81	0.81	0.78	0.83	0.72	0.82	0.91	0.81	0.05	0.76	0.83	0.79	0.78	0.79	0.03
Na_2O	0.21	0.21	0.22	0.19	0.20	0.22	0.18	0.17	0.20	0.20	0.20	0.22	0.02	0.23	0.24	0.21	0.08	0.19	0.06
NiO	0.14	0.16	0.18	0.13	0.20	0.18	0.17	0.12	0.06	0.14	0.13	0.17	0.04	0.09	0.13	0.11	0.08	0.10	0.02
Mg#	0.870	0.870	0.870	0.869	0.869	0.873	0.871	0.873	0.870	0.867	0.872	0.870	0.002	0.847	0.847	0.851	0.866	0.853	0.008
Total	101.2	101.6	102.1	101.5	101.8	101.6	101.7	101.4	101.4	100.9	101.3	101.7		99.99	101.3	100.3	100.5	100.5	

Appendix D-3 Orthopyroxene continued

Sample	BNH13								BN46													BN42			
Grains [a]	Opx1	Opx2	Opx3	Opx4	Opx5	Opx6	Opx7	SD[c] (±)	Opx1	Opx2	Opx3	Opx4	Opx5	Opx6	Opx7	Opx8	Opx9	Opx10	Opx11	SD[c] (±)	Opx1	Opx2	Opx3	SD[c] (±)
SiO_2	56.41	55.50	55.06	55.66	55.32	55.19	55.49	0.44	55.29	55.19	55.82	55.89	55.36	55.08	55.34	56.25	56.62	56.21	55.87	0.50	55.63	54.91	55.56	0.40
TiO_2	0.23	0.20	0.37	0.26	0.34	0.28	0.22	0.06	0.25	0.28	0.27	0.06	0.29	0.24	0.24	0.37	0.32	0.36	0.32	0.09	0.30	0.43	0.43	0.08
Al_2O_3	3.27	3.61	3.50	3.51	3.66	3.54	3.33	0.14	3.05	2.87	3.17	3.33	3.82	3.24	3.15	3.17	3.12	3.00	3.39	0.25	3.73	3.78	3.56	0.12
Cr_2O_3	0.31	0.36	0.30	0.31	0.31	0.25	0.19	0.05	0.11	0.15	0.17	0.31	0.24	0.18	0.14	0.15	0.13	0.09	0.14	0.06	0.28	0.30	0.21	0.05
FeO (t) [b]	8.06	8.16	7.84	7.87	8.17	8.41	8.45	0.24	9.48	9.40	9.78	9.55	9.33	9.49	9.90	9.51	9.04	9.84	9.40	0.25	7.31	7.79	7.78	0.27
MnO	0.10	0.13	0.13	0.09	0.16	0.13	0.13	0.02	0.18	0.14	0.11	0.08	0.08	0.13	0.13	0.13	0.13	0.18	0.18	0.04	0.06	0.10	0.18	0.06
MgO	31.10	31.24	31.70	31.65	32.23	31.74	31.99	0.39	31.57	31.59	31.02	31.44	30.27	31.51	30.30	30.73	30.81	30.55	30.32	0.54	30.92	31.74	32.07	0.59
CaO	0.66	0.64	0.66	0.64	0.60	0.61	0.64	0.02	0.80	0.80	0.76	0.60	0.75	0.79	0.80	0.81	0.82	0.83	0.80	0.06	0.76	0.75	0.77	0.01
Na_2O	0.15	0.16	0.12	0.12	0.13	0.13	0.11	0.02	0.13	0.19	0.15	0.17	0.17	0.17	0.13	0.13	0.11	0.15	0.15	0.02	0.13	0.14	0.17	0.02
NiO	0.13	0.11	0.17	0.16	nd	nd	nd	0.03	0.13	0.15	0.05	0.09	0.04	0.09	0.13	0.08	0.11	0.03	0.14	0.04	0.20	nd	nd	
Mg#	0.873	0.872	0.878	0.878	0.876	0.871	0.871	0.003	0.856	0.857	0.850	0.854	0.853	0.856	0.845	0.852	0.859	0.847	0.852	0.004	0.883	0.879	0.880	0.002
Total	100.4	100.1	99.83	100.3	100.9	100.3	100.6		101.0	100.8	101.3	101.5	100.4	100.9	100.2	101.3	101.2	101.2	100.7		99.31	99.94	100.7	

nd not determined; [a] Different numbers denote different grains; [b] Total Fe as FeO; [c] SD = Standard deviation.

Appendix D-4 Garnet

Sample	BN42			BN46				BNH5			BNO5	BNH13		
Grains [a]	Grt1	Grt2	Grt3	Grt1	Grt2	Grt3	Grt4	Grt1	Grt2	Grt3	Grt1	Grt1	Grt2	Grt3
SiO_2	42.17	41.95	42.38	41.94	41.56	41.41	41.7	42.48	41.99	42.38	42.45	41.94	42.01	41.87
TiO_2	0.36	0.39	0.33	0.20	0.28	0.28	0.28	0.19	0.18	0.14	0.42	0.34	0.29	0.39
Al_2O_3	23.66	23.36	23.95	23.27	23.34	23.34	23.34	23.78	23.89	23.92	23.36	23.80	23.81	23.79
Cr_2O_3	0.46	0.71	0.2	0.46	0.62	0.44	0.8	0.37	0.39	0.43	0.97	1.01	0.91	1.11
FeO (t) [b]	9.19	9.32	9.06	11.84	11.68	11.86	11.5	9.76	9.61	9.43	9.19	10.03	9.85	10.2
MnO	0.36	0.37	0.35	0.38	0.44	0.39	0.49	0.30	0.30	0.24	0.32	0.34	0.31	0.37
MgO	20.38	20.26	20.49	18.58	18.12	18.07	18.16	20.40	20.11	19.87	20.32	19.89	19.9	19.87
CaO	4.42	4.49	4.34	4.82	4.79	4.78	4.8	3.98	4.03	3.98	3.99	4.33	4.23	4.43
Total	100.98	100.85	101.1	101.53	100.82	100.57	101.07	101.35	100.59	100.62	101.11	101.67	101.31	102.03

[a] Different numbers denote different grains

[b] Total Fe as FeO

Appendix D-5 Ilmenite

Sample	BNC1			BNC2	BN92			BN46		BNH13			BN42	
Grains [a]	Ilm1	Ilm2	Ilm3	Ilm1	Ilm1	Ilm2	Ilm3	Ilm1	Ilm2	Ilm1	Ilm2	Ilm3	Ilm1	Ilm2
TiO_2	57.53	53.49	54.63	55.09	55.09	56.19	55.12	56.68	56.24	56.44	55.70	56.50	56.45	56.35
Al_2O_3	0.05	1.44	0.90	0.24	1.38	1.36	1.44	1.14	0.91	0.78	1.65	1.73	1.47	1.78
Cr_2O_3	1.06	2.42	1.80	1.10	1.84	1.98	2.05	0.69	0.72	1.63	1.26	1.16	1.45	1.47
FeO (t) [b]	30.91	28.80	30.14	32.24	26.89	27.47	26.41	31.28	31.85	29.52	30.31	29.97	28.42	28.72
MnO	0.18	0.16	0.21	0.26	0.34	0.30	0.31	0.20	0.40	0.23	0.44	0.39	0.23	0.29
MgO	12.38	13.10	12.02	11.09	13.66	13.53	14.23	11.72	11.07	12.54	11.87	12.03	13.12	12.93
CaO	0.03	0.05	0.03	0.04	0.02	0.02	0.07	0.04	0.05	0.03	0.03	0.04	0.03	0.04
Total	102.14	99.46	99.72	100.05	99.21	100.85	99.63	101.75	101.24	101.17	101.26	101.82	101.17	101.58

[a] Different numbers denote different grains

[b] Total Fe as FeO

Appendix D-6 Phlogopite and amphibole

Sample	BN46				BNC2			BN42			BNH13
Grains [a]	Phl-1	Phl-2	Phl-3	Amp1	Phl-1	Amp1	Amp2	Phl-1	Phl-2	Amp1	Amp1
SiO_2	38.39	38.68	37.96	39.51	37.38	54.07	51.78	38.56	37.88	50.31	56.04
TiO_2	5.18	5.23	5.16	6.37	7.13	4.83	3.93	4.95	6.49	2.96	3.38
Al_2O_3	15.72	16.21	15.57	14.73	15.18	15.38	18.56	15.43	15.48	19.63	19.24
Cr_2O_3	0.33	0.33	0.31	<0.04	0.60	<0.04	<0.04	0.62	0.62	<0.04	<0.04
FeO (t) [b]	6.36	6.19	6.22	9.63	6.69	5.24	7.91	5.27	5.40	6.65	5.04
MnO	0.03	0.00	0.00	0.17	0.04	0.06	0.20	0.06	0.03	0.14	0.12
MgO	19.26	18.99	19.28	13.44	17.37	3.58	5.54	18.40	19.22	5.17	3.23
CaO	0.07	0.07	0.02	9.74	0.04	5.87	7.28	0.02	0.03	10.41	7.31
Na_2O	0.76	0.75	0.69	2.98	0.59	3.28	0.67	0.59	0.53	0.96	0.98
K_2O	9.46	9.17	9.13	1.22	9.85	5.65	3.03	9.07	9.38	1.19	1.53
Cl	0.03	0.02	0.03	<0.02	0.02	<0.02	0.03	<0.02	0.02	<0.02	0.10
F	0.19	0.18	0.10	0.27	0.28	0.04	0.03	0.16	0.28	0.05	0.16
Total	95.77	95.81	94.83	98.09	95.49	98.18	99.00	93.42	95.47	97.53	97.13

[a] Different numbers denote different grains

[b] Total Fe as FeO

Appendix D-7 Spinel

Sample	BNC2					BNH5		
Grains [a]	Spl-1	Spl-2	Spl-3	Spl-4	Spl-5	Spl-1	Spl-2	Spl-3
SiO_2	0.15	0.15	0.15	0.17	0.17	0.03	0.02	0.03
TiO_2	0.81	0.65	0.73	0.74	0.83	0.49	0.48	0.90
Al_2O_3	58.76	60.67	59.42	61.57	58.86	56.99	57.82	47.20
Cr_2O_3	4.50	3.76	4.43	3.30	4.24	7.09	7.29	16.13
FeO (t) [b]	15.03	13.69	15.42	13.92	14.68	14.08	14.18	17.05
MnO	0.14	0.14	0.17	0.09	0.09	<0.03	<0.03	<0.03
MgO	19.65	20.40	19.59	20.64	19.85	19.61	19.69	17.57
CaO	0.02	0.03	0.01	0.02	0.00	0.00	0.00	0.01
Na_2O	0.01	0.01	0.01	0.02	0.09	0.02	0.02	0.01
NiO	0.44	0.26	0.35	0.30	0.29	0.50	0.44	0.46
Total	99.51	99.76	100.28	100.77	99.10	98.81	99.94	99.38

[a] Different numbers denote different grains

[b] Total Fe as FeO

Appendix E

Whole- rock major and selected trace element compositions for Pali Aike mantle xenoliths and host basalts

Rock type	Grt-Spl Lherzolite							Grt-Spl Harzburgite								Host Basalt		
Sample	LS33	TM0	TM2	LS50	BN73	LS1	BN32	TM14	TM15	BN92	BN50	PAHK1	PAK6	BN45	BN31	LLS1v	TM15v	PAHK1v
Major (wt%)																		
SiO_2	44.69	44.24	44.20	43.87	43.04	44.02	45.00	44.01	44.49	46.74	42.76	44.38	45.18	45.58	45.62	44.59	41.72	38.24
Al_2O_3	3.14	4.18	3.73	1.97	1.53	2.57	3.86	3.47	3.12	3.80	3.84	3.62	3.16	3.89	3.64	11.32	9.06	9.26
TiO_2	0.12	0.14	0.16	0.16	0.05	0.10	0.18	0.17	0.13	0.29	0.18	0.15	0.32	0.18	0.20	3.46	2.60	3.80
MgO	40.41	38.35	39.25	41.02	44.54	41.13	38.19	40.75	40.52	38.40	40.65	40.20	38.57	39.13	39.60	10.85	17.10	12.38
Fe_2O_3(t)	8.78	9.17	9.02	9.30	9.10	8.95	9.21	10.35	10.73	9.70	10.59	10.52	11.98	9.93	10.11	13.29	12.63	13.40
MnO	0.13	0.14	0.14	0.12	0.12	0.13	0.13	0.14	0.14	0.13	0.14	0.14	0.14	0.14	0.13	0.17	0.18	0.16
CaO	2.43	3.33	2.86	2.83	1.24	2.29	2.97	1.09	0.99	1.04	1.21	0.68	0.66	0.87	0.75	8.74	9.06	9.59
K_2O	0.00	0.00	0.02	0.00	0.00	0.01	0.04	0.02	0.00	0.00	0.01	0.01	0.01	0.01	0.00	1.95	1.66	0.50
P_2O_5	0.02	0.02	0.02	0.02	0.02	0.02	0.03	0.03	0.02	0.03	0.03	0.02	0.03	0.02	0.03	0.75	0.99	0.78
Na_2O	<0.05	<0.05	<0.05	<0.05	<0.05	<0.05	0.05	<0.05	<0.05	<0.05	<0.05	<0.05	<0.05	<0.05	<0.05	3.05	2.96	2.62
Sum	100.0	99.98	99.82	99.73	99.89	99.59	100.1	100.2	100.3	100.3	99.85	99.98	100.3	99.98	100.3	98.44	98.31	90.99
Trace (ppm)																		
Ni	1720	1740	1410	2370	2460	2250	1930	1710	1970	1550	1510	2190	2340	2330	2370	204	497	241
Cr	2800	2420	2780	2260	2360	2470	2620	2510	2540	2680	5440	2650	1730	2450	2170	313	650	295
Co	105	104	102	113	116	109	128	114	112	107	116	114	119	113	113	52	64	60
Zn	50	51	51	58	55	52	60	72	78	64	79	70	90	64	67	126	119	118
V	60	60	65	53	46	46	73	47	44	67	68	53	40	51	61	234	174	237
Zr	<10	11	18	12	<10	<10	20	17	18	17	16	15	25	16	15	245	235	231
Sr	13	18	15	16	10	14	21	9	8	7	14	7	10	6	8	765	958	782

Appendix E continued

Rock type	Spl Lherzolite		Spl Harzburgite						Grt Orthopyroxenite								Ol Websterite			
Sample	PA64	PAK1	LS5	PAK2	PAK3	LS100	PAK5	01BN	BNH13	BNC2	BNC1	BN43	BNO5	BNC3	BNH5	BN42	BNH7	BNC4	BN31x	LLS3
Major (wt%)																				
SiO_2	43.82	44.36	43.14	43.65	43.84	43.42	43.00	44.04	52.58	53.02	52.76	53.95	52.53	51.74	48.80	47.75	48.84	49.51	50.95	51.47
Al_2O_3	1.64	2.09	1.22	0.98	0.95	1.15	1.51	1.40	5.65	4.28	4.05	3.62	5.22	4.57	11.34	10.06	9.85	6.54	6.00	5.58
TiO_2	0.05	0.10	0.14	0.05	0.05	0.14	0.34	0.04	0.46	0.84	1.20	0.70	0.55	2.00	0.29	2.60	0.36	1.21	1.02	0.91
MgO	43.52	41.69	43.95	45.59	46.05	44.08	40.92	44.47	30.24	29.93	30.71	31.93	30.34	30.68	26.80	27.31	20.58	16.40	17.46	19.08
Fe_2O_3(t)	9.53	8.40	10.21	8.03	8.13	10.32	13.52	8.88	9.07	10.56	9.53	8.64	9.69	9.74	9.66	9.86	6.00	9.76	10.07	10.68
MnO	0.14	0.12	0.12	0.11	0.11	0.12	0.13	0.13	0.14	0.13	0.11	0.12	0.13	0.12	0.19	0.18	0.14	0.14	0.15	0.15
CaO	1.23	2.56	0.31	0.94	0.67	0.41	0.46	0.85	1.54	0.92	0.93	0.91	1.04	0.78	2.19	2.04	12.32	13.71	12.59	10.48
K_2O	0.01	0.01	0.01	0.01	0.01	0.00	0.01	0.01	0.27	0.14	0.02	0.02	0.02	0.03	0.01	0.01	0.03	0.07	0.01	0.00
P_2O_5	0.02	0.02	0.02	0.02	0.02	0.02	0.03	0.01	0.03	0.02	0.02	0.02	0.01	0.02	0.05	0.02	0.03	0.05	0.02	0.03
Na_2O	<0.05	<0.05	<0.05	<0.05	<0.05	<0.05	<0.05	<0.05	<0.05	<0.05	<0.05	<0.05	<0.05	<0.05	<0.05	<0.05	0.89	1.61	1.47	1.30
Sum	100.1	99.69	99.37	99.61	100.0	99.89	100.2	100.2	100.2	100.2	99.64	100.1	99.87	100.0	99.61	100.1	99.45	99.19	99.94	99.94
Trace (ppm)																				
Ni	2190	2280	2500	2510	2590	2320	2720	2450	761	971	991	743	1110	1290	698	808	575	528	481	480
Cr	1520	2230	2840	2760	2470	2770	2390	4080	2220	2060	2130	1840	2350	2740	2580	2690	3220	609	1000	1580
Co	110	103	116	109	109	117	143	123	66	78	79	76	79	78	63	71	39	59	58	63
Zn	48	40	76	47	47	76	104	58	66	85	67	65	67	67	57	52	57	61	66	78
V	46	55	32	34	31	29	59	46	83	105	137	93	115	143	94	163	179	276	249	215
Zr	<10	<10	<10	<10	<10	<10	10	<10	35	18	19	13	16	32	47	64	34	45	35	34
Sr	8	11	6	9	9	7	10	8	14	10	13	14	9	9	13	7	66	101	72	69

Note: All major and trace element data by X-ray fluorescence.

Grt = garnet; Spl = spinel; Fe_2O_3 (t) = total Fe expressed as Fe_2O_3.

Appendix F

Chalcophile element (Cu and S) and platinum-group element (Os, Ir, Ru, Pt and Pd) compositions for Pali Aike xeno

		PGE (ppb)						Trace element (ppm)	
Lithology	Sample	Os	Ir	Ru	Pt	Pd	PGE-total	Cu	S
	LS33	3.45	3.35	6.98	4.37	3.56	21.71	6.35	21.5
	Dup	2.79	2.92	5.97	4.76	3.30	47.06	7.20	20.1
	SD (%)	14.97	9.54	11.04	6.03	5.46		8.40	4.88
	TM0	2.48	2.14	4.61	4.21	3.90	17.35	25.1	51.0
	Dup	2.34	2.15	4.59	4.92	4.09	18.10		
	SD (%)	4.21	0.57	0.42	11.06	3.35			
Grt-Spl Lherzolite	TM2	1.64	1.43	2.15	2.82	1.32	9.35	5.17	18.4
	LS50	4.85	3.95	7.40	4.58	2.35	23.14	2.95	9.51
	BN73	2.11	2.39	7.10	4.24	3.69	19.52	5.41	11.7
	Dup	2.39	2.60	5.96	4.60	3.78	19.33		
	SD (%)	8.73	5.89	12.29	5.85	1.73			
	LS1-2	2.41	2.73	6.15	4.66	4.05	19.99	7.08	10.6
	BN32	3.20	3.44	6.63	12.45	4.07	29.79	3.95	23.2
	TM14	0.69	0.30	1.11	0.44	0.83	3.37	1.33	9.10
	TM15	1.37	1.06	2.36	2.53	3.45	10.77	2.98	20.0
	TM15-Dup	1.56	1.29	2.48	2.22	2.63	10.19		
	SD (%)	9.36	14.31	3.52	9.38	19.12			
	BN92	4.53	4.08	8.40	4.91	4.63	26.55	2.30	13.4
Grt-Spl	BN50	4.93	2.47	6.35	13.53	18.32	45.60	3.39	21.2
Harzburgite	BN50-Dup	5.55	2.64	6.65	14.95	21.22	51.02		
	SD (%)	8.36	4.76	3.33	7.06	10.38			
	PAHK1	3.90	3.42	7.20	5.04	4.61	24.2	4.87	5.19
	PAK6	0.82	0.50	1.72	0.68	1.12	4.8	1.65	7.02
	BN45	3.53	2.95	6.40	5.65	4.25	22.8	3.02	5.07
	BN31	2.92	2.61	5.40	3.14	1.89	16.0	2.48	24.8
Spl Lherzolite	PA64	4.28	4.55	7.91	10.87	4.93	32.5	8.16	35.9
	PAK1	2.36	2.19	4.96	4.17	3.59	17.3	11.7	43.6
	LS5	1.94	1.90	3.67	2.06	0.62	10.2	3.09	4.69
	PAK2	2.20	1.99	4.22	1.43	0.88	10.7	2.60	8.62
	PAK3	2.84	2.66	4.99	2.05	1.52	14.1	2.51	8.31
Spl Harzburgite	LS100	4.00	3.61	7.56	3.88	1.29	20.3	2.85	8.35
	PAK5	2.85	2.25	4.89	1.10	0.56	11.7	3.01	8.21
	PAK5-Dup							2.94	7.67
	SD (%)							1.74	4.84
	01BN	2.28	2.83	6.81	6.26	3.19	21.4	7.98	4.39
	BNH13	1.79	2.07	3.63	4.13	4.22	15.8	8.95	144
	Dup	1.95	1.69	3.52	4.00	4.23		8.04	148
	SD (%)	6.11	14.00	2.13	2.37	0.21		7.62	1.90
	BNC2	3.62	3.07	7.59	4.78	2.35	21.4	2.88	11.5
	BNC1	3.17	3.78	7.61	3.77	1.36	19.7	14.1	22.1
	BN43	2.30	4.99	4.82	2.60	1.68	16.4	2.74	10.1
Grt	BNO5	4.17	3.81	7.22	10.25	4.31	29.8	6.93	17.4
Orthopyroxenite	BNC3	3.57	3.53	5.23	3.25	1.44	17.0	5.95	15.2
	BNH5	1.69	1.37	1.70	3.41	4.76	12.9	10.3	138.1
	BNH5-Dup							9.46	142.7
	SD (%)							5.68	2.33
	BN42	0.19	0.02	0.13	0.61	1.47	2.41	31.5	245.8
	BN42-Dup							30.4	259.8
	SD (%)							2.57	3.91
	BNH7	0.29	0.12	0.28	0.63	0.96	2.28	4.18	57.9
Websterite	BNC4	0.26	0.05	0.17	0.57	0.71	1.76	10.7	34.8
	BN31x	0.17	0.03	0.12	0.46	0.35	1.14	7.45	24.0
	LLS3	0.71	0.10	0.29	1.75	1.07	3.92	21.2	89.5

Notes: Cu and S data by aqua regia digestion with ICP-AES; Os, Ir, Ru, Pt and Pd data by Fire Assay ICP-MS.
SD =standard deviation based on duplicate analyses; Dup = duplicate; Grt = garnet; Spl = spinel.

Appendix G

Whole-rock major and selected trace element compositions for Cerro del Fraile mantle xenoliths

	C-type					F-type	
Rock type	Spl Lherzolite[a]			Spl Lherzolite[b]		Spl Lherzolite	
Sample	Bxe11	Bxe35	Bxe31	Bxe31-1	Bxe32	Bxe1	Bxe22
Major (wt%)							
SiO_2	43.29	41.52	42.28	47.54	45.47	41.08	40.97
Al_2O_3	2.57	1.46	1.71	4.03	3.01	4.78	5.44
TiO_2	0.04	0.04	0.05	0.12	0.11	0.13	0.14
MgO	41.07	43.86	41.87	29.13	32.41	33.28	32.60
Fe_2O_3(t)	8.70	9.44	9.53	6.30	7.03	13.45	13.16
MnO	0.13	0.13	0.14	0.12	0.13	0.19	0.19
CaO	2.67	1.27	2.66	9.79	9.26	5.56	5.76
K_2O	<0.01	0.02	0.01	0.01	<0.01	<0.01	<0.01
P_2O_5	0.01	0.01	0.02	0.02	0.01	0.02	0.02
Na_2O	<0.01	<0.01	<0.01	0.11	0.01	<0.01	0.03
LOI	0.30	1.40	0.70	1.30	0.60	0.20	0.50
Sum	98.77	97.94	98.54	97.86	98.09	99.00	98.79
Trace (ppm)							
Cu	9	8	58	104	59	34	38
S	14	2	31	24	35	34	42
Ni	1899	2573	2340	1312	1575	1208	1166
Cr	2844	1615	2139	5267	4742	3463	3315
Co	103	114	112	68	78	110	107
Zn	53	54	56	42	36	84	78
V	61	32	50	141	108	114	112
Sr	7	8	15	17	13	34	42

Notes: Major elements, Ni, Cr, Co, Zn, V and Sr data by X-ray fluorescence; Cu and S data by aqua regia digestion with ICP-atomic emission spectrometer.

a = slightly metasomatized Spl lherzolite by websterite; b = highly metasomatized Spl lherzolite by websterite
Spl = spinel; Fe_2O_3 (t) = total Fe expressed as Fe_2O_3.